UNIVERSITÀ DEGLI STUDI DI SALERNO

Dipartimento di Ingegneria dell'Informazione
ed Elettrica e Matematica Applicata

UNIVERSITÀ DEGLI STUDI DI PALERMO

Dipartimento di Ingegneria

PHD IN PHOTOVOLTAICS

Curriculum: Design and Integration

Dottorato di Interesse Nazionale in Photovoltaics

Vehicle-Integrated Photovoltaic (VIPV): From Modelling Frameworks to Real-World Applications

Supervisor:
Prof. Guido Ala

Co-Supervisor:
Prof. Pietro Romano

PhD Program Director:
Prof. Giovanni Spagnuolo

PhD Candidate:
Hamid Samadi
Mat. 8860800020

Dedicated to all those without whom I would not be here today,
to my family, both by blood and by heart,
and especially to my beloved Arshiya and Forough.

تقدیم به خانواده‌ام،

چه آن‌ها که با من هم‌خون‌اند،

چه مثل خون در رگ‌های من...

تقدیم به عرشیای عزیزم و فروغ نازنینم،

و به تمام عزیزانی که بودنشان، دلیل ماندن و رفتن من است...

Abstract

The transition toward sustainable transport requires innovative solutions to reduce the carbon footprint of vehicles while enhancing their energy autonomy. Among emerging technologies, Vehicle-Integrated Photovoltaic (VIPV) systems represent a promising pathway to sustainable transport sectors through on-board solar generation. This thesis presents a structured and flexible framework for the analysis, design, and performance assessment of VIPV systems across multiple operational contexts. Starting from proposing a generalized approach, based on conventional PV methodologies adapted for moving vehicles, a data-driven framework relying on real-world driving data collected through smartphones and onboard sensors, is also developed. This methodological transition enables accurate simulation of irradiance, temperature, and energy yield without the need for complex test setups. To support broader use, the workflow was implemented in an open-source MATLAB library, VIPVLIB, ensuring transparency, reproducibility, and future extensibility by the research community. The proposed frameworks were applied through case studies on various vehicle types and scenarios, including public-transport fleets (minibus, bus, and tram) and disaster-relief operations, so demonstrating their scalability and adaptability. Furthermore, economic and environmental analyses were performed too, for evaluating the Levelized Cost of Electricity (LCOE), grid parity, and CO_2-emission reductions under different European and climatic contexts. Overall, this work contributes a holistic methodology bridging modelling and practice, offering decision-makers and researchers a robust toolset for assessing VIPV feasibility, optimizing designs, and accelerating the integration of solar energy in the early future transport systems.

Keywords: Vehicle-Integrated Photovoltaic (VIPV), Sustainable Mobility, Decarbonization Strategies, VIPV Performance Assessment

Table of Contents

List of Figures:

List of Tables:

1

Sustainable Mobility Transitions and Vehicle-Integrated Photovoltaic (VIPV)

This chapter establishes the motivation and contextual foundations for VIPV within sustainable mobility transitions. It first quantifies the environmental burden of transport, underscoring its dual role as a major source of global greenhouse gas (GHG) emissions and a driver of local air pollution and premature mortality. While global CO_2 emissions from power generation show signs of decoupling through renewable deployment, transport emissions have proven comparatively resistant to structural change, rebounding rapidly after pandemic-related declines. The analysis details transport's persistent reliance on petroleum fuels, and the associated climate and health externalities.

The chapter then examines the transition to electrification. It documents the rapid growth of electric vehicle (EV) sales and charging infrastructure, the policy and technological drivers enabling this expansion, and the conditions required for deep life-cycle decarbonisation, namely clean electricity supply, equitable and reliable charging access, and sustainable battery value chains. A European perspective is briefly discussed, highlighting persistent reliance on fossil fuels in the legacy fleet, disparities in EV uptake and charging access, and the relevance of strengthening public transport provision to support modal shift.

Against this backdrop, VIPV is introduced as a complementary, on-board solar generation strategy that can extend range, reduce charging frequency, enhance energy autonomy and disaster resilience, and lower transmission losses. The discussion clarifies benefits, technical challenges, and the relevance of VIPV to sunny, highly motorised European regions. The chapter concludes by positioning VIPV within an integrated policy and technology pathway, alongside grid decarbonisation, electrification, and mobility reform, and outlines the thesis structure that builds from these premises to modelling, case studies, and design guidance in subsequent chapters.

1.1. Environmental Impact of Transportation

Transportation is one of the most essential enablers of economic growth and social connectivity. It facilitates trade, supports urban and rural livelihoods, and allows for the global circulation of goods, people, and knowledge. However, the environmental costs of this mobility system are substantial. Among all sectors of economic activity, transportation is unique in that it directly contributes both to global climate change and to localized environmental health problems. Its contribution to greenhouse gas (GHG) emissions accelerates global warming, while its release of air pollutants such as fine particulate matter ($PM_{2.5}$), nitrogen dioxide (NO_2), ozone (O_3), and carcinogenic hydrocarbons directly undermine public health. The dual role of transport as both a climate and health stressor has made it a focal point of sustainability debates in the 21st century. Despite decades of international negotiations on climate change and air quality, transport remains one of the most difficult sectors to decarbonize due to its dependence on fossil fuels, embedded infrastructures, and the continuous growth in mobility demand [1], [2].

1.1.1. Global Greenhouse Gas Emissions by Sector

Globally, anthropogenic CO_2 emissions are concentrated in a few but key sectors: power generation, industry, transport, and buildings. Data from the International Energy Agency show that the power sector remains the single largest emitter, with annual emissions exceeding 14 gigatonnes (Gt) CO_2. Industry, including heavy manufacturing and industrial processes, follows with about 9 Gt CO_2, while transport accounts for approximately 8 Gt CO_2, making it the third-largest source of emissions. Buildings contribute a smaller but still significant share, around 3 Gt CO_2 annually [3].

Figure 1.1 compares these three major sectors between 2019 and 2022. The data highlight several important trends.

- The power sector dominates: its emissions are nearly double those of transport, but unlike transport, it has viable large-scale alternatives in the form of renewable energy technologies (e.g., wind, solar, hydropower).
- Transport's resilience to shocks: transport emissions temporarily declined in 2020 due to the COVID-19 pandemic and mobility restrictions. However, by 2022, they had largely rebounded to pre-pandemic levels, demonstrating the sector's strong dependence on fossil fuel demand and the lack of structural decarbonisation.
- Limited progress compared to power: while the power sector is slowly decoupling from fossil fuel reliance through renewable deployment, transport emissions remain relatively flat, indicating that efficiency improvements and vehicle electrification have yet to achieve a systemic impact.

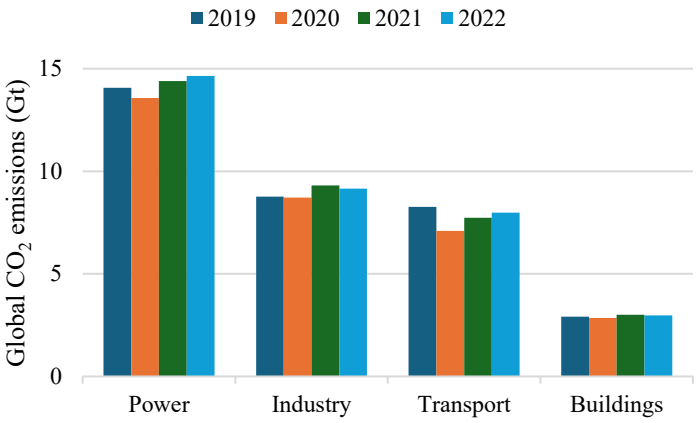

Figure 1.1. Global CO_2 emissions by sector, 2019–2022 (Gt CO_2). Source: IEA (2023).

1.1.2. Greenhouse Gas Emissions from Transport (Long-Term Trends)

Focusing in on transport-specific emissions reveals its central role in global warming. According to the IEA, transport accounted for nearly one-quarter of global energy-related CO_2 emissions in 2022. Over the past three decades, these emissions have grown steadily due to increasing demand for passenger mobility and freight transport, particularly in rapidly developing economies. Figure 1.2 shows the breakdown of global transport emissions by mode of transport between 1990 and 2022. Road transport is the dominant contributor, producing most emissions through passenger cars, freight trucks, and buses. Aviation and shipping have also shown strong growth, driven by globalization, e-commerce, and tourism. In contrast, rail and pipelines contribute comparatively minor shares, reflecting their greater energy efficiency and, in the case of rail, partial reliance on electrification [4].

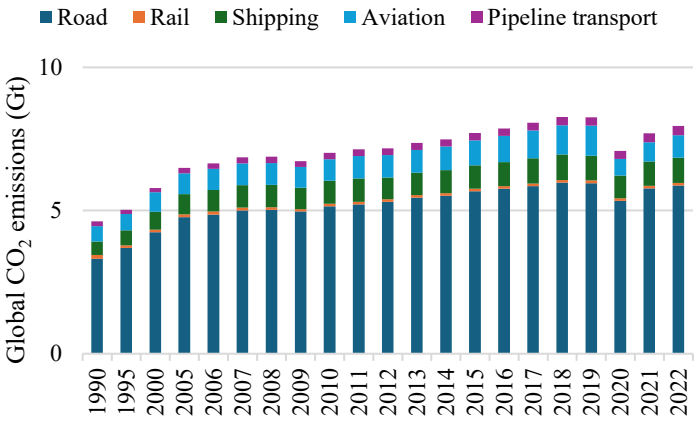

Figure 1.2. Global CO_2 emissions from the transport sector by mode of transport (1990–2022). Source: IEA (2023).

In the European Union, trends are more nuanced. Data from Eurostat indicate that overall GHG emissions fell substantially between 1990 and 2022, with the energy industry, households, and manufacturing all showing reductions of several hundred million tonnes of CO_2 equivalent. By contrast, emissions from transport, including international aviation, increased by nearly 30% during the same period (Figure 1.3). This divergence illustrates transport as the most persistent obstacle in Europe's decarbonisation pathway [5].

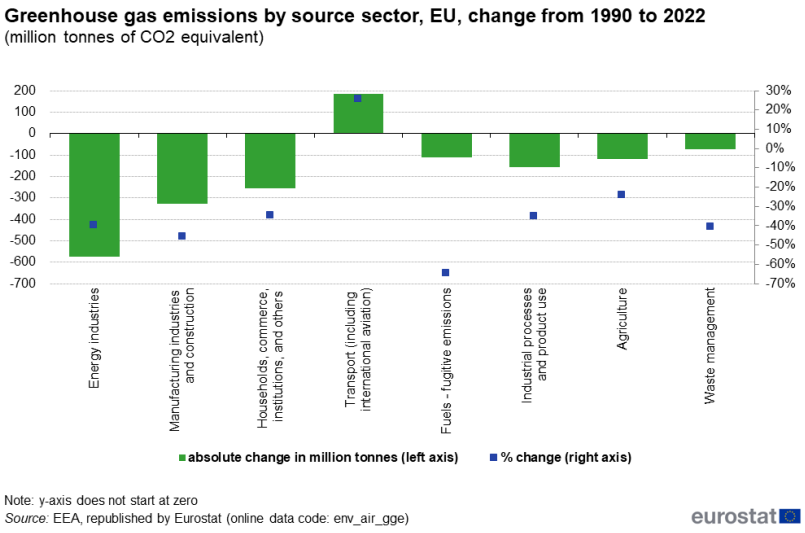

Figure 1.3. Greenhouse gas emissions by source sector in the EU, change from 1990 to 2022. Source: Eurostat/EEA (2023).

The persistence of transport emissions, even in regions with strong climate policies, reflects the combined challenges of technological inertia (e.g., internal combustion engine dominance), lifestyle choices (e.g., car dependency), and the slow turnover of vehicle fleets.

1.1.3. Energy Dependence of Transport

Transport's climate impact stems not only from the volume of activity but also from its near-exclusive reliance on fossil fuels. Figure 1.4 presents the evolution of global energy consumption in transport by fuel type since 1990. Petroleum products (gasoline, diesel, and jet fuel) overwhelmingly dominate the energy mix, while alternative fuels such as natural gas, biofuels, and electricity remain marginal [6].

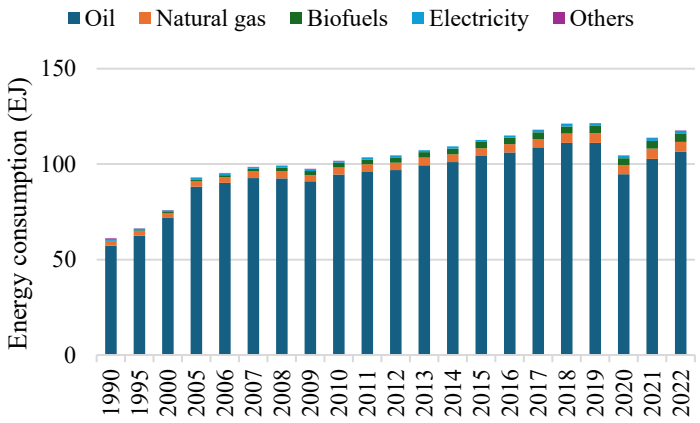

Figure 1.4. Global energy consumption in the transport sector by fuel type (1990–2022). Source: IEA (2023).

Despite political commitments and technological progress, the energy structure of transport has changed little in three decades. Several factors explain this inertia.

- High energy density of oil products: gasoline, diesel, and jet fuel provide more energy per unit of weight or volume than most alternatives, making them attractive for long-distance and heavy-duty applications.
- Established infrastructure: A global distribution and refuelling system for petroleum fuels already exists, lowering costs and reinforcing oil dependency.
- Slow fleet turnover: vehicles have long lifespans, meaning that even as new technologies emerge, it takes decades to replace existing fleets.
- Economic competitiveness: electric vehicles (EVs), hydrogen fuel cells, and advanced biofuels are advancing, but their cost, range, or infrastructure readiness still limit widespread adoption in many regions.

The persistence of oil dependence creates not only environmental but also geopolitical risks, exposing economies to oil price volatility and supply disruptions. This dual vulnerability underscores the urgency of accelerating the adoption of cleaner, renewable-based transport solutions.

1.1.4. Air Pollution and Health Burden

Beyond climate change, transportation is a major driver of local air pollution, which has immediate and severe impacts on human health. Vehicle exhaust contains a complex mixture of pollutants, including fine particulate matter ($PM_{2.5}$ and PM_{10}), nitrogen oxides (NO_x), carbon monoxide (CO), volatile organic compounds (VOCs), sulphur dioxide (SO_2), and polycyclic aromatic hydrocarbons such as benzo(a)pyrene (BaP). The World Health Organization estimates that 4.2 million premature deaths in 2019 are attributable to ambient (outdoor) air pollution. The health burden is dominated by cardiovascular disease (68%), followed by chronic obstructive pulmonary disease (14%), acute respiratory infections (14%), and lung cancers (4%). Fine particulate matter is considered the most harmful component, as it penetrates deep into the lungs and bloodstream, triggering inflammation, oxidative stress, and long-term tissue damage. Geographically, the burden is unevenly distributed. About 89% of pollution-related premature deaths occur in low- and middle-income countries,

particularly in South-East Asia and the Western Pacific. Nevertheless, even high-income regions like the EU face substantial mortality and morbidity burdens linked to transport-related air pollution [1].

1.1.5. Premature Deaths in Europe

The European Environment Agency (EEA) reports significant improvements in air quality since the early 2000s, driven by stricter vehicle standards, low-sulphur fuels, and air quality legislation. Between 2005 and 2020, premature deaths attributable to $PM_{2.5}$ exposure declined by approximately 45%, falling from over 400,000 to around 240,000 annually. Figure 1.5 presents this decline and projects future reductions under the Zero Pollution Action Plan (ZPAP), which targets a 55% reduction by 2030 compared to 2005 levels. While current trends suggest progress, additional policies and clean technologies are required to stay on track [7].

Figure 1.5.Premature deaths attributed to long-term exposure to $PM_{2.5}$ in EU-27 (2005–2020) and projection to 2030. Source: EEA (2023).

These improvements demonstrate the effectiveness of regulatory action but also highlight the scale of the remaining challenge. Hundreds of thousands of Europeans continue to die prematurely each year due to polluted air, a significant share of which is transport related.

1.2. Transition to Electrification

Electrification of road transport represents the cornerstone of sustainable mobility transitions. By replacing internal combustion engine (ICE) vehicles with battery electric vehicles (BEVs) and plug-in hybrid electric vehicles (PHEVs), direct tailpipe emissions of carbon dioxide (CO_2), nitrogen oxides (NO_x), and particulate matter (PM) can be substantially reduced. When powered by low-carbon electricity, EVs offer the potential for deep decarbonisation, reduced urban air pollution, and enhanced energy security by diversifying away from petroleum dependence. Over the last decade, the global uptake of electric vehicles has accelerated dramatically, transforming from a niche market into a central component of transport policy and industrial strategy. This section examines the rise of EVs, the enabling factors that underpin their growth, and the challenges that must be addressed for electrification to deliver its full environmental benefits [8], [9].

1.2.1. Global Trends in Electric Vehicle Adoption

Electric vehicle sales have experienced exponential growth in recent years. Annual sales rose from fewer than 500,000 in 2014 to nearly 14 million in 2023, equivalent to around 18% of global car sales. Figure 1.6 illustrates this surge in EV adoption by region and technology type (BEVs vs. PHEVs). China is the dominant market, accounting for more than half of global sales. Its leadership reflects a coordinated industrial policy, strong consumer subsidies, and massive investment in domestic battery supply chains. Europe has emerged as the second-largest EV market. Strict fleet emission standards, carbon pricing mechanisms, and government incentives have driven adoption. PHEVs initially played a major role, but BEVs are rapidly overtaking them as charging infrastructure expands [10].

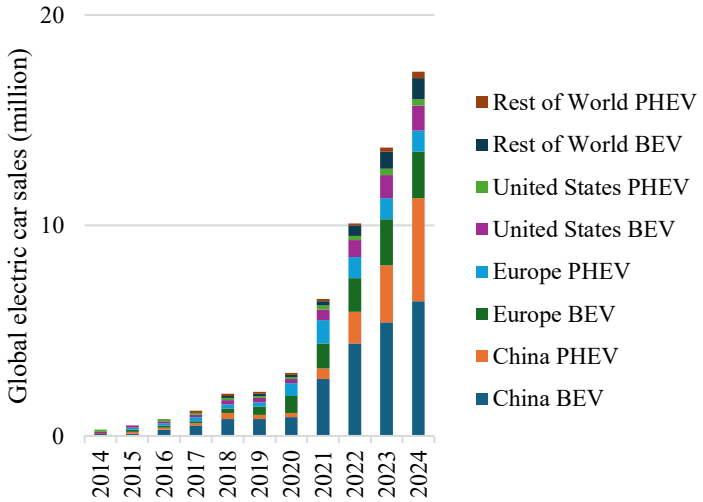

Figure 1.6. Global electric car sales by region and type (2014–2024). Source: IEA (2024).

1.2.2. Charging Infrastructure Development

The deployment of charging infrastructure is a decisive factor for consumer adoption and fleet electrification. Publicly accessible charging points have expanded rapidly since 2018, with growth led by China, followed by Europe and the United States. China has the largest charging network globally, with rapid expansion of fast chargers, especially in urban centres and along highways. Europe has established a balanced mix of slow (AC) and fast (DC) chargers, reflecting integration into residential, workplace, and highway systems. EU regulations, including the Alternative Fuels Infrastructure Regulation (AFIR), require uniform coverage across member states. United States deployment remains patchy, with higher densities in coastal states and limited rural coverage. Federal investments under the NEVI program aim to close these gaps. The balance between slow and fast charging also influences adoption. While slow charging dominates in residential and workplace contexts, fast charging is crucial for long-distance travel and commercial fleets. A steady rise in the share of fast chargers is observed, especially in China and Europe, to alleviate range anxiety [11], [12].

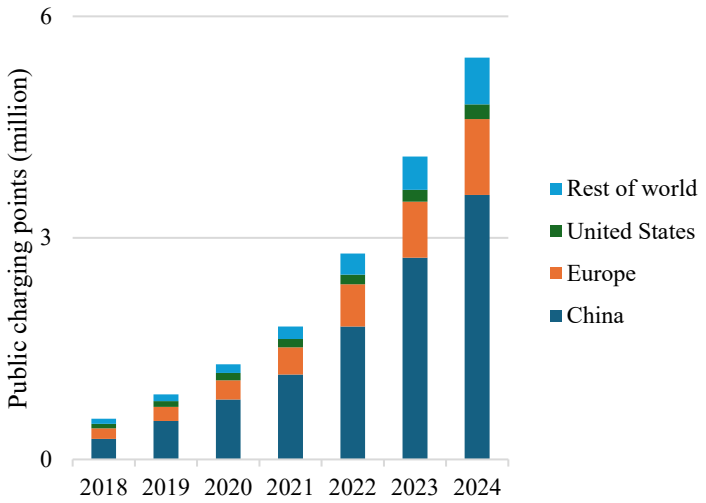

Figure 1.7. Global stock of public charging points by region (2018–2024). Source: IEA (2024).

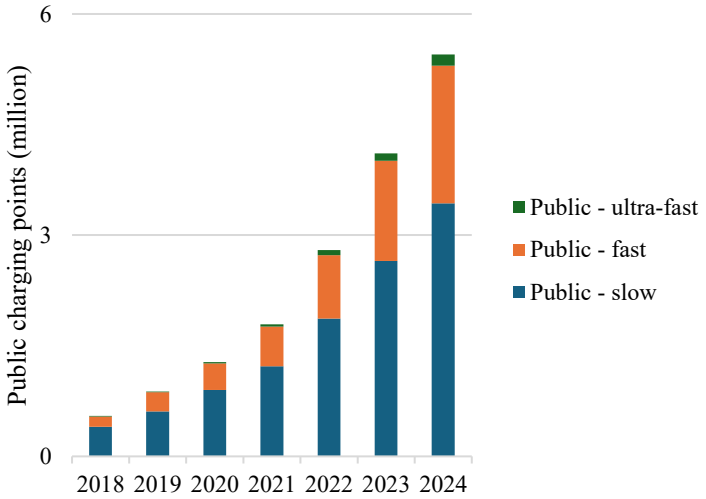

Figure 1.8. Global stock of public charging points by speed (2018–2024). Source: IEA (2024).

1.2.3. Affordability and Cost Parity

One of the major historical barriers to EV adoption has been the higher upfront purchase cost compared to ICE vehicles. However, this cost gap has narrowed significantly. Between 2018 and 2023, the price premium of BEVs relative to ICE cars declined steadily, driven by falling battery costs, scale efficiencies, and supportive incentives. In many cases, EVs are already competitive on a total cost of ownership (TCO) basis. Lower fuel and maintenance costs make EVs attractive for high-mileage users such as taxi and delivery fleets. Nevertheless, purchase price remains a challenge for lower-income consumers and in markets with limited subsidies [13].

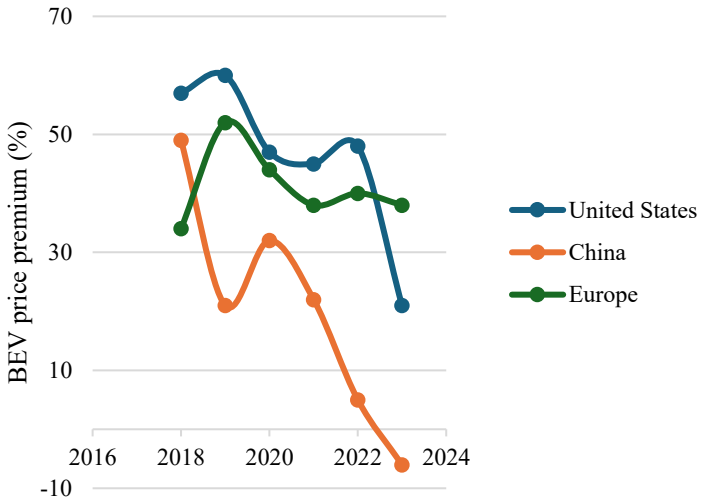

Figure 1.9. Battery electric car price premium compared to internal combustion engine cars (2018–2023). Source: IEA (2024).

1.2.4. Accessibility and Equity of Charging

Beyond total charging stock, the distribution and accessibility of chargers determine whether electrification is equitable and inclusive. In 2024, significant regional disparities were evident in the share of population living within 1 km of a charger. China achieved high accessibility in urban areas, supporting mass adoption. Europe has steadily increased accessibility, though rural regions remain underserved. United States still shows relatively low population coverage, with infrastructure concentrated in metropolitan areas. This uneven distribution creates charging deserts, particularly in rural and peripheral regions, which risks making EV adoption disproportionately accessible to urban, higher-income populations. Addressing this issue is critical for ensuring that electrification is a broad societal transition rather than a privilege of select groups [14].

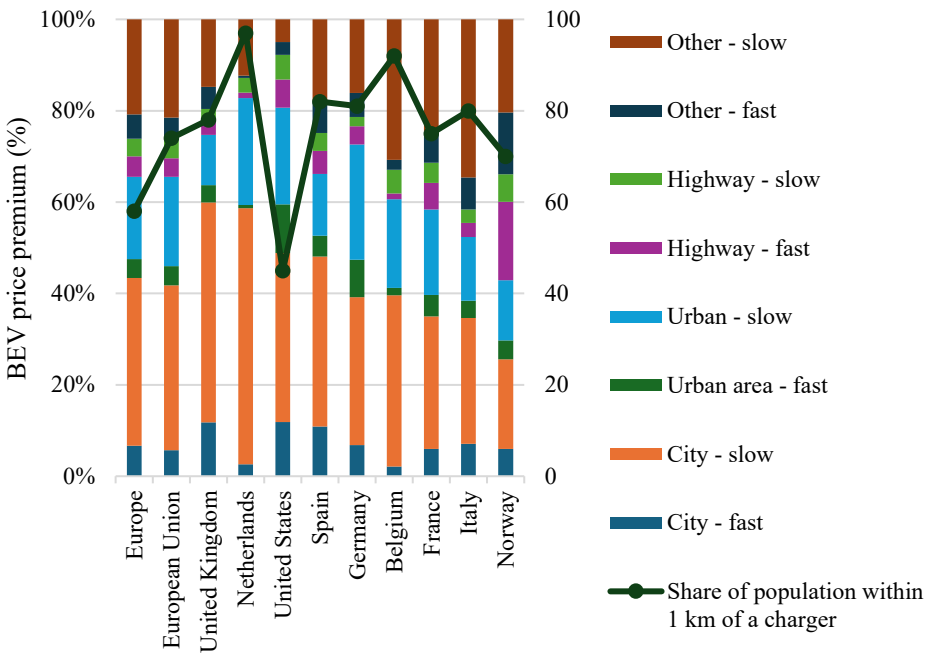

Figure 1.10. Type and location of public charging in selected regions and share of population within 1 km of a charger (2024). Source: IEA (2024).

1.2.5. Environmental Benefits and Challenges of EVs

Benefits [15], [16], [17]:

- **Climate mitigation**: BEVs eliminate direct tailpipe CO_2 emissions; when powered by clean grids, their life-cycle emissions are substantially lower than ICE vehicles.
- **Air quality improvement**: By removing exhaust pollutants, EVs contribute to lower NO_2 and $PM_{2.5}$ concentrations in urban areas, reducing premature deaths.
- **Energy efficiency**: Electric drivetrains achieve conversion efficiencies of 70–80%, compared to 20–30% for ICE vehicles.
- **Energy diversification**: Reduced dependence on petroleum improves energy security and aligns transport with renewable energy transitions.

Challenges [16], [18], [19]:

- **Battery material supply chains**: Mining of lithium, cobalt, and nickel raises environmental and ethical concerns, requiring sustainable sourcing and recycling strategies.
- **Grid integration**: Large-scale EV adoption increases electricity demand. Smart charging and vehicle-to-grid (V2G) technologies will be essential to maintain grid stability.
- **Carbon intensity of electricity**: In coal-dominated grids, the climate advantage of EVs is diminished, highlighting the need for simultaneous power sector decarbonisation.
- **End-of-life management**: Recycling systems for EV batteries remain underdeveloped; circular economy frameworks are needed to avoid shifting environmental burdens.

1.3. Vehicle-Integrated Photovoltaic (VIPV) Systems

1.3.1. Concept and Definition

The transportation sector, as discussed in the previous sections, is one of the largest contributors to global greenhouse gas (GHG) emissions and energy consumption. In particular, road transport is heavily dependent on fossil fuels, and while electrification offers a promising path forward, it also increases demand on electricity grids and depends on the availability of charging infrastructure. In this context, Vehicle-Integrated Photovoltaics (VIPV) has emerged as a complementary solution that can accelerate the decarbonisation of transport. VIPV refers to the integration of photovoltaic (PV) modules directly into the structural surfaces of vehicles, such as roofs, hoods, and side panels, allowing them to generate electricity from solar radiation during both driving and parking. With continued progress in PV technology, especially in lightweight and flexible designs, VIPV systems are becoming increasingly feasible for a variety of vehicle types [20], [21], [22], [23].

Unlike stationary PV systems (such as solar carports or charging stations), VIPV generates electricity on-board, delivering it directly to the vehicle's electrical system. This enables vehicles to meet part of their own energy demand using renewable energy, reducing the need for external charging and offering a decentralised approach to clean power generation within mobility systems [24], [25].

1.3.2. Advantages of VIPV

VIPV systems offer several compelling advantages that make them attractive as part of future sustainable transport strategies.

- **Range extension and reduced charging frequency**: By providing on-board renewable electricity, VIPV reduces the amount of grid electricity that electric vehicles (EVs) and plug-in hybrid electric vehicles (PHEVs) require. The generated energy can supply auxiliary loads, such as air conditioning, lighting, ventilation, and infotainment, or, depending on system capacity, contribute directly to traction power. This decreases the frequency of plug-in charging events and extends the effective driving range, particularly useful for urban and commuter vehicles [26].
- **On-board clean energy generation**: VIPV systems produce electricity wherever the vehicle is located, whether stationary or in motion. This decentralised generation contrasts with fixed PV installations, which are tied to specific sites, and makes use of the otherwise idle vehicle surfaces exposed to sunlight [27].
- **Disaster resilience and energy autonomy**: In the event of grid outages caused by natural disasters (e.g. earthquakes, floods, or wildfires), VIPV-equipped vehicles can act as mobile power sources for emergency loads. This capability increases the resilience of transport and energy systems and is particularly valuable for emergency fleets, public services, and remote areas [28], [29].
- **Compatibility with urban trends**: As cities become denser and parking or charging infrastructure faces space constraints, VIPV offers a distributed and flexible form of energy generation. It reduces dependence on centralised charging stations and can relieve pressure on urban grids, especially during peak demand periods [30].

These combined advantages highlight VIPV as a complementary solution that can enhance the performance, autonomy, and sustainability of future electric mobility systems.

1.3.3. Applications of VIPV

VIPV systems have been explored for a broad range of vehicle categories, each with distinct energy requirements, operating profiles, and available surface areas.

- **Passenger cars**: Private cars represent the largest market segment for VIPV development. Even though their available PV area is relatively small (typically 2–3 m²), they can achieve meaningful benefits by powering auxiliary loads or adding a few extra kilometres of range per day. This is especially useful for lightweight, short-range commuter vehicles [31], [32].
- **Commercial vehicles**: Delivery vans, refrigerated trucks, and long-haul lorries can use integrated PV modules to power refrigeration, ventilation, or lighting systems, lowering operational costs and reducing downtime for charging. Buses can integrate larger PV areas on their roofs to assist traction and auxiliary systems, particularly beneficial in hot climates where air conditioning loads are high [33].
- **Public transport**: VIPV-equipped buses and minibuses can reduce emissions and energy costs for public fleets, while lowering dependence on charging infrastructure. This is especially advantageous in regions with high solar irradiance and limited charging coverage [34].

Special platforms: aircraft, trains, ships, and boats have also been investigated as platforms for PV integration. In these cases, VIPV can power lighting, navigation, or auxiliary systems. Ships and yachts offer large available surfaces and long idle times, making them well-suited to PV generation for hotel loads (cooling, lighting, electronics) [35].

A systematic review of VIPV projects worldwide has categorised development by vehicle type and measured the mean PV surface available for each category.

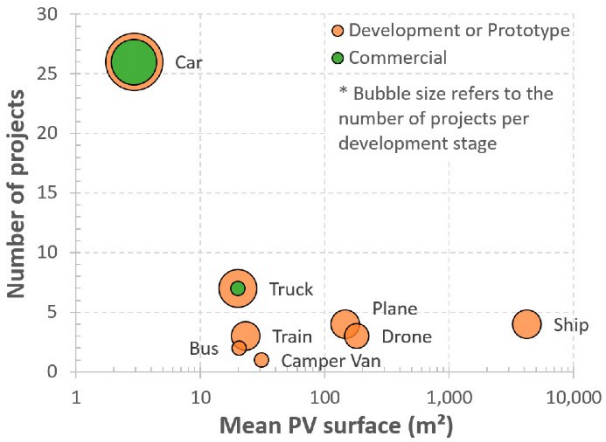

Figure 1.11. Number of VIPV projects by vehicle category and mean PV surface area [35].

As shown in Figure 1.11, passenger cars dominate current VIPV projects, while ships and heavy vehicles offer the largest technical potential but remain in earlier development stages. This illustrates a dual trend: high market readiness for small vehicles and high technical potential for large vehicles.

1.3.4. Technical Challenges and Limitations

Despite their promise, VIPV systems face several significant challenges that limit widespread deployment.

- **Weight and fragility of conventional PV modules**: Traditional crystalline silicon PV modules are heavy, rigid, and rely on glass encapsulation. These properties are not ideal for mobile applications where weight reduction is critical for efficiency [36], [37].
- **Complex vehicle geometries**: Vehicle bodies feature curved and three-dimensional surfaces, complicating the integration of flat PV panels. Ensuring sufficient irradiance capture on non-optimal orientations remains a major technical hurdle [38], [39].
- **Durability and safety**: Vehicle-mounted PV modules must withstand vibrations, mechanical impacts, temperature fluctuations, and weathering over long operational lifetimes. They must also comply with strict automotive safety standards, including crashworthiness and pedestrian protection regulations [40].
- **Lower irradiance capture and variable orientation**: Unlike stationary PV systems, vehicles are mobile and cannot consistently maintain optimal orientation towards the sun. Shading from surrounding buildings, trees, or even other vehicle parts can reduce energy yields [41].
- **Cost and standardisation**: VIPV systems are still relatively expensive, partly due to the lack of standardised manufacturing processes, mounting systems, and regulatory guidelines [42].

Recent research has focused on overcoming these limitations by developing lightweight and flexible PV technologies, such as thin-film modules, organic photovoltaics (OPV), and perovskite–silicon tandem cells. These emerging materials are more adaptable to curved geometries and offer improved resilience, making them promising candidates for large-scale VIPV integration [43].

1.3.5. Relevance to the European Context

Many regions in Southern Europe, such as Italy, Spain, and Greece, enjoy high solar irradiance, making them ideal for solar energy harvesting.

In such regions, VIPV can:

- offset part of daily driving energy, reducing pressure on public charging networks;
- improve the economics and convenience of EVs, especially for users without private home charging;
- support public transport electrification (buses, minibuses) by reducing operational energy demand and extending intervals between charging.

VIPV can therefore complement ongoing electrification policies, contributing to both energy diversification and decarbonisation of European transport systems. VIPV may not be a standalone solution but a complementary technology that can support the transition to electric mobility, particularly in sunny, highly motorised regions and for use cases with predictable daily driving profiles. As PV technology continues to improve in efficiency and flexibility, and as regulatory frameworks mature, VIPV has the potential to play a meaningful role in reducing transport emissions and advancing sustainable mobility.

1.4. Structure of the Thesis

This thesis is structured to progressively explore the potential of VIPV systems as a pathway for embedding renewable energy directly into the transport sector. Although VIPV is not a new concept, many of its technical, operational, and methodological dimensions remain underexplored. The present work therefore seeks to bridge these gaps by combining literature-based analyses, methodological developments, and applied case studies in diverse real-world transport contexts.

The research follows a bottom-up structure, beginning with the environmental motivations for transport decarbonisation (as already underlined in this chapter), the physical fundamentals of VIPV performance, and advancing toward the formulation, validation, and application of novel modelling frameworks.

Chapter 2 establishes the physical and technological basis for VIPV performance. It examines how installation geometry, surface curvature, shading, and temperature affect energy yield, and compares major PV technologies (crystalline silicon, thin-film, III–V, and transparent PV). It also discusses the electrical and thermal characteristics of mobile PV systems. These insights provide the necessary foundation for the modelling work developed in the following chapters. Chapters 3–6, translate theoretical understanding into applied investigations across four representative transport applications. Each case study evaluates both technical feasibility and environmental–economic benefits, while progressively advancing the simulation methodologies that underpin the thesis.

Chapter 3 develops a dedicated methodology for estimating VIPV energy generation under unpredictable and critical conditions, such as those encountered during disasters. The framework adapts VIPV simulation principles to low-predictability environments, demonstrating the potential of VIPV as a mobile renewable energy source for enhancing energy resilience and emergency preparedness.

Chapter 4 introduces a comprehensive optical–thermal–electrical model chain, implemented in the open-source MATLAB toolbox VIPVLIB, and validated on a minibus operating within the University of Palermo campus. While Chapter 3 and Chapter 4 present two distinct methodological developments, their connection is sequential and complementary: the first establishes the conceptual and parametric basis under constrained conditions, while the second completes and consolidates the full framework by integrating both the generalized and data-driven modelling approaches.

Chapter 5 extends the framework to airport contexts through a two-scenario analytical model, the Generalized Approach and the Data-Driven Approach, to quantify energy yield and emission savings across different climates and route types. Applied to European and Middle Eastern airports, it demonstrates the transferability and scalability of the developed framework to fleet-level assessments and identifies grid-parity thresholds for economic feasibility.

Chapter 6 applies the methodology to urban and inter-urban public transport, focusing on trams and buses in Palermo and shuttle buses in Brussels. It evaluates optical, thermal, and electrical performance under real driving conditions and compares environmental and economic indicators, illustrating the adaptability of VIPV models to diverse climatic and operational settings. And finally, Chapter 7 synthesises the findings of all case studies, summarising the main scientific and methodological contributions.

Overall, this thesis advances both the scientific understanding and practical assessment capabilities of VIPV systems. Its main novelties lie in the following.

- The formulation of a generalised methodology applicable across different vehicle categories and operational conditions.

- The creation of a multi-domain simulation framework that couples optical, thermal, and electrical processes using real driving data.
- The stepwise methodological development progresses from a generalised approach (Chapter 3) to a data-driven approach (Chapter 4), with both subsequently integrated and applied within a comprehensive general framework (Chapter 5).
- The application of VIPV analysis to multiple, underexplored transport segments, emergency fleets, institutional vehicles, airport operations, and public transport, offering one of the most comprehensive and cross-sectoral evaluations of VIPV systems to date.

Together, these contributions position the thesis as both a methodological reference and a possible way to the integration of solar energy in sustainable mobility systems, linking energy transition objectives with practical engineering applications.

2

Factors Influencing VIPV Performance

This chapter provides a comprehensive analysis of the fundamental parameters influencing the performance of VIPV systems, establishing the physical and technological basis for subsequent modelling and simulation developments. The discussion begins with the influence of installation position and usable vehicle surfaces, emphasizing how geometric complexity, curvature, and shading conditions govern the solar irradiance distribution over different vehicle panels. Comparative field studies and simulations are reviewed to illustrate how environmental factors such as seasonal variation, urban morphology, and operational dynamics affect irradiance ratios between roof, side, and rear surfaces under real-world conditions.

The chapter then examines the geometric and surface correction factors required to accurately quantify effective irradiance on curved or irregular vehicle bodies, introducing relevant dimensionless parameters for vehicle roofs that enable a generalized geometric representation across diverse vehicle types. The influence of PV technology choice is analysed next, comparing crystalline silicon, thin-film, multi-junction (III–V), and transparent solar cells in terms of efficiency, flexibility, weight, and integration feasibility. Particular attention is given to the structural innovations, such as lightweight encapsulation, shingled or segmented cell designs, and composite backings, that allow PV modules to conform to curved vehicle surfaces while maintaining mechanical integrity. Subsequent sections explore the electrical and thermal behaviours of VIPV systems, focusing on the role of interconnection strategies, bypass diode configurations, and shading mitigation in ensuring stable power output under non-uniform irradiance. The impact of temperature on module performance is also discussed in depth, with emphasis on the application and adaptation of the NOCT (Nominal Operating Cell Temperature) and Faiman models for mobile platforms [91-92]. The inclusion of vehicle-speed-dependent convective cooling and thermal inertia corrections is shown to be essential for achieving realistic temperature and energy yield predictions.

Overall, this chapter synthesizes the key physical, geometric, electrical, and environmental aspects that collectively determine VIPV performance. By integrating insights from previous experimental studies and theoretical analyses in the literature review, it establishes a solid conceptual framework that underpins the advanced simulation methodologies developed in the following chapters.

2.1. Installation Position and Usable Vehicle Surfaces

The physical placement of PV modules on a vehicle is one of the most fundamental factors determining the performance of VIPV systems. Unlike stationary PV installations, vehicles offer only a limited and irregular surface area for solar integration, spread across multiple geometrically complex and dynamically oriented body panels. As a result, the amount of solar irradiance captured, and consequently the energy generated, is highly dependent on where the PV modules are installed. The design must therefore carefully consider the choice of surfaces, their geometric characteristics, and the environmental and operational conditions under which the vehicle is used [35], [44].

2.1.1. Typical Surfaces for VIPV Integration

In most early VIPV studies and prototypes, PV modules were mounted exclusively on the roof, which is generally the flattest, strongest, and least shaded surface of the vehicle. The roof receives the greatest amount of direct solar radiation over the course of the day. Because of these advantages, it has become the standard reference surface in most research and commercial applications [45].

However, with advances in module design, including the development of lightweight polymer encapsulants, flexible thin-film laminates, and segmented crystalline silicon cells, VIPV integration has expanded beyond the roof to include the hood, trunk or rear deck, and side panels of vehicles. Some case studies have also used transparent or semi-transparent PV films on windows, allowing energy generation without blocking visibility [46], [47]. In addition, several studies have explored the use of modular or deployable PV structures to increase the active area, such as foldable solar awnings for camper vans, canopy-like modules on boats, or solar elements mounted on the spoilers and side fairings of trucks. These approaches demonstrate that the available area for VIPV can be creatively extended beyond fixed body surfaces, provided that additional weight, aerodynamic drag, and structural considerations are managed appropriately. This is especially relevant for larger vehicles such as buses, trucks, and ships, which have higher energy demands and more surface area to accommodate solar modules [28], [48].

2.1.2. Measured Contribution of Different Surfaces

The impact of installation position has been confirmed through experimental field studies. A case study in Hanover, Germany, involved a vehicle equipped with fifteen amorphous silicon (a-Si) modules with a total power of 2180 W_p, distributed as 875 W_p on the roof, 870 W_p on the sides, and 435 W_p on the rear. The vehicle was driven along a 36 km route under real conditions [49]. Results showed that the roof-mounted modules consistently received the highest irradiance, as expected. However, the side and rear modules still contributed significantly, especially under cloudy sky conditions dominated by diffuse radiation.

A second study conducted in Miyazaki, Japan, tested a similar configuration along a 15 km route in sunny weather [50]. The roof outperformed the other surfaces, but the difference between the roof and the sides was smaller than expected, showing how diffuse light increases the relative contribution of non-horizontal surfaces.

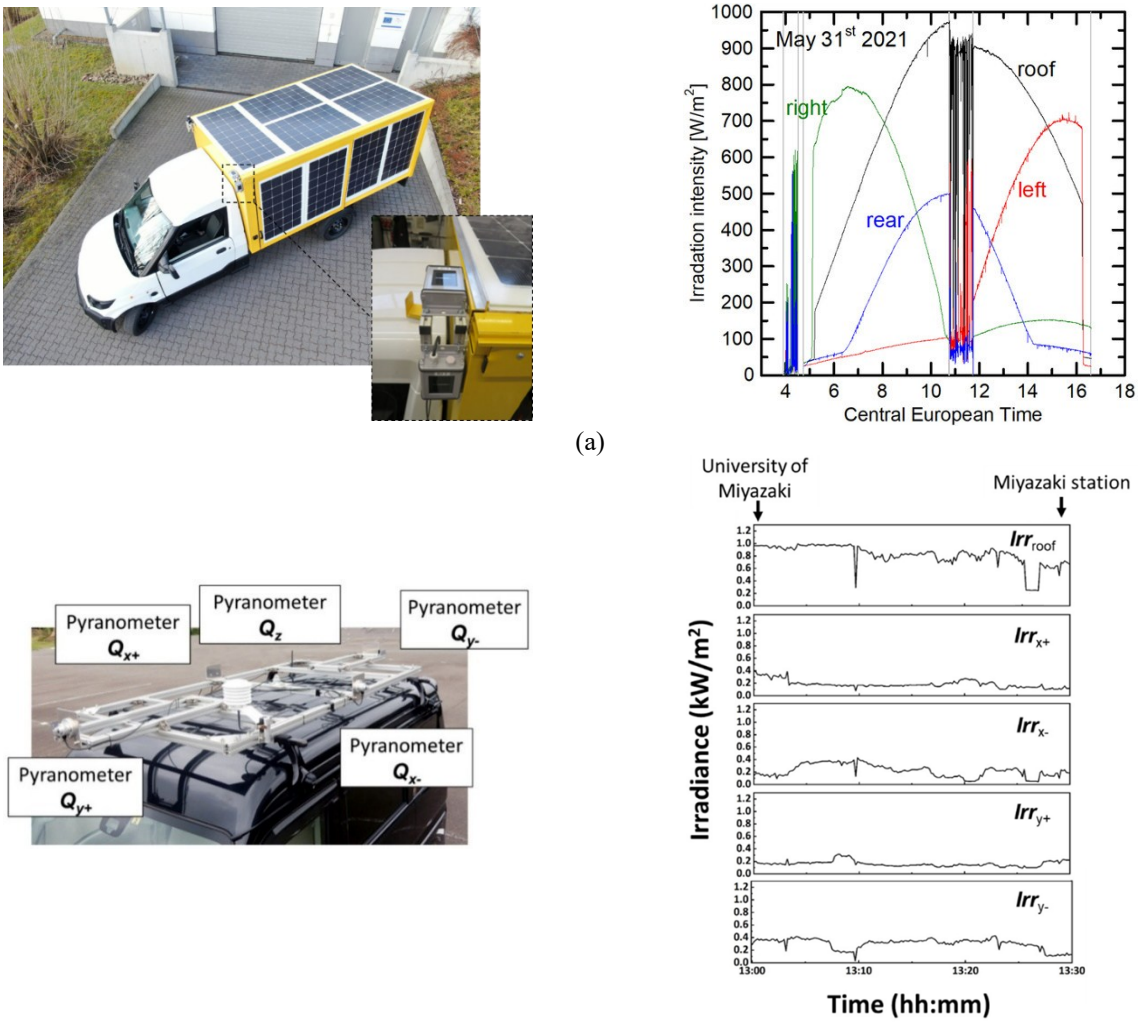

Figure 2.1. The irradiance received on the roof and side surfaces of a vehicle during real driving tests in (a) Hannover, Germany, and (b) Miyazaki, Japan, under different conditions [49], [50].

2.1.3. Seasonal and Urban Morphology Effects

Long-term measurements in Hannover have quantified how the contribution of different surfaces changes with season and street geometry. In this study, a van equipped with PV sensors was driven along a 21 km route covering narrow streets with tall buildings, wide slow streets, and wide fast arterial roads [51].

- Narrow streets with tall buildings (high shading, 30 km/h),
- Wide, slower streets with moderate building density (50 km/h),
- Wide, open roads with minimal shading (higher speeds, some overpasses).

The ratio of irradiance on the roof compared to the sides ranged from about 1.09 in winter to 3.85 in summer. In winter, when the solar altitude is lower and diffuse radiation dominates, the difference between roof and side panels was relatively small. In summer, when direct sunlight is stronger and the sun's path is higher, the roof received more than three times the irradiance of the sides. The test paths were balanced across cardinal directions (north–south and east–west), and each run lasted 40–55 minutes depending on traffic conditions.

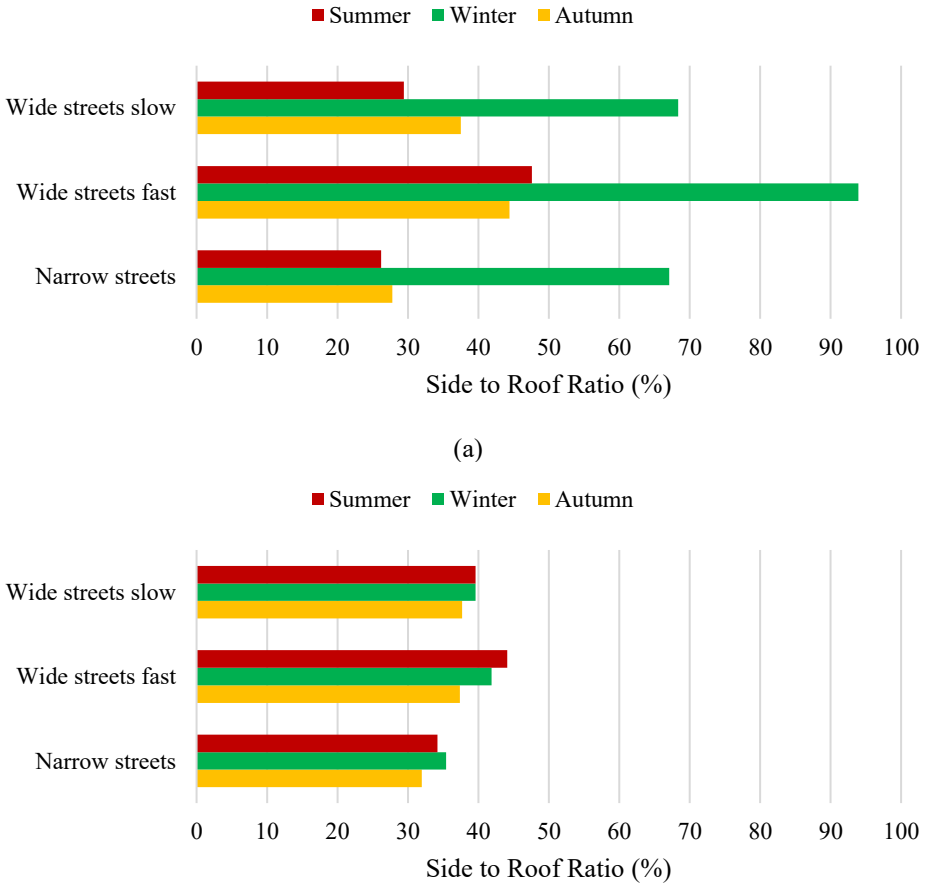

Figure 2.2. Ratio of irradiance on the sides compared to the roof in (a) sunny conditions, and (b) cloudy conditions, for different street types (narrow streets, wide slow streets, wide fast streets) and seasons [51].

Urban form also plays a crucial role because shading from buildings and roadside vegetation reduces the available irradiance. Narrow streets with high façades produced the largest roof-to-side irradiance gaps, while wide streets with lower buildings allowed more uniform solar exposure on all surfaces. These results show that irradiance distribution is highly context-dependent and that the layout of streets and buildings directly influences VIPV performance.

In winter, the lower solar elevation angle increases the incidence on vertical or tilted surfaces, allowing side panels to receive up to 90% of the irradiance measured on the roof. In summer, by contrast, when direct beam radiation dominates, side panels often receive only 25–35% of roof irradiance.

Golubev and Lunt [47] modelled a 2.6 m² crystalline silicon (c-Si) module mounted on the roof of a Jeep Grand Cherokee in Phoenix, United States. While the ideal daily conversion efficiency was around 20 %, the effective efficiency dropped to about 16 % once real-world factors such as off-angle irradiance and elevated module temperatures were included. This demonstrates how season, incidence angle, and thermal conditions interact to reduce real-world VIPV yields compared to theoretical estimates.

2.1.4. Shading and Operational Factors

As already stated, shading is one of the most critical and often underestimated causes of energy losses in VIPV systems, especially in dense urban environments [52]. A study by Karoui et al. [53] modelled shading in typical urban canyons in Paris with 10 m building heights and 11 m street widths. They compared a scenario with constant shading over the year to one with variable shading that was higher in winter. The results showed that shading can induce about 30 % annual energy loss, with monthly values ranging from 21 % to 69 %, and that the losses are highest in winter due to the lower solar elevation. Similarly, Brito et al. [54] reported that shading losses in Lisbon follow a strong seasonal pattern, with higher losses in winter and lower in summer.

Complementary field measurements by Araki et al. [55] used a fisheye camera mounted on a vehicle roof to record real shading conditions across different zones. They found average shading values of 11 % in open areas, 27 % in residential zones, and 46 % in dense building zones, confirming the strong dependence of shading on local morphology. These results are consistent with the Hannover data [51], where narrow streets with high façades caused the largest roof-to-side irradiance gaps.

Beyond shading, the operational profile of the vehicle also affects energy production. Passenger cars used mainly for commuting often spend long periods parked outdoors, meaning most of their solar energy is generated while stationary. In such cases, parking orientation, time of day, and nearby obstacles are critical. In contrast, long-distance buses, trucks, and delivery vans generate a large share of their solar energy while in motion. This has two implications: first, the airflow during motion enhances convective cooling, reducing module temperature and improving efficiency; second, intermittent shading from overpasses, trees, and roadside objects introduces fluctuations in solar yield [56], [57].

These factors underline that VIPV performance is not fixed but depends on how and where the vehicle is used. A well-designed system must therefore be tailored not only to the geometry of the vehicle and the PV technology, but also to the local urban context, climatic conditions, and typical driving and parking behaviour.

2.2. Effect of Curvature and Surface Correction Factors

While the choice of installation surface strongly influences the performance of VIPV systems, the geometrical shape and curvature of those surfaces also play a decisive role. Unlike stationary PV installations, which are typically mounted on flat panels with uniform orientation, vehicles have highly curved and complex body geometries. These curves reduce the effective irradiance received per unit of physical area and can also introduce optical and electrical losses. For this reason, it is essential to accurately characterise the geometry of vehicle surfaces when estimating the performance of VIPV systems [58], [59], [60].

2.2.1. Geometric effects of curvature on irradiance

A curved surface has a larger physical area than its flat projection onto a horizontal plane. While this increases the potential space for integrating solar cells, it also means that individual points on the surface are often tilted at an angle to the incoming sunlight. As a result, they receive less irradiance per unit area compared to a flat surface facing the sun. This effect is particularly pronounced for highly curved car roofs or rounded bus fronts, where some parts of the surface can be nearly vertical

or even facing away from the sun at certain times of day. This phenomenon can be expressed mathematically by introducing correction factors that relate the actual curved surface area to the effective projected area that receives sunlight [61], [62].

$$P = f \,.A_{Curved\ Surface} \,.Irr_{roof} \,.\eta_{PV} \quad (2.1)$$

$$f = f_1 f_2 f_3 \quad (2.2)$$

Where f is the curve correction factor, $A_{Curved\ Surface}$ is the surface area of the curved module, Irr_{roof} is the amount of radiation absorbed by the assumed car roof and η_{PV} is the efficiency of the solar cell, f_1 is the coverage factor, f_2 is the optical curve correction factor, and f_3 is the uneven expansion correction factor. The coverage coefficient can be obtained as follows [63]:

$$f_2 = \frac{A_{Projected\ Surface}}{A_{Curved\ Surface}} \quad (2.3)$$

As can be seen in Figure 2.3, the blue part corresponds to the predicted area and the gray part corresponds to the surface of the curve. According to the calculations, the value of f_2 for most commercial vehicles in the market is around 0.85 to 0.95. Furthermore, in this figure, the calculated values of the curve correction factor for four different levels with different values of f_2 can be seen. According to this diagram, when f_2 is equal to one (that is, the predicted surface area and the body surface are equal), the value of the curve correction coefficient will also be equal to 1 [64].

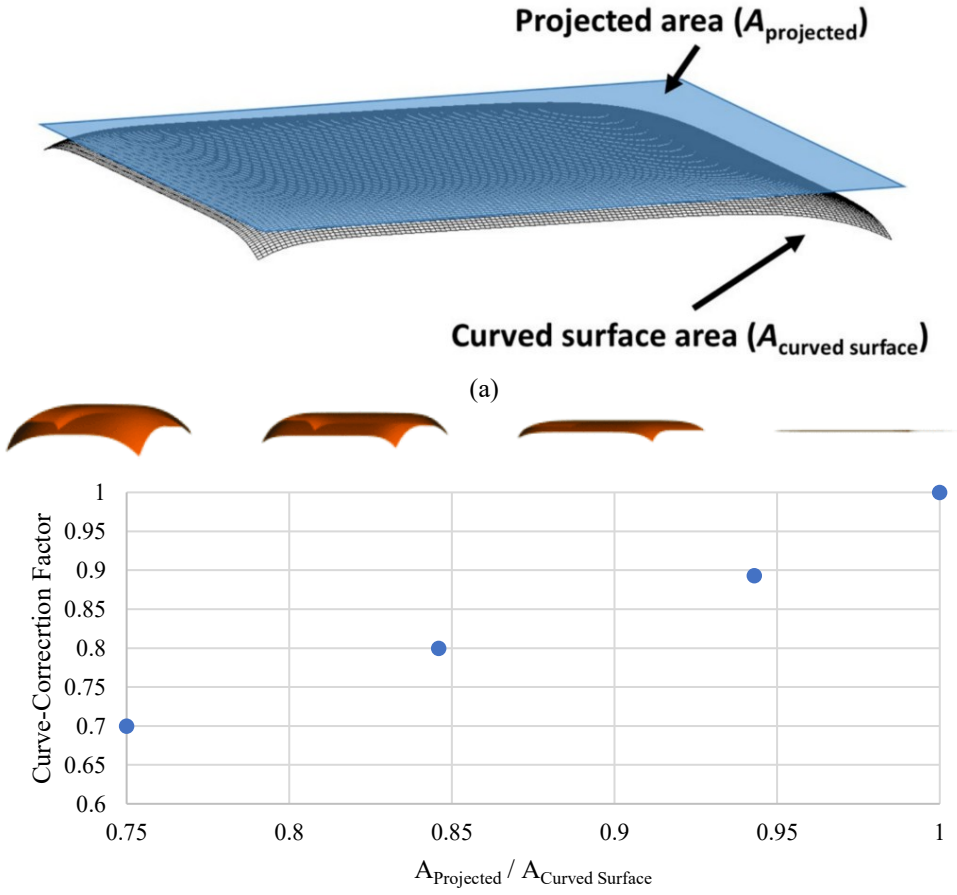

Figure 2.3. (a) Schematic of projected surface (blue part) and curved surface (gray part) and (b) calculated values for four different surfaces.

Naturally, the more cells are integrated into the car body, and the more surface of the car is exposed to sunlight, the system's output power increases. However, this value is different according to the physical limitations of the body and the type of solar cell in terms of flexibility or transparency. Additionally, the curvature of the corresponding surface causes some optical losses due to local cosine loss. All the parameters mentioned affect output power somehow. For this reason, to design a VIPV system, it is necessary to consider all the mentioned items. Since in addition to their effect on the output power, some cases have a mutual effect on each other. So, the number of cells that can be integrated on the body's surface can differ based on different conditions because in addition to mechanical factors such as curvature and strength, optical factors, and the discussion of the amount of incoming radiation are also essential [61].

2.2.2. Dimensionless geometric parameters for vehicle roofs

Using and defining dimensionless numbers for the independence of a study or a design from different parameters or reducing their number is a convenient and popular method among researchers. In this regard, and according to more than 200 models of roofs of different cars, its design can be described or analyzed with the help of eight dimensionless geometric parameters mentioned in Table 2.1, regardless of the car model. Equations 4–6 show the relationship between the mentioned parameters. Furthermore, for a better understanding of these parameters, the schematic of a car and its related parameters can be seen in Figure 2.4 [62].

$$f(x) = \frac{-tan\,(\theta_x)}{m_x}|X^{m_x}| \tag{2.4}$$

$$g_1(y) = \frac{-tan\,(\theta_{y1})}{m_{y1}}\left|(\frac{y}{r_1})^{m_{y1}}\right| \tag{2.5}$$

$$g_2(y) = \frac{-tan\,(\theta_{y2})}{m_{y2}}\left|(\frac{y}{r_2})^{m_{y2}}\right| \tag{2.6}$$

Table 2.1. Eight dimensionless parameters defined to describe the roof of different commercial vehicles [62].

Parameter	Details
m_x	Order of the curve of the ridgeline in the width direction
m_{y1}	Order of the curve of the front ridge of the side
m_{y2}	Order of the curve of the ridgeline behind the side
θ_x	Tangential angle in the width direction
θ_{y1}	Forward tangential angle
θ_{y2}	Backward tangential angle
r_1	Relative distance from the top of the vehicle roof to the front end
r_2	Relative distance from the top of the vehicle roof to the rear end

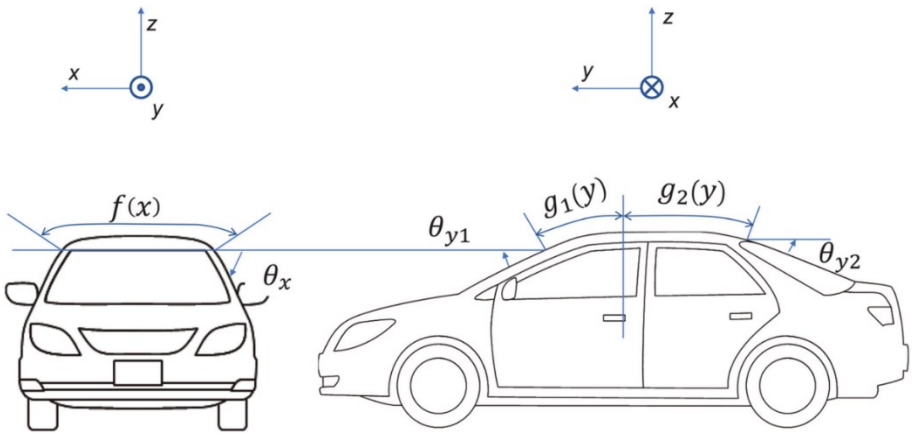

Figure 2.4. Schematic of a commercial vehicle and dimensionless parameters defined to describe its roof [62].

2.3. Types of PV Cells and Module Structures

The choice of PV cell technology and the structure of the modules in which they are embedded is another crucial determinant of the performance and feasibility of VIPV systems. Unlike stationary PV installations, where weight, flexibility, and curvature are less constraining, VIPV applications demand technologies that combine high efficiency with mechanical adaptability, low weight, and durability. The geometry-related limitations discussed in Section 2.2 mean that even if large surface areas are available, not all of this area can be used effectively unless the PV technology is compatible with the shape and structural constraints of the vehicle. A wide range of PV technologies has been developed over the past decades, and each presents different trade-offs in terms of efficiency, cost, flexibility, and mechanical strength. Figure 2.5 summarizes the attained and potential efficiencies of several major PV cell types currently relevant for VIPV systems [37], [65], [66].

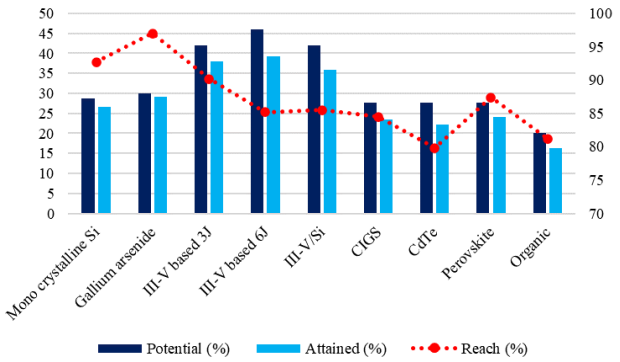

Figure 2.5. Comparison between potential and attained efficiency of different solar cell technologies relevant for VIPV.

2.3.1. Crystalline Silicon (c-Si)

Crystalline silicon (c-Si) solar cells are by far the most widely used PV technology globally, representing more than 90% of installed capacity worldwide. They are attractive for VIPV applications because of their high efficiency (20–24 % in commercial modules), long-term stability,

and mature mass-production infrastructure, which makes them relatively inexpensive compared to other technologies. Their robustness and proven durability under outdoor conditions are major advantages for automotive environments that involve mechanical vibrations, temperature cycling, and exposure to moisture and dust [65], [66], [67].

However, traditional c-Si modules are designed for stationary rooftop use and have a rigid architecture consisting of a glass front sheet, encapsulant layers (e.g. EVA), a polymer backsheet, and an aluminum frame. This structure, illustrated in Figure 2.6a, ensures long service life but results in relatively high weight and poor flexibility. The glass front sheet alone can account for nearly half of the total module mass, and the entire structure is difficult to bend without fracturing the silicon wafers. This makes conventional c-Si modules poorly suited to the curved body panels of vehicles. To overcome these limitations, researchers and industry have developed lightweight and flexible adaptations of c-Si modules. One approach replaces the glass front sheet with transparent polymers such as Ethylene tetrafluoroethylene (ETFE), polycarbonate (PC), or polymethyl methacrylate (PMMA). These materials are lighter, impact-resistant, and have lower thermal conductivity, which helps reduce heat accumulation in the cells [68], [69], [70]. On the rear side, composite backings such as glass-fiber reinforced polymer (GFRP) or honeycomb sandwich structures are used to maintain mechanical strength with much lower weight. These solutions are shown in Figure 2.6b, Figure 2.7 and Figure 2.8.

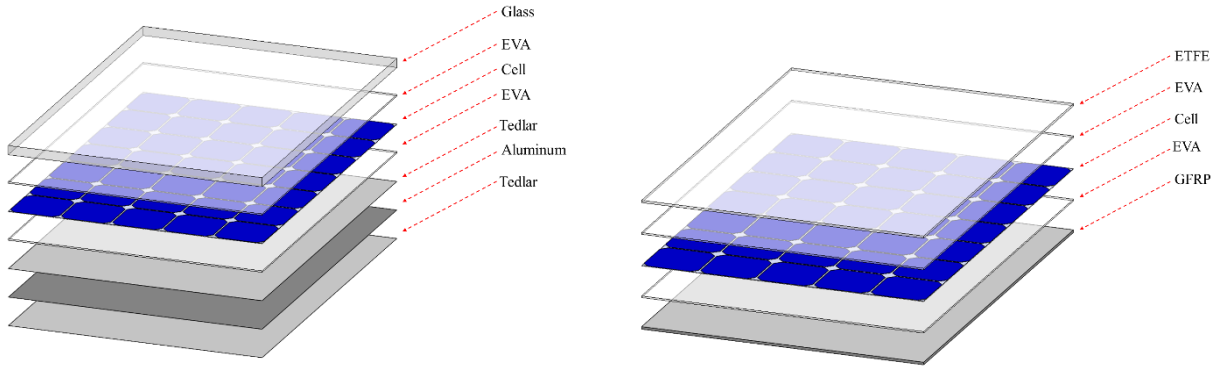

(a) (b)

Figure 2.6. General structure of (a) conventional and (b) lightweight silicon solar module [48].

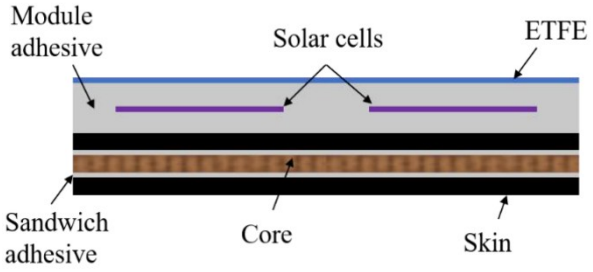

Figure 2.7. Lightweight VIPV structure using ETFE and honeycomb composite backing [68].

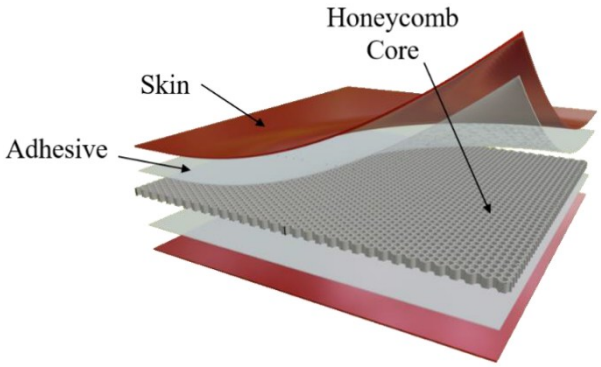

Figure 2.8. Honeycomb sandwich structure consisting of skins, core, and adhesive, designed to reduce weight while maintaining mechanical strength [68].

In addition to new encapsulation materials, geometric strategies can also help adapt c-Si to curved surfaces. Cell segmentation or shingling, where standard 6-inch cells are cut into smaller strips or triangles, reduces mechanical stress and allows the cells to conform to gentle curvature without cracking. Experiments have shown that while full-size cells fracture on surfaces with curvature radii around 1 m, segmented cells can survive lamination under the same conditions. Segmentation also reduces electrical mismatch losses because smaller cells have more uniform illumination on curved surfaces [62].

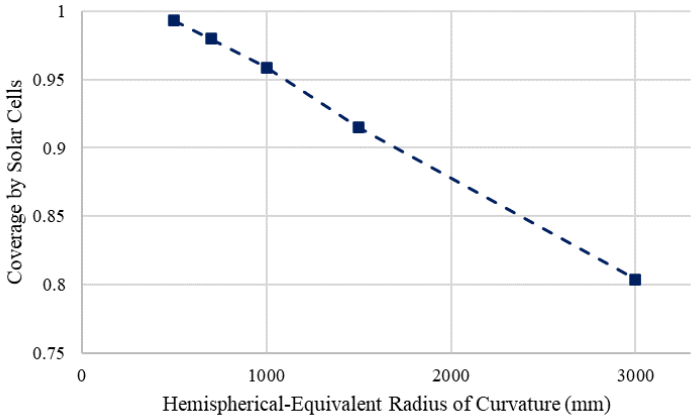

Figure 2.9. The coverage ratio of curved surface solar cells versus the equivalent hemispherical curvature radius [37], [62].

Overall, c-Si remains one of the most promising options for VIPV, particularly for large, relatively flat vehicles such as trucks, buses, or ships, where full-sized modules can be installed with minor adaptations. For passenger cars and light commercial vehicles, innovative encapsulation and segmentation techniques are required to address curvature and weight constraints. When these adaptations are applied, c-Si can deliver high energy yield with strong economic viability, making it a cornerstone technology for VIPV.

2.3.2. Thin-Film Solar Cells

Thin-film technologies, such as amorphous silicon (a-Si), CIGS (copper indium gallium selenide), and CdTe (cadmium telluride), are lighter and more flexible than crystalline silicon. Their flexibility makes them easier to integrate into surfaces with moderate curvature, such as bus or truck roofs, or marine decks. Although their efficiencies are generally lower than c-Si, the reduced weight and mechanical adaptability make them attractive for VIPV. For example, thin-film CIGS modules integrated on the roof of buses have been used to power auxiliary systems such as air conditioning, Wi-Fi routers, and USB charging ports. Such applications reduce the load on the main engine or battery and lead to fuel savings. One study reported a reduction of 1.7 liters of diesel per 100 km in a bus with a CIGS roof installation [71].

2.3.3. Multi-Junction and III–V Solar Cells

III-V Cells, such as Gallium arsenide (GaAs) and Indium gallium phosphide (InGaP), are used to produce multi-junction solar cells that achieve very high conversion efficiencies, currently over 40% in laboratory conditions and 30–35% in commercial modules. They accomplish this by stacking multiple semiconductor layers with different bandgaps, enabling them to capture a much broader portion of the solar spectrum than single-junction cells. Such high efficiency makes III–V cells attractive for VIPV applications where surface area is very limited, especially on passenger cars, where available roof areas are only about 2–3 m². For example, Toyota's experimental Toyota Prius Plug-in Solar integrated InGaP/GaAs/InGaAs modules across about 3 m² of its roof, hood, and rear body panels, achieving approximately 860 W of peak power with an efficiency of 34.9%, corresponding to ~28 km of additional driving range per day under ideal conditions. A similar project by Nissan using III–V modules on the Nissan e-NV200 achieved ~1150 W at 31.2% efficiency, yielding about 27 km of extra daily range. However, III–V modules also face serious cost, fragility, and integration challenges. They are typically grown on rigid substrates and are brittle, making them difficult to mount on curved surfaces without cracking. To address this, researchers have explored ultra-thin III–V layers (down to ~30 µm) combined with flexible encapsulants and concentrator optics. In these systems, small high-efficiency III–V cells are placed at the focal points of microlenses or mirrors to concentrate sunlight and boost output. Even under partially diffuse conditions, such concentrators can direct light from multiple angles onto the cells [37], [66], [72], [73].

A further innovation is the hybrid concentrator design, in which the gaps between the III–V cells under the lenses are filled with lower-cost cells such as c-Si. This "partial CPV" (concentrated PV) configuration maximizes both surface coverage and energy yield. The concept is shown schematically in Figure 2.10, comparing a conventional concentrator layout with the proposed hybrid approach [74], [75].

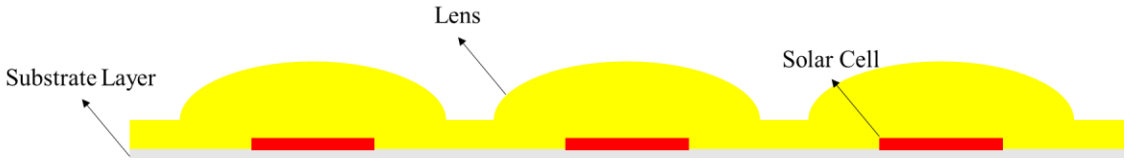

(a)

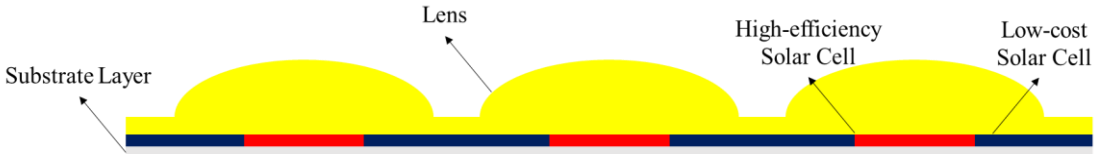

(b)
Figure 2.10. Schematic of concentrator structures for VIPV: (a) normal configuration, and (b) proposed structure (Partial CPV module) [48].

Despite their cost and fragility, the exceptional efficiency of III–V cells makes them very promising for applications with severe surface area constraints, and they are expected to play a growing role in VIPV if production costs can be reduced.

2.3.4. Transparent Solar Cells

A large portion of the exterior surface of modern passenger vehicles consists of glass elements such as windshields, side windows, rear windows, and panoramic roofs. These surfaces have traditionally been excluded from VIPV applications due to concerns about visibility, safety, and passenger comfort. However, the development of Transparent solar cells (TPVs) has opened the possibility of using these areas to generate solar power without obstructing the driver's field of view or reducing natural lighting inside the cabin. By converting mainly ultraviolet (UV) and near-infrared (NIR) radiation while allowing most visible light to pass through, TPVs can produce electricity while remaining visually transparent, making them highly suitable for integration into automotive glazing [76], [77].

Recent advances in materials science and simulation tools have greatly facilitated the assessment and design of such systems. With the help of numerical models and Artificial intelligence (AI)-based optimization, it is now possible to evaluate the potential energy yield of TPVs under realistic operating conditions, considering local irradiance patterns, driving behavior, and shading from the surrounding environment. A study investigating their potential on a Jeep Grand Cherokee estimated the annual contribution of TPVs integrated solely on the vehicle windows, assuming an average energy consumption of 26 kWh per 100 miles. The results indicated that window-based TPVs could supply enough electricity to power approximately 4200 miles per year in Phoenix, 4100 miles in Honolulu, 4000 miles in Los Angeles, 3200 miles in New York City, and 3100 miles in Lansing. These values demonstrate the considerable contribution that window-mounted PV could provide, especially for vehicles used extensively in sunny regions or parked outdoors for long periods [46], [47].

From a technological perspective, Perovskite solar cells are among the most promising candidates for transparent PV applications. Their high absorption coefficient and tunable band gap enable selective absorption of non-visible radiation while maintaining acceptable visible light transmission. In addition, many perovskite-based TPVs include metal oxide layers that block UV and IR radiation, which helps reduce unwanted cabin heating and consequently lowers the load on air-conditioning systems. Some studies have also shown that incorporating nanomaterials into the perovskite layers can further enhance their optical transparency and thermal stability, improving their suitability for long-term use on vehicle glazing. Nevertheless, integrating PV modules into vehicle windows introduces additional challenges that do not arise with opaque body panels. TPVs must comply with strict automotive glazing regulations, which vary between regions and define requirements for

parameters such as visible light transmission, UV filtering, thermal resistance, and impact safety. Differences in manufacturer policies and regional standards mean that the optical and thermal properties of TPVs must be carefully adapted to each target market to ensure safety and regulatory compliance. Furthermore, laminated glass structures are subject to continuous mechanical stress and thermal cycling, which can accelerate degradation if not properly addressed in module design [37], [76], [77].

In summary, transparent solar cells represent a promising pathway to expand the usable surface area for VIPV beyond conventional opaque panels. Their integration could significantly increase total energy yield, particularly for passenger vehicles with limited body area. While technical, regulatory, and durability challenges remain, the rapid progress of transparent PV technologies suggests they may soon become a viable complement to roof- or hood-mounted modules, enabling near full-surface solar harvesting on vehicles.

2.4. Interconnections and Electrical Architecture of VIPV Systems

Cell size and arrangement are also closely linked to electrical performance under non-uniform illumination. A comparative study between modules composed of 54 large cells (144 × 144 mm) and those using 176 smaller cells (80 × 80 mm) demonstrated that the smaller-cell module produced up to 25 % more power under simulated shading scenarios, confirming the advantage of cell miniaturization for VIPV conditions. This design approach, combined with appropriately placed bypass diodes, significantly improves energy yield on curved vehicle surfaces where irradiance distribution changes continuously [78].

The electrical architecture of VIPV systems plays a decisive role in determining their overall efficiency, energy yield, and operational reliability. While the choice of PV cell technology sets the theoretical maximum output, the actual energy harvested depends heavily on how the individual cells and modules are electrically interconnected and interfaced with the vehicle's onboard power system. Because vehicles are mobile platforms exposed to constantly changing irradiance, shading, and thermal conditions, VIPV systems face far more dynamic operating environments than stationary PV arrays, which demands a more sophisticated and carefully optimized electrical design [26], [79], [80].

In a typical VIPV layout, many small PV cells are arranged into modules that can be interconnected in series, parallel, or hybrid series-parallel configurations to meet the voltage and current requirements of the vehicle's direct current (DC) bus. Series connections raise the output voltage while parallel connections increase the current, and the chosen configuration must be compatible with the operational range of the vehicle's Maximum power point tracking (MPPT) converters. However, because illumination is often non-uniform across the surfaces of a vehicle, due to shading from components like roof racks, antennas, or mirrors, as well as surrounding infrastructure such as buildings or trees, modules are particularly vulnerable to mismatch losses. In series-connected strings, a single shaded cell can restrict current through the entire string, reducing the output and potentially causing localized reverse-bias heating or "hotspots." Parallel connections can suffer from circulating currents when different submodules are exposed to unequal irradiance or temperature conditions. As a result, the interconnection strategy must minimize electrical mismatch while still delivering the required electrical characteristics to the vehicle system [78].

A key element for reducing mismatch losses is the use of bypass diodes, which are installed across cell groups to allow current to flow around shaded or underperforming areas. When a portion of the

module becomes shaded, its bypass diode becomes forward-biased and provides an alternative current path, preventing current blockage and protecting the affected cells from overheating. Because shading in VIPV systems is highly localized and often transient, modules typically require a higher density of bypass diodes than conventional flat PV panels. Experimental studies on curved rooftop vehicle modules have shown that increasing the number of bypass diodes can improve daily energy yield by more than 10 % under partial shading conditions. However, this must be carefully balanced, as adding too many diodes increases internal resistance, costs, and design complexity. A custom arrangement based on simulated shading patterns and curvature is usually more effective than simply applying standard layouts from fixed PV modules [78].

2.5. Thermal Behavior and Modelling of VIPV Systems

Temperature is a critical factor governing the performance of VIPV systems. Like all PV devices, solar cells operate most efficiently within a defined temperature range, and their output declines as temperature rises beyond this range. For example, Crystalline silicon (c-Si) cells typically experience a power reduction of about 0.4–0.5% for every Celsius degree increase in module temperature [81]. This sensitivity means that VIPV modules, which are often exposed to intense solar radiation while parked or operating in hot climates, can suffer substantial energy yield losses if thermal effects are not properly managed [82], [83]. Experimental results have shown that higher module temperatures directly reduce the open-circuit voltage, as illustrated in Figure 2.11, where modules installed on two different vehicles exhibited a clear voltage drop as temperature increased [84].

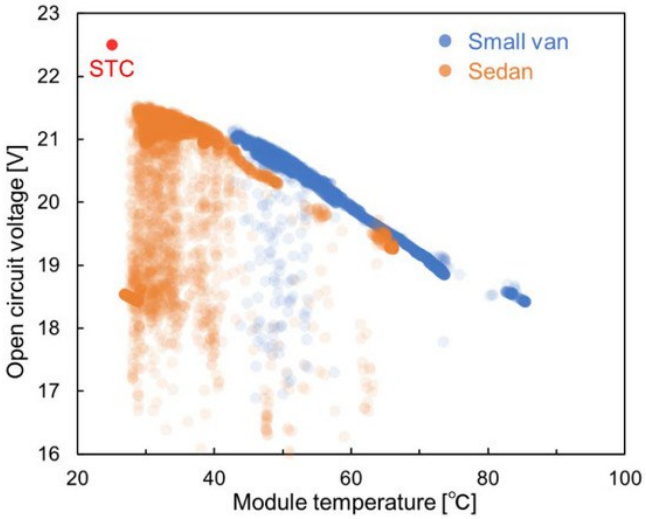

Figure 2.11. Effect of increasing the temperature of the solar module installed on two different cars on the open circuit voltage [84].

Unlike stationary PV systems, however, VIPV installations benefit from an inherent mitigating mechanism: convective cooling during motion. When the vehicle is in motion, the airflow over its body enhances heat dissipation from the modules, reducing their operating temperature and partially recovering lost efficiency. This phenomenon represents a significant advantage of mobile PV, though

it also introduces strong variability, VIPV systems may perform quite differently depending on whether the vehicle is stationary or moving [85].

Accurate prediction of thermal behavior is therefore essential for assessing VIPV performance, yet it is challenging due to the transient and dynamic nature of vehicle operation. Researchers commonly adapt models originally developed for stationary systems, such as the NOCT model [86] and the Faiman model [87]. The NOCT approach provides a simple empirical estimate of module temperature based on ambient temperature and solar irradiance under a standard operating point. While widely used, it assumes steady-state conditions and a constant convective cooling rate, which makes it poorly suited to vehicles where solar input and airflow change rapidly during driving.

The Faiman model offers a useful improvement by explicitly including the effect of wind speed on convective heat transfer. When vehicle speed is used as a proxy for wind velocity, this model more accurately captures the temperature reduction that occurs during driving compared to parked operation. This makes it better suited for distinguishing between thermal behavior at rest, where heat accumulation dominates, and in motion, where airflow stabilizes module temperature. However, both NOCT and Faiman are fundamentally steady-state models and therefore do not account for thermal inertia, the tendency of modules to respond gradually rather than instantaneously to rapid fluctuations in irradiance.

Because vehicles experience highly variable solar input due to passing clouds, shadows from buildings, or transitions between open and urban routes, ignoring thermal inertia can lead to overestimation of temperature swings and underestimation of power output. To address this, several studies have proposed averaging the results for module temperature over time intervals of 15–25 minutes, which better reflects the delayed thermal response of PV modules. This approach has been shown to significantly improve the agreement between modelled and measured output during real driving cycles [88].

In summary, temperature effects are a major performance-limiting factor for VIPV systems, and reliable modelling of these effects is essential. While conventional NOCT and Faiman models provide a useful starting point, they must be adapted to reflect the mobile and transient nature of vehicle operation. Incorporating vehicle speed-dependent convective cooling through the Faiman approach, along with smoothing techniques to account for thermal inertia, yields more realistic temperature predictions and therefore more accurate estimates of VIPV energy yield in real-world conditions.

2.6. Summary and Concluding Remarks

This chapter has presented a comprehensive overview of the key parameters that influence the performance of VIPV systems. The analysis highlighted how energy yield is not solely determined by the nominal efficiency of the photovoltaic PV technology used, but rather by a complex interplay between geometric, material, electrical, thermal, and environmental factors.

It was shown that the installation position and geometry of vehicle surfaces govern the amount and distribution of solar irradiance, with the roof generally receiving the highest exposure but also presenting challenges due to curvature and limited area. The choice of PV cell technology was discussed in detail, emphasising how each category, from Crystalline silicon and thin-film to III–V semiconductor and Transparent solar cells, offers unique trade-offs between efficiency, flexibility, weight, and suitability for different vehicle types. The electrical architecture was shown to be equally

critical, as improper interconnections or insufficient bypassing can lead to severe mismatch losses under the highly non-uniform illumination typical of moving vehicles.

Thermal effects were identified as another major constraint, with temperature rises significantly reducing power output. Finally, the chapter underlined how environmental and operational conditions, including seasonal variations, shading patterns in urban settings, and driving or parking behaviour, strongly influence the real-world performance of VIPV systems.

Understanding these parameters is essential as a foundation for the following chapters, which will focus on the development of dedicated modelling frameworks and simulation methodologies for VIPV applications. The insights presented here provide the necessary physical and technical background to accurately represent VIPV behaviour in models and to support the design of systems that are both efficient and practically deployable.

3

VIPV for Disaster Response: Methods and Case Studies

This chapter investigates the application of VIPV systems as a mobile energy supply strategy in disaster and emergency scenarios, where the continuity of power supply is often severely compromised. In such contexts, conventional grid infrastructure may be damaged or inaccessible, making the availability of self-sustained and rapidly deployable energy sources essential for effective disaster response and recovery operations. Integrating PV modules into vehicles and mobile unit offers a promising solution to enhance energy resilience, enabling the generation of on-site renewable electricity without dependence on external grids or fuel logistics.

The proposed approach explores the potential of VIPV-equipped emergency vehicles, including ambulances, trucks, and mobile service units such as containers and operating rooms, to act as autonomous or auxiliary power generators during crisis situations. By harnessing solar energy directly from the vehicle's integrated surfaces, these systems can support vehicle's needs or auxiliary loads such as communication systems, lighting, refrigeration, and medical equipment. To evaluate this potential, a dedicated methodology was developed by adapting VIPV simulation frameworks to reflect the uncertain and dynamic conditions typical of disaster environments. This approach accounts for variable meteorological conditions, reduced solar availability, and operational conditions. Simulation results demonstrate that the VIPV can contribute to disaster resilience and emergency preparedness, even under suboptimal environmental conditions. For instance, ambulances analysed under worst-case winter scenarios (e.g., December) were able to generate sufficient energy to power essential medical devices for 1 to 15 hours per day, depending on configuration and irradiance levels. Over the course of a year, the integrated system could produce up to 2 MWh of electricity, corresponding to a reduction of approximately 0.5 tons of CO_2 emissions. Moreover, mobile operating rooms equipped with optimized PV layouts exhibited the capability to generate up to 120 times the daily energy demand required by medical devices, illustrating the scalability and flexibility of the proposed concept.

Overall, the outcomes of this study highlight the relevance of VIPV systems as decentralized and rapidly deployable energy solutions in post-disaster contexts. Beyond their direct operational benefits, such systems can play a critical role in strengthening the energy autonomy, sustainability, and resilience of emergency response infrastructures, representing an important contribution to the broader transition toward low-carbon and adaptive energy systems.

3.1. VIPV Systems in a Disaster Context

Disasters, natural or human-made, can severely disrupt critical infrastructure, with power outages among the most consequential impacts [89]. The loss of electricity compromises not only households and businesses but also emergency response, where continuous power is indispensable for medical services, rescue operations, and communications [90]. Because restoration can take hours or days, energy resilience is a central pillar of disaster management [91]. Ensuring a stable power supply in such contexts demands prioritization of critical loads, efficient use of available resources, and integration of renewable technologies to reduce dependence on fuel-based systems [92], [93].

Several approaches to disaster energy resilience have been explored. Candan et al. [94] proposed an algorithm that enhances grid resilience by prioritizing household appliances and integrating EVs and localized PV, showing that EV batteries can act as mobile storage to support critical loads. Vaziri Rad et al. [95] investigated standalone renewable solutions for post-disaster settings, identifying PV-battery-hybrid generator configurations for homes and healthcare facilities via multi-criteria decision making; their work emphasized that hybridization is necessary to mitigate the intermittency of solar and wind. Saboori [96] introduced mobile battery storage, optimizing logistics, siting, and power transfer for trucks and trains, and demonstrating meaningful flexibility gains for affected grids.

Yet these solutions face limitations. Stationary PV can be damaged by earthquakes or debris [97], while mobile storage is constrained by logistics and finite capacity [98], [99], underscoring the need for mobile and self-sufficient supply options [100]. A promising strategy is VIPV, PV cells integrated into vehicles, enabling generation and storage while retaining mobility [37]. Unlike conventional BEVs used purely as storage or stationary systems, VIPV-equipped vehicles can act (even within limited production due to available surface area) as self-sustaining power sources for critical applications, medical equipment, communications, temporary shelters, without relying on external infrastructure [48], [101].

Early work has explored PV-equipped vehicles in emergency contexts. The FIVE project [102] integrated PV into emergency medical vehicles to cut fuel dependence and improve operations. Hasan et al. [103] proposed a water ambulance with intelligent energy management for continuous medical power. Araki et al. [28] used Monte Carlo simulations to assess PV-equipped vehicles powering temporary disaster stations; however, their focus leaned toward stationary use rather than the mobile nature of emergency vehicles.

Two gaps remain. First, the role of VIPV is often overlooked in disaster-response energy portfolios: while EVs are proposed as mobile storage, VIPV can provide both mobile storage and on-board generation [104], [105]. Second, methodologies to evaluate VIPV under disaster uncertainty are scarce. Existing VIPV assessment methods seldom accommodate unpredictable routes, variable duty cycles, or rapidly changing shading and operating conditions [45], [57], [106], [107], [108]. To address these gaps, we adapt VIPV simulation methodologies to capture dynamic and uncertain disaster scenarios and conduct a sensitivity analysis on geographic location and vehicle movement, providing a fuller picture of VIPV feasibility in emergencies.

This chapter focuses on integrating solar cells into emergency vehicles to supply on-board demand or to power vital medical devices in mobile care units. Ambulances and trucks across mobile and stationary modes, have been investigated; trucks are also assessed as carriers for containers and mobile operating rooms. For stationary operation, we evaluate the potential of single- and dual-axis tracking [109]. A geographical analysis is applied across Palermo, Rome, and Milan, representing different latitudes and solar resource regimes. Critical medical loads are identified and compared

against VIPV generation, assuming that existing traction batteries in ambulances and trucks support both vehicle operation and the VIPV subsystem. Operational conditions and standby charging losses to determine feasible energy production and storage, have been analysed. For containers and mobile operating rooms, battery sizing in stationary mode is adapted from existing off-grid methods. Finally, using grid emission factors [110], we estimate avoided CO_2 to highlight the broader sustainability value, secondary in emergencies but relevant for long-term planning.

In this chapter, Section 3.2 frames the research gap, objectives, and contributions. Section 3.3 details the methodology (solar resource, shading treatment, performance ratio, operating modes, and metrics). Section 3.4 describes case studies and system setup. Section 3.5 presents results (energy yield, solar range, seasonal profiles, tracker net benefits, battery sizing, medical-load coverage, emissions). Section 3.6 provides discussion, and Section 3.8 closes with conclusions.

3.2. Research Gap, Objectives, and Contributions

Although interest in resilient energy systems has grown considerably in recent years, the potential of VIPV in disaster scenarios remains largely unexplored. Most studies addressing post-disaster energy supply focus on electric vehicles (EVs) primarily as mobile storage systems, neglecting their possible role as mobile energy generators when equipped with integrated PV modules [104]. This oversight is significant because, unlike conventional EVs that must rely entirely on pre-charged batteries, VIPV-equipped vehicles can actively generate electricity while in motion or parked, reducing dependence on damaged infrastructure. Furthermore, the few existing works that evaluate VIPV systems often assume deterministic operating conditions, such as fixed routes or predictable irradiance, which do not reflect the stochastic and highly variable nature of disaster environments. Emergency vehicles must operate under uncertain routes, irregular duty cycles, and rapidly changing shading or weather conditions, factors that current assessment methodologies generally fail to capture [45], [106], [107].

To address these gaps, this chapter aims to develop and apply a dedicated methodological framework for evaluating the feasibility and performance of VIPV systems under disaster conditions. The first objective is to adapt existing VIPV simulation approaches to account for operational uncertainty, explicitly incorporating variable driving-to-standby ratios, shading conditions, and standby charging losses. Building on this framework, the study evaluates the energy production and solar range of VIPV-equipped emergency vehicles, specifically ambulances and trucks, across different geographic contexts represented by three Italian cities with different solar resources: Palermo, Rome, and Milan. In parallel, the methodology assesses the capability of these systems to power critical medical devices in mobile care units, comparing the energy required by such equipment to the energy generated under both typical and worst-case seasonal conditions.

In addition to mobile vehicles, this study also examines stationary deployments, such as containers and mobile operating rooms that can be transported to disaster sites. For these systems, the analysis includes the effect of integrating solar tracking mechanisms, evaluating whether the additional energy gained from single- or dual-axis trackers justifies their own energy consumption [109]. Finally, the study quantifies the potential reduction in CO_2 emissions achieved by substituting VIPV-generated electricity for conventional grid power, using power-sector emission factors to estimate the associated sustainability benefits [110]. Although reducing emissions is a secondary consideration during emergencies, demonstrating these benefits can support the broader case for adopting VIPV technologies in public-sector fleets.

Overall, the contributions of this chapter. First, it introduces a methodological adaptation that treats operational uncertainty and environmental variability as core parameters in VIPV performance modelling. Second, it provides a multi-scenario comparative analysis of energy yield, solar range, and battery requirements across different vehicle types and locations. Third, it links this technical evaluation to real-world disaster response needs by estimating the capability of VIPV systems to operate vital medical devices in worst-case conditions. By combining these elements, the chapter contributes a practical and comprehensive framework to support the integration of VIPV technology into emergency response strategies.

3.3. Methodology

To evaluate the potential of VIPV systems in disaster scenarios, a dedicated methodology was developed by adapting general PV performance equations to the specific operational characteristics of vehicles. This section presents the fundamental calculation framework, focusing on energy generation estimation, solar irradiance assessment, and performance ratio determination.

3.3.1. Energy Generation Estimation

Generally, the amount of power produced by a fixed photovoltaic system W_{PV}, can be calculated using Equation 3.1 [28]:

$$P = f \,.\, A_{Curved\,Surface} \,.\, Irr_{roof} \,.\, \eta_{PV} \tag{3.1}$$

Where η represents the efficiency of PV system, H ($\mathrm{W/m^2}$) is irradiance, A ($\mathrm{m^2}$) is area, and PR is the performance ratio. In VIPV systems, due to the curvature and complex shape of the vehicle body, PV cells may not entirely cover it. Therefore, by applying a coverage ratio to A in Equation 3.1, the amount of power produced by a VIPV system W_{VIPV} can be calculated using Equation 3.2 [29, 30]:

$$W_{VIPV} = \eta \cdot H \cdot Sr \cdot PR \tag{3.2}$$

Where Sr represents the PV coverage area ($\mathrm{m^2}$) and is defined by:

$$Sr = \alpha \cdot A \tag{3.3}$$

In Equation 3.3, α represents the percentage of the vehicle's surface area that is covered by PV cells, while A refers to the area of the specific section of the vehicle (e.g., roof, sides) where PV is installed.

3.3.2. Solar Irradiance Assessment

Solar radiation that reaches the Earth's surface consists of direct (beam), diffuse, and reflected components. In this study, reflected radiation is neglected, and only direct and diffuse irradiance are considered [31].

$$H = DHI \cdot (\frac{180 - \beta}{180}) + DNI \cdot cos\,(\theta) \tag{3.4}$$

$$\begin{aligned} cos\,\theta = {} & sin\,\delta\,sin\,\emptyset\,cos\,\beta - sin\,\delta\,cos\,\emptyset\,sin\,\beta\,cos\,\gamma + cos\,\delta\,cos\,\emptyset\,cos\,\beta\,cos\,\omega \\ & + cos\,\delta\,sin\,\emptyset\,sin\,\beta\,cos\,\gamma\,cos\,\omega + cos\,\delta\,sin\,\beta\,sin\,\gamma\,sin\,\omega \end{aligned} \tag{3.5}$$

Where DHI is Diffuse Horizontal Irradiance, DNI is Direct Normal Irradiance, β is inclination of PV panel, θ is angle of incidence of beam radiation on a surface, and γ is azimuth angle (Figure 3.1).

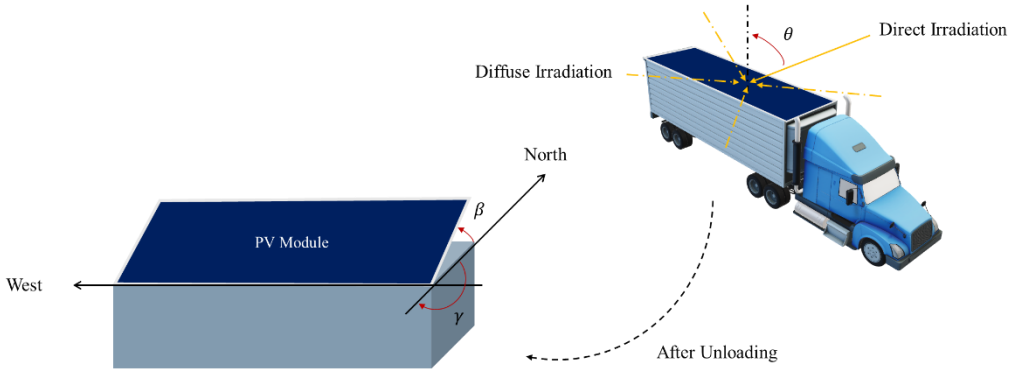

Figure 3.1. Schematic of solar angles definition.

All irradiance calculations were performed using Meteonorm software [111] and the computed results were used for subsequent analysis. By defining specific conditions, such as zero inclination, single-axis tracking, or dual-axis tracking, the software generated hourly irradiance data for three different Italian cities: Palermo, Rome, and Milan. These cities were selected to represent different geographical locations and latitudes, influencing solar radiation levels. Palermo, located in the south, has a Mediterranean climate characterized by hot, dry summers and mild, wet winters, offering high solar potential. Rome, in central Italy, experiences a temperate climate with balanced seasonal variations, while Milan, in the north, has a humid subtropical climate with colder winters and moderate summers, leading to lower overall irradiance. The monthly average direct normal irradiance (DNI), diffuse horizontal irradiance (DHI), and global horizontal irradiance (GHI) values for Palermo, Rome, and Milan in 2020 [112] are illustrated in Figure 3.2.

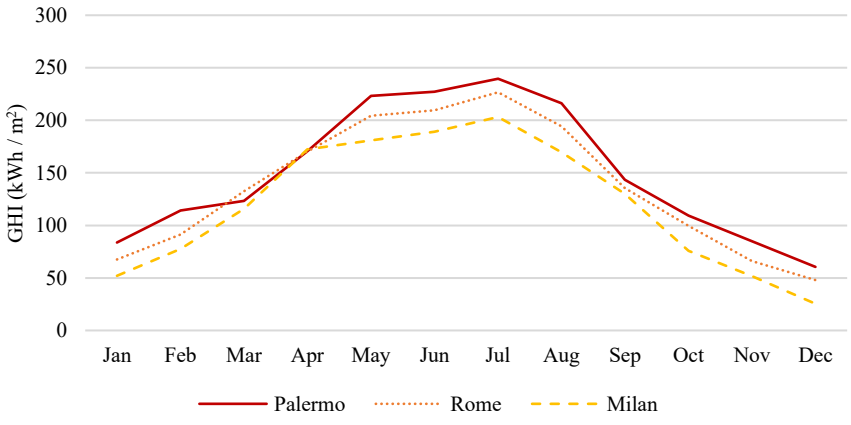

(a)

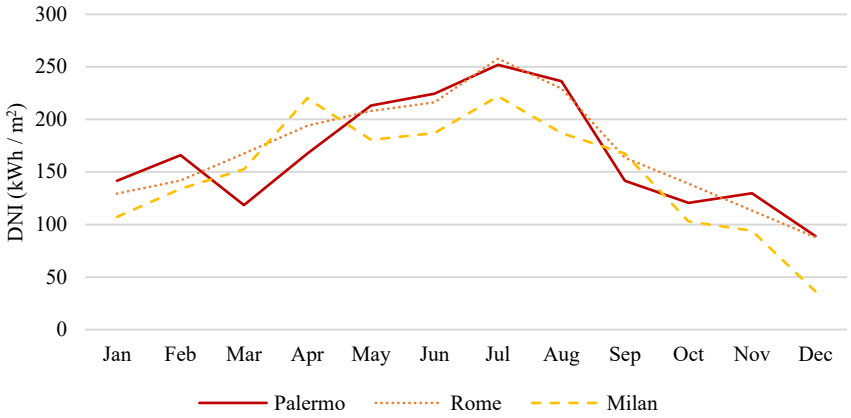

(b)

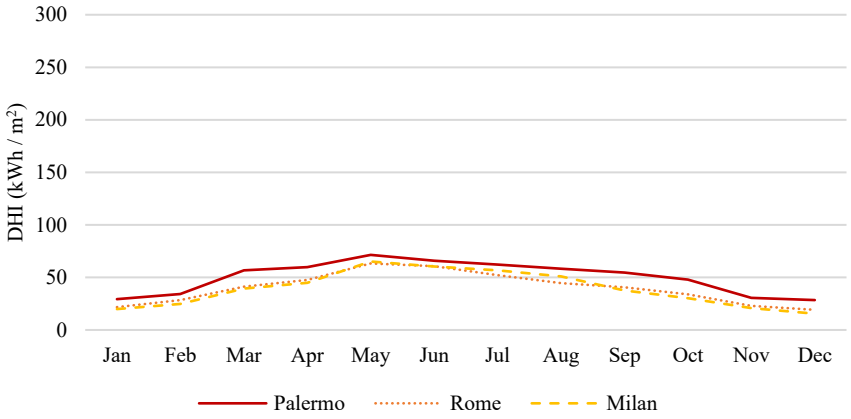

(c)

Figure 3.2. Monthly average values of (a) global horizontal irradiance (GHI), (b) direct normal irradiance (DNI), and (c) diffuse horizontal irradiance (DHI) for Palermo, Rome, and Milan in 2020 [112].

3.3.3. Shading Considerations

Shading is a critical factor influencing the performance of PV systems, particularly in VIPV applications. In fixed PV systems, shading is typically more manageable, as it can be reduced through careful system design and installation in locations with minimal obstructions. However, in VIPV systems, shading evaluation becomes more complex due to the vehicle's movement [54]. The shading level varies dynamically, depending on factors such as the vehicle's mode (e.g., parking or driving), the surrounding environment, and the specific routes taken. In disaster situations, the unpredictability of shading becomes even more pronounced because both the timing and location of the disaster are unknown. While GIS-based methods can estimate shading effects in some cases [113], using them is challenging in disaster scenarios where the environment is highly variable and unpredictable. In these scenarios, shading can result from both typical obstructions (e.g., buildings or trees) and temporary obstacles, such as debris or damaged infrastructure. Additionally, atmospheric factors such as smoke or dust may further reduce the direct irradiance received by the vehicle's PV system.

By considering shading as a dynamic loss factor, this work highlights the ability of VIPV systems to provide reliable energy in unpredictable and challenging conditions, emphasizing their relevance for emergency response and disaster recovery applications. The impact of different shading levels (0% to 80%) on energy generation has been investigated. Like previous studies [79], [114], [115], [116],

shading was modelled as a ratio to account for its impact on direct irradiance. For instance, a shading level of 40% means that the vehicle receives only 60% of the direct irradiance during each hour. This reduction is applied uniformly across all hours, allowing us to evaluate the average effect of shading on energy generation over time.

To maximize solar energy utilization, it is assumed that PV modules operate at their maximum power point (MPP). Although tracking the MPP under partial shading can be challenging, the shading ratio is expected to inherently account for any associated losses. With this assumption, the analysis focuses on modelling peak power output rather than the detailed behaviour of the entire PV module, simplifying the evaluation while still providing a reasonable estimation of system performance [114].

3.3.4. Performance Ratio Evaluation

Generally, each photovoltaic system comprises two main parts: energy production and conversion which is shown in Figure 3.3. However, each part of this diagram can be extended and may have more components based on the system application. This figure illustrates the basic structure where energy production involves receiving solar radiation and converting it into electrical energy through photovoltaic cells. The conversion part includes the electrical components that regulate, store, and distribute the generated electricity to power various applications [117].

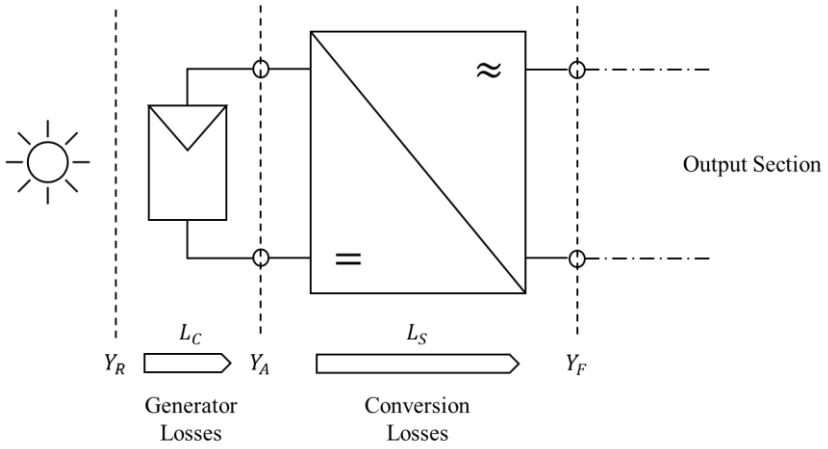

Figure 3.3. Specific yields of a photovoltaic system.

The overall performance ratio of the PV system is calculated by multiplying the performance ratios of the energy production and conversion sectors. According to Equation 3.1, the performance ratio of a photovoltaic system can be defined as Equation 3.6 [117].

$$PR = PR_{Generation} \cdot PR_{Conversion} = \frac{Y_F}{Y_R} \tag{3.6}$$

$$PR_{Generation} = 1 - L_C = \frac{Y_A}{Y_R} \tag{3.7}$$

$$PR_{Conversion} = 1 - L_S = \frac{Y_F}{Y_A} \tag{3.8}$$

$$Y_R = \frac{G}{H_{STC}} \tag{3.9}$$

$$Y_A = \frac{E_{DC}}{W_{STC}} \quad (3.10)$$

$$Y_F = \frac{E_{AC}}{W_{STC}} \quad (3.11)$$

By dividing the radiation energy G (kWh/m² per Year) by $H_{STC} = 1000$ W/m² [118] obtained Y_R represents the reference yield, which is the number of sun full load hours at the generator level per year. Y_A (kWh/W$_P$) per year is array yield and Y_F (kWh/W_P per year) is final yield, representing the number of plant full load hours per year. By dividing the PV energy generation E_{DC} (kWh per year) and the energy fed into the grid E_{AC} (kWh per year) by the power of PV panels W_{STC} (W$_P$) obtained Y_A and Y_F, respectively.

Generator losses L_C can arise from several factors. These include the actual power output of the modules being lower than the values specified in their data sheets, higher module temperatures exceeding 25 °C, and the presence of soiling or partial shading on the modules. Additional causes of losses are mismatches between modules in a string, operating conditions where modules are not functioning at their maximum power point (MPP), and ohmic losses occurring in the direct current (DC) lines. System losses L_S are primarily attributed to the inverter, with several factors contributing to these losses. One key factor is the inverter's efficiency, which is typically less than 100%, leading to energy being dissipated as heat during the conversion process [117].

3.4. Case Studies

To evaluate the feasibility of VIPV systems for disaster-response applications, four representative case studies were selected. These include two mobile emergency vehicles, the WAS E 500 ambulance and the Tesla Semi truck, as well as two stationary mobile units, a standard container and a mobile operating room. These platforms were chosen because they represent different operational modes, surface areas available for PV installation, and energy demand profiles.

3.4.1. Overview and Specifications

The main physical characteristics of the selected case studies are summarized in Table 3.1. The table reports the available roof area suitable for PV installation and the effective usage percentage, which accounts for surface obstructions such as ventilation units, antennas, or curved areas unsuitable for module mounting.

Table 3.1. Dimensions and specifications of selected case studies [119], [120], [121], [122].

Type	Model	Roof Area (m²)	Area Usage (%)
Ambulance	WAS E 500	8.17	79
Truck	Tesla Semi	34.00	96
Container	Dry Cargo	28.30	95
Mobile Operating Room	Expandable	66.12	94

The ambulance and truck were analysed in both driving and standby conditions, while the container and mobile operating room were assessed in stationary conditions after deployment. This differentiation makes it possible to explore how VIPV performance varies between mobile and static applications.

3.4.2. Ambulance and Truck

Solar cells were integrated into the roofs of ambulances and trucks with $\beta = 0$, and the elevation was assumed to be constant (the road pitch angle was set to zero). The vehicles were considered in both driving and parking operating conditions. In contrast, the container and mobile operating room were positioned in a fixed location, and β was not constant. To calculate energy generation during both driving and standby modes, Equation 3.2 is adapted as follows [45]:

$$E_{VIPV,\ Driving} = \frac{1}{1000}\sum_{h=1}^{8784} \eta \cdot H_h \cdot Sr \cdot PR \cdot R\ (kWh\ per\ Year) \tag{3.12}$$

$$E_{VIPV,Standby} = \frac{1}{1000}\sum_{h=1}^{8784} \eta \cdot H_h \cdot Sr \cdot PR \cdot (1 - R) - L_{CH}\ (kWh\ per\ Year) \tag{3.13}$$

$$E = E_{VIPV,Standby} + E_{VIPV,\ Driving} \tag{3.14}$$

Where L_{CH} (W) represents standby charging losses, H_h ($\mathrm{W/m^2}$) is hourly irradiance, and R is driving to park ratio.

To obtain the system's performance ratio, as described in Section 2.2, the performance ratios for both the generation and conversion components must be computed. The performance ratio for the generation component can be calculated as follows [117], [118]:

$$PR_{Generation} = \frac{Y_A}{Y_R} = \frac{\frac{E_{DC}}{W_{STC}}}{\frac{G}{H_{STC}}} = \frac{PV_{OUT}}{\frac{GTI_{opta}}{H_{STC}}} \tag{3.15}$$

Where PV_{OUT} ($\mathrm{kWh/kW_P}$ per Year) is specific photovoltaic power output and GTI_{opta} ($\mathrm{kWh \cdot m^{-2}}$ per Year) is global tilted irradiance at optimum angle. These parameters for each region are available on Global Solar Atlas [123]. In this method, the PV_{OUT} is considered as the array yield (Y_A) for the respective city, while the GTI_{opta} is used to represent the yearly radiation energy (G) for that city. Due to equation (6), to calculate $PR_{Conversion}$, the L_S value is set to 2% [45]. The calculated PR values for Palermo, Rome, and Milan are presented in the following table:

Table 3.2. Calculated performance ratio values for different Italian cities.

	Palermo	**Rome**	**Milan**
PV_{OUT} ($\mathrm{kWh/kW_P}$ per Year)	1564.20	1520.30	1382.80
GTI_{opta} ($\mathrm{kWh/m^2}$ per Year)	1943.10	1870.70	1681.50
$PR_{Generation}$ (%)	80.50	81.27	82.24
$PR_{Conversion}$ (%)	98.00	98.00	98.00
PR (%)	78.89	79.64	80.60

Temperature significantly impacts PV performance, with higher temperatures typically reducing the efficiency of solar cells [83], [124]. In contrast, cooler climates result in a higher PR due to reduced thermal losses. Although Palermo experiences higher irradiance compared to Milan, the PR in Milan remains slightly higher.

In critical emergency response situations, such as those requiring ambulances, it is difficult to apply standard values for operational parameters due to the highly variable nature of the scenarios. Therefore, various driving to standby ratios (R) were considered to assess their impact on energy production for the WAS E 500 ambulance. R ranging from 40% to 80% to capture potential operating conditions that ambulances may encounter. For example, when $R = 0.4$, this indicates that during each hour, the ambulance is in driving mode for 40% of the time and in standby mode for the remaining 60%. In standby mode, the ambulance is either providing on-site healthcare services or transporting patients to the vehicle.

For Tesla Semi, R was defined as shown in Figure 3.4, following the guidelines in [125]. Due to these standards, drivers must take a break (45 minutes) after each 4.5 hours of driving during working day.

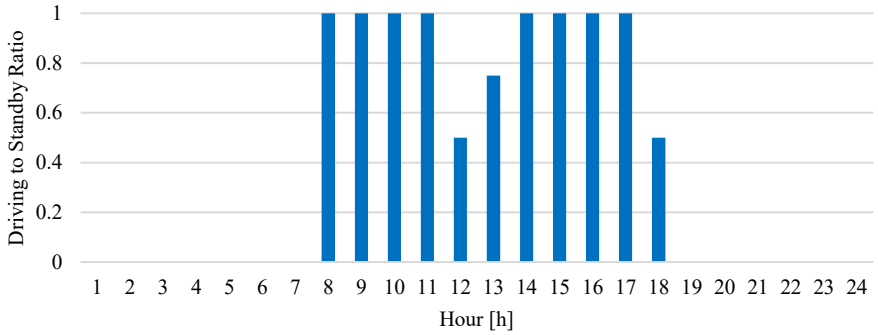

Figure 3.4. Driving-to-standby ratio profile for the Tesla Semi during working days [125].

When an electric vehicle is parked with the ignition turned off, the circuit contactors in the drivetrain battery typically remain open, preventing any charging. To enable solar charging, the vehicle must be placed in an operational state that allows high-voltage battery charging. In this state, the circuit contactors close, activating essential safety monitoring systems such as the Battery Management System (BMS) and Vehicle Management System (VMS). However, this activation introduces standby operational losses, denoted as L_{CH}. Based on the literature review and calculated values of L_{CH} for similar trucks or case studies [45], [56], L_{CH} was analyzed through a sensitivity analysis using values of 0, 25, 100, and 700 W. If the vehicle is in standby mode and L_{CH} exceeds the energy generated by the VIPV system in standby mode ($E_{VIPV,Standby}$), the system is assumed to shut down to prevent battery discharge, leading to $E_{VIPV,Standby} = 0$. The specific yields of the VIPV system, considering L_{CH}, are presented in Figure 3.5.

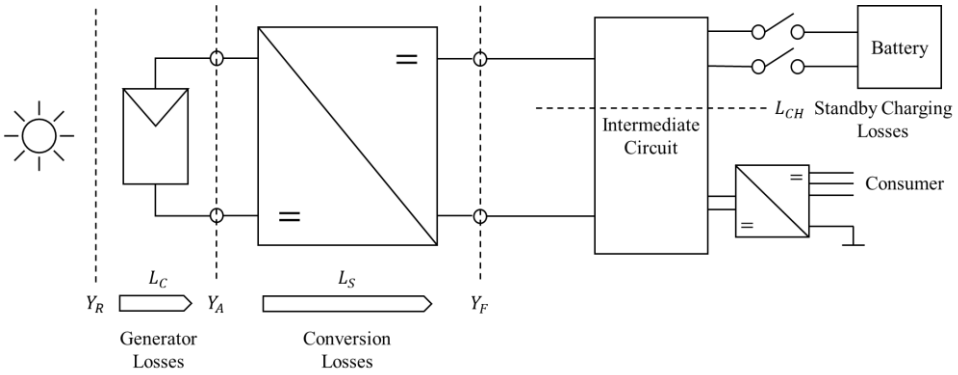

Figure 3.5. Specific yields of VIPV system which integrated into ambulance and truck.

The solar range of the vehicle can be calculated as follows:

$$Solar\ Range = E \cdot C_{Average}\ (km) \tag{3.16}$$

The average consumption $C_{Average}$ (kWh/km) for Tesla Semi is assumed to be 1.25 kWh/km. Additionally, based on the available data for battery capacity and the range of the WAS E 500 ambulance, $C_{Average}$ was determined to be 0.58 kWh/km [121], [122].

3.4.3. Container and Mobile Operating Room

To determine the generated energy by solar cells integrated into the container and mobile operating room, Equation 3.2 is rewritten as follows:

$$E = \frac{1}{1000} \sum_{h=1}^{8784} \eta \cdot H_h \cdot Sr \cdot PR\ \ (kWh\ per\ Year) \tag{3.17}$$

Due to the stationary nature of these systems, like other fixed PV installations, various factors such as temperature, Maximum Power Point Tracking (MPPT) losses, storage system losses, and converter losses can impact the system's overall performance ratio. Therefore, rather than using a general performance ratio for the energy generation and conversion segments of the system, specific values for each of these losses, as recommended in [115], [116], are detailed in Table 3.3.

Table 3.3. Estimated losses in stationary systems.

	Value (%)
Temperature Losses	9
MPPT Losses	5
DC/DC Conversion Losses	5
Battery Charging Losses	2

This leads to a DC charging/discharging loss of 2%. Additionally, the DC/DC converter contributes an extra loss of 5%. The converter's efficiency is further reduced to 95% due to the lack of MPP tracking. A performance loss of 9% is also likely, attributed to increased temperatures and suboptimal

irradiance conditions. By accounting for these losses and calculating the performance ratio for each component, the overall system performance ratio can be determined by multiplying all individual ratios. Notably, based on these values, the performance ratio for the integrated PV system in the container and mobile operating room is estimated to be approximately 80%.

3.4.4. Selected Solar Modules

For various reasons, such as the complex shape of the vehicle body, the impact of the additional weight of the panel on fuel consumption, aerodynamics, etc., the choice of solar panels for VIPV systems requires careful consideration of multiple standards [50]. These considerations necessitate adherence to multiple standards to ensure optimal performance under varying operational conditions. Given the dynamic nature of vehicle use and mobility, the chosen solar panels must demonstrate durability and resilience against diverse weather and climate conditions. Therefore, the type of solar cell selected significantly influences the overall performance and efficiency of the system [126].

Various types of solar cells, including multi-junction, silicon, perovskite, flexible, etc., have been employed in VIPV systems [35]. Due to the impact of environmental factors such as strong winds and aerodynamics, especially in this application, these elements have been carefully considered in selecting an appropriate solar cell. In this study, PV cells from the LE series of SunGold company were selected [127]. The specifications of the chosen solar cell are outlined in Table 3.4.

Table 3.4. Specifications of selected solar cells.

Model	Power (W_p)	Cell Efficiency (%)	Number of cells	Cell Dimension (mm)	Module size (mm)
LE - M2	270	22.7	4 · 18	182 · 91	1755 · 780 · 4

These cells incorporate Ethylene Tetrafluoroethylene (ETFE) instead of glass which reduces their weight [70]. Moreover, the 22.7% efficiency of this solar cell type makes it a suitable choice for this application. Solar cells using ETFE can reduce the weight from the typical 10-15 $kg \cdot m^{-2}$ seen in glass-structured cells to approximately 6 kg/m^2 or even less [69]. Removing glass does not affect their strength or ability to endure harsh conditions. For instance, according to company datasheets, the 100 W solar panel flex is engineered to withstand extreme winds up to 2400 Pa and snow loads up to 5400 Pa [127]. This design ensures that the panels maintain structural integrity and continue to perform efficiently even under severe environmental stress. Existing literature also corroborates these findings, highlighting the panels' effectiveness and resilience in various adverse conditions [68], [69], [70]. Thus, the selection of these specific solar cells addresses the concerns about environmental impact, ensuring that the system remains lightweight, durable, and efficient, even in challenging local conditions.

3.5. Results and Discussion

This section presents the main outcomes of the analysis, focusing on the energy production potential of VIPV systems integrated into the selected emergency platforms: the WAS E 500 ambulance, the Tesla Semi truck, a mobile operating room, and a standard dry cargo container. The discussion

addresses energy production and solar driving range, seasonal variations, the influence of operational parameters, battery sizing for stationary units, and the environmental benefits in terms of avoided emissions.

3.5.1. Energy Production and Solar Range

Due to their mobile solar energy generation capabilities, the WAS E 500 ambulance and the Tesla Semi truck were specifically analysed for their potential application in disaster response. Additionally, based on available data regarding the average energy consumption of these vehicles, this study evaluated the feasibility of using solar-generated energy to meet their operational demands. Table 3.5 presents the results of the sensitivity analysis conducted on various parameters for the WAS E 500 and Tesla Semi. The table contains values obtained for the maximum and minimum of each parameter, providing insights into the variability of energy efficiency under different conditions.

Table 3.5. Energy production and solar range of the WAS E 500 ambulance and Tesla Semi truck under different conditions.

Parameters		***E* (MWh/Year)**						**Solar Range (km/Year)**					
Value		**WAS E 500**			**Tesla Semi**			**WAS E 500**			**Tesla Semi**		
		PA	RO	MI	PA	RO	MI	PA	RO	MI	PA	RO	MI
L_{CH} (W)	0	1.89	1.79	1.34	9.54	9.05	6.75	3253	3085	2302	7633	7238	5402
	700	1.13	1.07	0.80	8.79	8.28	6.09	1952	1851	1381	7030	6628	4873
R (%)	40	1.51	1.42	1	-	-	-	2611	2451	1730	-	-	-
	80	1.60	1.51	1.11	-	-	-	2757	2607	1917	-	-	-
Shading (%)	0	1.79	1.69	1.24	9.50	9.01	6.71	3078	2911	2136	7603	7207	5371
	80	0.92	0.86	0.76	5.13	4.81	4.30	1588	1481	1315	4104	3849	3444

Among the three analysed cities, Palermo exhibited the highest annual energy production due to its greater solar irradiance. However, the impact of standby charging losses (L_{CH}) was significant. When $L_{CH} = 700$ W was considered, it meant that during each hour in standby mode, any generated energy below 700 W was disregarded to prevent battery discharge. The difference in total annual energy generation between $L_{CH} = 0$ W and $L_{CH} = 700$ W represents the energy lost due to standby consumption. This energy loss varied based on both the vehicle's operational pattern (driving-to-standby ratio, R) and the available solar radiation in each city. For the ambulance, increasing L_{CH} from 0 to 700 W resulted in an approximately 40% reduction in total energy production. However, for the truck, this reduction has a limited variation across cities: approximately 8% in Palermo, 9% in Rome, and 10% in Milan. These differences can be attributed to variations in solar radiation levels and the vehicle's operational profile. The truck, with a larger PV surface area and different R values, spent more time in driving mode, reducing the overall impact of L_{CH} on energy production. It is important to note that for this analysis, R was set to 0.6 for the ambulance, while for the truck, it followed the values in Figure 4. To further analyze the impact of R variations, R was adjusted between 0.4 and 0.8 for the ambulance. In this analysis, L_{CH} was set to 100 W to evaluate the effect of the

driving-to-standby ratio under average conditions and compare it with other obtained results. The findings indicate that increasing R from 0.4 to 0.8 led to an increase in E by approximately 6% in Palermo and Rome, and 11% in Milan.

The effect of shadowing was examined by varying it from 0% to 80% while keeping $L_{CH} = 25$ W and $R = 0.6$ for the ambulance. Since shading was applied only to direct radiation, its impact was more pronounced in cities where direct radiation constituted a significant portion of total irradiance. As a result, Palermo and Rome experienced greater reductions in energy generation compared to Milan, where diffuse radiation played a more substantial role. For example, for the truck, an 80% shading level resulted in an energy loss of approximately 36% in Milan, while the losses are similar in Rome (47%) and Palermo (46%). Finally, based on the obtained energy values and the average energy consumption of each vehicle, the solar range for each case study under the specified conditions has been calculated.

Additionally, the distribution of daily energy generation across different months is presented to highlight seasonal variations. The ambulance and truck were analysed under average conditions for Rome, which exhibited a relatively typical energy generation profile based on the obtained results. Figure 3.6a illustrates the results for the ambulance with $R = 0.6$. It is important to note that for both the truck and ambulance, the presented results correspond to $L_{CH} = 100$ W.

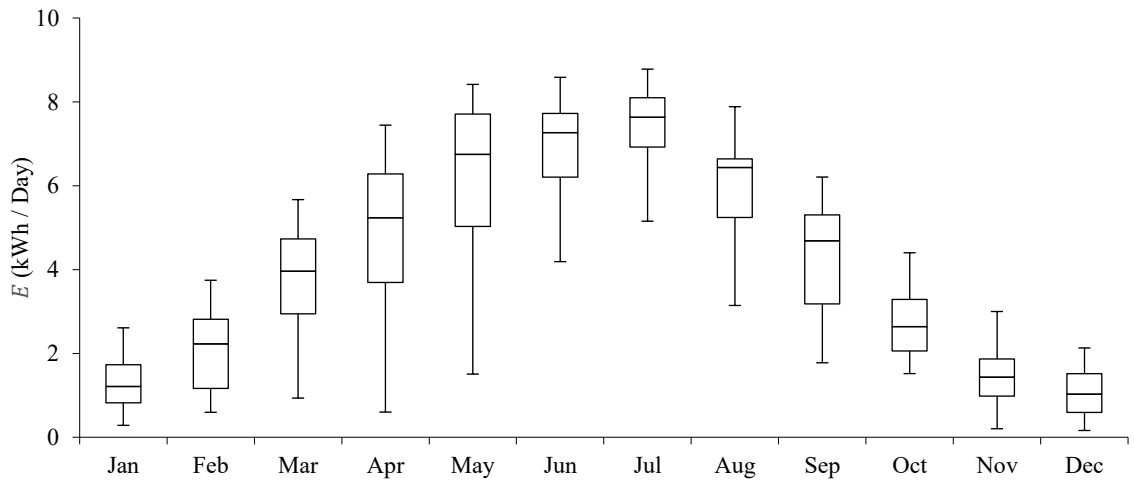

(a)

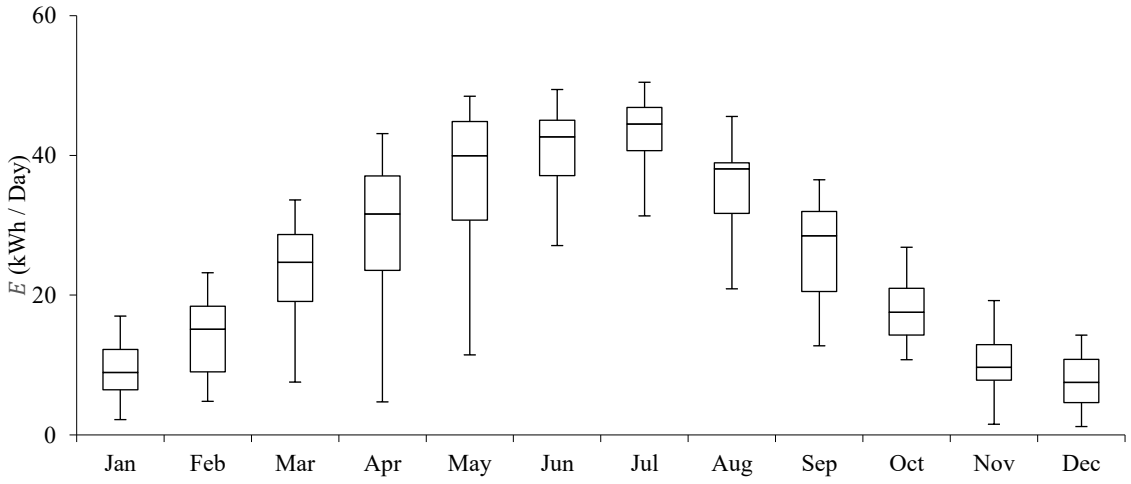

(b)

Figure 3.6. Monthly variation of daily energy generation for (a) ambulance and (b) truck in Rome.

To better understand the effects of L_{CH} and R on the energy produced by the ambulance under different operational scenarios, two different conditions have been investigated: $L1 = 100$ W, $L2 = 700$ W and $R1 = 0.4$, $R2 = 0.8$, with a fixed shading ratio of 20%. These scenarios were chosen to reflect different ambulance roles. In the first one, the ambulance is primarily engaged in providing local healthcare services, meaning it operates within a limited area and spends most of its time in standby mode. This reflects situations where the ambulance remains near a medical facility or within a community, delivering healthcare services on-site with minimal driving. Therefore, $R1 = 0.4$ was considered to represent this operational pattern. In contrast, the second scenario assumes the ambulance is mainly used for patient transportation, meaning it spends more time in driving mode. For this reason, $R1 = 0.8$ was selected. Additionally, to analyze the combined impact of L_{CH} and R, each scenario was further examined by varying L_{CH} between 100 W and 700 W (denoted as $L1$ and $L2$, respectively). The previous results indicated that daily energy generation reached its peak in July and its lowest point in December. Therefore, to better understand seasonal variations, we analyzed the distribution of daily generated energy in these two months across the three cities, as illustrated in Figure 3.7. Based on these results and considering the average consumption of the ambulance, the VIPV system can extend the ambulance's range by up to 4 km/Day in December and up to 13 km/Day in July.

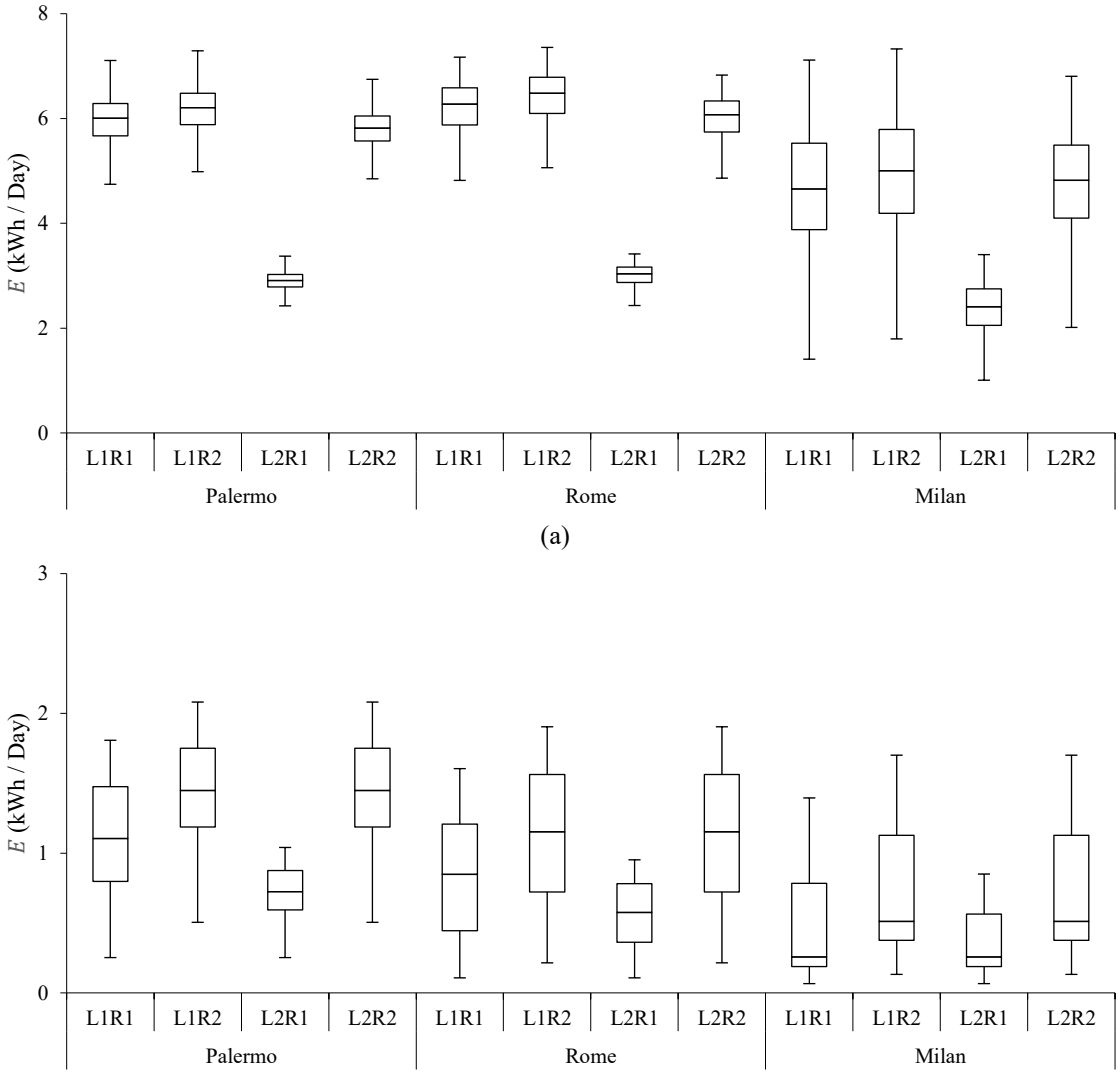

Figure 3.7. Daily energy production for the ambulance in (a) July and (b) December across different operational scenarios and cities.

The energy production and solar range of each vehicle fluctuate daily and monthly due to variations in the amount of solar radiation received throughout the year. Figure 3.8 presents the number of days in each month where the solar range of the Tesla Semi falls within defined ranges, for different locations. For instance, in May, the Tesla Semi exceeded a solar range of 30 km/Day on 22 days in Palermo, 19 days in Rome, and 9 days in Milan. It is important to note that the values shown in this figure are based on the condition where $L_{CH} = 0$ W, representing the scenario with no standby charging losses.

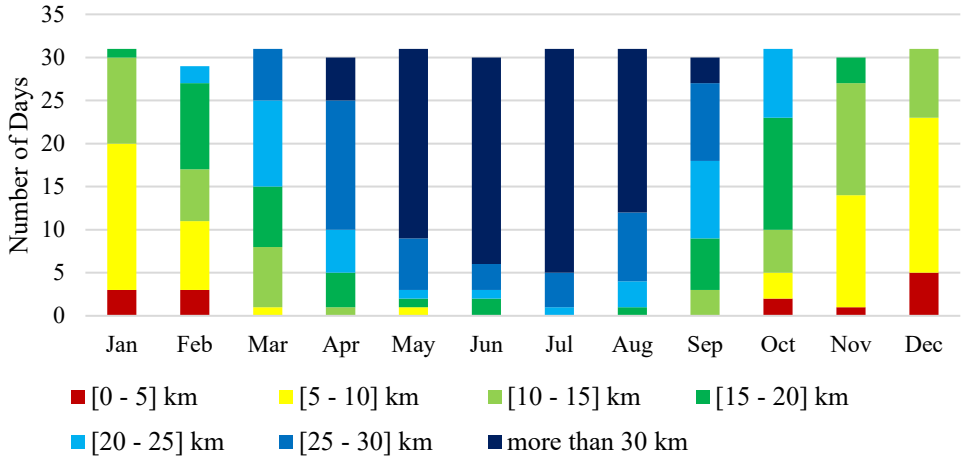

(a)

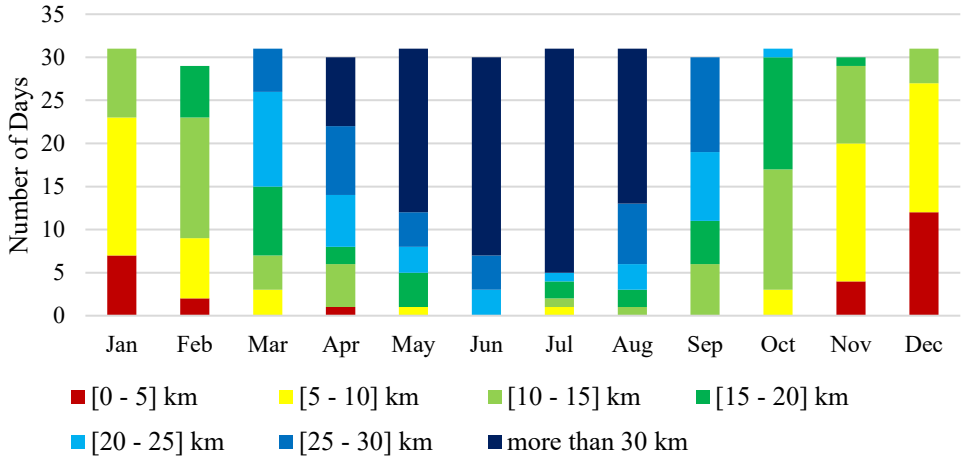

(b)

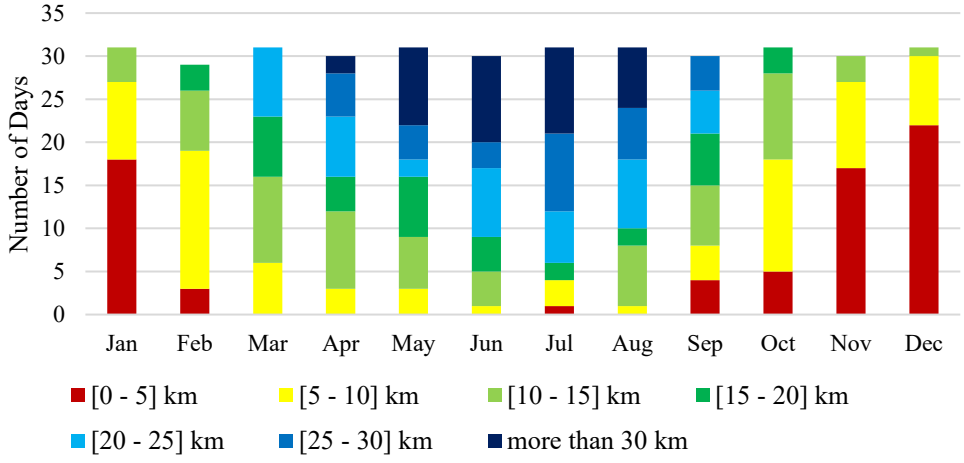

(c)

Figure 3.8. Number of days that the solar range of Tesla Semi is in defined ranges for (a) Palermo (b) Rome (c) Milan when $L_{CH} = 0$ W.

Regarding the container, it is supposed detached from the truck and positioned in a fixed location. The focus is on evaluating how advanced technologies, such as solar trackers, can enhance energy production compared to keeping the container mounted on the truck without any further adjustments. The daily energy output of the solar cells integrated into the container roof was analysed under

different configurations: a fixed installation with a tilt angle of $\beta = 0$, as well as installations equipped with one-axis and two-axis solar trackers, as illustrated in Figure 3.9.

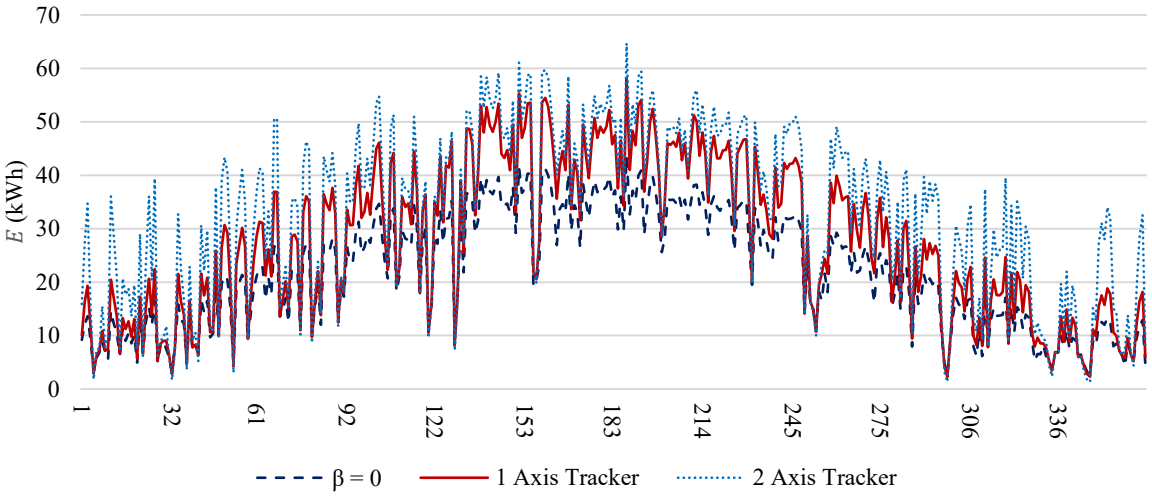

(a)

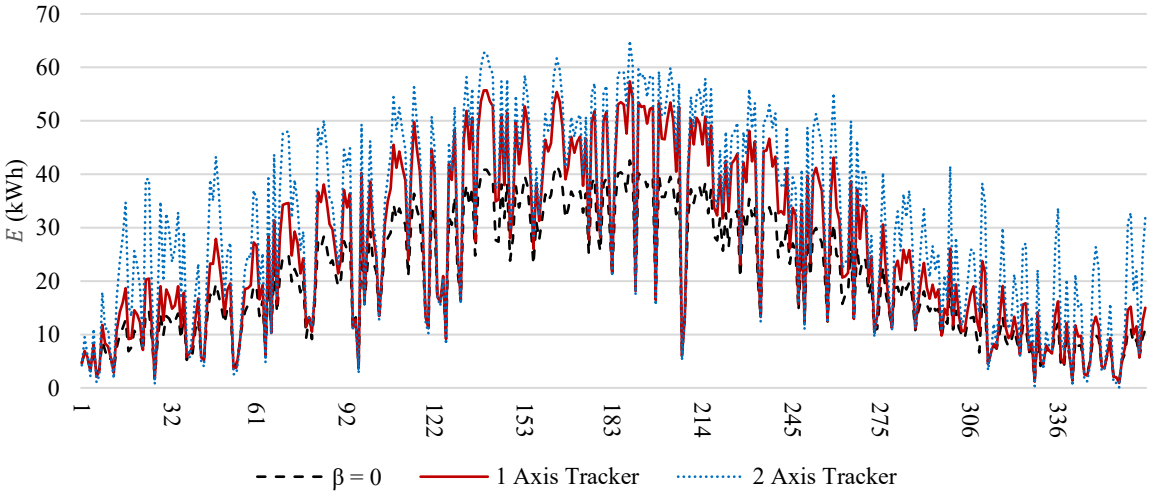

(b)

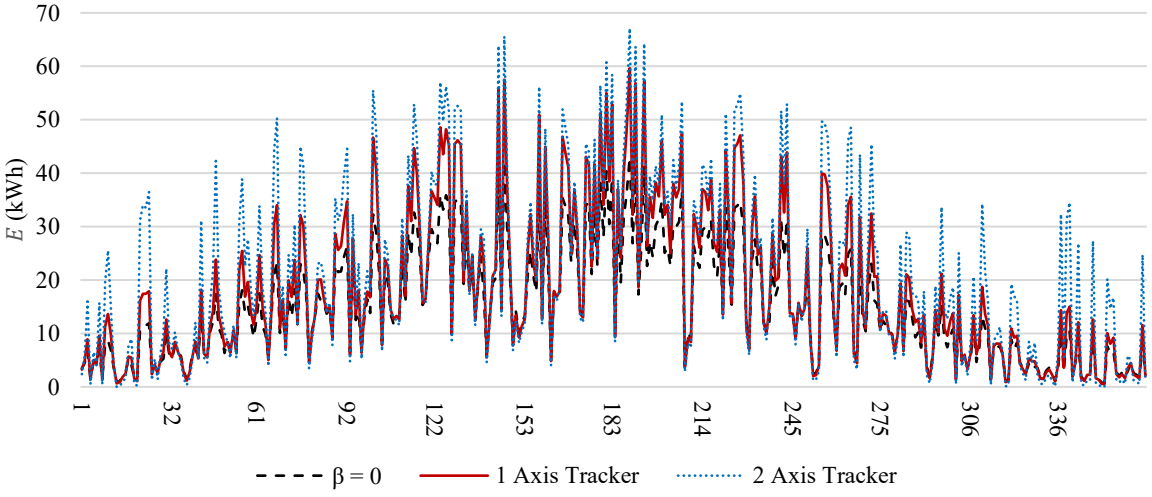

(c)

Figure 3.9. Daily net energy production from solar cells integrated into the roof of the container for (a) Palermo (b) Rome (c) Milan.

In Figure 3.9, the energy consumption of tracking systems is also considered [128], [129], [130]. While solar trackers generally enhance energy production by optimizing the panel's orientation to capture more solar radiation, their effectiveness varies depending on seasonal changes and local weather conditions. In some cases, the total received irradiance with a fixed panel ($\beta = 0$) can be higher than with tracking systems. This occurs particularly on cloudy days when most of the solar radiation is diffuse. Since diffuse irradiance is uniformly distributed across the sky, tilting the panels does not significantly improve energy capture, making a fixed-angle configuration more effective in such conditions. Additionally, there are some days when the increase in energy production from tracking systems is relatively small. As shown in Figure 3.9, when factoring in the energy consumption of the tracking mechanism itself, the net energy gain may be negligible compared to a fixed-tilt system. This highlights the importance of evaluating whether the additional energy yield from solar tracking justifies its own energy consumption under different environmental conditions.

As already underlined, the potential of integrating photovoltaic cells into the roof of a mobile operating room has been also investigated. In fact, sometimes, mobile operating rooms may be necessary during disasters, because the primary focus is on preserving the health of the injured. To examine the variation in daily energy production across different months, Figure 3.10 presents the distribution of daily generated energy from the integrated solar cells for July and December.

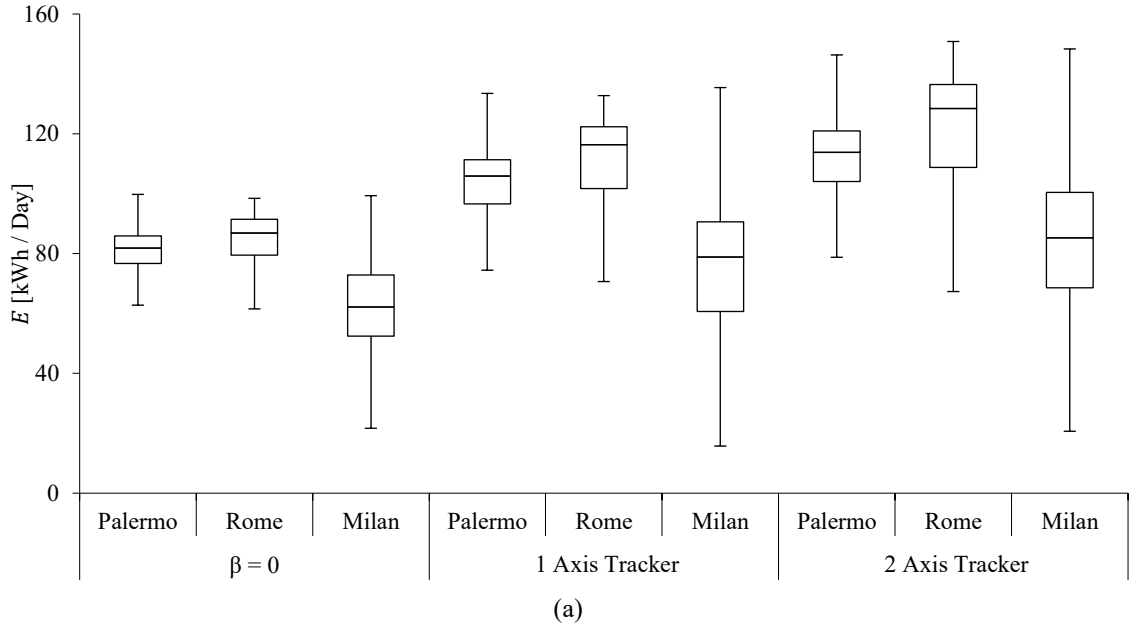

(a)

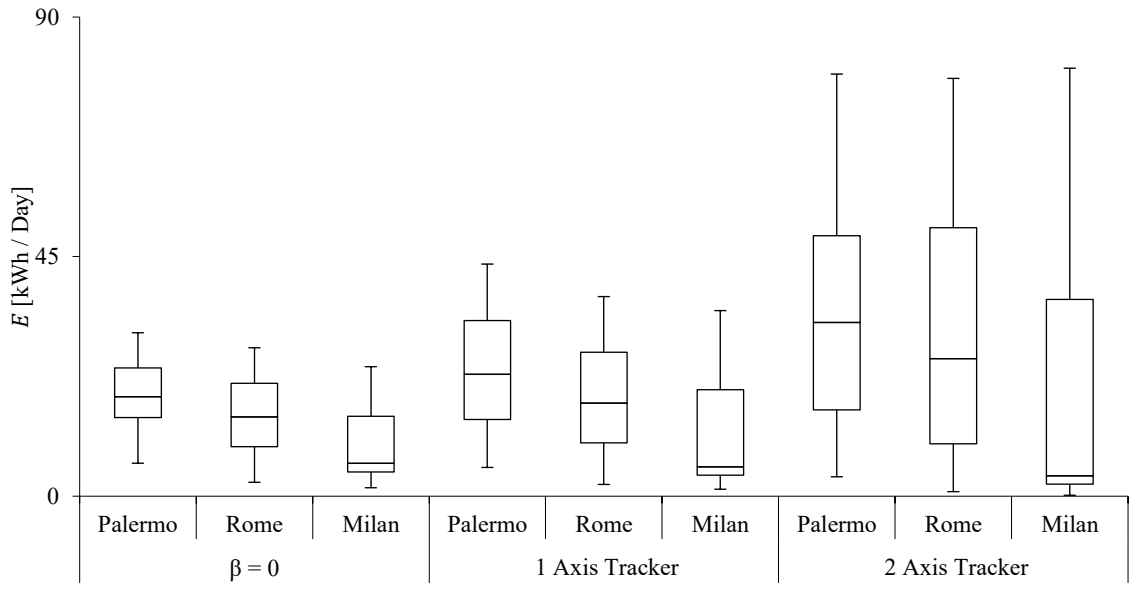

(b)

Figure 3.10. Distribution of daily energy produced by the solar cells integrated into the mobile operating room in (a) July and (b) December for Palermo (PA), Rome (RO), and Milan (MI).

The results demonstrate significant differences influenced by weather conditions and seasonal changes. Also notably, daily energy generation can vary within a month due to factors such as weather patterns and cloud cover. Such insights are crucial for effective energy management, particularly in disaster scenarios, as they enable better utilization of renewable resources to meet energy demands across varying time frames.

3.5.2. Battery Sizing

As discussed in the previous section, trucks and ambulances utilized their existing onboard batteries to support both vehicle operations and PV system. The impact of various work conditions and standby charging losses (L_{CH}) was also analyzed to quantify the energy produced and stored under different scenarios. In this section, the focus shifts to containers and mobile operating rooms, which may serve as examples of off-grid systems.

In traditional off-grid PV systems, the design process begins with identifying the energy loads and determining the required daily energy consumption [117], [131]. Based on this, usually, the necessary PV panel capacity and battery size are then calculated to meet the energy demand. However, in our system, the approach is reversed. Instead of designing the system based on energy demand, we first assess the energy production potential of the PV modules integrated into the available roof space of each case study. Since the installation area is limited, the PV system can only generate a fixed amount of energy, as determined in previous section. For this reason, the battery size is determined based on the available PV energy production rather than the required energy demand. Battery capacity (kWh) was calculated as follows:

$$Battery\ Capacity = \frac{E \cdot N_A}{DoD} \tag{3.18}$$

Where E represents the daily energy production, N_A denotes the number of autonomy days and DoD is the depth of discharge of the battery. In this study, DoD was considered as 0.75 and N_A was set to

3 [40]. The results obtained for calculating the required battery size across different cities and case studies are presented in Table 3.6.

Table 3.6. The obtained results for battery sizing across different cities and case studies.

		E (kWh/Day)			Required Battery (kWh)		
		Palermo	Rome	Milan	Palermo	Rome	Milan
Container	$\beta = 0$	21.91	20.58	15.18	87.64	82.32	60.72
	1 Axis Tracker	27.71	26.11	18.42	110.82	104.45	73.67
	2 Axis Tracker	32.28	31.15	21.46	129.13	124.62	85.84
Mobile Operating Room	$\beta = 0$	50.66	47.58	35.09	202.64	190.32	140.36
	1 Axis Tracker	64.1	60.45	42.66	256.4	241.8	170.64
	2 Axis Tracker	75.3	72.69	50.27	301.2	290.76	201.08

The mentioned results for battery sizing in Table 3.6 are based on the obtained energy production data, and suitable battery capacities can be rounded up to ensure reliable operation and availability.

3.5.3. Load Analysis of Critical Healthcare Equipment

In disaster scenarios, the energy required to power critical medical equipment takes precedence over other needs. Ensuring the health and survival of individuals is paramount, and as such, energy for operating vital devices has been prioritized as the primary requirement. This prioritization allows for a clear understanding of the energy production potential and its ability to support critical healthcare equipment before addressing secondary energy demands.

Data on the energy requirements for operating medical equipment in an Intensive Care Unit (ICU) were gathered through a comprehensive literature review [103], [132], [133], [134], as illustrated in Figure 3.11.

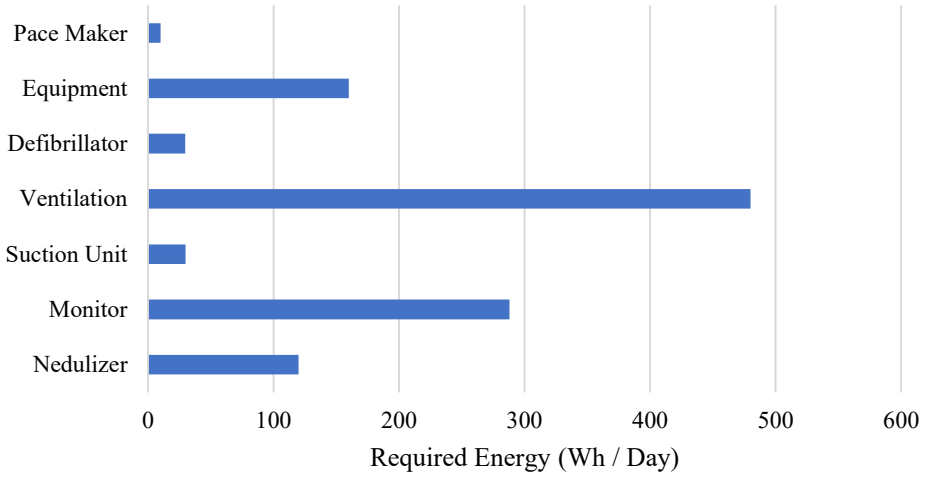

Figure 3.11. Daily energy requirements for various medical equipment in an ICU.

This data was adapted to address disaster scenarios where a reliable and consistent energy supply is essential. To align with these critical situations, the operational hours of each piece of equipment were analysed based on their importance. For example, essential devices such as monitors and ventilators, which play a crucial role in sustaining life or checking vital signs, were identified as requiring uninterrupted operation (24/7). This ensures continuous patient care and highlights the capability of the energy produced in each case study to support these critical devices. It should be noted that the total daily energy requirement, based on the values presented in Figure 3.11, is approximately 1.12 kWh/Day. Additionally, if all the mentioned medical devices are used continuously for one hour, the required energy amounts to 0.09 kWh. However, under the considered operational scenario, where these devices are utilized throughout the day, the average hourly energy demand is approximately 0.05 kWh.

By understanding how long the generated energy can sustain such equipment, this study underscores the vital role of energy production in maintaining healthcare services during emergencies. Hence, to evaluate whether the generated energy can reliably supply the critical energy requirements for healthcare devices under worst-case conditions, the analysis compares the obtained energy production with the essential loads. For each case study and location, July and December were selected as representative months for summer and winter, respectively, since they exhibit the highest and lowest levels of energy production. The minimum daily energy generated in these months was determined and compared with the daily energy demand of vital devices. The results of this analysis are presented in Figure 3.12, where the line graphs represent December, and the bar charts correspond to July.

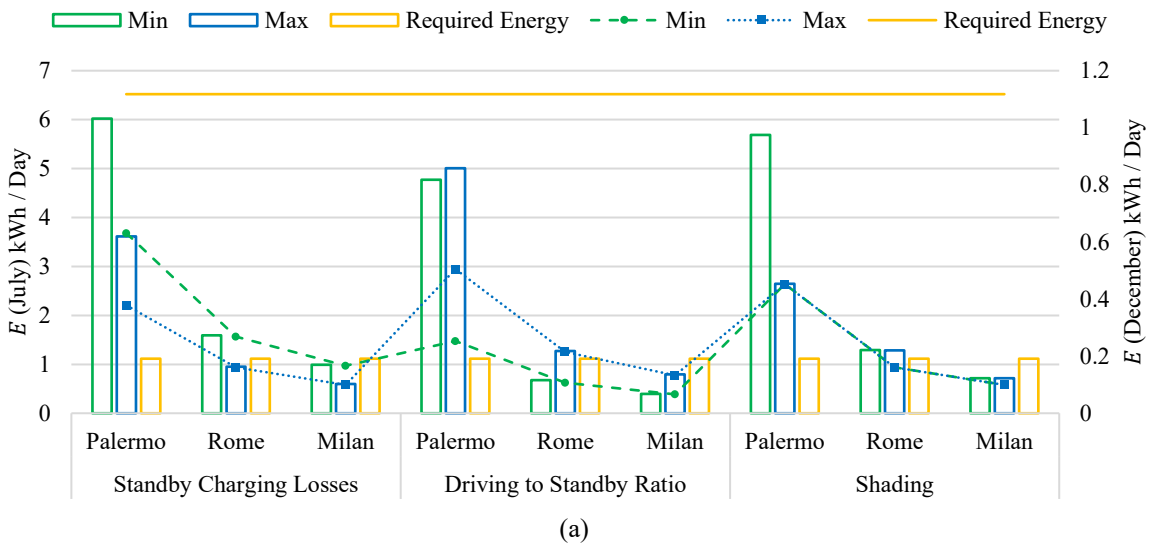

(a)

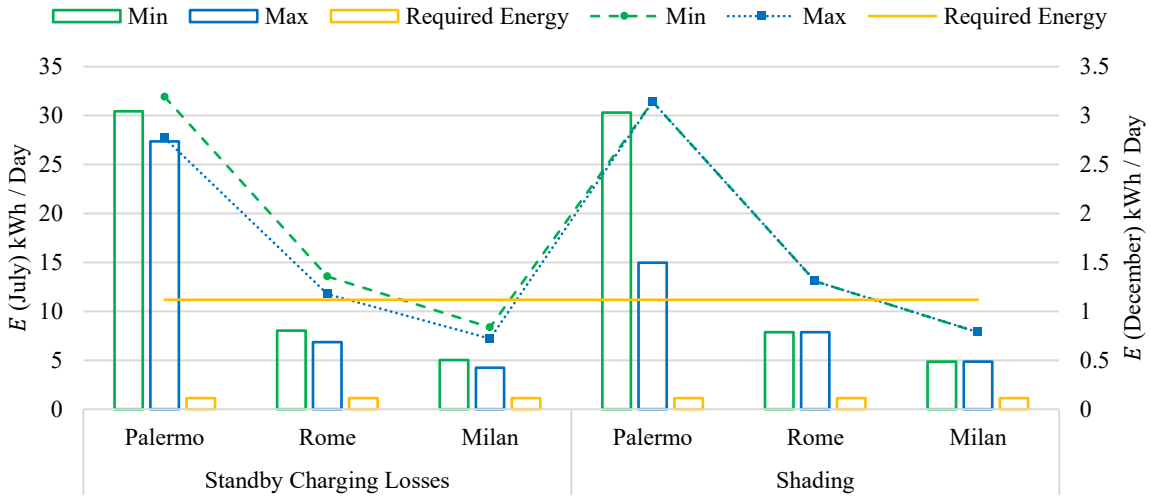

(b)

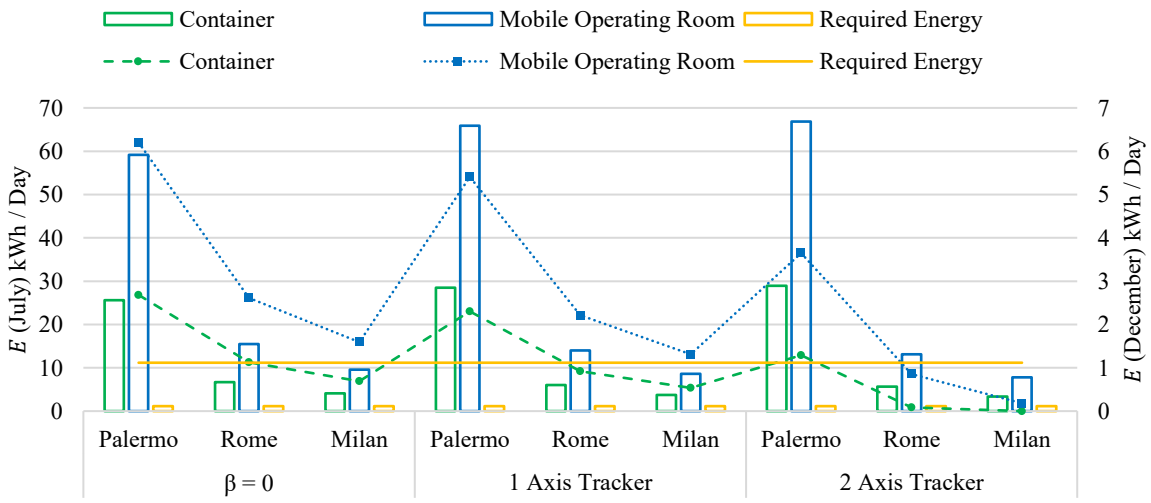

(c)

Figure 3.12. The minimum daily energy production in July and December for different case studies, parameters, and cities for (a) Ambulance, (b) Truck, and (c) Container and Mobile Operating Room.

For both the ambulance and the truck, the terms "Max" and "Min" in the figures represent the energy production corresponding to the maximum and minimum values of a given parameter. For instance,

in the case of standby charging losses (L_{CH}), the maximum and minimum values were set at 700 W and 0 W, respectively. All other conditions and parameters were kept consistent with those outlined for obtaining the values in Table 3.5. Although the VIPV system may not always provide sufficient energy to power all medical devices for an entire day, it can still supply energy for durations ranging from 1 to 15 hours, even under the lowest production conditions. Additionally, the average energy production across the analysed months was significantly higher than these minimum values. For instance, in July, although daily energy production in Milan and Rome sometimes fell below the required energy at certain times, the average generated energy consistently exceeded the required amount.

For the container and mobile operating room, the minimum daily energy production in July and December is shown in Figure 3.12 c, considering three different configurations: a fixed installation with zero inclination and systems with solar tracking. In July, the results indicate that these case studies could fully meet their energy demands, with production ranging from 3 to 60 times the required energy. However, in December, accounting for the energy consumption of tracking systems, some cases in Milan and Rome showed instances where net energy production was close to zero when two-axis trackers were used. On other days, when a two-axis tracker was used, the average energy produced by the container in Milan and Rome was 9.3 and 14.11 kWh, respectively.

3.5.4. CO_2 Emissions

Based on the results in Table 3.5 and the emissions factors from the power sector, the amount of reduced emissions due to using VIPV system and its energy production instead of using grid power, can be calculated (Table 3.7) [135]:

$$CO_2\ reduction = E \cdot Emission\ intensity \quad (3.19)$$

To assess the quantity of CO_2 emissions saved, we rely on available data, utilizing emission factors from the power sector in 2020 [110], which was 259.8 g CO_2/kWh.

Table 3.7. CO_2 emissions reduced values for WAS E 500 and Tesla Semi.

Parameters	Value	WAS E 500			Tesla Semi		
		Reduced emissions (Ton CO_2/Year)					
		Palermo	Rome	Milan	Palermo	Rome	Milan
L_{CH} (W)	0	0.49	0.47	0.35	2.48	2.35	1.75
	700	0.29	0.28	0.21	2.28	2.15	1.58
R (%)	40	0.45	0.43	0.30	-	-	-
	80	0.48	0.45	0.33	-	-	-
Shading (%)	0	0.46	0.44	0.32	2.47	2.34	1.74
	80	0.24	0.22	0.20	1.33	1.25	1.19

As already underlined, although reducing emissions is a secondary concern in emergency scenarios, it underscores the broader sustainability advantages of integrating solar energy into mobile applications.

3.6. Conclusions

Ensuring a reliable energy supply in disaster scenarios is a critical challenge, particularly when grid networks are compromised. This study proposes the evaluation of the potential of VIPV systems to support emergency response efforts by generating energy for both vehicle mobility and essential medical devices. By adapting existing methodologies to account for the unpredictable nature of disasters, energy production under various operational conditions and environmental factors, has been assessed.

While this study primarily focuses on emergency scenarios, long-term energy production results highlight the broader potential of integrating PV systems into emergency vehicles. The results indicate that integrating photovoltaic systems into ambulances can generate, depending on location, between 0.76 to 1.89 $\mathrm{MWh/Year}$, also leading to carbon dioxide savings of 0.2 to 0.549 tons, also underlining the broader sustainability advantages of integrating solar energy into mobile applications. Additionally, the truck's solar range exceeded 30 km/Day for 38 to 99 days of the year, depending on the city. These PV-equipped vehicles can serve dual purposes, functioning under normal conditions while also offering a resilient energy source during emergencies. By considering these results, different cities can proactively equip emergency vehicles with VIPV technology, ensuring they are prepared for rapid deployment in disaster zones.

Considering the energy demand for vital medical devices, where the total daily requirement was 1.12 kWh, the hourly consumption varies between 0.05 kWh in the defined scenario and 0.09 kWh when all devices operate simultaneously. Even under the most challenging conditions, the ambulance's VIPV system could supply medical devices for one to fifteen hours per day. The study also examined the role of solar tracking systems in enhancing energy production for container and mobile operating room in fixed installations. While tracking generally increases energy yield, its own energy consumption, can sometimes reduce net energy output. In some cases, such as during winter in Milan, the energy consumed by dual-axis tracking resulted in zero net energy production. Additionally, in cloudy conditions where diffuse radiation dominates, fixed installations with zero inclination sometimes performed better than tracking systems. In extreme wind conditions (more than 35 $\mathrm{m/s}$), which are common in disaster scenarios, keeping panels at zero inclination is also a safer and more stable option. However, the mobile operating room, under optimal conditions in July, produced more than 120 times the required energy.

Although this study focused on specific vehicles and case studies, the proposed methodology can be extended to other emergency and utility vehicles. While energy production from a single VIPV-equipped vehicle may sometimes be limited, energy losses can be minimized by integrating additional storage solutions, such as portable batteries, or by enabling vehicles to share power. This approach could enhance the overall efficiency and reliability of VIPV systems in disaster response. To further improve resilience, future studies may explore how data from past disasters could be used to predict access routes for emergency vehicles, ensuring more efficient deployment of energy resources.

4

VIPV for Campus and Institutional Vehicle Fleets

This chapter presents the development of a comprehensive framework for the modelling and performance evaluation of VIPV systems, integrating optical, thermal, and electrical sub-models. The proposed framework builds upon and extends methodologies originally developed for fixed PV systems, adapting them to the unique geometrical, operational, and dynamic characteristics of vehicular applications. Its main objective is to enable realistic assessment of the solar irradiance received by the vehicle, the resulting PV module temperature, and the overall electrical energy production under real driving conditions.

A contribution of this work is the implementation of the framework as an open-source MATLAB toolbox, named VIPVLIB, which facilitates the simulation of VIPV performance using both meteorological datasets and real-world driving data collected via smartphone-based sensors. This integration allows the model to dynamically update the vehicle's position and orientation at one-second intervals, thereby capturing the rapid variations in incident solar irradiance caused by movement and changing solar geometry. To ensure a balance between computational efficiency and accuracy, different temporal resolutions were investigated for the optical model. The thermal model was enhanced to account for the combined effects of vehicle speed, convective cooling, and thermal inertia, significantly improving temperature and power prediction accuracy. The proposed framework was experimentally validated using a minibus operating within the University of Palermo campus, serving as a representative case study. The analysis revealed that the vehicle roof receives approximately 45–47% of the total annual solar irradiation, corresponding to annual energy yields of around 4.3 MWh/year for crystalline silicon (c-Si), 3.7 MWh/year for cadmium telluride (CdTe), and 3.1 MWh/year for copper indium gallium selenide (CIGS) modules. The corresponding CO_2 emission reductions ranged from approximately 3.5 tons/year for internal-combustion vehicles to about 2 tons/year for electric ones.

Overall, the proposed framework provides a real-data-driven, modular, and scalable approach for the assessment of VIPV systems under realistic conditions. It not only enhances the understanding of the complex interactions between optical, thermal, and electrical domains in mobile PV applications but also establishes a foundation for future developments in fleet-scale optimization, control strategies, and life-cycle-based eco-design of solar-powered transport systems.

4.1. VIPV for Institutional Vehicle Fleets

The increasing demand for environmentally sustainable and efficient transportation systems have intensified the need for innovative solutions [44], including the use of renewable energy and clean fuel alternatives [136],[137]. A notable advancement in this field may be the integration of photovoltaic (PV) systems into vehicles, known as Vehicle-Integrated Photovoltaics (VIPV) [138]. VIPV involves using vehicle surfaces, such as the roof, back, and sides, to harness sunlight [59]. These surfaces can generate solar energy, whether the vehicle is stationary or moving [54]. This energy can then supplement or even replace traditional fuel sources, helping to reduce greenhouse gas emissions and decrease dependence on fossil fuels [115]. As the world focuses more on achieving carbon-neutral transportation, VIPV has emerged as a possible interesting innovation with the potential to provide major environmental benefits [139], [140]. Moreover, in recent years, advancements in solar cell efficiency, lightweight materials, and advanced energy management systems have significantly enhanced the feasibility of VIPV systems [68], [141], [142]. However, the practical implementation of VIPV systems is inherently complex, not only because moving vehicles experience dynamic conditions, including variations in orientation, speed, and shading [48], but also due to the real, useful and safe positioning of PV systems on various vehicle surfaces. These factors necessitate a detailed understanding of how solar radiation interacts with vehicle surfaces under real-world conditions.

Many experimental investigations into VIPV systems have been conducted. For example, Peibst et al. [80] analysed a truck equipped with amorphous silicon PV modules along a 36 km route in Hannover, Germany. Their study, conducted on 31 May 2021, examined solar radiation received on the roof, sides, and back of the vehicle under both stationary and moving conditions. Results showed that the roof consistently received the highest levels of irradiance, though the distribution varied based on factors such as the time of day and vehicle movement. Pyranometer measurements captured detailed irradiance patterns, emphasizing the importance of considering vehicle dynamics and module positioning in optimizing energy generation. Similarly, Ota et al. [39] investigated solar radiation on a vehicle travelling a 15 km route in Miyazaki, Japan. This study highlighted how geographic location, weather conditions, and seasonal variations significantly influence solar irradiance levels, further illustrating the challenges of predicting PV performance in dynamic conditions. Building on these efforts, Wetzel et al. [143] conducted a detailed analysis of a van equipped with PV modules over a 21 km route in Hanover, Germany, between 2019 and 2020. This research considered a variety of urban environments, such as narrow streets with high building density, wide streets with slower traffic, and fast-moving open roads. The study found that radiation levels on the roof were often 1.09 to 3.85 times higher than those on the sides, with shading from buildings in narrower streets being a significant limiting factor. Moreover, weather conditions have a deep impact on energy generation, with sunny conditions providing higher irradiance, though seasonal variations moderated these differences in winter months.

Experimental investigations into VIPV systems have provided valuable insights into their performance under diverse operating scenarios. While these experimental findings are valuable, they also highlight the challenges associated with physical testing [144]. Anyway, developing and testing physical prototypes may be very expensive and the results may not be immediately useful, especially given the wide range of variables influencing VIPV performance. Otherwise, simulation-based approach may provide a scalable and flexible way for studying VIPV systems in a pre-prototyping phase, so reducing previous listed uncertainties, and bridging the gap between experimental observations and real-world applications [28], [58], [107], [124].

Unlike many other research areas, there is no widely recognized and standardized methodology for simulating VIPV systems. Although numerous methodologies have been proposed [29], [45], [57], [79], [106], selecting the right one for a given study remains a significant challenge. This study aims to address this challenge by proposing an open-source model chain that organizes the simulation process for VIPV systems. The proposed framework offers both accuracy and flexibility, ensuring that it can be adapted to various case studies. This approach allows researchers to tailor the model to specific conditions or extend it by incorporating additional factors for more comprehensive simulations.

The framework consists of three cores, each designed to model critical aspects of a VIPV system.

- Optical Model, analyses how sunlight interacts with the vehicle's surface, considering factors such as shading and the effects of the vehicle's body curvature.
- Thermal Model, examines the temperature variations in PV modules due to environmental conditions and heat dissipation, as temperature significantly impacts PV efficiency.
- Electrical Model, simulates the electrical behaviour of the PV system, including energy generation and power output.

For each of these cores, the most appropriate methodologies were carefully selected to build a robust and reliable simulation framework. To simulate the VIPV system under actual driving conditions, real-world driving data were collected through a smartphone equipped with MATLAB Mobile. The data includes essential parameters such as vehicle speed, GPS coordinates, and environmental conditions. These parameters were processed in MATLAB to simulate the performance of the VIPV system in real-time. This approach enabled the development of a simulation-based framework using real data.

To experimentally validate the proposed methodology, a case study was conducted using a minibus operating within the University of Palermo (UNIPA) campus. The minibus was chosen because of its frequent use for passenger transport and consistent operational patterns. By studying this vehicle in a controlled environment, reliable data could be collected to evaluate the performance of the VIPV system under real-world conditions. Additionally, to simulate the energy produced by the VIPV system, we considered the vehicle's energy consumption across different operational scenarios. This comparison enabled us to assess the feasibility and potential benefits of integrating VIPV systems into vehicles. Furthermore, we explored the sustainability implications of integrating VIPV systems into various types of vehicles, including Electric Vehicles (EVs) and Internal Combustion Engine (ICE) vehicles. This allowed us to compare the impact of VIPV systems on different vehicle types and assess their contribution to sustainable transportation, as a first step towards a future comprehensive life cycle assessment analysis

4.2. Literature Review

To investigate the distribution of solar irradiance on vehicle surfaces, many studies have used simulation-based approaches. Kutter et al. [45] investigated the integration of PV systems into the roofs of commercial trucks and vans in Europe. Their study used hourly solar data to estimate annual solar energy generation for different vehicle types, such as parcel delivery vans, rural delivery trucks, and long-haul trucks. However, their approach only considered the roof of the vehicles and did not account for shading effects. Expanding on this, Kim et al. [106], analysed the potential for solar energy generation on high-speed trains in South Korea. They used a dynamic model to calculate solar

irradiance on the roofs of moving trains and incorporated shadow effects from nearby objects. This method relied on Geographic Information Systems (GIS) data and included a Digital Surface Model (DSM) with a resolution of 3 m to improve accuracy. The calculations were performed at a high temporal resolution, with solar irradiation estimated for each minute. Similarly, Oh et al. [57], studied solar buses in Seoul, South Korea using high-resolution GIS data to calculate solar power generation, and considering the specific location of each bus and the surrounding environment, including road networks, topography, and building heights. Similarly, their calculations also used a high temporal resolution, performing estimations every minute to accurately model solar irradiance and energy generation along each bus route.

In addition to solar irradiance, the temperature of PV modules significantly affects their efficiency, as higher temperatures generally reduce performance [145], [146], [147], [148]. Researchers have used different methods to calculate module temperatures [46], [83]. For example, the Nominal Operating Cell Temperature (NOCT) [86] and Faiman [87] models are widely used for stationary PV systems. However, these models do not account for the thermal inertia of fast-moving PV systems. To address this, Patel et al. [88] proposed averaging temperature variations over periods of 1000 to 1500 seconds to account for the thermal inertia in moving PV systems.

Beyond temperature considerations, recent studies have focused on developing accurate predictive models for PV performance under dynamic conditions. Abdelhamid et al. [79] developed an optimized model for on-board PV systems in plug-in electric vehicles, which integrates both electrical and thermal effects under varying operational conditions. Their approach used a single-diode model (SDM) to calculate key performance indicators such as voltage, current, and power. They applied a four-parameter framework that incorporated curve-fitting techniques to estimate essential factors such as light-generated current, saturation current, diode ideality factor, and series resistance. In another related study, Mallon et al. [114] investigated the integration of on-board PV modules in heavy-duty electric vehicles, focusing on an electric bus to evaluate energy generation under different configurations. The study employed an electrical model based on SDM to assess how power output varied with changes in temperature and solar radiation. This approach included a peak power temperature coefficient to capture the sensitivity of PV performance to temperature fluctuations, complemented by a thermal model based on NOCT model to estimate operating temperatures under varying environmental conditions, including solar irradiance and ambient air temperature.

4.3. Methodology

Figure 4.1 shows a schematic of the proposed approach. In the proposed framework, the three models operate sequentially and exchange data in real time. The optical model first determines the solar irradiance incident on each vehicle surface based on driving and environmental data. These irradiance values then serve as inputs to the thermal model, which estimates the corresponding PV module temperatures. Finally, both irradiance and temperature are used by the electrical model to calculate instantaneous power generation and cumulative energy output. This integrated workflow ensures continuous coupling among the three models, reflecting the dynamic behaviour of a moving vehicle.

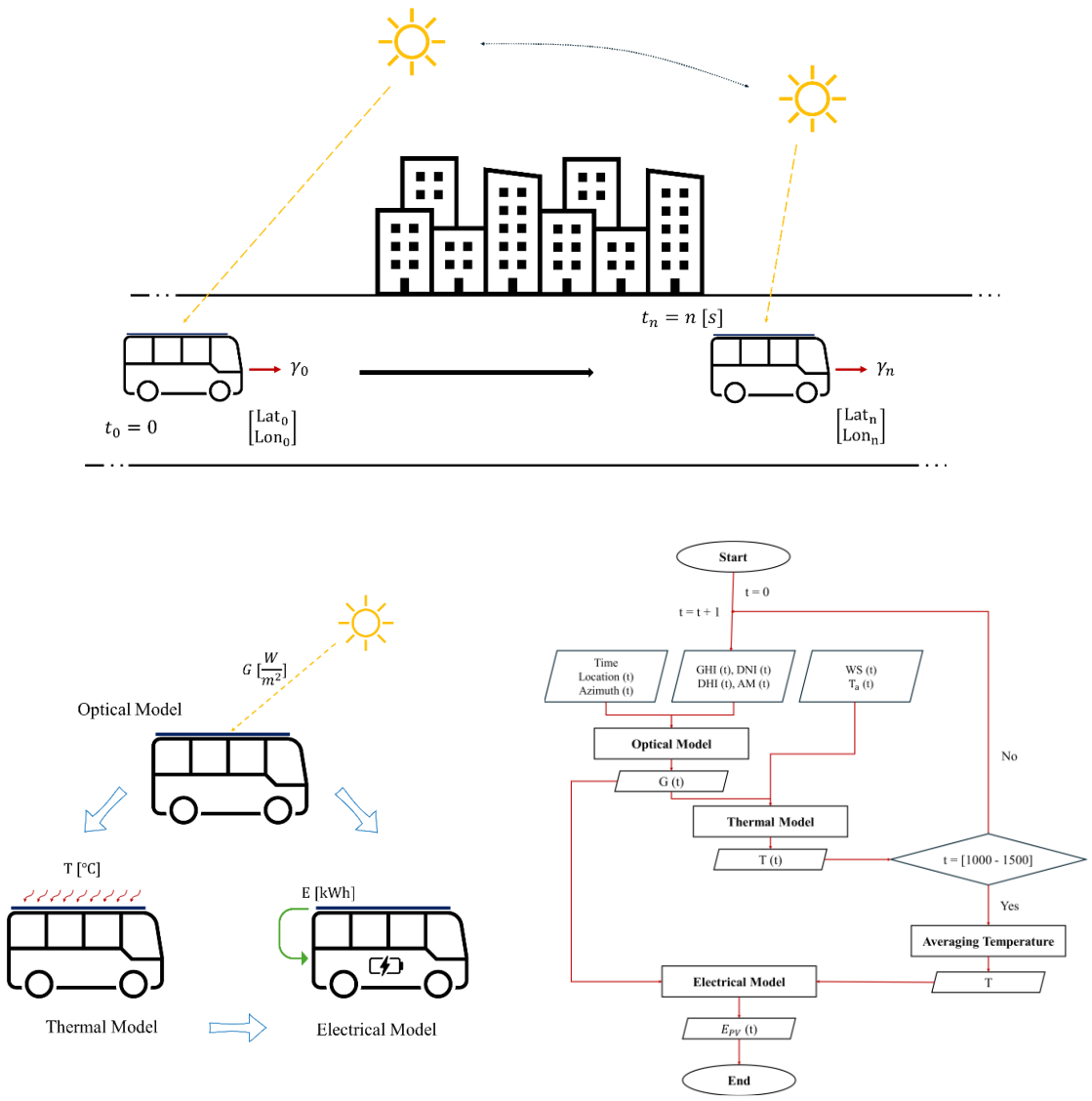

Figure 4.1. The proposed model chain for investigating the performance of VIPV systems.

The optical model developed in this study builds upon methodologies proposed by Perez et al. [149] and King et al. [150], which estimates the diffuse and direct irradiance received by surfaces based on weather data and geographic location. These methods are typically applied to stationary PV systems and calculate irradiance on surfaces with defined tilt and orientation over a specified time range. To address this, our methodology accounts for vehicle movement, as the position of the vehicle relative to the sun will continuously change. These variations mean that, depending on the time ($t = [t_1, \dots, t_n]$) and position ($\begin{bmatrix} Latitude \\ Longitude \end{bmatrix} = [\begin{matrix} Lat_1 \\ Lon_1 \end{matrix}, \cdots, \begin{matrix} Lat_n \\ Lon_n \end{matrix}]$), each solar cell integrated into different surfaces of the vehicle will experience varying azimuth (γ). Consequently, the irradiance received by each surface will vary every second.

Real-time driving data was collected using the MATLAB Mobile application, which utilizes smartphone sensors to capture detailed information on the vehicle's geographic position, speed, and direction of travel. Data points were recorded at one-second intervals, resulting in a high-resolution

temporal dataset. The vehicle's path is thus modelled as a sequence of discrete positions with continuously updated orientation. This dynamic input allows the optical model to compute irradiance for each surface, roof, back, and sides, at every time step, reflecting the actual conditions experienced by the vehicle during motion. Furthermore, to understand how the choice of temporal resolution affects the accuracy of optical model, simulations were run at different time intervals: 1, 2, 3, 4, 5, and 10 minutes. These results were compared against the one-second baseline to evaluate the potential errors introduced by coarser time steps. This analysis highlights the importance of high-resolution modelling, especially for mobile PV systems where rapid changes in environmental exposure are frequent.

To provide the necessary meteorological data for simulation, Typical Meteorological Year (TMY) files were used. These datasets compile representative hourly weather conditions over a full year for specific geographic locations. For this study, TMY data for Palermo was obtained from the Photovoltaic Geographical Information System (PVGIS) portal [112]. The TMY datasets include essential parameters such as Direct Normal Irradiance (DNI), Diffuse Horizontal Irradiance (DHI), ambient temperature (T_a), and wind speed (WS). Since the optical and thermal models operate on a per-second basis, linear interpolation was applied to the TMY data to transform it into a higher temporal resolution. The use of TMY data was preferred because it provides a statistically consistent representation of long-term meteorological conditions and is widely adopted in PV system modeling, ensuring comparability with other studies. However, TMY data represent averaged weather patterns and do not capture short-term fluctuations or extreme conditions that may occur in real driving environments. This simplification can introduce some uncertainty in second-by-second VIPV simulations, where transient irradiance or temperature spikes could slightly alter results. Future developments may address this limitation by coupling the model with high-frequency meteorological data or real-time measurements collected through onboard sensors.

Thermal behaviour was analysed using both the Nominal Operating Cell Temperature (NOCT) model and the Faiman model. These approaches estimate the PV module temperature based on external environmental conditions and module-specific properties. To account for thermal inertia, which becomes significant in fast-moving PV applications, the method proposed by Patel et al. [88] was incorporated. This ensures that transient thermal effects, such as delayed temperature response due to rapid changes in environmental conditions or vehicle motion, are appropriately considered. The integration of optical and thermal models forms the foundation for estimating electrical energy generation. To perform this estimation, the single-diode model was employed. This model calculates the power output of the PV system at each second, using inputs from the optical and thermal simulations. The results are then aggregated to evaluate performance across various timeframes, including daily, monthly, and annual periods.

Given that photovoltaic technologies differ in characteristics such as conversion efficiency, temperature coefficient, and spectral response, their performance can vary significantly under dynamic operating conditions [37]. To explore this, a comparative analysis was conducted on three widely used PV technologies: crystalline silicon (c-Si), copper indium gallium selenide (CIGS), and cadmium telluride (CdTe). Each technology was evaluated in the context of VIPV to understand how it responds to changes in irradiance, temperature, and orientation over time.

Finally, to complement the energy generation analysis, a vehicle model was developed to estimate energy consumption during motion. This model is essential for comparing the amount of energy generated by the VIPV system with the actual demand of the vehicle under different driving scenarios.

All the models proposed in this study, the optical, thermal, electrical, and vehicle consumption models, are discussed individually and in greater detail in the following sections.

4.3.1. Optical Model

Solar radiation has three main components: direct, diffuse, and reflected ones. In this study, the reflection component wasn't considered; therefore, the total irradiance incident on the solar cells integrated into the vehicle can be expressed as in Equation 4.1 [151]:

$$G_t = G_b + G_d \tag{4.1}$$

Although direct solar irradiance (G_b) travels in a straight path to the PV module, diffuse solar irradiance (G_d) consists of rays scattered by atmospheric particles, approaching the solar module from different directions. Another important factor considered in the optical model is the shading, which directly affects the amount of incoming irradiance available to the photovoltaic system. The impact of shading varies significantly across different environments due to factors such as the density of trees, buildings, and other obstructions along the paths. When shading is not severe, its effect can be approximated using a constant shading loss factor, as defined in Equation 4.2 [29], [114], [115]:

$$G_{b\,(Shading)} = \eta_{Shading} \cdot G_b \tag{4.2}$$

where $G_{b\,(Shading)}$ represents the direct irradiance accounting for shading effects, allowing for a simplified yet effective assessment of the shading's influence on the overall performance of the VIPV system. The impact of the shading on the diffuse irradiance could be modelled considering a sky view factor approach [152] but, except in severe shading conditions, it may be neglected: this is the choice adopted in the proposed approach. The curvature of the vehicle body also has an impact on the harvesting of solar energy. Ota et al. [153] introduced geometric parameters and proposed a metric known as the Curve Correction Factor (CF) to account for this curvature during the simulation process. This factor allows for a more accurate estimation of the PV system's performance by compensating for the effects of the vehicle's curved surface on solar energy capture. By incorporating the CF, the model can better reflect the real-world performance of vehicle-integrated photovoltaic systems, ensuring a more reliable analysis of their efficiency. By using CF, finally, the total received irradiance on the vehicle body, accounting for both shading effects and CF, is expressed as follows:

$$G = CF \cdot (G_{b\,(Shading)} + G_d) \tag{4.3}$$

By using Equation 4.4, the amount of direct irradiance on a surface can be calculated [79]:

$$G_b = DNI \cdot cos(AOI) \tag{4.4}$$

where DNI stands for Direct Normal Irradiance and AOI stands for Angle of Incidence. DNI is the direct component of the irradiance received per unit area by a surface that is always oriented perpendicular (normal) to the sun's rays coming directly from the sun's current position in the sky. The AOI is the angle between the incoming solar rays and the normal to the surface receiving the radiation. The Angle of Incidence (AOI) is calculated using the following equation [150]:

$$AOI = cos^{-1}[cos(\beta) \cdot cos(\theta_Z) + sin(\beta) \cdot sin(\theta_Z) \cdot cos(\gamma_S - \gamma)] \tag{4.5}$$

In this context, β represents the tilt angle of the PV surface relative to the horizontal plane, γ denotes the azimuth angle of the PV surface (the angle between the projection of the normal to the surface and a reference direction such as north), θ_Z is the solar zenith angle (the angle between the sun's rays and the vertical direction), and γ_S is the solar azimuth angle (the angle between the projection of the sun's rays on the horizontal plane and the north direction). The angle of incidence, along with other relevant solar angles, is depicted in Figure 4.2.

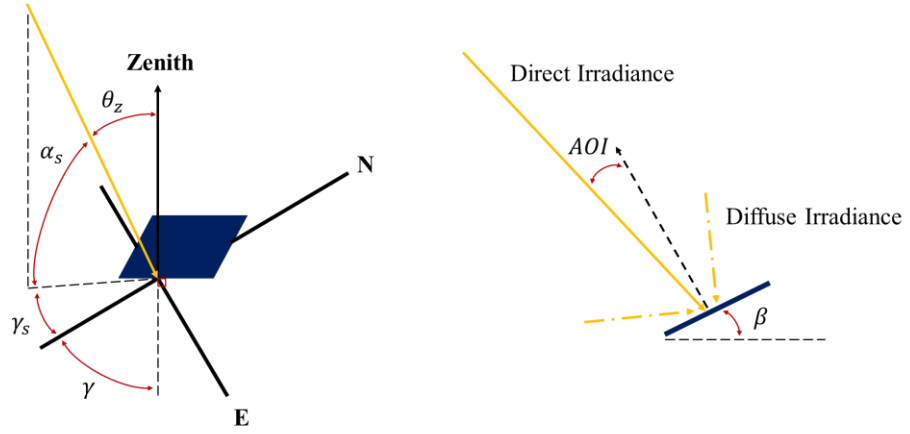

Figure 4.2. Illustration of different solar angles.

Based on the method proposed by Perez et al. [149], the diffuse irradiance received on a tilted surface (G_d) can be calculated as follows:

$$G_d = DHI \cdot \left[\frac{(1-F_1)\cdot(1+cos\,\beta)}{2} + F_1 \cdot \frac{A}{B} + F_2 \cdot sin\,\beta\right] \quad (4.6)$$

$$A = max(0, cos\,AOI)\ , \qquad B = max(0.087, cos\,\theta_Z) \quad (4.7)$$

where F_1 and F_2 are coefficients that express the degree of circumsolar and horizon/zenith anisotropy, respectively. These coefficients vary as functions of sky conditions and can be calculated as follows:

$$F_1 = F_{11} + F_{12} \cdot \Delta + F_{13} \cdot \theta_Z \quad (4.8)$$

$$F_2 = F_{21} + F_{22} \cdot \Delta + F_{23} \cdot \theta_Z \quad (4.9)$$

It should be noted that F_{11}, F_{12}, F_{13} and F_{21}, F_{22}, F_{23} are Perez et al. [149] model coefficients, which were calculated based on the sky's clearness (ε):

$$\varepsilon = \frac{DHI + DNI}{DHI + \kappa \cdot {\theta_Z}^3} \cdot \frac{1}{1 + \kappa \cdot {\theta_Z}^3} \quad (4.10)$$

Where κ is a constant equal to 1.041. Based on the obtained value of ε and its range, Perez et al. [149] calculated the corresponding coefficients. Additionally, by using extraterrestrial normal irradiance (E_a) and Air Mass (AM), the sky's brightness (Δ) can be determined as follows:

$$\Delta = \frac{DHI \cdot AM}{E_a} \quad (4.11)$$

The air mass can be calculated as follows [44]:

$$AM = \frac{1}{cos(\alpha_S) + 0.50572 \cdot (6.07995 + (90 - \alpha_S))^{-1.6364}} \quad (4.12)$$

where α_S is the solar elevation angle, the angle between the sun's rays and the horizontal plane, which indicates how high the sun is in the sky.

$$\alpha_S = 90 - \theta_Z \quad (4.13)$$

Additionally, the extraterrestrial normal irradiance (E_a) is calculated using the following equation:

$$E_a = E_{sc} \cdot \left(\frac{R_{av}}{R}\right)^2 \quad (4.14)$$

$$\left(\frac{R_{av}}{R}\right)^2 = 1.00011 + 0.034221 \cdot cos(b) + \frac{0.00128}{sin(b)} + 0.000719 \cdot cos(2b) + 0.000077 \cdot sin(2b) \quad (4.15)$$

$$b = 2\pi \cdot \frac{doy}{365} \tag{4.16}$$

where E_{sc} solar constant ($1367\ W/m^2$) represents the average solar radiation received outside the Earth's atmosphere on a surface perpendicular to the sun's rays, doy is the day of the year, R_{av} is the average distance from the Earth to the sun, and R is the actual distance from the Earth to the sun on a given day.

4.3.1.1. VIPVLIB

PVLIB toolbox in MATLAB [154] provides a set of functions for simulating PV system performance. Some functions available in the PVLIB library are based on methodologies like those proposed in the previous section. For instance, the pvl_getaoi function in PVLIB calculates the angle of incidence (AOI) using the methodology developed by King et al. [150] and it requires inputs such as γ, γ_S, θ_Z, and β. Parameters such as extraterrestrial normal irradiance (E_a) can be calculated either through analytical expressions (Eqs. 14–16) or using built-in PVLIB functions such as $pvl\_extraradiation$ and $pvl\_date2doy$ to determine E_a and doy. Although PVLIB was originally developed for fixed PV installations, its functions were adapted and integrated into an open-source model chain developed in this study to account for vehicle dynamics. Figure 3 illustrates the structure and data flow of the optical model, where selected PVLIB functions are combined with real driving and geographical data to compute irradiance on vehicle surfaces in motion. This open-source framework, referred to as "VIPVLIB," includes an optical model based on adapted PVLIB functions, along with thermal and electrical models developed following the methodology proposed in this work. The complete model chain has been made available to support further research in the field of VIPV systems. The thermal and electrical models will be described in detail in the following sections.

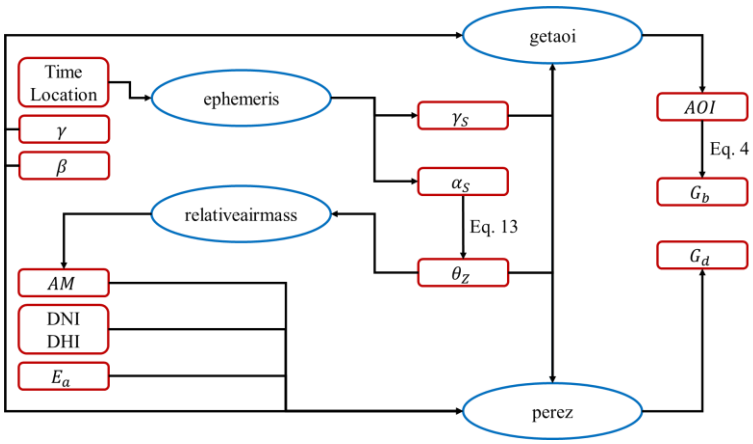

Figure 4.3. Flowchart of the Optical Model Process Using PVLIB Functions.

4.3.2. Thermal Model

The thermal model refers to the calculation of the temperature of the PV module (T_{module}) by utilizing meteorological data, the vehicle's velocity, and the solar irradiance obtained from the optical model. As already underlined, NOCT and Faiman methods have been used. The NOCT method provides an estimate of the PV module temperature under specific reference conditions: 800 W/m^2 irradiance, 20 $°C$ ambient temperature, and 1 m/s wind speed. This method is useful for standardizing temperature predictions across different PV technologies and is as follows [86]:

$$T_{module} = T_a + \frac{G_t}{800} \cdot (NOCT - 20) \quad (4.17)$$

where T_a represents the air temperature. In this work, the NOCT is 48 [$°C$]. The Faiman method uses a heat balance equation to model the thermal behavior of the PV cells, considering factors such as air temperature (T_a) $°C$, wind speed m/s, and the specific thermal properties of the PV module. By using Equation 18, T_{module} can be calculated through the Faiman method [87]:

$$T_{module} = T_a + \frac{G_t}{U_0 + U_1 \cdot WS} \quad (4.18)$$

where U_0 represents the constant heat transfer component W/m^2K, U_1 represents the convective heat transfer component $W/m^3s\ K$, and WS represents the wind speed m/s. When the vehicle is in motion, the wind speed is determined based on its instantaneous speed. When the vehicle is parked, the ambient wind speed is used. Since wind speed data from TMY is recorded at a height of 10 m above ground, it is adjusted to the roof height using the following equation [112]:

$$WS_{Roof} = WS_{TMY} \cdot (\frac{h_{Roof}}{10^{0.2}}) \quad (4.19)$$

Therefore, as discussed in [155], when the vehicle is stopped (speed = 0), the wind speed was adjusted based on the height of the minibus roof to simulate natural airflow. It should be noted that the temperature of the PV modules was first obtained every second using the two mentioned methods. Then, following the approach proposed by Patel et al. [88], the second-by-second temperature data were averaged over intervals of 1000 to 1500 seconds and used in the electrical model instead of directly using the instantaneous values. This averaging range was chosen because Patel et al. [88] demonstrated that beyond approximately 1000–1500 s, the thermal parameters of PV modules reach steady convergence, indicating that this period represents the characteristic thermal time constant of a moving PV system. Averaging over this interval effectively filters short-term fluctuations while preserving the real thermal response of the modules under dynamic conditions.

4.3.3. Electrical Model

To calculate the amount of P_{PV}, generated power from the PV modules, this work proposes an electrical model incorporating previous results, including G_t and T_{module}, as follows [114], [156]:

$$G_d = DHI \cdot \left[\frac{(1 - F_1) \cdot (1 + cos\,\beta)}{2} + F_1 \cdot \frac{A}{B} + F_2 \cdot sin\,\beta\right] \quad (4.20)$$

$$A = max(0, cos\,AOI)\ , \qquad B = max(0.087, cos\,\theta_Z) \quad (4.21)$$

The value of the temperature coefficient (k), which depends on the type of solar cell used, is specified in Table 1. A_{PV} refers to the PV coverage area m^2, while α denotes the percentage of the vehicle's surface area covered by PV modules. In this study, the values of efficiency of the power converter (η_{Co}) and reference temperature (T_{ref}) were set to 96% and 25°C respectively, following the work of [57], [106], [114]. By calculating the generated power, we can obtain comparable data to investigate and analyse the potential integration of different PV modules into the minibus. This approach enables a systematic evaluation of the effectiveness and efficiency of PV cell applications in automotive contexts.

4.3.4. Vehicle Model

The vehicle model was developed to estimate the power demand and total energy consumption of the system. It assumes that the driver closely adheres to the reference speed profile provided by the drive

cycle. Based on Newton's second law of motion, the total road load is computed as the sum of various forces acting on the vehicle, including the inertial force $\overrightarrow{F_i}$ (due to vehicle acceleration a_V), the gravitational force $\overrightarrow{F_S}$ from road gradients, rolling resistance $\overrightarrow{F_r}$, and aerodynamic drag $\overrightarrow{F_a}$, as shown in the following equation [114], [157]:

$$\overrightarrow{F_t} = \overrightarrow{F_i} + \overrightarrow{F_s} + \overrightarrow{F_r} + \overrightarrow{F_a} \tag{4.22}$$

Figure 4.4 shows a schematic representation of the vehicle model, and the forces considered. Where M is the total mass kg, g gravitational acceleration m/s^2, ρ is the air density kg/m^3, α_r is road inclination, c_{rr} is rolling resistance coefficient, c_d is the air drag coefficient, A_f is the frontal area m^2, and V is the vehicle speed m/s.

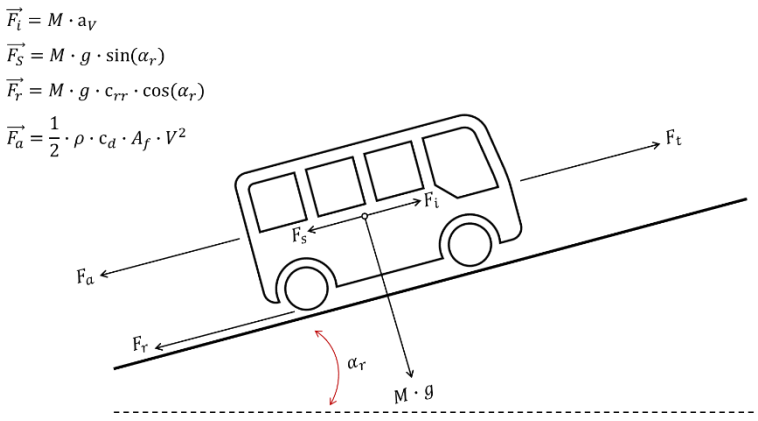

Figure 4.4. Vehicle model diagram.

The total power P_{tot} (in W) and total energy consumption E_{tot} (in Wh) are computed using the following equations [157]:

$$P_{tot} = F_t \cdot V;\ E_{tot} = \int P_{tot}\, dt \tag{4.23}$$

4.4. Case Study

A practical vehicle was selected to apply the proposed methodology based on its frequent usage and operational characteristics. An electric minibus, commonly used within the University of Palermo (UNIPA) campus, was chosen for this study. This vehicle plays a key role in transporting numerous people around the campus and between departments. Its consistent route, daily operation schedule, and medium-speed driving profile make it an ideal candidate for testing the dynamic behavior of VIPV systems. Its regular operation in a real-world environment provides an excellent opportunity to investigate the performance of a VIPV system under typical usage conditions, offering valuable data for assessing its efficiency and practical applicability. The vehicle used in this study was the Karsan e-Jest minibus, and its general dimensions are provided in Table 4.1.

Table 4.1. Dimensions of the Karsan e-Jest minibus in this study [157], [158].

	Considered dimensions [mm]
Length	5854
Width	2055

Height	2800

These dimensions have been extracted from the vehicle's official catalogue [157], [158]. It is important to note that, in this study, it was assumed that PV modules could not fully cover the entire external surface of the minibus. Several factors contribute to this limitation, including the curvature of the vehicle's surfaces, the presence of windows, air-conditioning ducts, and other structural features that impede complete coverage. Table 4.2 details the percentage of the surface area covered by PV modules for different sections of the minibus, as considered in this study. These values were estimated from direct measurements and visual assessment of usable surfaces, ensuring realistic assumptions for the modelling phase.

Table 4.2. PV coverage for different surfaces of the minibus.

Surfaces	**PV coverage [%]**
Top	60
Back	70
Right	40
Left	50

This study also explores different PV technologies to investigate VIPV performance. The specifications of these solar cells are detailed in Table 4.3.

Table 4.3. Specifications of the PV modules [81], [159].

PV Module	**Efficiency [%]**	$\boldsymbol{k}$ **[%/°C]**	$\boldsymbol{U_0}$ **[$W/m^2°C$]**	$\boldsymbol{U_1}$ **[$W/m^3°C$]**
c-Si	21.6	- 0.47	30.02	6.28
CIGS	15.1	- 0.45	22.19	4.09
CdTe	18.6	- 0.34	23.37	5.44

Table 4.3 provides key parameters such as the cell efficiency (η_{PV}), temperature coefficient (k, in $\%/°C$), and thermal coefficients (U_0 and U_1), which are critical for accurately modeling the thermal and electrical behavior of the PV modules. Moreover, Table 4.4 presents the required parameters for vehicle modelling [157].

Table 4.4. Vehicle model parameters [157].

Parameter	**Variable**	**Value**
Vehicle Mass [kg]	M_V	5000
Aerodynamic Drag Coefficient	c_d	0.36
Rolling Resistance Coefficient	c_{rr}	0.011
Air Density [kg/m^3]	ρ	1.202

It should be noted that a 95 % drivetrain efficiency and a constant auxiliary load of 2 kW, accounting for the energy consumption of onboard systems such as air conditioning and lighting, were added to the total power calculation [157].

4.4.1. Vehicle Motion

The movement and orientation of the minibus were tracked using MATLAB Mobile, which utilizes the sensors of a smartphone to gather critical data, including location, speed, and azimuth. This approach facilitated the collection of key inputs essential for the proposed methodology. The location and speed data were recorded at one-second intervals, offering a detailed representation of the minibus's trajectory over a complete trip. Location data, as depicted in Figure 4.5, illustrate the vehicle's path during its operational cycle. The route included five bus stops, which played a key role in assessing the movement pattern and enhancing the model's precision. Data collection was performed on typical working days to ensure that the recorded conditions reflected normal operational activity.

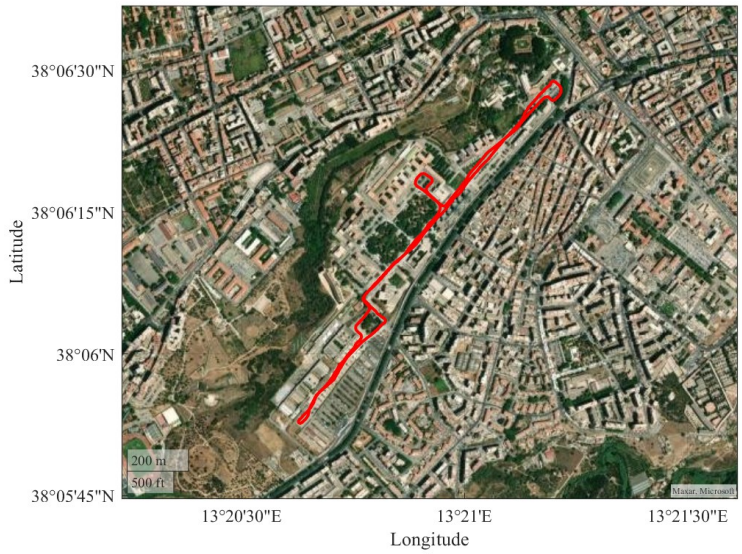

Figure 4.5. The pathway of the minibus across the University of Palermo (UNIPA) campus (Source: MATLAB).

The ability to capture and utilize such detailed data enhances the robustness of the proposed approach, allowing for a comprehensive analysis of the VIPV system's performance under realistic operating conditions. The speed profile of the minibus along the mentioned pathway is shown in Figure 4.6. As illustrated, the complete drive cycle was 20 minutes (1200 seconds). This figure provides a detailed view of the speed fluctuations throughout the cycle, reflecting typical operational conditions.

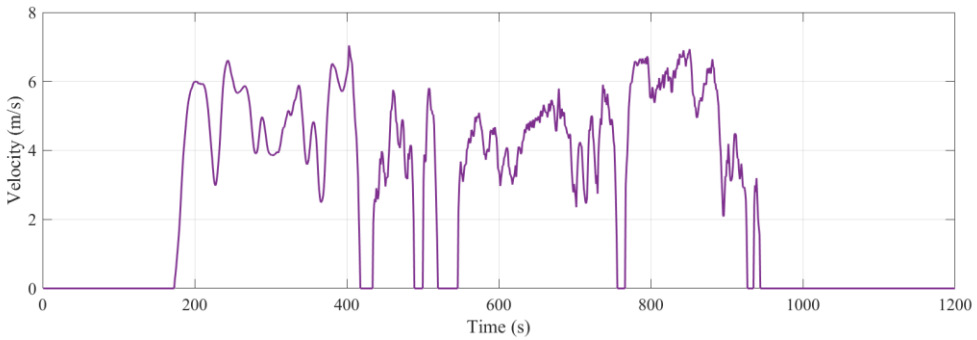

Figure 4.6. The drive cycle of the minibus.

Understanding speed variations and operational patterns is essential for accurately modelling the minibus and estimating its energy consumption. To explore these aspects, different operational scenarios were considered. The minibus's operation was based on a drive cycle of 20 minutes, with the working hours set from 08:00 to 15:00. Under these conditions, the minibus could either operate continuously or run only once per hour. Depending on the operational pattern, this results in the vehicle completing between 7 and 21 trips within the defined working hours.

During the data collection process, the number of passengers onboard the minibus was also recorded, as shown in Figure 4.7. This information provided key insights into the passenger dynamics across different trips. Two scenarios were developed to examine how the number of passengers affects energy consumption:

- Full Capacity: In this scenario, the minibus operates with a constant number of passengers, assuming full capacity of 22 passengers for the entire trip duration.
- Variable Passenger Count: The number of passengers changes dynamically at each stop, reflecting real-world boarding and alighting patterns (as illustrated in Figure 7).

The average weight of each passenger was 70 kg, which contributed to the vehicle's total load.

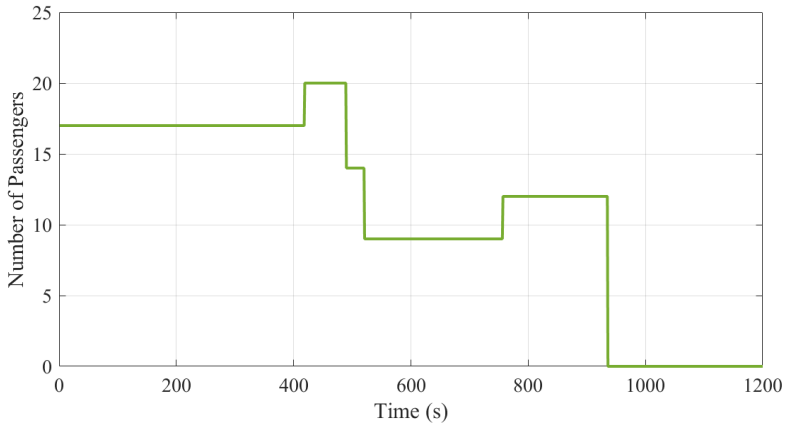

Figure 4.7. The variations in number of passengers during the trip.

Although Figures 4.6 and 4.7 present one representative cycle for clarity, multiple trips were recorded under typical operating conditions during different times of the day. The selected dataset was verified to be consistent with the average behaviour of the minibus and is therefore considered representative for modelling purposes and for extrapolation to yearly operation.

The collection of azimuth data resulted in a total of 63,401 values, reflecting the vehicle's directional changes at a high frequency of at least 50 measurements per second. The azimuth data were averaged over one-second intervals to synchronize them with other time-based variables. This approach preserved the essential directional variations of the minibus while significantly reducing the dataset to a manageable size. The resulting averaged azimuth (Az) values are shown in Figure 8, providing a clear representation of the vehicle's orientation throughout its operational cycle.

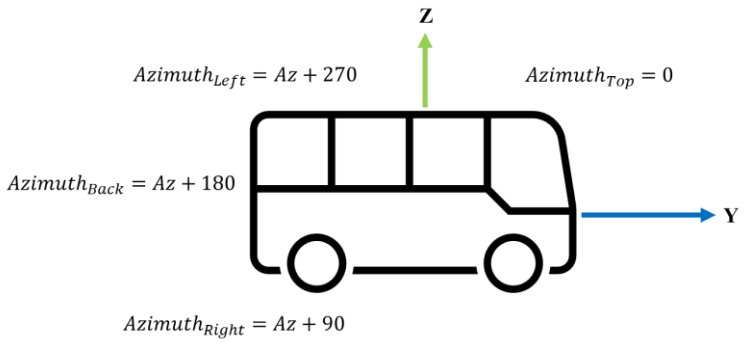

(a)

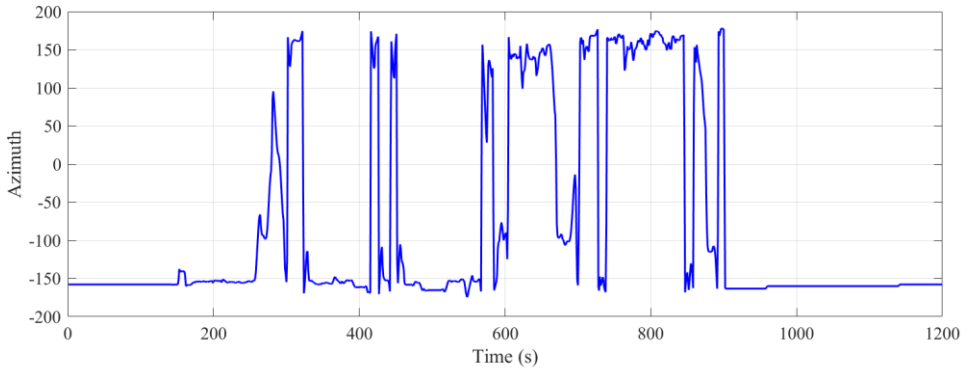

(b)

Figure 4.8. (a) The coordinates and (b) the azimuth during the minibus trip.

This processed azimuth dataset is pivotal for subsequent analyses, particularly in calculating solar angles within the optical model. The synchronization and averaging processes also align the azimuth data with other collected variables, ensuring temporal consistency and enabling integrated use within the optical, thermal, and electrical modelling chain.

4.5. Results and Discussion

4.5.1. Analysis of VIPV System Performance

The discussion in this section is organized into three main parts. The first part focuses on analysing the performance of the VIPV system, with a detailed examination of the results obtained from the optical, thermal, and electrical models. In the second part, based on the output of the electrical model and various defined operating scenarios, the vehicle's energy consumption is compared with the energy generated by the VIPV system. Finally, the third part discusses the environmental impact by

comparing emissions across different vehicle types, highlighting the potential benefits of integrating VIPV systems. This structure allows us to move from component-level behaviour (irradiance and temperature) to whole-vehicle implications (energy balance and emissions).

As mentioned earlier, data collection was conducted on April 11th between 12:00 and 12:20. Accordingly, the simulation was first performed for the optical model using this specific time interval. The results of the optical model, showing the irradiance distribution across different parts of the vehicle, are presented in Figure 4.9.

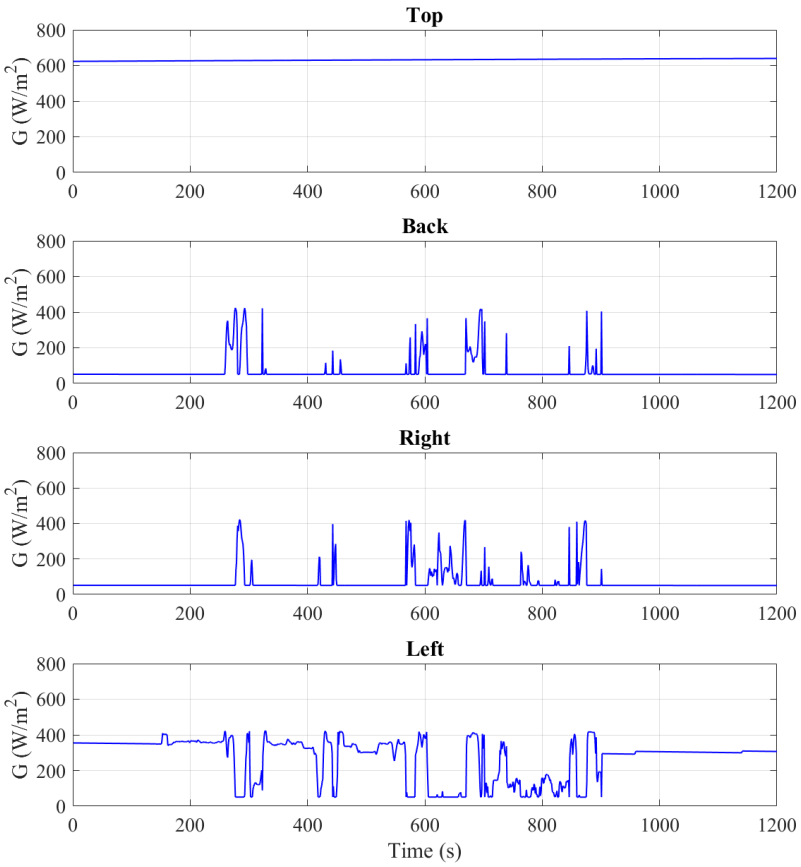

Figure 4.9. The received irradiance by different sections of the minibus on April 11th, from 12:00 to 12:20.

The analysis reveals that the top surface (roof) of the minibus generally receives higher irradiance compared to its other sides. However, this difference is influenced by seasonal variations and other environmental factors. To investigate these variations in more detail, a continuous operating scenario was simulated in which the vehicle runs from 08:00 to 15:00, with the drive cycle repeated throughout this period. This ensures comparable exposure across days and emphasizes the effect of solar geometry. Figure 4.10 presents the monthly solar irradiation received by different sections of the minibus, along with the percentage contribution of each surface to the total solar irradiation.

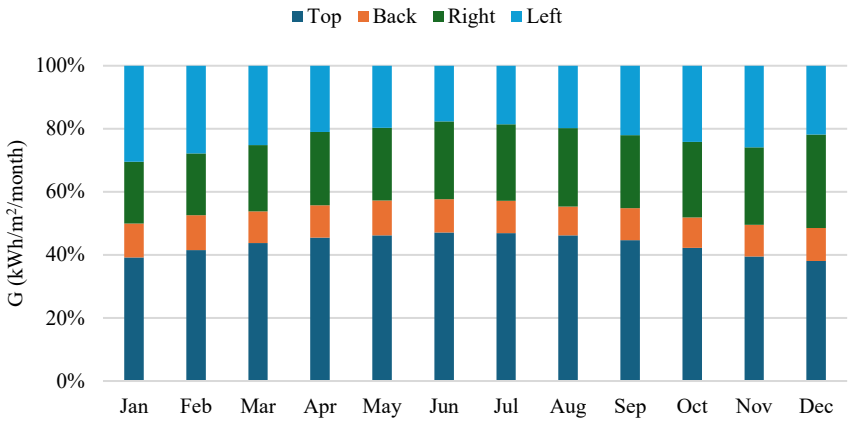

Figure 4.10. Fraction of monthly irradiation for the different sections of the minibus.

Figure 4.10 illustrates the monthly distribution of solar irradiation received by each surface of the minibus and how it varies due to seasonal changes, the sun's position, and the angle of incidence. The top surface consistently captures the largest portion of solar energy throughout the year, confirming its primary role in the total irradiation collected by the vehicle. As shown, this surface reaches its highest contribution during June and July, accounting for about 46–47% of the total irradiation, while during the winter months (December and January), it decreases to around 38–39%. By contrast, the side and back surfaces absorb lower but still significant shares. The right side shows its maximum contribution during summer (around 25%) and maintains relatively stable levels across most months. The left side, on the other hand, becomes more dominant during the winter months, reaching about 22–23% of the total irradiation, which can be attributed to lower solar elevation angles that favor lateral surfaces under certain orientations. The back surface contributes less overall, typically ranging between 10–13%, with slightly higher values in spring months.

This pattern also reflects the effect of vehicle orientation and sun angles along the route. Differences between the right and left sides result from variations in the minibus's heading during its circular pathway. Although the route is circular, the vehicle does not spend equal time on outbound and return legs because of stop locations and dwell times. The observed seasonal and directional fluctuations highlight the importance of using high temporal resolution in simulations to accurately represent dynamic variations in irradiation. In this study, simulations were performed at a per-second resolution to capture rapid changes in solar angles, vehicle heading, and location. In what follows, we quantify how coarser sampling can distort these effects.

To evaluate the influence of temporal resolution on the estimation of solar irradiation for VIPV, the simulation was repeated at progressively coarser time steps (1, 2, 3, 4, 5, and 10 minutes) and compared with the baseline 1-second resolution. Figure 4.11 illustrates how temporal downsampling affects both the spatial geometry of the vehicle path and the resulting irradiation estimates for different surfaces. The path plots show that as the time step increases, the number of recorded points along the route drastically decreases, removing small heading fluctuations and geometric details. This loss of directional information strongly affects surfaces with orientation-dependent exposure. The bar chart of annual irradiation shows that while the top surface remains almost unaffected, the side and back surfaces become increasingly inconsistent. The absolute percentage error plot confirms this: the top surface remains below 1% error, while the back surface shows extreme sensitivity (errors exceeding 100%), and the right and left sides reach up to 35–40% error at some resolutions.

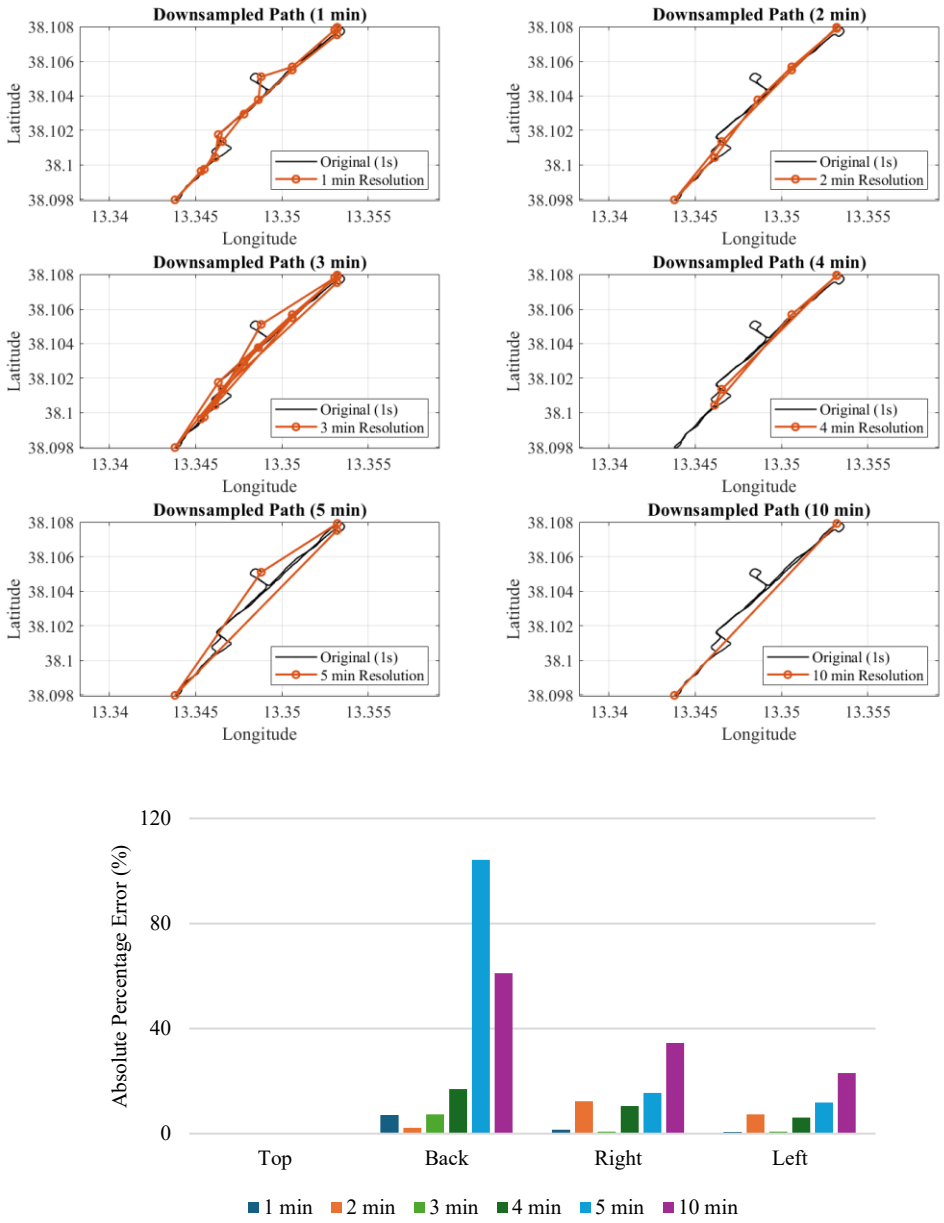

Figure 4.11. Effect of temporal resolution on path geometry and annual irradiation estimation for each vehicle surface.

After determining the irradiance using the optical model, the temperature of the integrated PV modules on different surfaces of the minibus can be calculated through the thermal model. Figure 4.12 presents the moving average temperature for each cycle from 08:00 to 15:00 on April 11th.

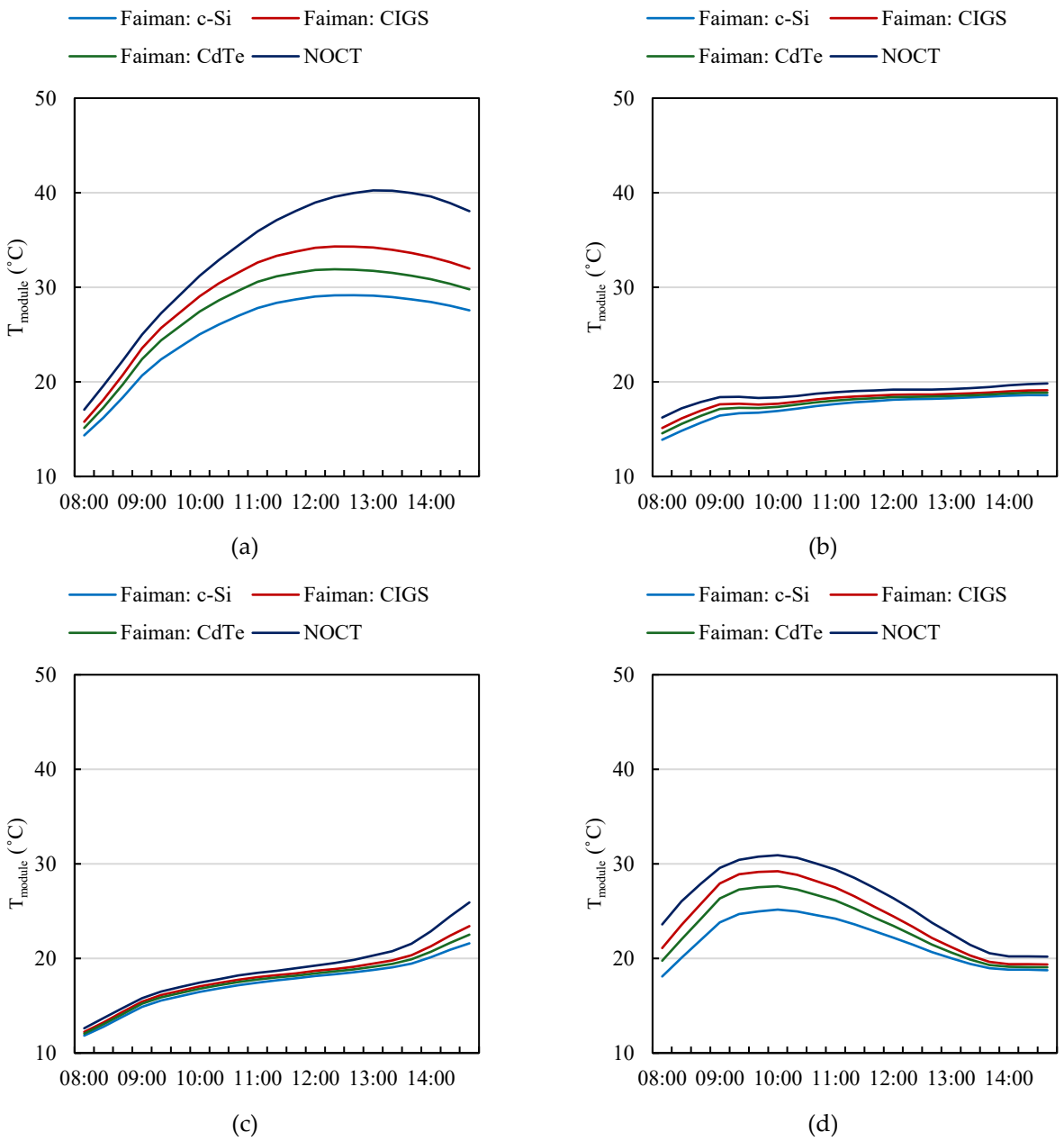

Figure 4.12. Calculated module temperatures using the Faiman and NOCT models for various PV module types which integrated into (a) top, (b) back, (c) right, and (d) left surfaces on April 11th, from 08:00 to 15:00.

As shown in Figure 4.12, in the NOCT model, the PV technology does not significantly affect the results. In contrast, the Faiman model incorporates different coefficients for various solar cell types, leading to varied temperature outcomes for each type. A key advantage of the Faiman model in the VIPV context is its consideration of wind speed. By including wind speed as a factor, the Faiman model offers a more accurate estimation of PV module temperatures under real-world operating conditions, making it potentially more suitable for this application.

In general, lower PV module temperatures lead to higher efficiency and greater power output, as reduced thermal losses improve the overall performance of solar cells. Based on the results obtained from the thermal model, the Faiman model was selected to calculate PV module temperatures for use in the electrical model. Figure 4.13 presents the total yearly electrical energy generated by different types of solar modules installed on various surfaces of the minibus.

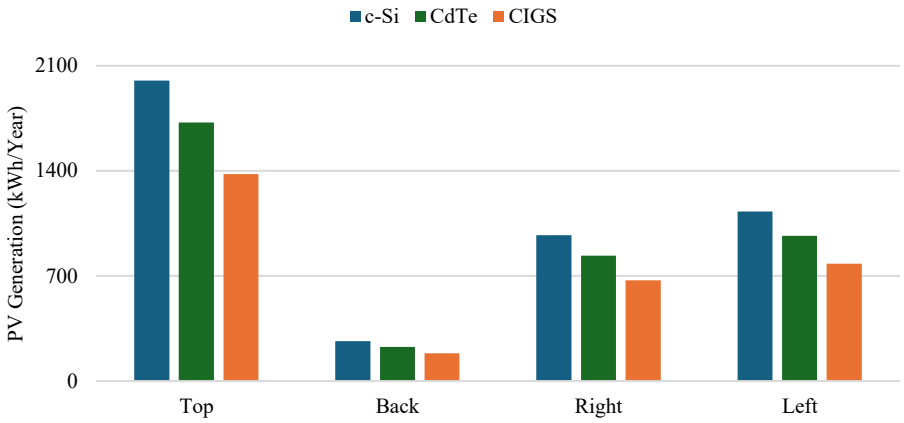

Figure 4.13. Yearly electrical energy generated by different types of solar modules integrated into various surfaces of the minibus, based on results from Faiman model.

The crystalline silicon (c-Si) photovoltaic modules produced more energy due to their higher efficiency. Hence, Figure 4.14 illustrates the distribution of daily energy generated across different months by the c-Si modules integrated into various sections of the minibus. These results provide valuable insights into how seasonal variations and environmental conditions, such as temperature and solar irradiance, impact energy production throughout the year.

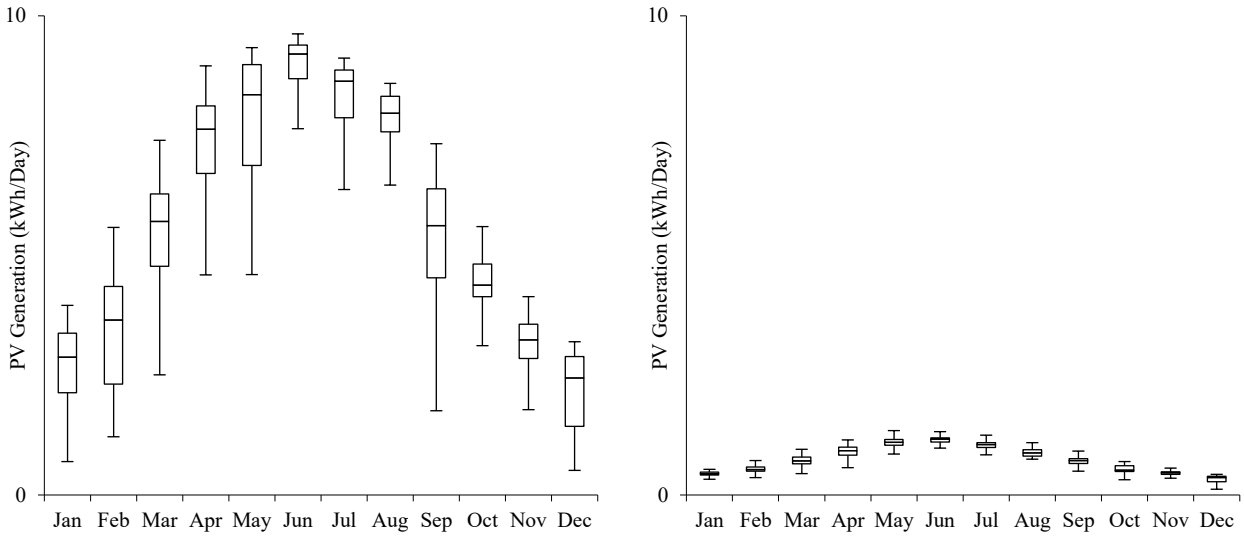

(a) (b)

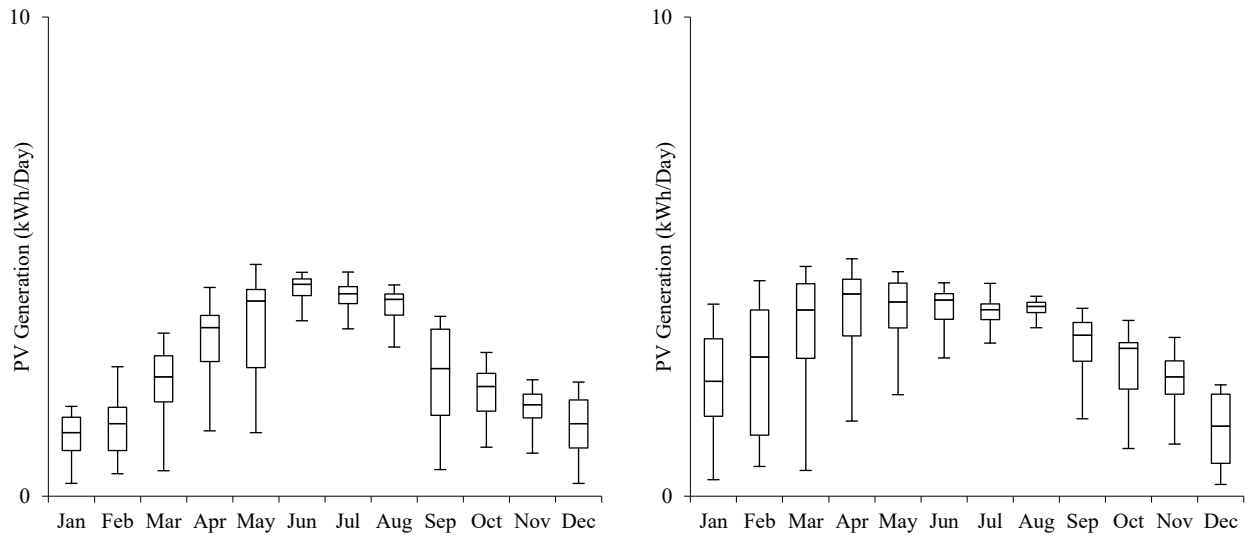

(c) (d)

Figure 4.14. Distribution of daily PV generation across different months using crystalline silicon (c-Si) photovoltaic modules integrated on the (a) top, (b) back, (c) right, and (d) left sides of the minibus (Blue stars: min outlier, red stars: max outlier).

4.5.2. Analysis of Different Operating Scenarios on Energy Consumption

Based on the vehicle model, the results obtained for the power and energy requirements of the minibus are presented in Figure 4.15. These results correspond to two different scenarios regarding the number of passengers. In the first scenario, the minibus is at full capacity with 22 passengers, while in the second scenario, the number of passengers varies based on data collected during the trip.

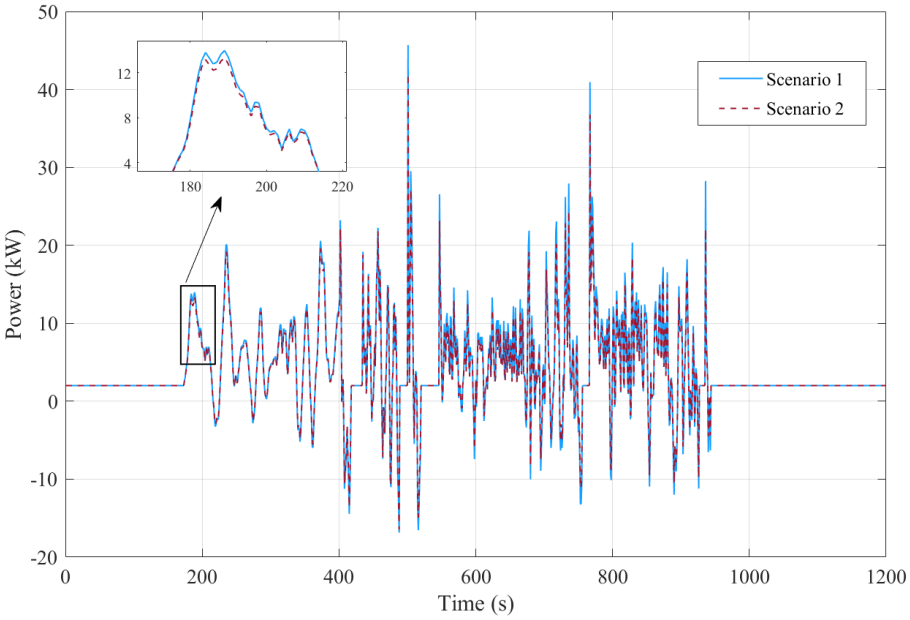

(a)

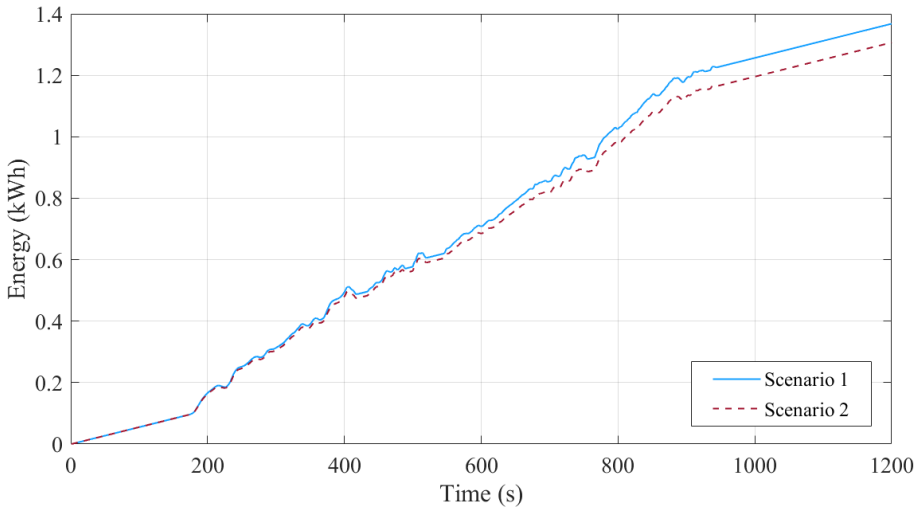

(b)

Figure 4.15. Estimated (a) power requirements (b) energy requirements of the minibus in both defined scenarios.

The required energy for the minibus was calculated as about 1.4 kWh for the first scenario (full capacity) and 1.3 kWh for the second scenario (variable passengers). These results show that the impact of the passenger load is not very relevant to the energy requirements of the minibus, with a slight reduction in energy demand when the number of passengers is lower, as observed in the second scenario.

In the following, we also compared different operational conditions for the minibus. This comparison was made to investigate the impact of these different working conditions on energy generation. In the first case, we assumed the minibus operates continuously without any gaps during work hours, from 08:00 to 15:00. In the second scenario, we considered the minibus operating once per hour. When parked, the minibus is always in the sunshine. The number of cycles the minibus completes during the day directly impacts energy consumption. In the continuous operation scenario, the minibus (Full capacity scenario) undergoes 21 cycles per day, while in the hourly operation scenario, only 7 cycles occur. As shown, this results in an energy consumption of approximately 29 kWh/day in the continuous scenario and approximately 10 kWh/day in the hourly scenario, assuming the bus is full during these cycles. The number of days in each month that the VIPV system can power the minibus is determined based on the energy generated and consumed in each scenario. Figure 16 presents this data as a percentage, illustrating the monthly contribution of the VIPV system to fulfilling the vehicle's energy requirements throughout the year.

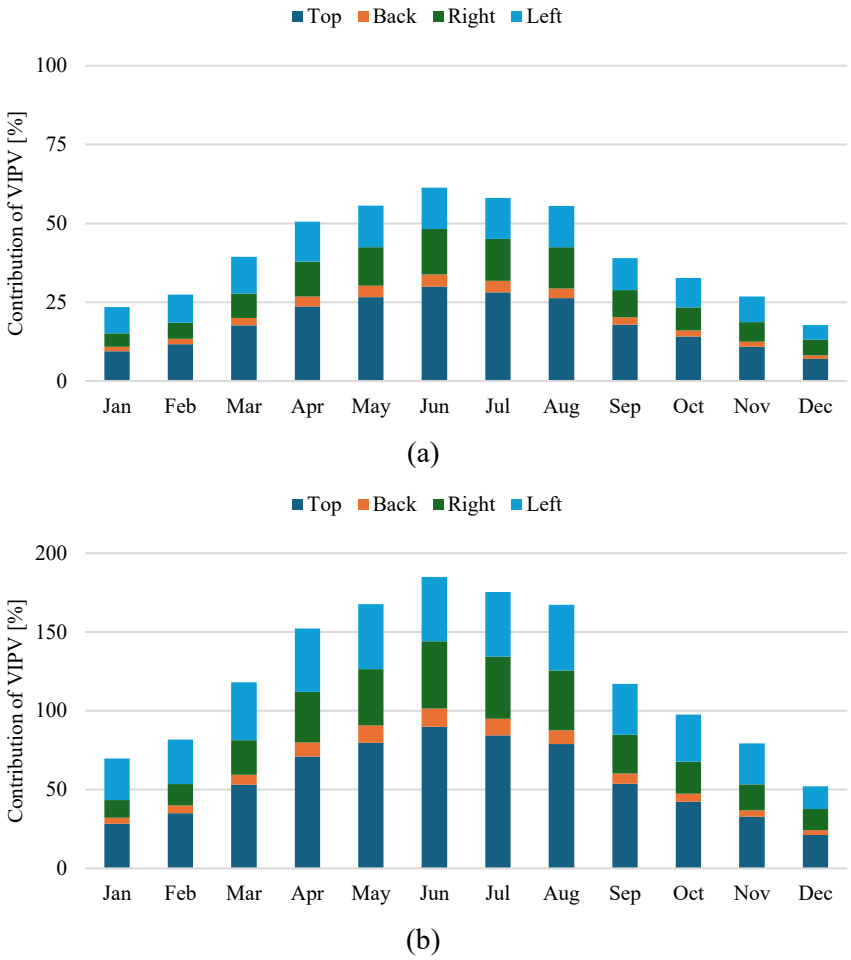

Figure 4.16. The monthly contribution of the VIPV system to the energy requirements of the minibus under two scenarios: (a) continuous operation and (b) hourly operation.

As shown in this figure, in the hourly scenario, the energy generated by the VIPV system exceeds the energy consumption from April to August. This is due to the lower energy requirements in the hourly scenario compared to the continuous scenario, also the vehicle is parked during gap times in areas without shading, leading to higher solar irradiance and increased energy generation.

4.5.3. Analysis of CO_2 Emissions by Vehicle Type

Although EVs are increasingly promoted in Europe and other regions, internal combustion engine (ICE) vehicles are still widely used in many areas. Previous sections of this study focused on the case study of an electric minibus. In this section, the analysis of a minibus powered by an internal combustion engine is also presented to assess how CO_2 emissions vary when the VIPV concept is applied to ICE vehicles. In ICE vehicles, electrical energy required for auxiliary systems is typically generated by an engine-driven alternator. The alternator increases the engine's mechanical load, resulting in additional fuel consumption and emissions. A VIPV system can offset part of this load by providing clean electrical energy, thereby reducing fuel usage and its associated emissions. Referring to the alternator, the emissions saved can be estimated using the following equation [56], [160], [161]:

$$Em_{ICE} = W \cdot \frac{V_{Fuel} \cdot C_{Fuel}}{\eta_{Alt}} \tag{4.24}$$

where V_{Fuel} l/kWh is the fuel consumption to energy content ratio, η_{Alt} is the efficiency of the alternator, C_{Fuel} gCO_2/l is the CO_2 conversion factor of the fuel, and W is the energy generated by VIPV. In the previous section, the energy generated by VIPV (W) over different time steps, particularly over the course of one year for the electric minibus, was calculated. However, to ensure a fair comparison under identical conditions of solar irradiation and module area, it is assumed that the energy production from VIPV is the same across all vehicle types: electric, petrol, and diesel. For petrol and diesel fuels, the values of V_{Fuel} and C_{Fuel} were considered as 0.264 l/kWh and 2330 gCO_2/l, and 0.220 l/kWh and 2640 gCO_2/l, respectively [56]. Based on these assumptions and data, the potential amount of emissions saved by using VIPV technology in different ICE vehicle types can be estimated and is presented in Figure 4.17.

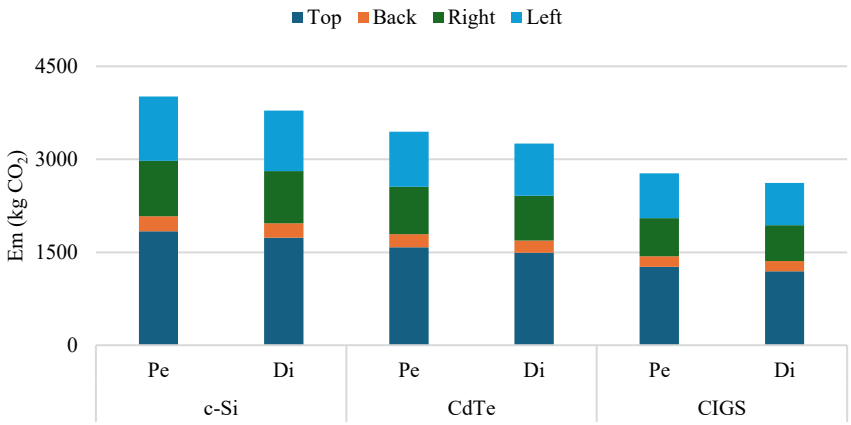

Figure 4.17. Emission savings achieved by using VIPV for diesel and petrol minibuses.

In this context, sustainability considerations can also be integrated by assessing how the VIPV concept may contribute to the green transition. Unlike ICE vehicles, which emit greenhouses gasses (measured in $kgCO_2\ eq$) directly from their tailpipes during operation, EVs produce no direct CO_2 emissions. This can represent a significant step toward sustainability if it is ensured that in the $kgCO_2\ eq$ generated by the production of battery and electronic components of EV is not too high. However further life cycle assessment (LCA) studies are necessary to evaluate the carbon footprint of different VIPV combinations along their life cycle that is the reason why in this study we focus our attention on the use phase as first. Another important component to consider is the electricity used to charge EVs. It is often sourced from the power grid, which may still partially depend on fossil fuels, thereby indirectly contributing to CO_2 emissions. The emissions saved by using VIPV in EVs can be estimated using the following equation [29]:

$$Em_{EV} = W \cdot Em_{Grid} \tag{4.25}$$

where Em_{Grid} $gCO_2\ eq/kWh$ is the grid emission intensity. Since the simulation model used Typical Meteorological Year (TMY) data corresponding to the period from 2005 to 2018 in Palermo, the evaluation of grid emissions was based on this timeframe. During these years, the grid's emission intensity in Italy declined, reflecting a transition toward cleaner energy sources. For example, while the grid emission factor was approximately 0.487 $kgCO_2\ eq/kWh$ in 2005, it decreased to about 297 $gCO_2\ eq/kWh$ in 2018 [162]. The variations in emissions saved by using VIPV technology in the electric minibus are presented in Figure 4.18.

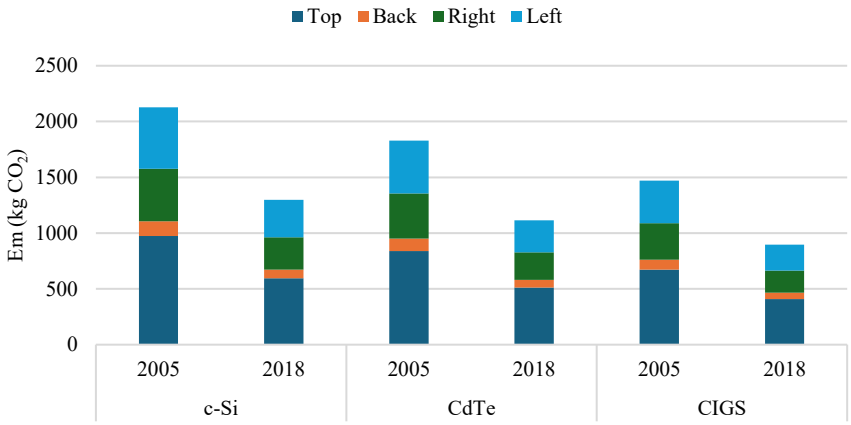

Figure 4.18. Emission savings achieved by using VIPV for electric minibus.

As many countries transition toward renewable energy sources, the carbon intensity of electricity generation is gradually decreasing. This shift directly affects the environmental benefit of substituting grid electricity with solar energy, such as through VIPV systems. However, the impact of this substitution varies significantly depending on the country's energy mix. In some European countries, where the electricity grid already has a low emission intensity, the environmental advantage of adding solar modules may be limited. In contrast, countries with grids that rely heavily on fossil fuels can benefit more from integrating renewable sources [163]. For instance, Iran's share of renewable energy in its electricity mix has been relatively low, peaking at around 9.5% [164]. The country's grid emission factor in 2022 was approximately 0.494 $kgCO_2\,eq/kWh$ [165]. In China, although a downward trend is expected, the grid emissions by 2030 are still projected to remain relatively high, in the range of 0.629–0.736 $kgCO_2\,eq/kWh$ [166]. As for Italy, while exact national projections for the 2030 grid emission factor are not available, individual energy companies have set their own targets. A2A aims to reduce its direct emissions by 46% compared to 2017 levels, targeting an emission factor of 0.230 $kgCO_2\,eq/kWh$ by 2030 [167]. This goal is supported by the expansion of renewable capacity (at least 1.6 GW), optimization of combined-cycle gas turbines, and a complete phase-out of coal and heavy oil. Similarly, Enel has committed to reducing its direct emissions to 0.082 $kgCO_2\,eq/kWh$ by 2030, as approved by the Science Based Targets initiative (SBTi) [168]. Although these companies' targets do not directly represent national grid emissions, they reflect the influence of energy mix diversification and sector-specific contributions to decarbonization. Overall, the emissions associated with electricity use are highly dependent on each country's energy mix [163], [169]. Based on the results shown in Figure 18, which illustrate the emission savings from using VIPV systems between 2005 and 2018, these savings are expected to decrease by 2030.

All the values mentioned for EVs and ICE vehicles refer to avoided emissions, which are based solely on energy consumption during driving. However, the net reduction in emissions from using a VIPV system is calculated as the difference between the emissions avoided and the emissions associated with the PV system itself [170]. While PV systems do not produce direct emissions during operation, their manufacturing, installation, and end-of-life processes do contribute to environmental impacts. To evaluate the real sustainability benefit, an LCA analysis is needed [171], [172]. For example, an LCA analysis of a light electric utility vehicle in Cologne, Germany, considered emissions associated with raw material extraction, solar cell and module manufacturing, inverter and structure production, and system installation and operation, focusing on the global warming potential (GWP) and using 1 kWh of onboard PV electricity generation as the functional unit [169]. It was found that the emission

factor of the VIPV electricity was 0.357 $kgCO_2\ eq/kWh$, while the average grid electricity had an emission factor of 0.435 $kgCO_2/kWh$. However, the benefit of VIPV was highly sensitive to shading and system lifetime. When the shading factor increased from 30% to 40%, the emission factor of the PV system exceeded that of the grid, resulting in no environmental gain. The same study showed that extending the system's operational lifetime from 8 to 12 years reduced the emission factor by about 0.221 $kgCO_2\ eq/kWh$. Another study assessed the solar energy potential of parking spaces in Berlin, incorporating data on shading from trees and buildings using digital surface models and weather-based solar simulations [173]. The findings indicated that VIPV systems could increase daily driving range by 7 to 14 km, amounting to a median annual gain of 2527 km. The study concluded that, based on the assumptions of Kanz et al. [169], the average shading losses for typical parking spaces exceeded 50%, which meant that VIPV systems, in those locations, were less sustainable than conventional grid-based charging. Another study conducted a cradle-to-gate life cycle assessment to estimate the greenhouse gas emissions associated with VIPV systems [174]. This assessment covered the entire production process, from raw material extraction to the final assembly of the solar modules and accounted for the carbon intensity of the electricity used both at the manufacturing sites and in the countries where the vehicles are operated. They applied their assessment framework to a specific case study in which monocrystalline silicon was extracted and refined in China, while the modules were assembled in the Netherlands. This process resulted in approximately 0.118 $kgCO_2\ eq$ per square meter of solar module. The findings suggest that electric vehicles equipped with integrated PV systems are generally more environmentally beneficial in countries with high solar irradiation. However, in regions where the electricity grid is already low in carbon emissions, the additional emissions from manufacturing the VIPV system may not be justified. In such cases, a longer vehicle lifespan would be required to achieve a net reduction in emissions.

Generally, various case studies assume that the lifetime of VIPV systems ranges between 8 and 15 years [175]. Most of the environmental impact associated with VIPV systems occurs during the manufacturing phase. Therefore, longer operational lifetimes help offset this impact more effectively over time [171]. For this reason, using solar parking, which refers to fixed photovoltaic systems installed in parking areas, is sometimes considered more sustainable than VIPV systems [163]. One reason is that residential and fixed PV systems typically have longer lifespans, often ranging from 25 to 35 years. For example, using the same PV technologies considered in this study, including monocrystalline silicon, multicrystalline silicon, CIGS, and CdTe, and assuming a service life of 30 years for PV modules and 15 years for inverters, the associated emissions can be approximately 0.036, 0.044, 0.036, and 0.025 $kgCO_2\ eq/kWh$, respectively [176]. However, as transport is responsible for around 30% of energy-related greenhouse gas emissions in the EU [177], developing PV modules specifically tailored for VIPV applications can play a key role in supporting the rapid growth of these technologies in the near future.

Although a full life cycle assessment is not the main objective of this paper, incorporating the discussed sustainability aspects into the analysis allows for a better understanding of the broader impact of VIPV systems. The examples provided highlight how environmental performance is influenced by contextual factors such as shading, local climate, vehicle usage patterns, and system lifetime. As a result, in some cases, the integration of a VIPV system may not lead to a net sustainability benefit. These findings show that while VIPV can offer significant sustainability advantages under favourable conditions, it may not always be the most effective solution. For example, in some countries like Sweden, emissions may increase by up to 15% instead of decreasing. However, according to previous studies [174], [178], in several European countries such as Italy, Spain, and Portugal, the potential greenhouse gas (GHG) reduction from using VIPV systems can

reach, or even exceed, 40%. In the specific case study presented in this paper, the comparison between internal combustion engine vehicles and electric vehicles shows that the amount of emissions avoided by using VIPV is significantly higher for internal combustion engine vehicles. When these avoided emissions are evaluated alongside the emissions produced during the manufacturing and lifecycle of the photovoltaic system, the results can be more favourable. This is especially true in locations such as the UNIPA campus, where high solar irradiance and minimal shading create ideal conditions for solar energy generation.

4.6. Conclusions

This chapter presents a structured and flexible simulation framework for VIPV systems. The proposed model chain, comprising optical, thermal, and electrical models, offers a simulation-based approach using real-world driving data instead of relying solely on experimental setups. This approach not only reduces the need for costly and often case-specific testing but also improves scalability and applicability across various vehicle types and operational conditions.

Real-time data were collected using only a smartphone, enabling precise irradiance modeling without the need for complex and expensive instrumentation. This makes the method valuable for widespread feasibility studies and early-stage assessments of VIPV systems. Furthermore, while the framework incorporates methodologies originally developed for fixed PV systems, these were carefully modified for moving vehicles, considering the dynamic nature of vehicle motion, including discrete positioning in the optical model and wind-related effects and thermal inertia, in the thermal model.

To support broader use and future development, an open-source simulation tool, referred to as 'VIPVLIB', was developed based on the proposed methodology and using PVLIB functions. This tool is made publicly available to assist researchers working on VIPV-related topics.

Experimental validation was carried out through a case study using a campus minibus operating at the University of Palermo. The full model chain was applied under real driving conditions, and its results were analysed from multiple perspectives. One of the investigations focused on the effect of time resolution in simulations. While top surfaces exhibited negligible error across various time intervals, substantial deviations were observed for more dynamic side and rear surfaces, highlighting the importance of high temporal resolution for accuracy, particularly in mobile PV applications.

Additionally, the study analysed the impact of driving scenarios, seasonal irradiance variation, PV technology selection, and passenger load on energy consumption. Results revealed that under optimal summer conditions, the VIPV system could fully meet the hourly energy demand of the vehicle. However, when considering continuous operation, energy autonomy was achievable for only a limited period each year, emphasizing the importance of operational context in evaluating system feasibility.

The research also explored broader sustainability aspects, comparing different vehicle types, including electric and internal combustion engine vehicles, and assessing the potential emission reductions enabled by VIPV integration. Although a detailed LCA was beyond the scope of this work, the study draws on existing literature to contextualize the environmental impact of VIPV, highlighting how operational lifetime and grid cleanliness influence overall sustainability outcomes. Additionally, this research addresses some limitations of previous studies in LCA, which often focus solely on integrating PV systems into vehicle roofs, overlooking both the influence of vehicle dynamics and the potential contributions of other surfaces. By integrating these overlooked factors, through using

our proposed framework provides a more complete and realistic approach to evaluating sustainability in VIPV systems and lays the foundation for future advancements in the field.

Future research should focus on extending the model to other climatic regions, integrating real-time, high-frequency meteorological and shading data, and coupling the VIPV framework with advanced traffic or drive-cycle models as well as real energy-consumption datasets. Incorporating battery storage, inverter behaviour, and more detailed life-cycle assessment will further strengthen its applicability for full-vehicle energy and environmental evaluations.

5

VIPV for Airport Ground Operations

Airports represent some of the most energy-intensive infrastructures within the global transport sector, encompassing a wide range of stationary and mobile energy demands that contribute significantly to overall operational emissions. The decarbonization of ground operations therefore constitutes a critical component of the broader strategy toward sustainable aviation. In this context, VIPV emerge as a promising complementary solution to conventional electrification, enabling on-board renewable energy generation and reducing dependence on external power supply systems.

While numerous studies have investigated fixed PV installations in airports, such as rooftop systems, carports, or adjacent solar farms, the potential of mobile PV integration on airport ground vehicles has received very limited attention. To date, no structured methodology has been established to systematically evaluate the feasibility, energy yield, and environmental–economic performance of VIPV systems within the airport context. Addressing this research gap, the present chapter introduces a two-scenario analytical framework designed to assess VIPV performance for different categories of airport ground vehicles. The first scenario, referred to as the Generalized Approach, estimates the annual solar energy production based on representative irradiance data, available vehicle surface area, and the ratio between driving and standby times. This simplified method provides an accessible means to evaluate potential VIPV applications under limited data conditions. The second scenario, termed the Data-Driven Approach, integrates detailed GPS-based driving data to capture the dynamic effects of vehicle orientation, speed, and operating conditions on solar irradiance and energy yield. Together, these two complementary approaches offer a balance between general applicability and data-specific accuracy, enabling both preliminary assessments and detailed performance analyses.

The proposed framework was applied to a selection of European and Middle Eastern airports, encompassing diverse climatic conditions and operational patterns. Simulation results indicate that VIPV systems could potentially supply energy equivalent to 1,700–5,500 km/year for airport buses, 650–5,000 km/year for minibuses, and 840–6,180 km/year for luggage tractors, depending on solar availability, surface area, and vehicle utilization. The corresponding avoided CO_2 emissions were shown to be strongly dependent on the carbon intensity of the local electricity grid, while grid-parity analysis revealed particularly favourable conditions in regions with high solar irradiance and elevated electricity costs. Overall, the outcomes of this study demonstrate that the integration of photovoltaic modules into airport ground vehicles can meaningfully contribute to the decarbonization of airport operations. Beyond the specific case studies analysed, the proposed methodology is transferable to other VIPV applications, providing a practical and replicable tool for evaluating the technical, environmental, and economic potential of solar-assisted vehicle fleets in diverse operational and geographical contexts.

5.1. VIPV for Ground Support Vehicles (GSVs)

The global transition toward low-carbon mobility is accelerating, with growing emphasis on reducing greenhouse gas (GHG) emissions across all transport sectors. Airports are central to this transformation because they represent complex, energy-intensive infrastructures that combine large terminal buildings, extensive lighting, heating and cooling systems, and diverse fleets of ground support vehicles (GSVs). While much of the international debate has focused on aircraft emissions, ground operations also account for a significant share of the environmental footprint and cannot be overlooked [179]. Decarbonizing these activities has therefore become a priority, with the electrification of GSVs and airport service fleets emerging as a key step toward sustainable airport operations [180], [181].

However, electrification by itself introduces new challenges. On the one hand, it reduces direct combustion emissions and local pollutants; on the other, it increases reliance on charging infrastructure and grid electricity, which in many regions still relies heavily on fossil-based generation [182], [183]. This dependency can reduce the net environmental benefit of electrification, while also creating operational constraints in busy airports where the availability of vehicles and charging turnaround times are critical for smooth ground operations.

Vehicle-Integrated Photovoltaics (VIPV) offer a promising complementary solution. By embedding photovoltaic modules directly onto the vehicle body, VIPV allows electricity to be generated at the point of use. This not only reduces dependence on centralized charging stations but also extends vehicle autonomy and enhances operational flexibility. Moreover, energy harvested during standby or parking periods can be stored and used later, directly contributing to reduced grid demand and emission reduction targets [37], [48]. For airport fleets, which typically operate during daylight hours, follow relatively predictable duty cycles, and offer large available surfaces, the VIPV concept is especially relevant. Despite these advantages, the application of VIPV in airports has received very limited attention. To date, most research and real-world deployments of solar technologies in airports have focused on fixed installations such as rooftops, carports, or ground-mounted systems [184], [185].

The technical evaluation of VIPV poses its own challenges, since the energy yield depends not only on solar resources and installed PV area but also on vehicle dynamics, such as movement, orientation, and operational cycles. Several modelling approaches have been proposed to address these aspects [57], [58], [59], [79]. In this context, the present work contributes by proposing methodologies into a structured two-scenario framework tailored for VIPV applications. The first scenario offers a generalized approach that does not rely on detailed driving behavior. Vehicle activity is simplified into driving and standby modes, represented by time fractions for each hour. This allows the use of global horizontal irradiance applied to the vehicle roof, combined with simplified assumptions such as flat road conditions, general losses, and performance ratios. While simple, this scenario enables long-term assessments of technical, economic, and environmental potential using readily available data, making it particularly valuable as an accessible entry point for early-stage analyses (particularly in airport applications).

The second scenario, by contrast, is designed for cases where detailed driving data are available. Vehicle position, orientation, and speed are incorporated to calculate dynamic irradiance on multiple surfaces, providing a more accurate representation of real-world operating conditions. This scenario can accommodate both repetitive cycles and variable routes, enabling deeper investigation of VIPV performance, operational strategies, and system-level impacts.

The novelty of this study lies in two key aspects. First, it organizes the methodology into a coherent and transferable framework, filling the gap between oversimplified models and data-intensive approaches. Second, it applies this framework to the underexplored case of airport ground vehicles, thereby highlighting a promising application domain for VIPV. While the airport case study demonstrates the potential of the methodology, the framework is designed to be flexible and transferable, offering a structured reference for assessing VIPV in a wide range of transport sectors.

Through this contribution, the study provides both a methodological foundation and a practical demonstration of VIPV potential, supporting researchers, engineers, and decision-makers in advancing sustainable mobility solutions. By integrating renewable generation directly into vehicle fleets, the proposed framework may contribute to the broader goal of achieving zero-emission and energy-self-sufficient airport operations.

5.2. Methodology

The energy yield of VIPV systems was estimated using a combination of simplified and detailed modelling approaches. Two scenarios were defined to reflect different levels of data availability and modelling complexity. The first scenario provides a generalized framework that relies only on basic irradiance data and simplified operational assumptions, whereas the second incorporates detailed driving profiles and environmental conditions, allowing for a more accurate and dynamic representation of real-world performance.

5.2.1. General PV Power Model

The power output of a PV system can be expressed as [29]:

$$P = \eta \cdot G \cdot A_{PV} \tag{5.1}$$

where η is the overall system efficiency, G is the incident solar irradiance ($\mathrm{W/m^2}$), and A_{PV} is the effective PV area ($\mathrm{m^2}$). The overall efficiency is defined as the product of the PV module efficiency (η_{PV}) and the efficiency of the power conversion system (η_{Conv}).

$$P = \eta_{PV} \cdot \eta_{Conv} \cdot G \cdot (A \cdot \alpha) \tag{5.2}$$

Here, A is the available geometric surface area of the vehicle, and α is the coverage ratio that accounts for the fraction of usable surface suitable for PV installation. Solar irradiance (G) is composed of three main components: direct (beam), diffuse, and reflected [151].

$$G = G_b + G_d + G_r \tag{5.3}$$

In this study, only the direct and diffuse components were considered. To better approximate real operating conditions, two correction factors were introduced:

- a curvature factor ($CF = 0.9$) to account for reduced effective capture due to curved vehicle surfaces [153], and
- a shading loss factor ($\eta_{Shading} = 0.75$) representing partial obstruction from nearby objects or the vehicle itself.

Thus, the effective irradiance was calculated as:

$$G = [(\eta_{Shading} \cdot G_b) + G_d] \cdot CF \quad (5.4)$$

5.2.2. Scenario 1: Generalized Approach

In the first scenario, vehicle operation was simplified into two modes: driving and standby. This approach is particularly relevant when detailed driving data are not available. The fraction of time spent in each mode was represented by a driving-to-standby ratio (R), applied on an hourly basis.

Energy generation in each mode was estimated as [29], [45]:

$$E_{Driving} = \sum_{n=1}^{8760} \eta_{PV} \cdot \eta_{Conv} \cdot G_h \cdot (A \cdot \alpha) \cdot PR \cdot R \quad (5.5)$$

$$E_{Standby} = \sum_{n=1}^{8760} \eta_{PV} \cdot \eta_{Conv} \cdot G_h \cdot (A \cdot \alpha) \cdot PR \cdot (1 - R) - L \quad (5.6)$$

$$E = E_{Standby} + E_{Driving} \quad (5.7)$$

where L represents standby charging losses (W), G_h represents hourly irradiance (W/m^2), PR represents the performance ratio and R represents the driving-to-park ratio. The performance ratio was calculated as [45]:

$$PR = \frac{PV_{OUT}}{\frac{GTI_{opta}}{H_{STC}}} \quad (5.8)$$

where PV_{OUT} is specific photovoltaic power output (kWh/kW_P per Year) and GTI_{opta} is the global tilted irradiance at the optimum angle (kWh/m^2 per Year). These parameters for each region are available on the Global Solar Atlas [123]. It should also be noted that the standard test condition irradiance (H_{STC}) is taken as 1000 (W/m^2), which is the internationally recognized reference solar irradiance level used for evaluating PV system performance under ideal conditions.

This scenario provided long-term estimates of annual energy yield under simplified assumptions, enabling further evaluation of sustainability and economic performance.

5.2.3. Scenario 2: Data-Driven Approach

When detailed driving data were available, more comprehensive scenario was applied. This approach accounted for additional effects such as thermal behaviour, vehicle speed, and irradiance on multiple surfaces (roof, sides, and rear).

The temperature-corrected power output is expressed as [106], [114]:

$$P = \eta_{PV} \cdot \eta_{Conv} \cdot G \cdot (A \cdot \alpha) \cdot (1 + k \cdot (T - T_{ref})) \quad (5.9)$$

The PV module temperature (T) was estimated using the Faiman model [87], [155]:

$$T = T_a + \frac{G}{U_0 + U_1 \cdot WS} \tag{5.10}$$

$$WS_{Roof} = WS_{TMY} \cdot (\frac{h_{Roof}}{10^{0.2}}) \tag{5.11}$$

where T_a represents the air temperature, U_0 represents the constant heat transfer component W/m^2K, U_1 represents the convective heat transfer component $W/m^3s\ K$, and WS represents the wind speed m/s. Since wind speed data from Typical Meteorological Year (TMY) files are given at 10 m height, they were adjusted to the height of the vehicle roof, using Equation 13. It should be noted that, when the vehicle is stopped (Speed = 0), the wind speed is adjusted based on the height of the minibus roof to simulate natural airflow. When the vehicle is in motion, the wind speed is considered the same as the vehicle speed, thus neglecting the wind speed.

For irradiance estimation, the model extended calculations beyond the roof to all relevant vehicle surfaces. The direct and diffuse irradiance on a tilted surface were calculated as [149], [150], [151]:

$$G_b = DNI \cdot [cos(\beta) \cdot cos(\theta_Z) + sin(\beta) \cdot sin(\theta_Z) \cdot cos(\gamma_S - \gamma)] \tag{5.12}$$

$$G_d = DHI \cdot \left[\frac{(1 - F_1) \cdot (1 + cos\,\beta)}{2} + F_1 \cdot \frac{A}{B} + F_2 \cdot sin\,\beta\right] \tag{5.13}$$

$$A = \max(0, \cos AOI)\ , \qquad B = \max(0.087, \cos\theta_Z)$$

where DNI and DHI are the direct normal and diffuse horizontal irradiance, respectively; β is the surface tilt angle; θ_Z is the solar zenith angle; γ_S is the solar azimuth angle; and γ is the surface azimuth. The coefficients F_1 and F_2 are anisotropy and horizon brightening factors, respectively, which adjust the distribution of diffuse irradiance.

These equations, originally developed for fixed PV systems, were adapted to moving vehicles by discretizing the driving pathway into one-second intervals. At each step, the sun's position relative to each vehicle surface was calculated using driving data (latitude, longitude, orientation, and speed). The modelling was implemented using VIPVLIB [186], as introduced in Chapter 4, an extended version of PVLIB [154] developed to capture vehicle dynamics and VIPV-specific conditions.

5.2.4. Environmental and Economic Assessment

Beyond energy yield, two additional performance metrics were evaluated.

- Avoided emissions (Em_{Avoid}) were calculated as [29]:

$$Em_{Avoid} = E \cdot CI \tag{5.14}$$

where E represents the annual energy production (kWh) and CI is the carbon intensity of the regional grid ($kgCO_2/kWh$). Since carbon intensity varies significantly between regions, being higher in grids dominated by fossil fuels and lower in those with larger shares of renewables, the environmental benefits of VIPV deployment are strongly location, dependent.

- Levelized Cost of Electricity (LCOE) was used to evaluate economic feasibility [187]:

$$LCOE = \frac{C_{life}}{E_{life}} \tag{5.15}$$

where E_{life} represents the total lifetime energy production, and C_{life} represents the total life cycle cost. This metric provides the average cost of electricity generation over the system lifetime, enabling direct comparison of VIPV with grid electricity and other energy technologies.

5.3. Case Studies

To demonstrate the applicability of the proposed two-scenario framework, two sets of case studies were conducted. Scenario 1 emphasizes a generalized assessment across multiple geographical locations using only basic irradiance and operational data, whereas Scenario 2 focuses on detailed route-based analyses that incorporate real GPS-derived driving profiles. Together, these case studies illustrate how the methodology can be adapted to different levels of data availability, from early-stage feasibility screening to high-resolution, dynamic simulations.

5.3.1. Scenario 1

In the first scenario, the model was applied to a set of international airports to examine how climatic conditions, electricity prices, and grid carbon intensity influence the performance of VIPV systems. Within Italy, three locations were considered, Milan, Rome, and Palermo, representing different climatic conditions and electricity price contexts, while also reflecting differences in airport scale and operational demand. To broaden the analysis within Europe, airports in Lisbon, Frankfurt, and Copenhagen were included, capturing diverse solar resources and market conditions. Finally, three major hubs in the Middle East, Doha, Dubai, and Istanbul, were studied as examples of environments with very high solar potential but comparatively lower electricity prices, highlighting the trade-off between abundant solar resources and economic feasibility.

Figure 5.1 presents the carbon intensity (CI) of national electricity grids in 2024 [188], alongside the non-household electricity prices [189], [190], [191]. Among the European locations, Lisbon exhibited the lowest CI value (0.101 $kg\ CO_2/kWh$), reflecting its renewable-rich grid, while Doha showed the highest (0.49 $kg\ CO_2/kWh$), consistent with its heavy reliance on fossil fuels. Electricity prices showed a strong contrast across the studied locations, ranging from as low as €0.03/kWh in Doha to €0.27/kWh in Copenhagen. These values provide critical benchmarks for assessing grid parity conditions of VIPV-generated electricity [189], [190], [191].

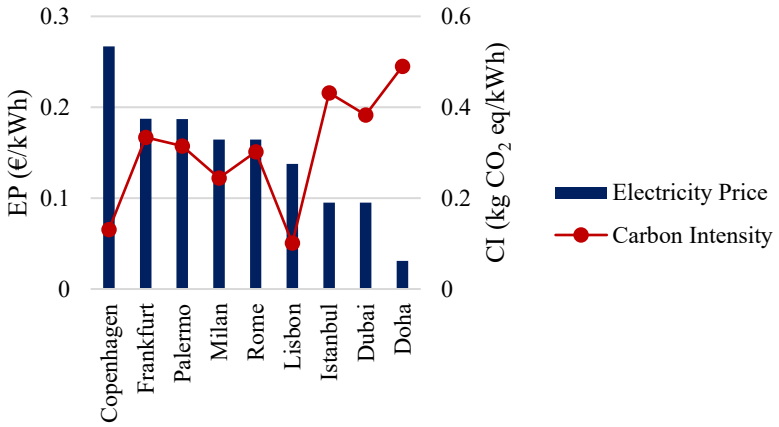

Figure 5.1. Electricity prices (bars, $€/kWh$) and grid carbon intensity (red line, $kg\ CO_2/kWh$) across selected airports [188], [189], [190], [191].

For all locations, the PV system lifetime was assumed to be 10 years, with an annual degradation rate of 1%. Although this value is higher than typical degradation rates of fixed PV systems (often 0.5% or lower), it was chosen as a conservative assumption reflecting the more demanding operating conditions of VIPV. Such conditions include vibration, intermittent shading, mechanical wear, and stronger thermal cycling. The assumed module efficiency was approximately 21%, corresponding to a surface power density of 210 W_p/m^2 [45], which was used to calculate the installed PV capacity available on buses, minibuses, and luggage tractors.

5.3.2. Scenario 2

Unlike vehicles that follow fixed or repetitive drive cycles, airport ground vehicles operate along highly variable and often unpredictable routes. Their movement depends on daily operational needs, which means trips rarely follow a standardized pattern. This makes it challenging to define representative duty cycles for simulation. Therefore, Scenario 2 was designed not to establish general driving cycles but to show the capability of the proposed framework to integrate real-world driving data and capture the dynamic effects of vehicle motion on VIPV performance.

The analysed datasets correspond to passenger shuttle buses operating at normal commercial airports, transferring passengers between aircraft and terminals. Because these data were based on real operating conditions, they inherently reflect many con-textual factors such as airport size, apron configuration, trip type (arrival, departure, or towing), and local congestion. As a result, each dataset provides a realistic snapshot of typical movement patterns within airport environments.

To illustrate this approach, GPS-based datasets from four international airports were analysed: Istanbul Sabiha Gökçen, Rome Fiumicino, Milan Bergamo, and Palermo Airport. Figure 5.2 shows the routes of the vehicles during several trips at these airports.

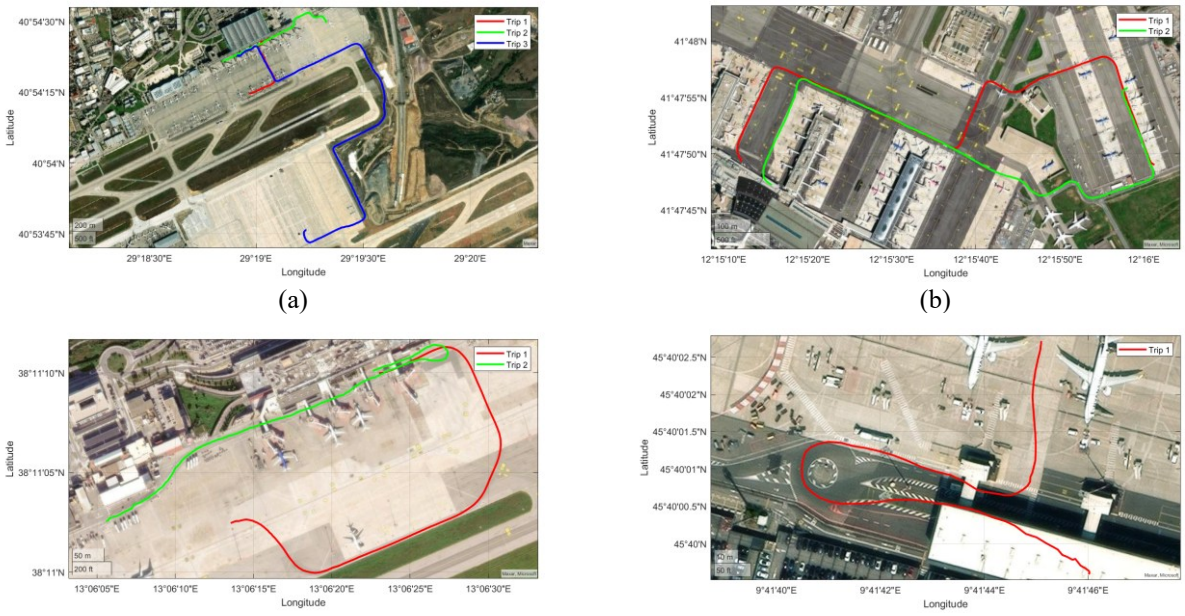

Figure 5.2. Vehicle routes during representative trips at (a) Istanbul Sabiha Gökçen, (b) Rome Fiumicino, (c) Palermo, and (d) Milan Bergamo airports. Source: MATLAB.

At Istanbul Sabiha Gökçen Airport, three independent trips were available, ranging in duration from 3 to 10 minutes. The variety in trip length, route geometry, and vehicle orientation offered valuable insight into the influence of operational diversity on VIPV performance. At Rome Fiumicino and Palermo airports, two trips of approximately 5 minutes and 2 minutes were considered, respectively. Finally, a short trip of less than 1 minute was analysed at Milan Bergamo Airport. Figure 5.3 presents the corresponding speed profiles and azimuth variations during these trips, highlighting the operational diversity among locations.

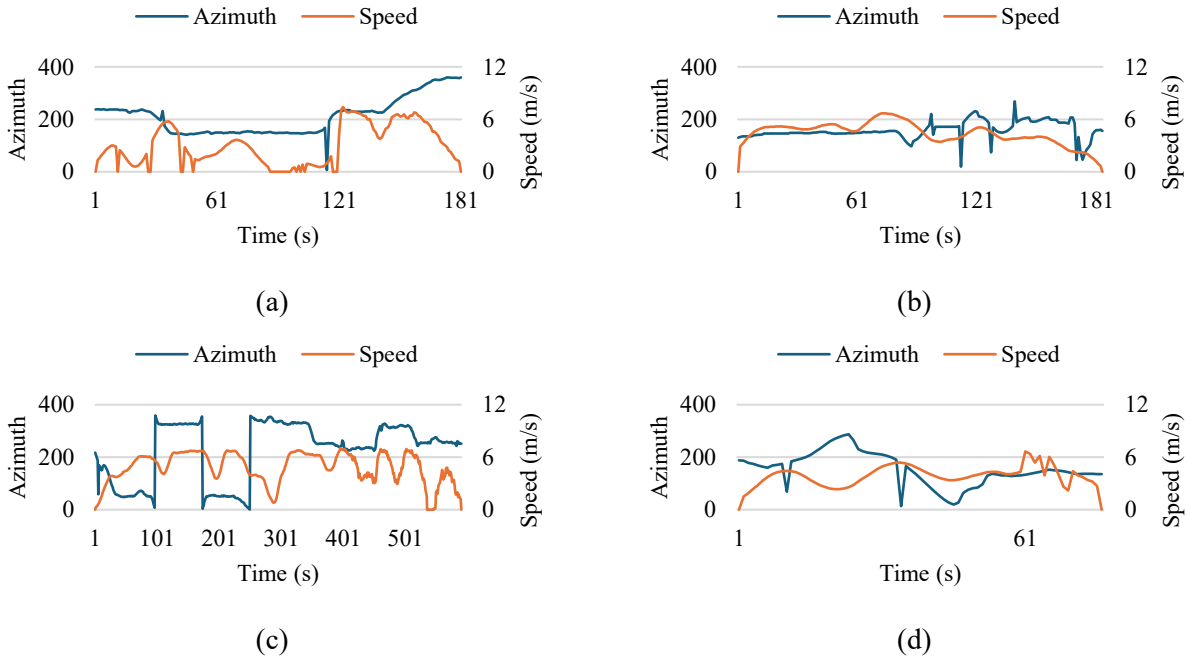

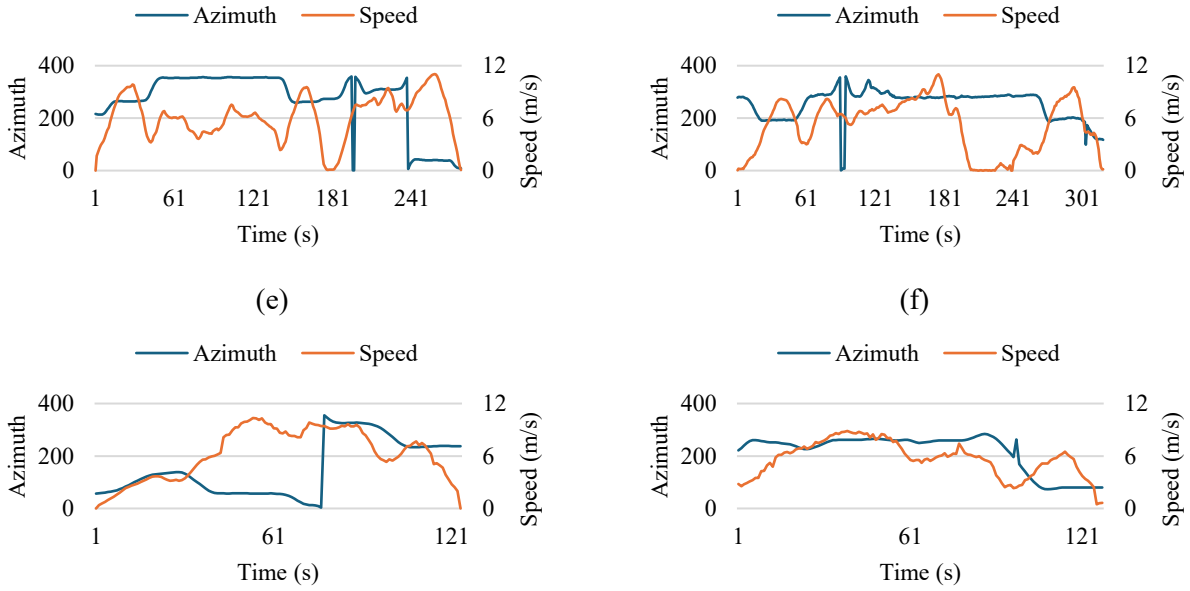

Figure 5.3. Vehicle speed profiles and azimuth angle variations during trips: Istanbul (a) Trip 1, (b) Trip 2, (c) Trip 3; Milan (d); Rome (e) Trip 1, (f) Trip 2; Palermo (g) Trip 1, (h) Trip 2.

While the duration of some trips, such as the one at Milan Bergamo Airport, is short, these real datasets effectively demonstrate how the framework performs under diverse and realistic operational conditions. The variability among airports, routes, and time spans provides a useful cross-section of airport operations. Longer datasets would indeed enable seasonal or probabilistic analysis, but even with limited samples, the framework can identify trends and sensitivities related to solar exposure, orientation, and movement dynamics.

To improve robustness, future studies could expand the dataset and include confidence intervals to quantify the variability across different trip categories (arrivals vs. departures) or congestion levels. Nevertheless, in authors opinion, the current results already demonstrate the flexibility of the framework and its applicability to operational data typical of passenger airports.

It should be noted that, the values of efficiency of the power converter (η_{Co}) and reference temperature (T_{ref}) were set to 96% and 25°C respectively [106]. The PV module technology used in the simulations was crystalline silicon (c-Si). Detailed electrical and thermal parameters of the module technology are provided in Table 5.1.

Table 5.1. Electrical and thermal parameters of crystalline silicon PV modules used in the case studies [81].

PV Module	Efficiency (%)	k (%/°C)	U_0 ($W/m^2 \cdot °C$)	U_1 ($W/m^3 \cdot °C$)	SPD (W_p/m^2)
c-Si	21.6	−0.47	30.02	6.28	210

5.4. Results and Discussion

5.4.1. Scenario 1

To investigate the technical feasibility of VIPV under different operating conditions, a sensitivity analysis was carried out on two key parameters: standby charging losses (L) and the driving-to-park ratio (R). Since the first scenario is generalized and considers the vehicle in driving or parked mode within each hour, different values of these parameters can represent a wide range of real operating conditions, reflecting how often the vehicle is in motion and how much energy is consumed by auxiliary systems when stationary. This approach allows the evaluation of system behavior without requiring detailed trip data, while still it captures the main effects of usage patterns and standby consumption on overall performance.

Standby losses represent the auxiliary consumption required to keep systems active while the vehicle is parked (e.g., BMS operation, etc). Two levels were considered: 100 W (L1, low-loss) and 700 W (L2, high-loss) [29]. The driving-to-park ratio was varied across four values: 0.2 (R1), 0.4 (R2), 0.6 (R3), and 0.8 (R4).

Annual energy production was first estimated across nine cities, for installed PV areas ranging from 3 to 30 m². Figure 5.4 illustrate representative results for selected cases (R1L1, R1L2, R3L1, and R3L2). These combinations were selected to show the influence of both operational factors, the proportion of driving time (R) and the magnitude of standby losses (L), on the yearly energy balance. Comparing R1 and R3 highlights the impact of more intensive vehicle use, while comparing L1 and L2 reveals how auxiliary consumption can reduce the net energy gain, particularly for systems with limited installed area.

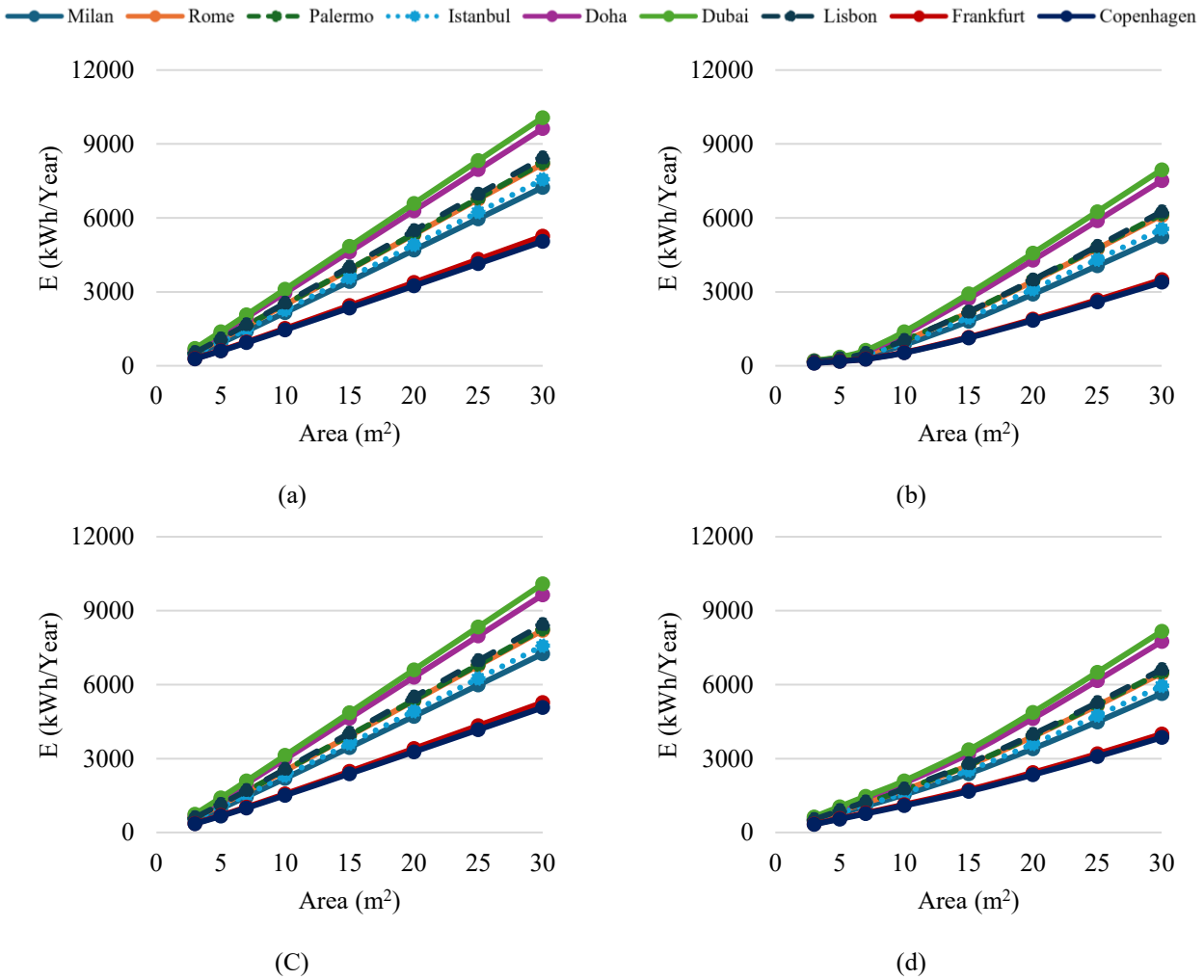

Figure 5.4. Yearly energy production of VIPV systems for different cities and PV areas under selected operating conditions: (a) R1L1, (b) R1L2, (c) R3L1, (d) R3L2.

Under low-loss conditions (L1), energy generation increases almost linearly with PV area. However, under high-loss conditions (L2), the increasing becomes nonlinear, especially for small PV areas where standby consumption represents a large fraction of the total power harvested. Across all cases, Doha and Dubai produced the highest annual yields due to their high solar resource, followed by Palermo, Rome, and Lisbon, while Copenhagen and Frankfurt showed the lowest performance.

Another analysis focused on three representative PV areas: 3 m² (luggage tractor), 7 m² (minibus), and 20 m² (bus). For each class of vehicle, the achievable solar driving range was calculated by dividing the annual energy yield by the average consumption per km. Results (Figure 5.5) showed ranges of:

- Buses (1.2 kWh/km) [114]: ~1700–5500 $km/year$,
- Minibuses (0.47 kWh/km) [158]: ~650–5000 $km/year$,
- Luggage tractors (0.13 kWh/km) [192]: ~840–6180 $km/year$.

These findings demonstrate that even under conservative assumptions, VIPV could cover a meaningful portion of yearly driving needs, particularly in sunny locations. In addition, Figure 5.6 presents the variations in daily energy production obtained from the VIPV system for the minibus (7 m² PV) across different cities within the R3L2 driving profile. This example was selected to illustrate how local climatic conditions and seasonal irradiance significantly influence the achievable energy yield.

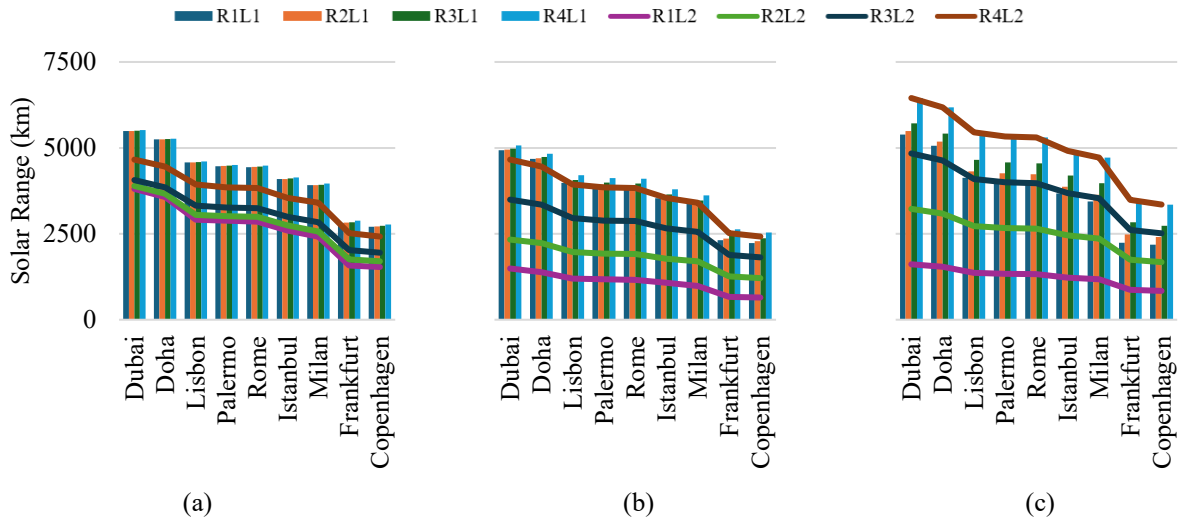

Figure 5.5. Annual solar driving range achievable by VIPV for three representative vehicle types: (a) bus (20 m² PV), (b) minibus (7 m² PV), and (c) luggage tractor (3 m² PV), under different cities and working conditions.

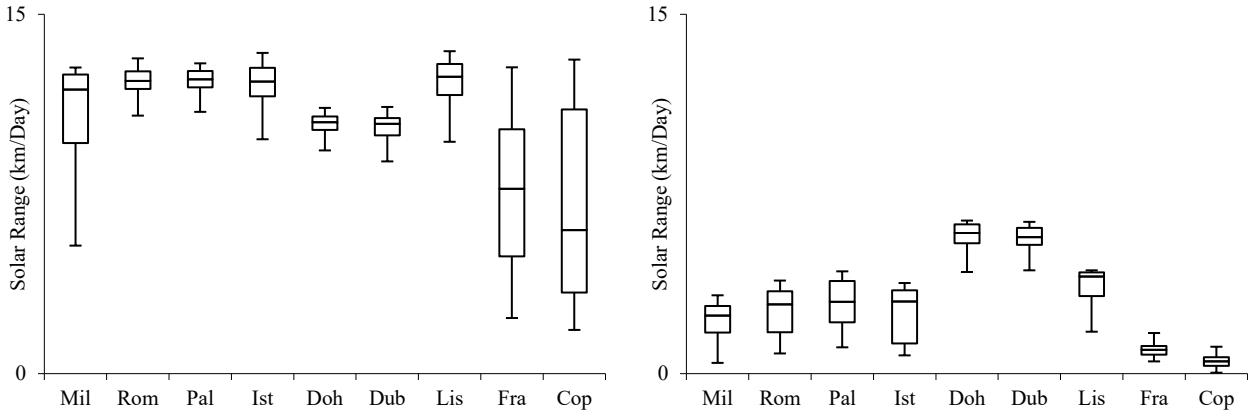

Figure 5.6. Daily solar driving range achievable by VIPV for the minibus (7 m² PV) in R3L2: (a) July (b) December.

Environmental benefits were quantified as avoided CO_2 emissions by multiplying annual generation with the regional grid carbon intensity. Figure 5.7 shows that avoided emissions strongly depend not only on irradiance but also on the carbon intensity of the local grid. For example, Lisbon, with low grid carbon intensity, yielded modest avoided emissions despite good irradiance, whereas Doha, with a highly carbon-intensive grid, showed the largest potential reductions.

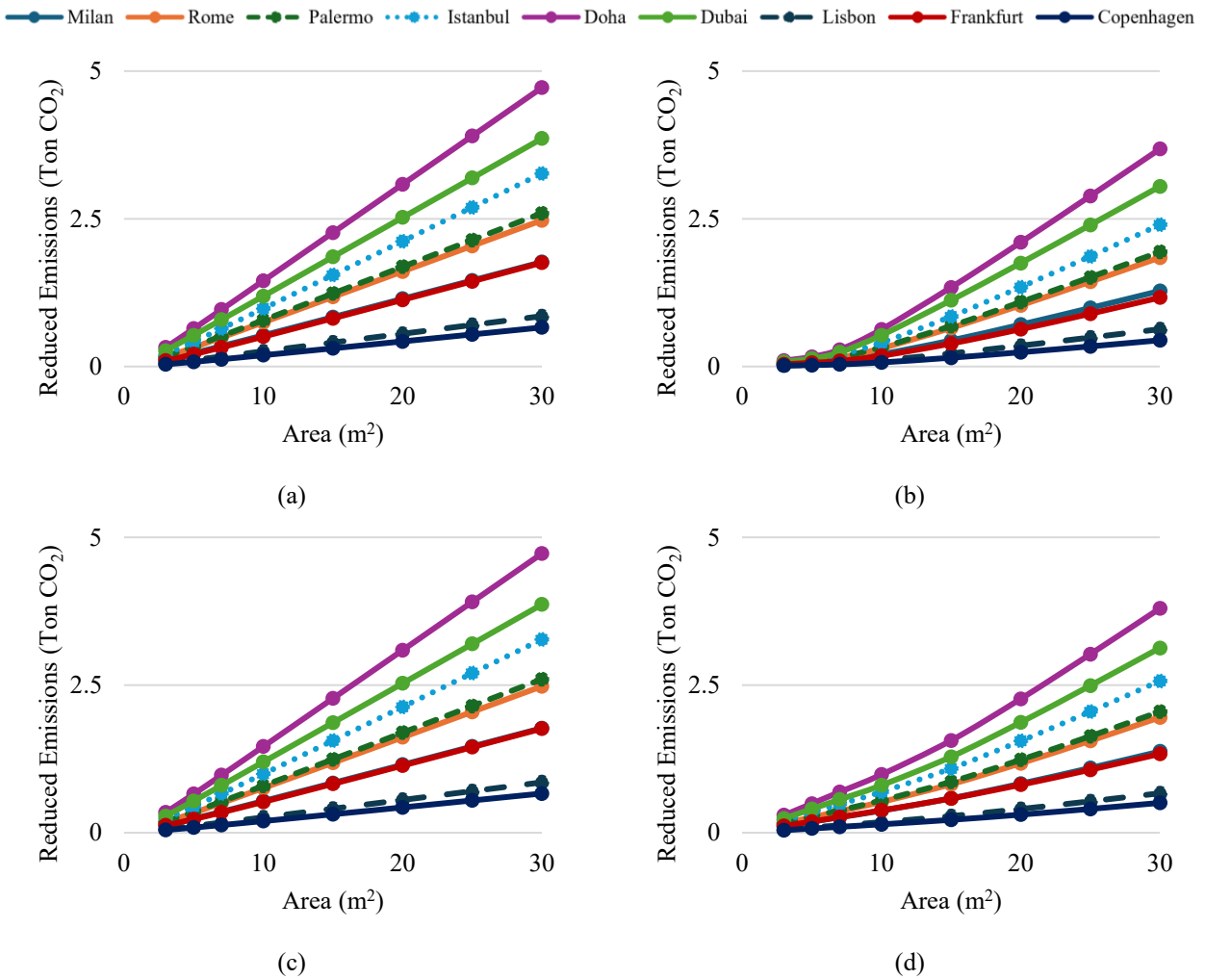

Figure 5.7. Annual avoided CO_2 emissions from VIPV systems in different cities and PV areas under selected operating conditions: (a) R1L1, (b) R1L2, (c) R3L1, (d) R3L2.

Finally, the economic potential of VIPV was analysed using the Levelized Cost of Electricity (LCOE) as a benchmark for grid parity. Under operating condition R3L1 (moderate driving, low losses) and R3L2 (moderate driving, high losses), results were compared against regional electricity prices assuming a $WACC_{real}$ of 3% (Figure 5.8). Additional sensitivity analyses at $WACC_{real}$ values of 2% and 5% were performed for the R3L2 case (Figure 5.9).

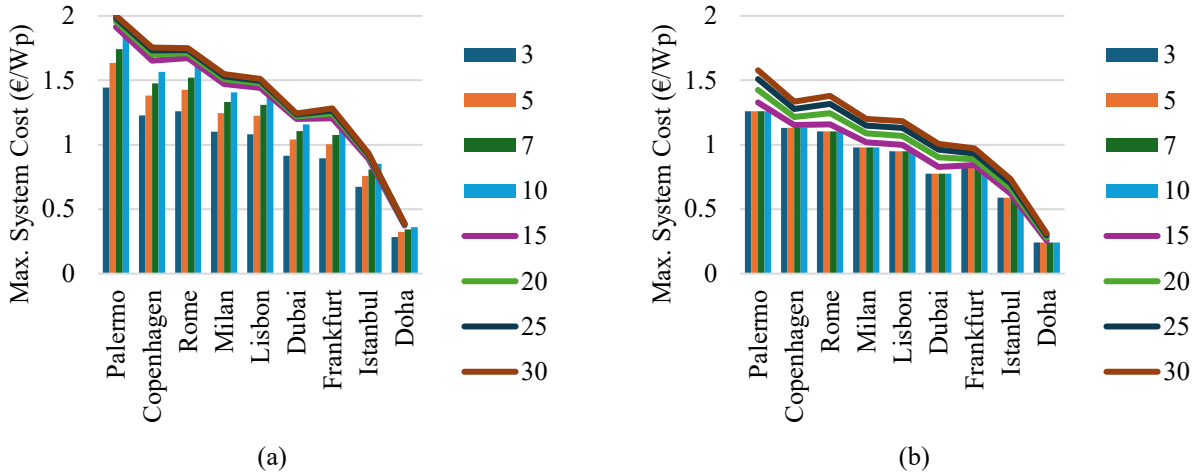

Figure 5.8. Maximum system costs at grid parity for different cities under $WACC_{real}$ = 3%: (a) R3L1, (b) R3L2.

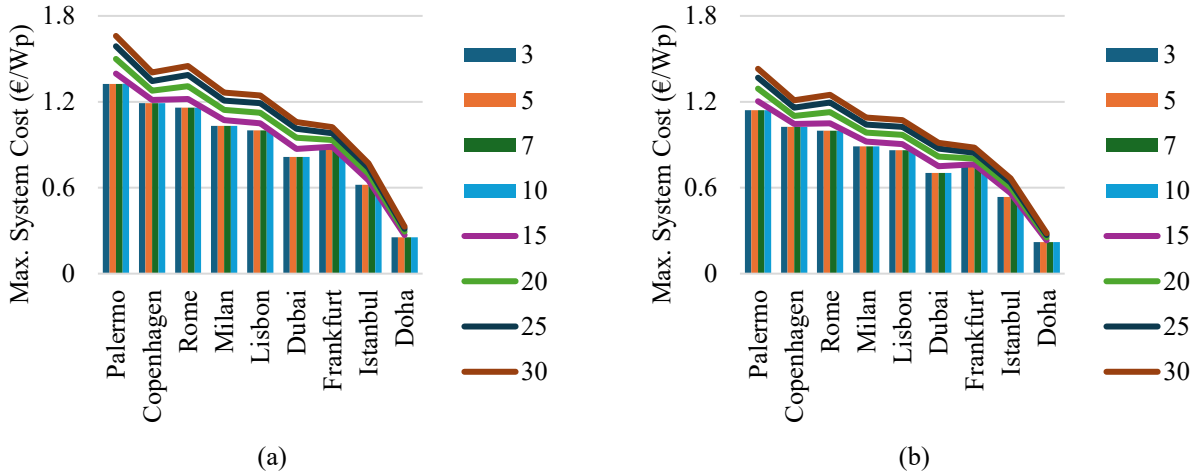

Figure 5.9. Maximum system costs at grid parity for different cities under operating condition R3L2 with: (a) $WACC_{real}$ = 2%, (b) $WACC_{real}$ = 5%.

5.4.2. Scenario 2

Figure 5.10 shows PV module temperature profiles for trips in Istanbul, Rome, Milan, and Palermo. The influence of both ambient conditions and vehicle speed on module temperature is evident, with higher irradiance and lower airflow leading to higher module temperatures.

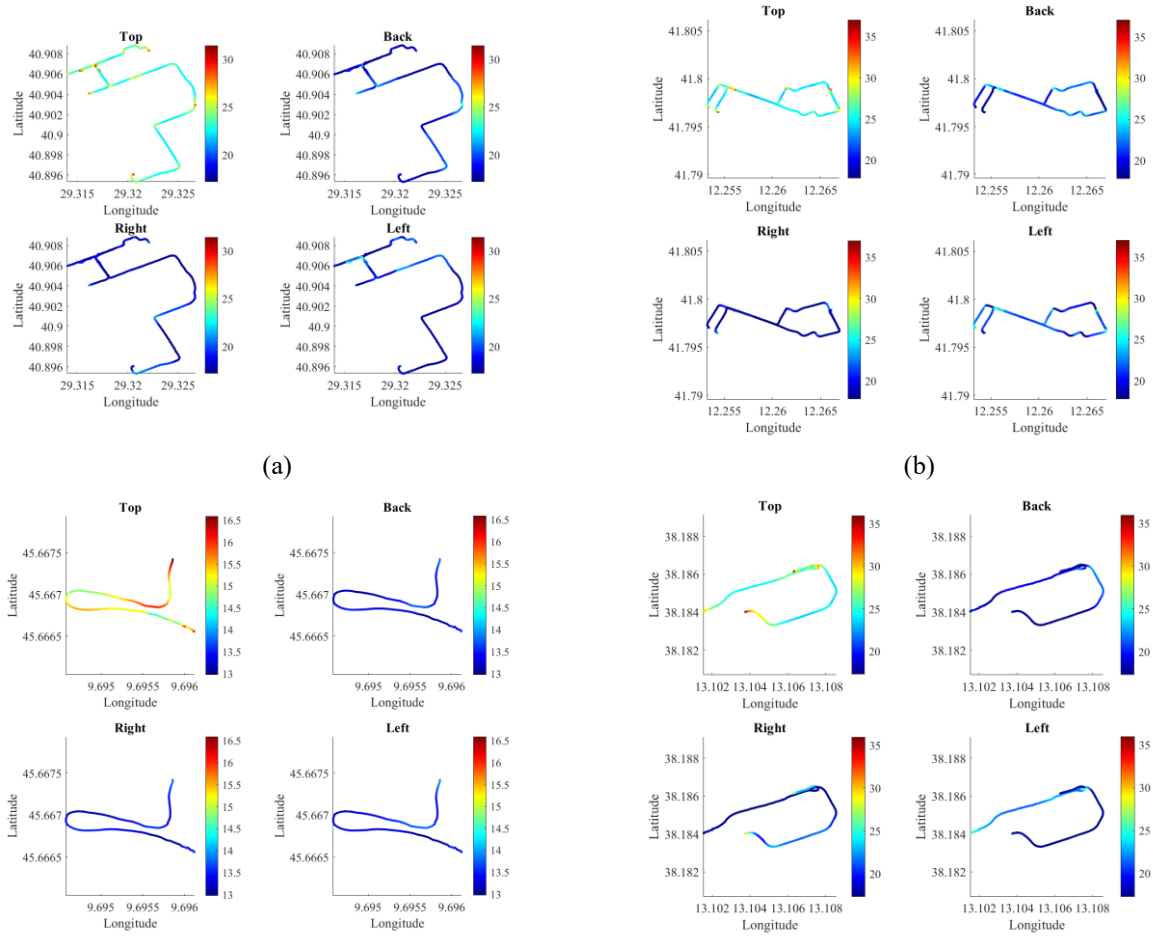

Figure 5.10. Temperature profiles of PV modules integrated on vehicle surfaces during trips at: (a) Istanbul, (b) Rome, (c) Milan, and (d) Palermo.

Figures 5.11 and 5.12 illustrate the energy production per square meter of PV integrated into different vehicle surfaces (roof, sides, rear) for trips conducted at different times of the day (morning vs. afternoon) and seasons (July 30 vs. December 27). Seasonal and diurnal variations were clearly observed: July trips produced significantly more energy than December trips, and afternoon trips showed different surface contributions compared to early morning trips due to changes in sun position.

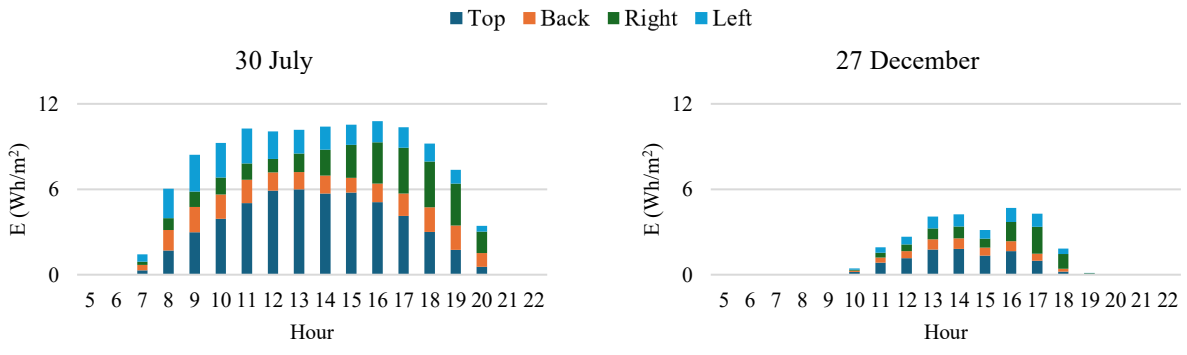

(**a**)

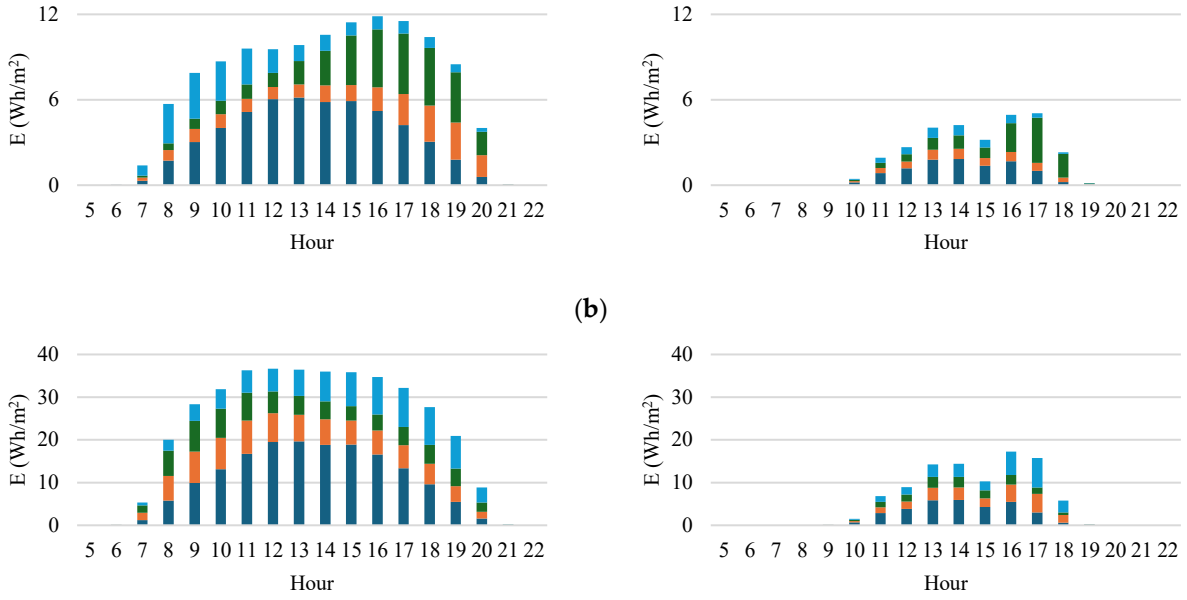

(**b**)

(**c**)

Figure 5.11. Energy production per square meter of PV installed on vehicle surfaces (roof, back, left, right) during three trips in Istanbul, conducted on July 30 and December 27: (a) Trip 1, (b) Trip 2, (c) Trip 3.

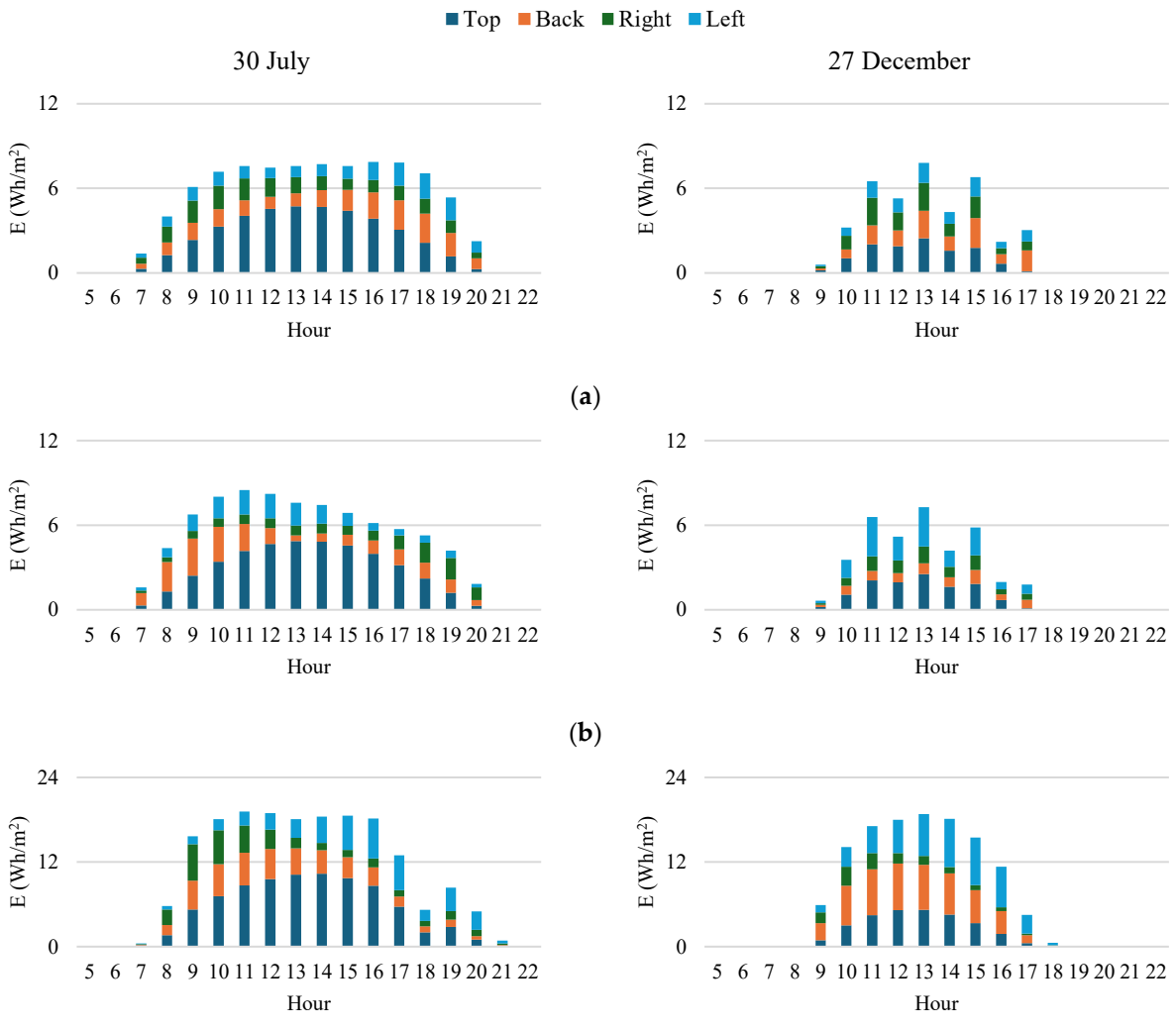

(**a**)

(**b**)

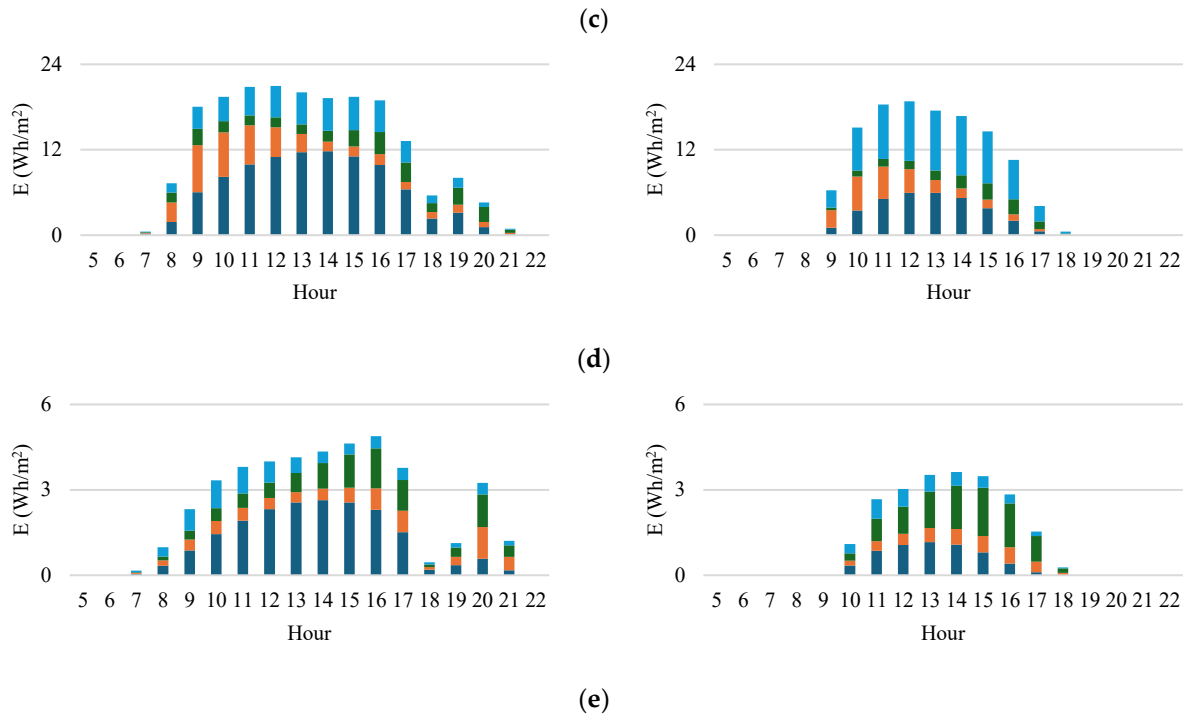

Figure 5.12. Energy production per square meter of PV installed on vehicle surfaces during trips in: (a) Palermo Trip 1, (b) Palermo Trip 2, (c) Rome Trip 1, (d) Rome Trip 2, (e) Milan.

These figures highlight the variations in energy generation results between different trips, which are primarily influenced by the changing azimuth angles of each vehicle surface throughout the journeys. Because the orientation of the vehicle relative to the sun varies with the path taken, each surface (top, back, left, and right) experiences different irradiance levels depending on its alignment during the trip. This effect becomes more pronounced when trips occur at different times of the day, due to the sun's movement, and during different seasons, as demonstrated by the simulations on July 30 and December 27.

The analysed trip in Milan was relatively short, lower than two minutes. This reflects a common scenario in certain airports where the distance between aircraft and terminals is minimal, and as a result, shuttle buses may not be used extensively and often remain parked. This situation presents an opportunity: when vehicles are not in use, they can be parked in non-shaded areas, fully exposed to sunlight to maximize solar energy harvesting. Furthermore, since the vehicle's energy consumption is zero during these times, the generated solar energy can be stored for later use. Consequently, this stored energy can contribute to vehicle operation during active periods, effectively increasing the solar range and improving the overall utility of the VIPV system.

5.5. Conclusion

This chapter has presented the application of a structured framework for evaluating the performance of VIPV in airport ground operations. The novelty lies in two aspects: first, the organization of modelling approaches into two complementary scenarios that address both limited-data and detailed-data conditions; and second, the application of this framework to the underexplored but highly relevant context of ground operations in airports.

Scenario 1 established a generalized methodology capable of producing long-term estimates of energy yield, avoided emissions, and grid parity using only minimal input data. This scenario demonstrated that even under conservative assumptions, VIPV can meaningfully extend the driving range of buses, minibuses, and luggage tractors, thereby reducing their dependence on external charging. The results also revealed that performance is highly sensitive to local boundary conditions, including solar irradiance, electricity prices, and grid carbon intensity, confirming the importance of contextualized analysis.

From a practical perspective, the proposed framework can serve as a decision-support tool for airport operators, fleet managers, and vehicle manufacturers in assessing the technical and environmental feasibility of VIPV adoption. It enables the identification of optimal vehicle types, operating conditions, and parking strategies for maximizing solar utilization. Moreover, the model can support airport decarbonization planning, investment analysis, and sustainability reporting by quantifying avoided emissions and comparing on-vehicle solar generation with grid-based charging. By integrating the results of both generalized and data-driven approaches, the framework offers a scalable methodology that can be used for feasibility screening, operational planning, and policy evaluation.

Taken together, the two scenarios demonstrate the flexibility of the proposed framework. It can be used both as a screening tool in early-stage assessments where data availability is limited, and as a comprehensive simulation environment when high-resolution driving datasets are accessible. This dual capacity makes the framework highly transferable, not only within the airport context but also to a broad range of transport applications where VIPV integration may be feasible.

Looking forward, future research should focus on the following aspects.

- Expanding the collection of GPS-based driving datasets to establish more representative duty cycles;
- refining predictive models that can capture the statistical variability of airport ground operations; and
- exploring operational strategies, such as vehicle positioning during idle periods, that can enhance the effective contribution of VIPV.

By addressing these directions, the potential of VIPV to support sustainable mobility and decarbonization goals can be more fully realized. Within the broader context of this thesis, the airport case study illustrates not only the technical feasibility but also the methodological adaptability of VIPV analysis, reinforcing its role as a viable and scalable strategy for future transport systems.

6

VIPV for Public Transportation Systems

In this chapter, the feasibility, performance, and environmental–economic implications of Vehicle-Integrated Photovoltaic (VIPV) systems are investigated for public transportation applications under two representative contexts. The objective is to provide a comprehensive assessment of the potential role of VIPV technologies in supporting sustainable mobility through on-board renewable energy generation and the consequent reduction of emissions and operating costs.

In the first part, the analysis focuses on urban public transport modes within the city of Palermo, Italy, considering both tramway systems and urban buses as representative cases. For the tram application, the study evaluates the integration of photovoltaic (PV) modules along the roof of Line 1 of the Palermo tram network, adopting a dynamic irradiance modelling approach based on tram motion data and meteorological inputs. This methodology allows for the estimation of energy yields for two PV technologies, crystalline silicon (c-Si) and copper indium gallium selenide (CIGS), which reached approximately 256 kWh/m² and 177 kWh/m² per year, respectively. The VIPV integration for urban buses in Palermo was analysed using high-resolution driving and operational data. The results demonstrate that VIPV systems can contribute a meaningful share of the on-board electricity demand, effectively reduce greenhouse gas emissions while achieve competitive energy costs compared to grid electricity and conventional charging tariffs. These findings reinforce the potential of VIPV as a viable and sustainable solution for enhancing the energy autonomy and environmental performance of urban transport fleets. The second part of the chapter extends the investigation to airport shuttle buses, representing a distinct operational context characterized by mixed routes and variable irradiance conditions. The Charleroi Airport–Brussels South Station connection in Belgium was selected as a case study due to its combination of highway, semi-urban, and urban segments, which enables a detailed evaluation of the influence of route characteristics, driving conditions, and shading patterns on VIPV performance.

Overall, the outcomes of these case studies provide valuable insights into the adaptability and scalability of VIPV technology across different transportation modes and geographical contexts. The results demonstrate that the integration of photovoltaic modules into public transport vehicles can significantly contribute to the decarbonization of urban and inter-urban mobility systems, supporting the broader objectives of energy transition and sustainable transport planning.

6.1. Part I: Urban Public Transportation

The rapid expansion of urban populations, combined with rising energy demand and the scarcity of open spaces for large-scale renewable installations, has accelerated the adoption of integrated photovoltaic (PV) technologies in cities. Among these, building-integrated photovoltaics (BIPV) and vehicle-integrated photovoltaics (VIPV) are increasingly recognized as promising solutions. They enable on-site electricity generation without requiring additional land and contribute directly to decarbonization efforts in densely populated areas [48], [60], [139].

While BIPV systems are now widely implemented, applying PV technologies to moving platforms such as vehicles involves additional complexities. Vehicle motion creates continuously changing solar angles and shading conditions, which strongly influence irradiance profiles [54], [113]. The curvature and orientation of vehicle surfaces also affect optical incidence, while varying operating temperatures influence PV efficiency and long-term degradation. These challenges make it essential to use accurate, motion-aware simulation tools and case-specific assessments to evaluate the real potential of VIPV systems [39], [58].

Public transport vehicles, such as buses and trams, offer a particularly promising platform for VIPV integration. They have large surfaces suitable for PV installation and follow predictable routes and schedules, allowing reliable modelling of their solar energy potential [140]. Additionally, they often remain parked outdoors for extended periods, enabling solar generation even when idle. From an environmental perspective, electrified public transport systems produce zero tailpipe emissions, but their indirect climate footprint depends on the carbon intensity of the local electrical grid. In regions where fossil fuels still dominate electricity production, VIPV can directly displace grid-supplied electricity, reducing both operational costs and emissions [29].

6.1.1. Tram Systems

With increasing global concern over urban air pollution and climate change, electric transportation systems have become central to sustainable urban planning. Trams are a key component of this transition due to their high passenger capacity, fixed routes, and zero direct emissions. By offering a reliable alternative to private cars, they help reduce traffic congestion, cut energy consumption in dense urban areas, and support broader decarbonization strategies [193], [194].

However, while trams produce no emissions during operation, they typically draw power from the electrical grid. The climate impact of this electricity depends heavily on the local energy mix, which in many regions still contains a substantial share of fossil fuels. As a result, efforts to further reduce the carbon footprint of tram systems have focused on integrating renewable energy sources for traction power [195], [196].

In recent years, various solutions have been proposed to enhance the sustainability of tram networks. Research has explored hybrid systems combining proton exchange membrane fuel cells (PEMFCs), lithium-ion batteries (LIBs), and supercapacitors (SCs), supported by advanced energy management strategies. Other studies have considered renewable energy integration, such as hydrokinetic turbines, biomass gasifiers, and stationary PV installations along tram lines or at depots. Yet, most PV-related efforts have focused on these fixed infrastructures rather than on-board generation [197], [198].

By contrast, vehicle-integrated photovoltaics mounted directly on tram surfaces could generate electricity during operation and while parked, reducing dependence on external power supply. Despite this potential, VIPV remains scarcely studied for rail-based systems, especially trams. This chapter addresses this research gap through a detailed case study of Palermo Tram Line 1, investigating the technical feasibility of installing PV modules on tram roofs, quantifying their energy generation and avoided emissions, and evaluating economic viability using grid parity analysis.

6.1.2. Bus Systems

Buses are another cornerstone of sustainable urban mobility, serving as flexible, high-capacity transport options and forming the backbone of many public transport networks. As cities transition to low-emission fleets, electric buses are increasingly deployed, yet they still rely on grid electricity whose carbon footprint depends on the local energy mix [114].

Unlike trams, which follow fixed routes with dedicated tracks, buses operate on regular roads and are subject to more variable driving conditions, shading environments, and surface geometries. These factors complicate VIPV integration but also present opportunities. Buses have extensive roof, side, and rear surfaces that are often exposed to sunlight and can be used to host PV modules. Their operating schedules also typically include long idle periods, during which VIPV can continue generating electricity and partially recharge batteries [57], [140].

In this context, this chapter investigates the potential of integrating PV modules into public transport buses operating on Palermo Bus Line 109. Both internal combustion engine (ICE) buses and electric buses are considered. The analysis evaluates the following aspects.

- Technical aspects, including the solar irradiance received by different surfaces, PV module temperature, and energy production across seasonal and daily cycles.
- Environmental impacts, estimating avoided emissions based on reduced fuel consumption (ICE buses) or displaced grid electricity (electric buses).
- Economic viability, quantified using the Levelized Cost of Electricity (LCOE) and comparing roof-only versus full-surface (roof, sides, back) installations for both standard buses and minibuses.

By combining these two case studies, this chapter provides a comprehensive assessment of the role that VIPV can play in decarbonizing public transport fleets. It demonstrates how the unused surfaces of buses and trams can become productive energy-generating assets, reducing operating costs and emissions while supporting the transition to sustainable urban mobility.

6.2. Methodology

The methodology integrates solar geometry calculations, meteorological data processing, thermal modelling, and power estimation, all adapted for mobile conditions. The approach aims to capture the highly variable operating environment of public transport vehicles, where motion, orientation, and shading continuously change throughout the day.

The total irradiance (G) considered as the sum of direct (G_b) and diffuse (G_d) components as follows:

$$G_t = G_b + G_d \tag{6.1}$$

where the direct component is [150]:

$$G_b = DNI \cdot cos(AOI) \tag{6.2}$$

$$AOI = cos^{-1}[cos(\beta) \cdot cos(\theta_Z) + sin(\beta) \cdot sin(\theta_Z) \cdot cos(\gamma_S - \gamma)] \tag{6.3}$$

and the diffuse component is [149]:

$$G_d = DHI \cdot \left[\frac{(1 - F_1) \cdot (1 + cos\,\beta)}{2} + F_1 \cdot \frac{A}{B} + F_2 \cdot sin\,\beta\right] \tag{6.4}$$

$$A = max(0, cos\,AOI)\ , \qquad B = max(0.087, cos\,\theta_Z)$$

where DNI is Direct Normal Irradiance, DHI is the diffuse horizontal irradiance, AOI is Angle of Incidence, β is the tilt angle, θ_Z is the solar zenith angle, and F_1 and F_2 are complex empirically fitted functions that describe circumsolar and horizon brightness. Meteorological inputs, including, DNI, DHI, ambient temperature, and wind speed, were taken from PVGIS Typical Meteorological Year (TMY) datasets for Palermo [112]. These data provide long-term hourly averages that represent typical operating conditions.

Dynamic motion data (speed and azimuth profiles) were collected along both the tram and bus routes. These data were processed using VIPVLIB [199], an open-source MATLAB toolbox derived from PVLIB [154] and specifically adapted for mobile systems. VIPVLIB calculates the sun's position relative to each vehicle surface for every second of motion, enabling the computation of time-resolved irradiance on all surfaces (roof, sides, and back for buses, and roof wagons for trams).

PV module temperature (T) was estimated using the Faiman model, which includes convective cooling effects from airflow [87]:

$$T_{module} = T_a + \frac{G_t}{U_0 + U_1 \cdot WS} \tag{6.5}$$

where T_a is the air temperature, U_0 is the constant heat transfer component $W/m^{2}°C$, U_1 is the convective heat transfer component $Ws/m^3\ °C$, and WS represents the wind speed m/s. During vehicle motion, the wind speed was assumed equal to the driving speed, while for stationary conditions it was replaced by the measured natural airflow. Because meteorological inputs were taken from Typical Meteorological Year (TMY) files, in which wind speed is reported at 10 m height, it was adjusted to the vehicle roof height (h_{Roof}) through the following relation [155]:

$$WS_{Roof} = WS_{TMY} \cdot (\frac{h_{Roof}}{10^{0.2}}) \tag{6.6}$$

To reflect the thermal inertia of PV modules, instantaneous temperature values were averaged over 1000–1500 second intervals before being used for power calculations, as suggested by Patel et al. [88].

Finally, to estimate the electrical output based on the received irradiance and module temperature, the output power was calculated using the following equation [106], [114]:

$$P_{PV} = \eta_{PV} \cdot \eta_{Co} \cdot A \cdot \mathrm{G} \cdot (1 + k \cdot (T_{module} - T_{ref})) \tag{6.7}$$

$$A = \alpha \cdot \mathrm{A}_{Vehicle} \tag{6.8}$$

where k is the temperature coefficient $(\%/°C)$, η_{PV} is efficiency of the PV module, η_{Co} is efficiency of the power converter, G is solar irradiance (W/m^2), T_{ref} is the reference temperature (25 °C) [114], T is PV module temperature, A is the surface area of the vehicle (m^2) and α is PV coverage ratio (%).

6.2.1. Loss Assumptions and Adjustments

Because mobile PV systems are affected by non-ideal factors, additional correction factors were included.

Shading losses were applied as fixed fractions of the direct irradiance [29]. The assumed values were based on the typical surrounding environment along each route, such as buildings and trees along the bus corridor and nearby infrastructure along the tram line.

- Tram route: 30% loss
- Bus route: 40% loss

Curvature correction was applied to bus side and roof surfaces to account for optical losses from the curved body geometry ($CF = 0.9$) [39].

These losses were applied multiplicatively to the irradiance values before thermal and power calculations.

$$G = CF \cdot (G_{b\,(Shading)} + G_d) \tag{6.9}$$

6.3. Case Studies

To evaluate the feasibility of VIPV systems in public transportation, a dynamic simulation framework was developed and applied to both the Palermo Tram Line 1 and Palermo Bus Line 109 case studies. These cases were selected to represent two major modes of public transportation with distinct operational profiles, rail-based and road-based, and to explore the feasibility of VIPV systems under their respective geometric and dynamic constraints.

6.3.1. Tram Line 1 (Palermo)

Line 1 of the Palermo Tram runs for approximately 5.5 km, linking Palermo Centrale station to Roccella Terminal. This corridor was selected because it represents a typical urban tram route, combining city-centre sections with more open areas. Importantly, the alignment has relatively wide spacing between the tracks and surrounding buildings, reducing persistent shading and making it suitable for on-board PV integration. However, to realistically represent intermittent shading from buildings, poles, and vegetation along the route, a 30% loss was applied to the direct irradiance component.

Figure 6.1. Route of Palermo Tram Line 1 (from Palermo Centrale to Roccella Terminal). Source: Google Earth.

The tram consists of five articulated wagons (Figure 6.2). Data on vehicle geometry were provided by AMAT Palermo [200], the city's public transport operator. Wagon 3 houses some equipments and was therefore excluded from PV coverage. The remaining wagon roofs (1, 2, 4, and 5) were considered for PV installation.

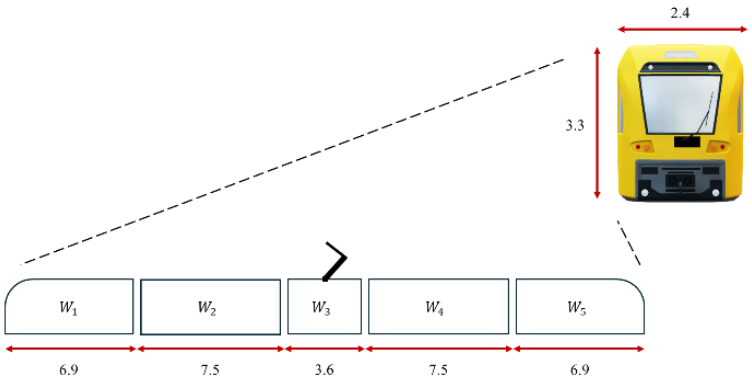

Figure 6.2. Dimensions and layout of the tram wagons (Wagon 3 excluded from PV installation).

Tram speed and azimuth profiles were recorded for first wagon during typical operations in both directions. Since the tram is a coupled system, the motion of the remaining wagons was reconstructed by applying appropriate time offsets based on their fixed inter-wagon spacing. To include stop times, a dwell of approximately 9 minutes was added at each terminal for passenger exchange and operational checks. As a result, the full round-trip duration was estimated at about 1 hour, including movement and dwell.

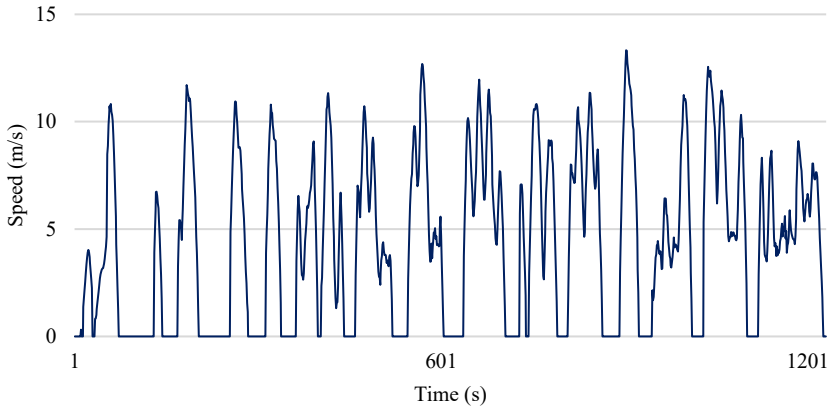

(a)

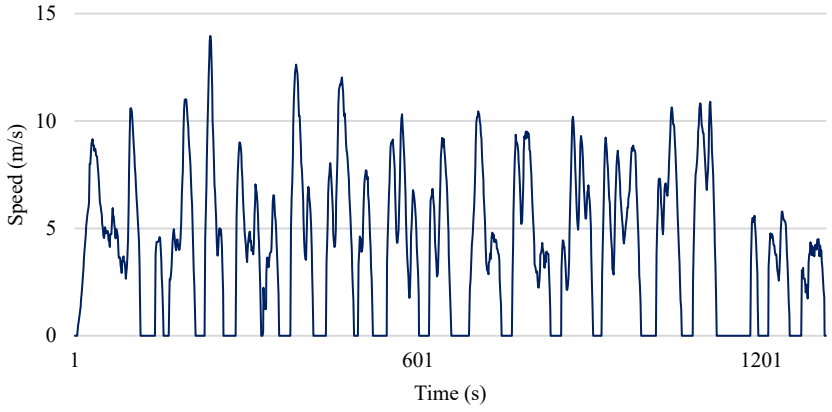

(b)

Figure 6.3. Speed profiles for (a) the route from Palermo Centrale to Roccella Terminal and (b) the return route.

6.3.2. Bus Line 109 (Palermo)

Bus Line 109 links Parcheggio Basile (near the University of Palermo) with Palermo Centrale, traversing dense urban corridors with frequent intersections and roadside buildings. Because of the narrower road profile and frequent proximity to buildings and trees, a 40% loss was applied to the direct irradiance to represent route-environment shading conditions. This assumption reflects the much stronger shading variability seen along this corridor compared to the tram route.

Figure 6.4. Route of Palermo Bus Line 109 (Parcheggio Basile - Palermo Centrale). Source: MATLAB.

Speed and azimuth were recorded with MATLAB Mobile during a representative weekday trip and used as dynamic inputs. This dataset captures real operational dynamics including acceleration, braking, and turns. It was used directly as input to the VIPV simulation chain to dynamically compute the angle of incidence and convective cooling conditions.

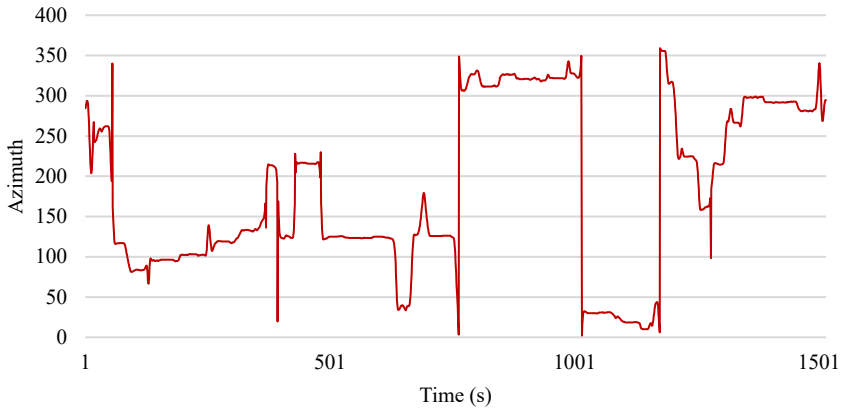

Figure 6.5. Azimuth angle profile during the recorded bus trip.

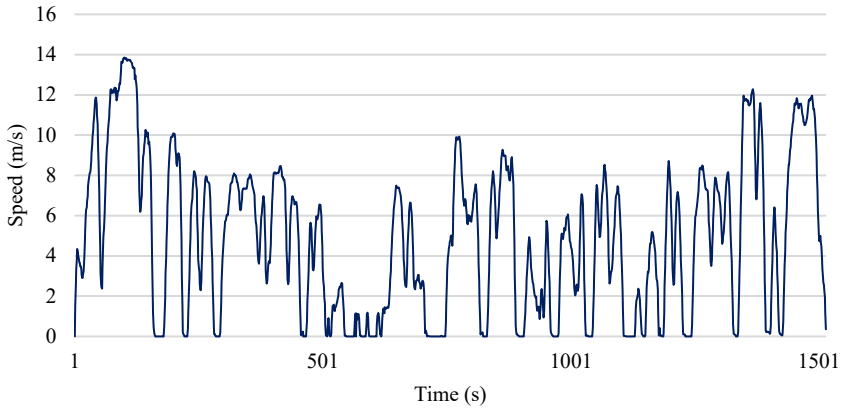

Figure 6.6. Drive cycle (speed profile) during the recorded bus trip.

Two bus sizes were considered to explore scaling effects: a standard bus and a minibus. PV modules were considered for roof, left side, right side, and back surfaces, with coverage ratios based on available flat areas (detailed later in results).

Table 6.1. Surface areas and PV coverage ratios for standard bus and minibus [114], [158].

	Bus		Minibus	
	$A_{Vehicle}$ (m^2)	α (%)	$A_{Vehicle}$ (m^2)	α (%)
Top	33.2	60	12.03	60
Back	8.81	75	5.75	70
Right	44.1	40	16.4	40
Left	44.1	40	16.4	50

Unlike the tram, where both c-Si and CIGS were studied, the bus simulations used only c-Si modules, chosen for their high efficiency and robustness under the stronger vibration and thermal cycling typical of road transport.

Table 6.2. Parameters of PV modules used in the tram and bus case studies [81].

PV Module	Efficiency (%)	k $(\%/°C)$	U_0 $(W/m^2 \cdot °C)$	U_1 $(W/m^3 \cdot °C)$	SPD (W_p/m^2)	Used in
c-Si	21.6	−0.47	30.02	6.28	210	Tram & Bus
CIGS	15.1	−0.45	22.19	4.09	151	Tram only

6.4. Results and Discussion

6.4.1. Tram

Figure 6.7 reports PV module temperatures during a complete cycle on three representative days (11 April, 11 July, 11 December). Two technologies were evaluated: CIGS (Fig. 6.7a) and c-Si (Fig. 6.7b). The dashed traces are second-by-second temperatures; the solid markers are 1200-s averages used in the power model to capture thermal inertia. Three patterns emerge clearly. First, seasonality dominates: July peaks around the 45–50 °C range, April sits near 25–35 °C, and December remains close to 10–15 °C across the cycle. Second, operational phases matter: transient spikes align with low-speed running and station dwell, when convective cooling drops; during higher-speed segments, airflow over the roof suppresses cell temperature despite similar irradiance. Third, technology choice influences operating temperature: for the same duty cycle, c-Si runs a few degrees cooler than CIGS, reflecting differences in heat rejection (U_0, U_1) and packaging.

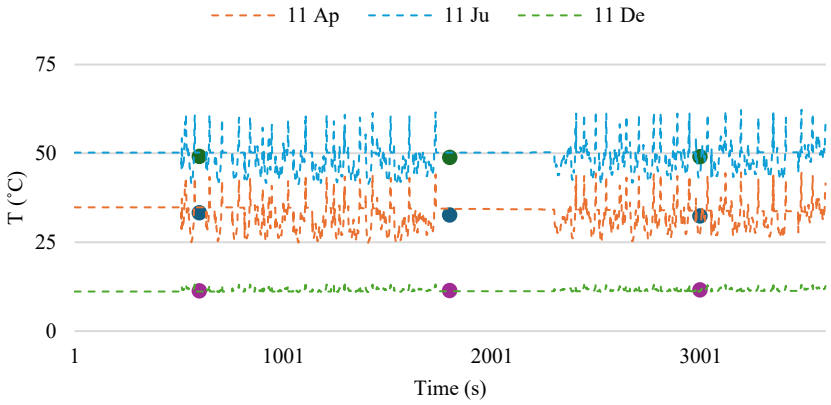

(a)

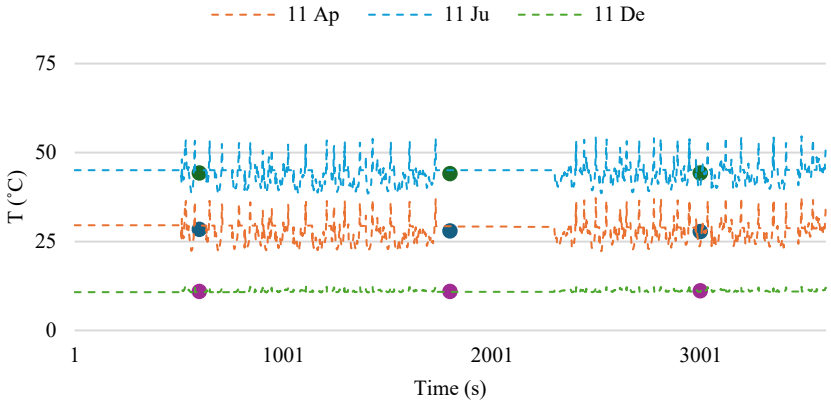

(b)

Figure 6.7. Module temperature during a full-service cycle (instantaneous: dashed; 1 200-s average: markers): (a) CIGS, (b) c-Si; 11 Apr, 11 Jul, 11 Dec.

Daily temperature envelopes for the two technologies are shown in Figure 6.8. The bell-shaped curves mirror solar forcing: July exhibits the widest excursion (late-morning rise to ~50 °C and a gentle afternoon roll-off) and December maintains a flat, cool profile. These temperature fields explain much of the yield contrast discussed below because both c-Si and CIGS carry negative temperature coefficients (−0.47 %/°C and −0.45 %/°C, respectively).

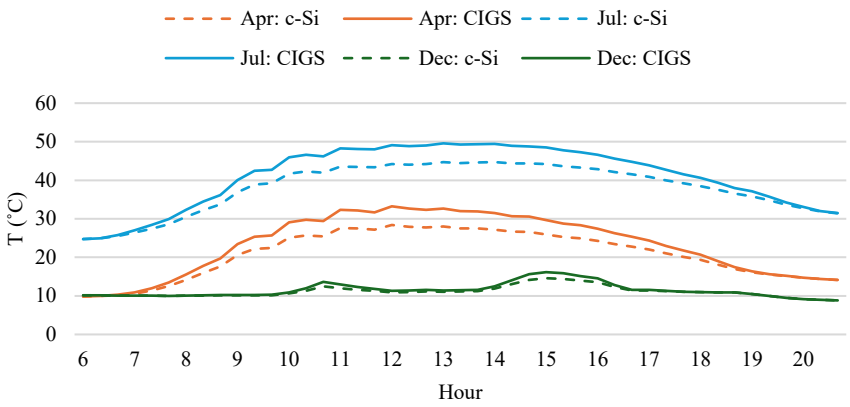

Figure 6.8. Daily temperature envelopes for c-Si and CIGS (11 Apr, 11 Jul, 11 Dec).

Hourly, per m^2 energy production for first wagon in July vs. December is plotted in Figure 6.9. As expected, July delivers a long, symmetric generation window (~06:00–21:00), while December is constrained to ~07:00–18:00. Across both months, c-Si consistently outperforms CIGS, because (i) c-Si has higher efficiency and (ii) its slightly cooler operation reduces thermal losses during the hottest hours. The December curves also show a relatively flat mid-day plateau, consistent with lower solar altitude.

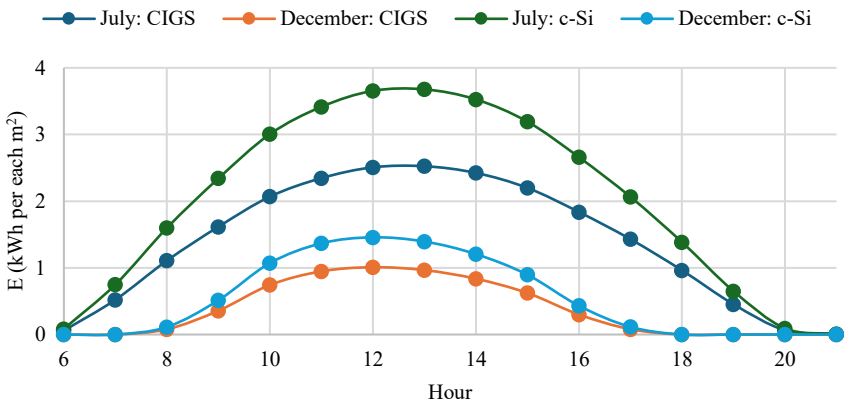

Figure 6.9. Hourly energy per m² on W_1 (July vs. December) for c-Si and CIGS (06:00–21:00).

The monthly specific yield (per m^2 on W_1) is provided in Figure 6.10. Peak months are late spring/early summer, with maxima of ~33 kWh/m^2 for c-Si and ~23 kWh/m^2 for CIGS in June. The shoulder months (Mar–Apr and Sep–Oct) retain a substantial share of the summer peak, underscoring the advantage of Palermo's latitude and the relatively open urban corridor chosen, even after we conservatively apply a 30% loss on direct irradiance for urban shading along Line 1 and a 10% curvature penalty for roof integration.

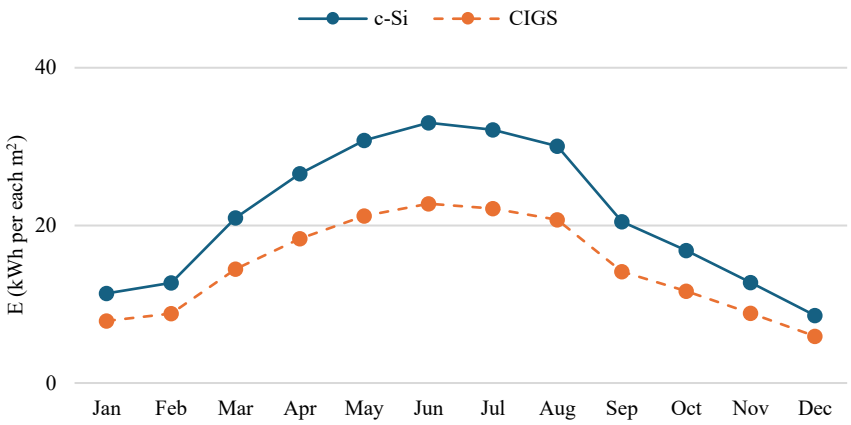

Figure 6.10. Monthly energy per m² on W_1 for c-Si and CIGS.

By considering all wagons except W_3, which is reserved for equipment, and assuming 60% usable roof coverage, total monthly tram-level generation is shown in Figure 6.11. Mid-summer output reaches roughly 1.3–1.4 MWh/month with c-Si and ~0.9–1.0 MWh/month with CIGS; winter months drop to the 0.3–0.5 MWh/month range, which aligns with the shorter photoperiod and cooler but lower-insolation conditions. Over the year, this integrates to ~10.6 MWh for c-Si and ~7.3 MWh for CIGS.

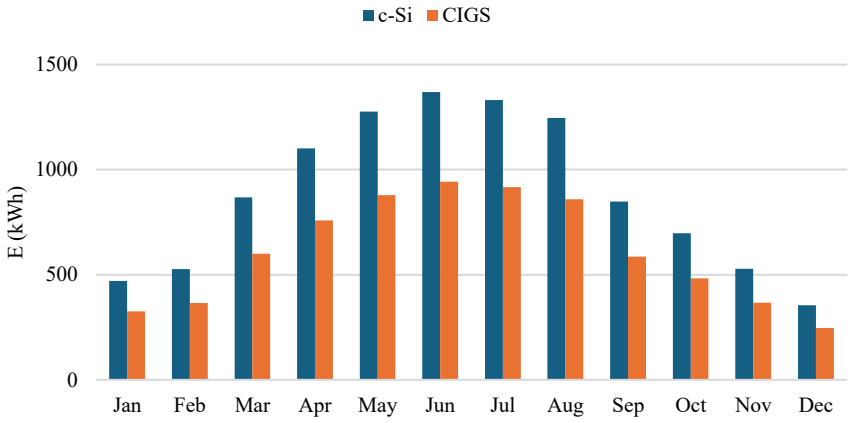

Figure 6.11. Total monthly energy from all wagons (except W_3) assuming 60% roof coverage and stated loss factors.

Translating energy into environmental benefit, Figure 6.12 overlays monthly avoided CO_2 (bars) against the grid carbon intensity (CI) profile used for Palermo (green line) [188]. Two aspects set the pattern: (i) how much the tram produces that month and (ii) how carbon-intensive the displaced grid electricity is. Hence avoided emissions spike when generation and CI are both high (late summer/early autumn in the adopted series), and they soften when either generation dips (winter) or CI drops. On an annual basis, the replacement of grid electricity with VIPV yields meaningful savings, order tonnes of CO_2 per year, and does so without requiring extra land or additional trackside assets.

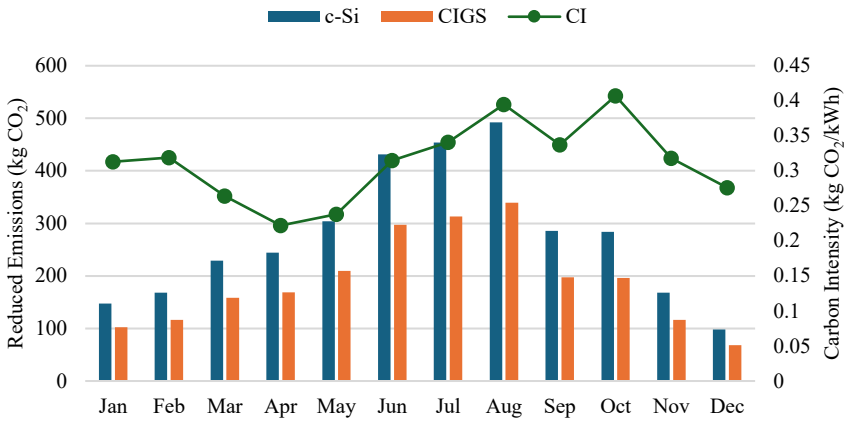

Figure 6.12. Avoided CO_2 by month (bars) and Palermo grid carbon intensity (line).

6.4.2. Bus

Figure 6.13 shows the instantaneous irradiance measured on the four main surfaces (top, back, right, and left) at noon on a representative summer day (30 July). The top surface received consistently higher irradiance values, often above 500 W/m², reflecting its favourable orientation and minimal shading. The results from a winter day (27 December) show a contrasting pattern. As illustrated in Figure 6.13b, irradiance on the roof is significantly lower and more variable, while the sides, particularly the left side, receive relatively higher irradiance during certain segments, as the lower solar altitude increases the exposure of vertical surfaces. The corresponding temperature maps in Figure 6.13b confirm the cooler winter operation, with module temperatures remaining near ambient (15–25 °C) and showing much less spatial variation than in summer. These findings highlight that the contribution of side surfaces becomes more important in winter, while the roof dominates in summer. To better understand the thermal behaviour under these irradiance patterns, Figure 6.13a presents the module temperature distributions along the bus route on the same summer day. Roof modules frequently reached 45 °C, especially in sections with prolonged exposure and low vehicle speeds, while side and back surfaces remained notably cooler, rarely surpassing 35 °C. This temperature pattern directly influences energy output because of the negative temperature coefficient of crystalline silicon modules (−0.47 %/°C).

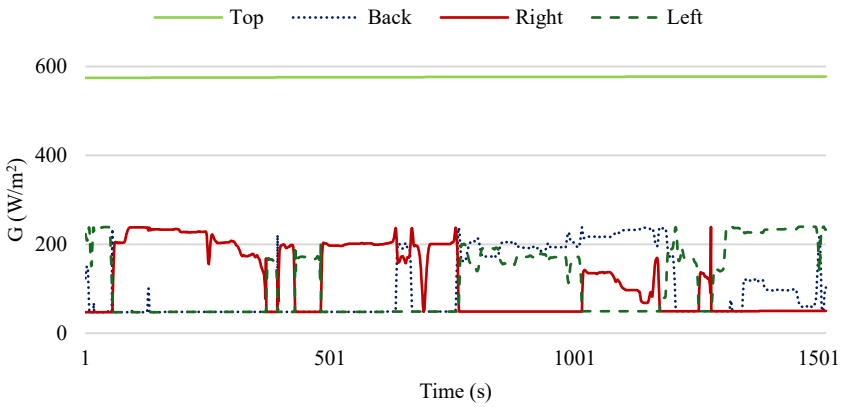

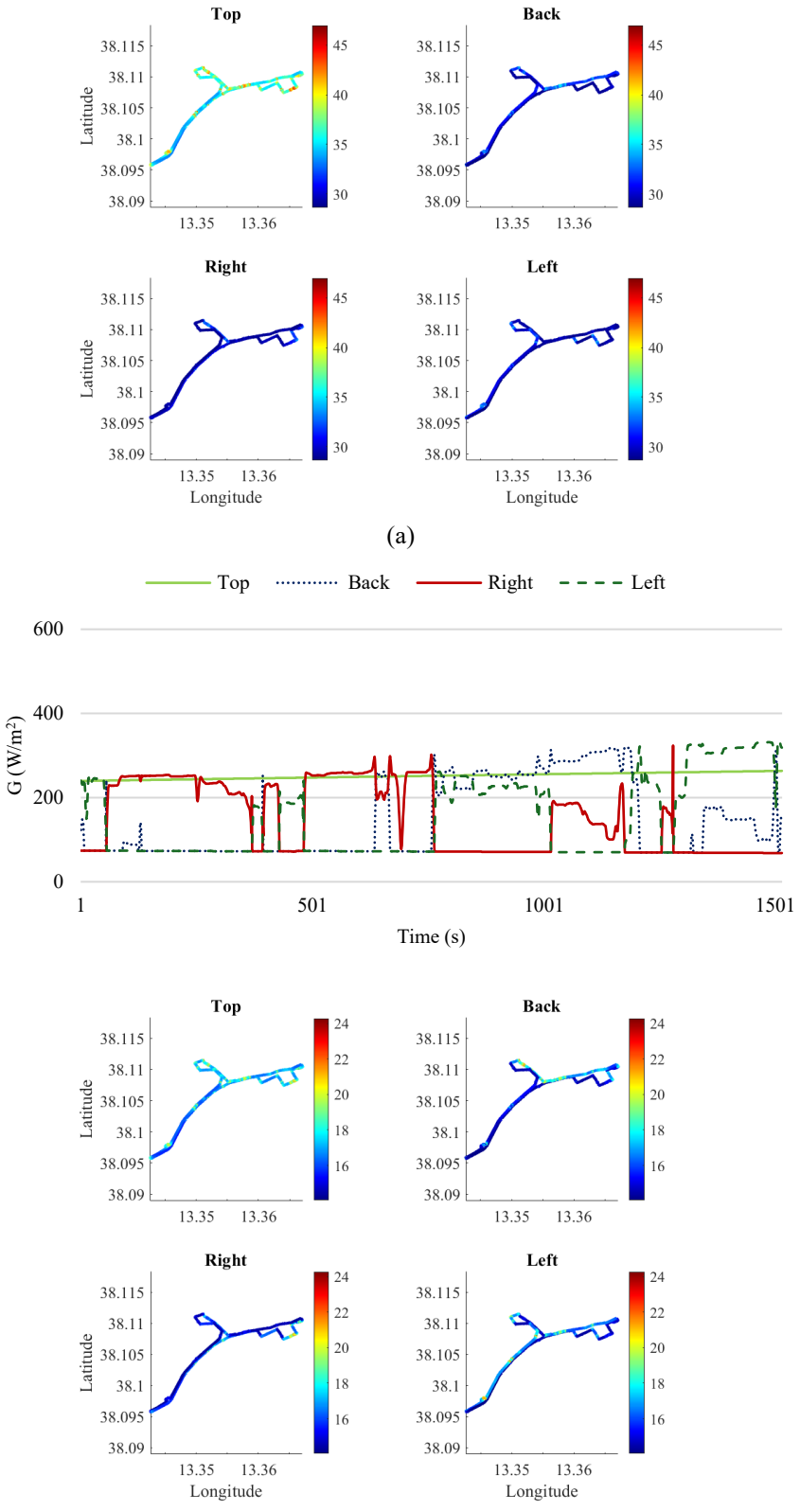

Figure 6.13. Instantaneous irradiance received on different bus surfaces (top, back, right, left) and spatial distribution of PV module temperatures (°C) along the bus route for each surface at noon on (a) 30 July (b) 27 December.

Figure 6.14 summarizes the monthly average energy production per square meter for each surface. The roof clearly outperforms all other surfaces, peaking at about 38 kWh/m² in June–July, while the

sides contribute between 8–15 kWh/m² depending on the month. The back consistently produces the least due to its near-vertical position. Nevertheless, side surfaces provide a valuable complementary contribution during winter months when roof irradiance is lower, underlining the advantage of multi-surface integration.

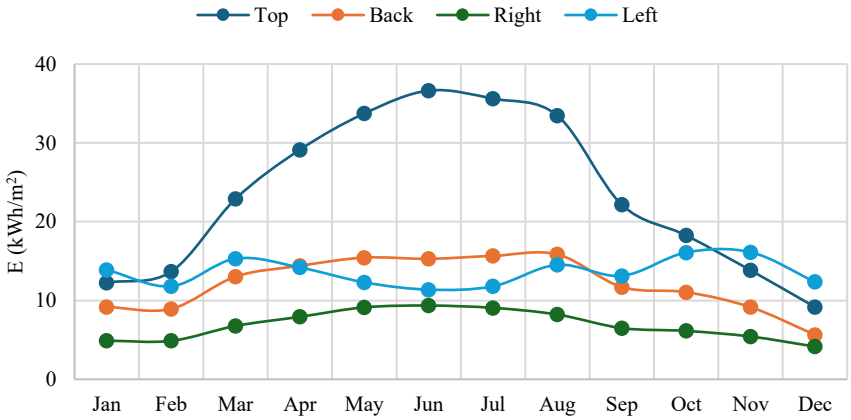

Figure 6.14. Monthly average energy production per square meter of installed PV on different bus surfaces.

The environmental benefits of VIPV integration differ depending on whether the vehicle is a diesel bus or an electric bus. For diesel buses, the electricity generated by VIPV directly displaces the electricity that would otherwise be produced by the alternator. The corresponding reduction in CO_2 emissions can be estimated using [56]:

$$Reduced\ Emissions_{ICE} = E \cdot \frac{V_{Fuel}}{\eta_{Alt}} \cdot C_{Fuel} \tag{6.10}$$

where $V_{Fuel}\ l/kWh$ is the fuel consumption to energy content ratio, η_{Alt} is the efficiency of the alternator, $C_{Fuel}\ gCO_2/l$ is the CO_2 conversion factor of the fuel, and E is the energy generated by VIPV. The adopted parameter values for Palermo are: $\eta_{Alt} = 0.67$, $V_{Fuel} = 0.22\ l/kWh$, $C_{Fuel} = 2.64\ kgCO_2/l$, and diesel cost considered to be 1.63 €/l [56], [201]. The calculated results are presented in Table 6.3.

Table 6.3. Yearly energy production, fuel savings, emission reductions, and cost savings from VIPV integration in ICE buses.

	roof-only	full-surface
E (kWh/m^2)	281	671
Fuel savings (l/m^2)	92	221
Em ($kg\ CO_2/m^2$)	243	582
cost savings (€/m^2)	150	359

The associated environmental benefits for electric vehicle were quantified based on the carbon intensity (CI) of the Sicily grid. As shown in Figure 6.15, the avoided emissions from VIPV electricity closely follow the seasonal variation in both production and CI. During summer, avoided emissions

peak around 25 kg CO_2/m^2 per month, while in winter they decrease to below 15 kg CO_2/m^2. These results confirm that VIPV integration can effectively reduce the operational carbon footprint of electric buses, particularly when generation coincides with periods of higher grid CI.

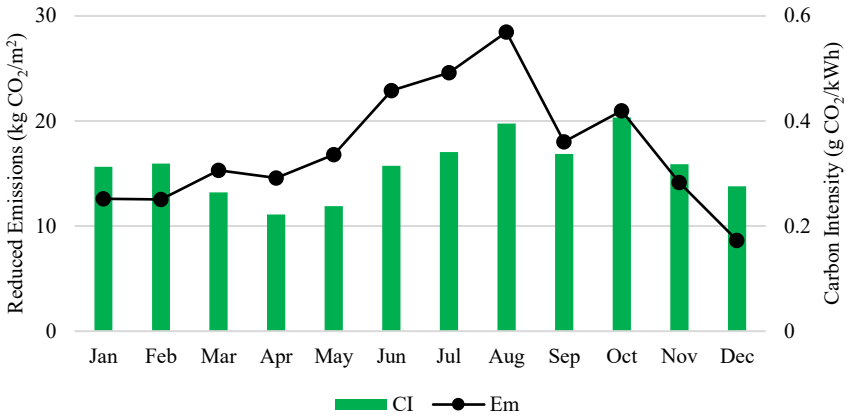

Figure 6.15. Avoided CO_2 emissions from VIPV electricity versus monthly carbon intensity (CI) of the Sicily grid.

To evaluate the scalability of this concept, both a standard bus and a minibus were assessed, using the surface areas and coverage ratios given in Table 6.1. Figure 6.16 compares the total yearly energy output from each surface type. The standard bus generated approximately 5.6 MWh from the roof and an additional 5.3 MWh from the sides and back combined, achieving 10.9 MWh/year in total. The minibus produced 2 MWh from the roof and 2.5 MWh from the sides and back, for a total of 4.5 MWh/year. Table 6.4 summarizes the resulting avoided CO_2 emissions: 3.4 ton/year for the standard bus and 1.4 ton/year for the minibus, showing that even smaller public transport vehicles can substantially benefit from VIPV integration.

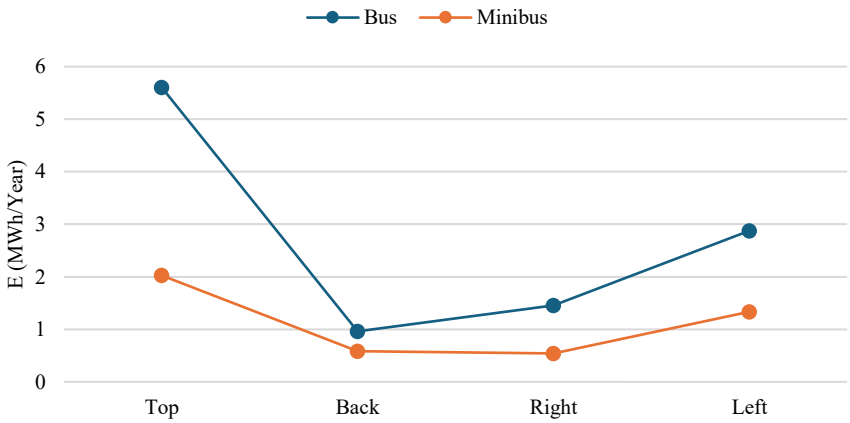

Figure 6.16. Yearly energy production from different surfaces for the standard bus and minibus.

Table 6.4. Yearly energy production and avoided emissions for bus and minibus under different surface integration scenarios.

	E ($MWh/Year$)	Em ($ton\ CO_2/Year$)

	roof-only	full-surface	roof-only	full-surface
Bus	5.6	10.9	1.8	3.4
Minibus	2	4.5	0.6	1.4

The temporal distribution of energy production was also analysed to assess the consistency of supply. Figure 6.17 shows the hourly energy output from a fully integrated standard bus in July and December. For July, energy generation starts around 06:00, increases steadily to a plateau between 10:00 and 16:00 (reaching 3.5–4.0 kWh per hour), and declines toward sunset at 21:00. The narrow interquartile ranges indicate stable irradiance and predictable performance during summer. In contrast, the December profile: energy generation is confined to 09:00–18:00, with a lower midday peak (~2 kWh per hour) and broader interquartile ranges, indicating greater variability. This reflects shorter daylight hours, lower sun angles, and more frequent shading during winter.

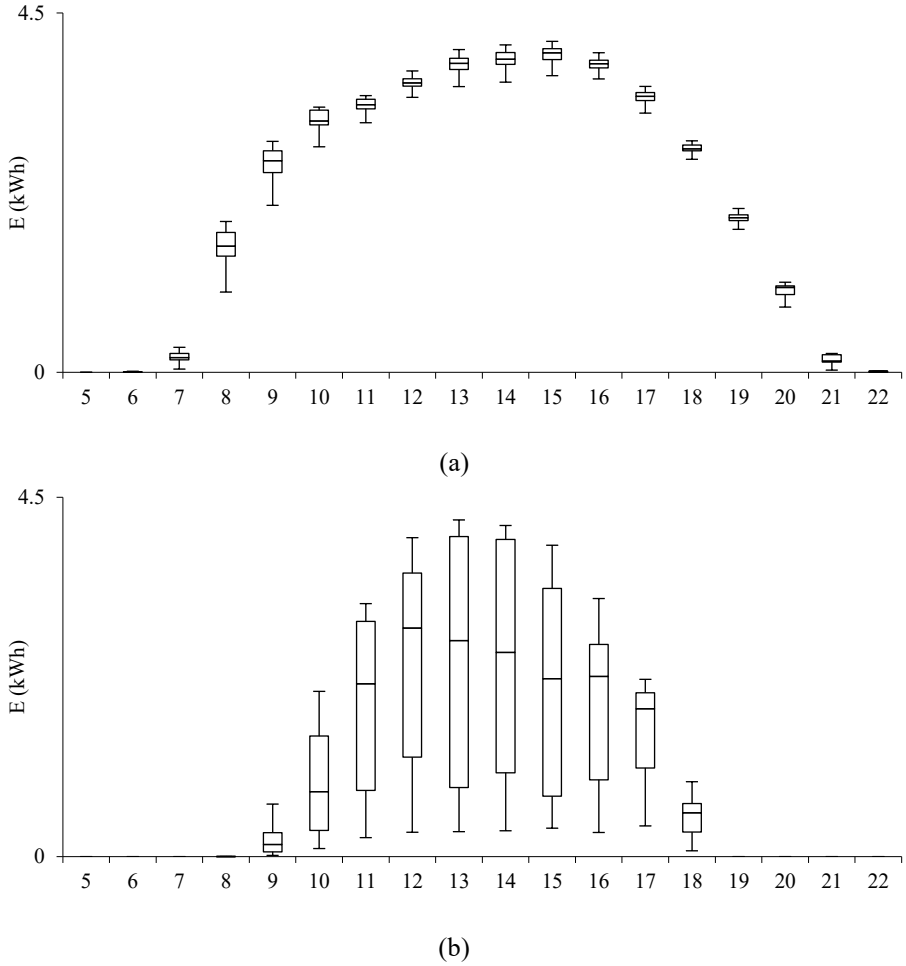

Figure 6.17. Hourly energy production from a fully integrated bus in (a) July (b) December.

Economically, the system's feasibility was assessed using the Levelized Cost of Electricity (LCOE). Assuming system prices of 1.0 €/W_p and 1.7 €/W_p, a 10-year lifetime, and 1 % annual degradation, Table 6.5 reports the resulting LCOE values. For the standard bus, the LCOE ranged from 0.092–0.157 €/kWh for roof-only integration and 0.147–0.250 €/kWh for full-surface coverage. For the minibus, values were 0.093–0.157 €/kWh and 0.150–0.256 €/kWh, respectively. Even at the higher

cost scenario, these values are close to or below the average household electricity price in Italy (0.311 €/kWh) [202] and well below public charging tariffs in Palermo (0.47–0.75 €/kWh) [203], confirming the strong economic competitiveness of VIPV electricity for public transport.

Table 6.5. LCOE values for standard bus and minibus under different system costs and surface coverage scenarios.

	1.7 €/Wp		1 €/Wp	
	roof-only (€)	full-surface (€)	roof-only (€)	full-surface (€)
Bus	0.157	0.250	0.092	0.147
Minibus	0.157	0.256	0.093	0.150

Overall, these results demonstrate that VIPV systems can provide a substantial portion of the energy demand of public buses, especially when all available exterior surfaces are utilized. The system shows strong seasonality, with summer producing about twice the energy of winter, yet it offers clear operational, environmental, and cost benefits, supporting its viability as a sustainable solution for urban public transport.

6.5. Conclusions

In the first part of this chapter, we investigated the potential of VIPV as a renewable energy solution for public transportation systems, focusing on two real-world case studies in Palermo: the Line 1 tram and the Line 109 bus route. Both case studies applied a high-resolution VIPV modelling framework that incorporated second-by-second vehicle motion data, meteorological inputs from TMY datasets, and detailed thermal modelling using the Faiman model. The goal was to evaluate the technical feasibility, environmental benefits, and economic viability of integrating PV modules into these large public transport vehicles under real operational conditions.

The results demonstrated that the integration of PV systems into tram and bus surfaces can produce substantial amounts of renewable energy directly onboard the vehicles, thereby reducing their reliance on external grid electricity. In the tram case, crystalline silicon (c-Si) modules installed on the roof of the wagons achieved annual yields of about 10.6 MWh, while copper indium gallium selenide (CIGS) modules produced around 7.3 MWh. These values were obtained after accounting for realistic shading losses (30% based on the urban path characteristics) and installation constraints, such as excluding the central technical wagon. Similarly, in the bus case study, a fully covered standard electric bus generated approximately 10.9 MWh/year, while a smaller minibus produced about 4.5 MWh/year. Even when only the roof was considered, buses produced more than 5 MWh annually, showing that significant contributions can be achieved even with partial coverage.

From an environmental perspective, the integration of VIPV resulted in notable reductions in greenhouse gas emissions. For the tram system, replacing grid electricity with VIPV-generated energy avoided approximately 3.3 tons of CO_2 annually with c-Si and 2.3 tons with CIGS. In the bus case, VIPV reduced emissions by 3.4 tons of CO_2 per year for the standard bus and 1.4 tons for the minibus. These reductions are particularly valuable in regions where the electricity grid still relies heavily on fossil fuels, and they contribute directly to local decarbonization strategies for public transportation networks.

The techno-economic analysis further confirmed the feasibility of these systems. The levelized cost of electricity (LCOE) for tram-based VIPV systems was found to be competitive with local grid electricity, with break-even system prices of 2.608 €/W_p for c-Si and 2.503 €/W_p for CIGS, assuming a 10-year lifetime, 3.2% real WACC, and 1% annual degradation. In the bus study, LCOE values ranged from 0.092 to 0.157 €/kWh for roof-only systems and from 0.147 to 0.250 €/kWh for full-surface systems. These values are below or close to the average household electricity price in Italy (0.311 €/kWh) and much lower than public charging tariffs in Palermo (0.47–0.75 €/kWh), confirming the strong cost competitiveness of VIPV electricity for public transport fleets.

Overall, this chapter has shown that VIPV represents a technically feasible, environmentally beneficial, and economically promising solution to support the decarbonization of urban public transportation systems. The results highlight several key insights:

- large transport vehicles provide sufficient surface area for meaningful PV integration without compromising their primary operational functions;
- multi-surface integration (roof + sides) enhances production, especially in winter when solar altitude is low;
- incorporating real driving profiles and thermal inertia effects is essential to accurately assess VIPV performance in mobile applications.

These findings underline the potential role of VIPV as a complementary energy source in sustainable transport strategies. Future research should explore long-term durability and maintenance aspects, the optimization of PV layouts to account for roof-mounted auxiliary systems, and the integration of smart energy management systems to synchronize VIPV generation with vehicle operational schedules and depot charging. Expanding these studies to larger fleets and different climatic zones would provide further evidence to support widespread adoption of VIPV in public transportation.

6.6. Part II: Airport Shuttle Buses

In recent decades, the rapid growth of the global economy has led to a substantial increase in the demand for air travel. Between 2005 and 2021, this demand more than doubled, and only in 2021, approximately 2.3 billion passengers were transported worldwide, an increase of 28.1% compared to the previous year [204], [205]. While the aviation sector plays a crucial role in enhancing global connectivity and economic development, this surge in air traffic has brought with it several pressing challenges. Among these are increased greenhouse gas emissions, local air pollution, traffic congestion around airports, and difficulties related to landside accessibility. Addressing these issues is essential in ensuring the long-term sustainability of airport-related transportation systems [206].

One critical area of concern lies in ground access to airports. As passenger volumes grow, the need for efficient, reliable, and environmentally sustainable transport options becomes more urgent. In many airports, particularly those where rail infrastructure is not yet fully developed, shuttle buses remain the primary mode of transportation connecting airport terminals with surrounding urban areas. These buses play a vital role in managing passenger flows, yet their reliance on internal combustion engines (ICEs) makes them significant contributors to urban air pollution and carbon emissions [207], [208].

In response to the environmental impact of conventional vehicles, the electrification of road transport has emerged as a key strategy in global efforts to reduce carbon emissions [209]. In the European Union, for instance, the transport sector is responsible for nearly 30% of energy-related greenhouse gas emissions, prompting widespread initiatives to transition to cleaner energy sources [210]. Electric buses (e-buses) have gained increasing popularity in recent years due to their potential to deliver zero tailpipe emissions, improved fuel efficiency, and decreased dependence on fossil fuels. Between 2014 and 2019, the number of e-buses operating in Europe rose from approximately 200 to over 2,200, indicating a significant shift toward sustainable public transit solutions [211].

However, the environmental benefits of electric vehicles are closely linked to the source of the electricity used to power them. If the energy used for charging is derived from non-renewable sources, the overall sustainability gains can be limited [29]. Therefore, integrating renewable energy into electric mobility systems is becoming an area of growing interest [37]. Among various renewable sources, solar energy presents a particularly promising solution due to its widespread availability and compatibility with mobile applications [54]. One innovative approach to utilizing solar energy in transport systems is the integration of PV panels directly into the body of the vehicle, a concept known as VIPV [48].

VIPV systems enable vehicles to generate their own electricity using solar power, which can be used for auxiliary functions or, in the case of electric vehicles, to partially power traction systems [59]. This not only reduces reliance on the electric grid but also extends the operational range of the vehicle and lowers charging frequency [44]. Although several studies have examined the feasibility and performance of VIPV systems in general vehicular applications [39], [153], [161], [173], [175], their implementation in specific, high-utilization transport scenarios such as airport shuttle services remains underexplored.

Airport shuttle buses offer a compelling context for investigating VIPV technology due to their unique operating profiles. These vehicles typically run continuously throughout the day, often covering diverse environments, including highways, semi-urban, and urban areas, with varying traffic conditions and solar exposure. As such, they present both challenges and opportunities for evaluating the real-world potential of VIPV systems under dynamic conditions.

In this part, we investigate the technical potential of integrating VIPV systems into airport shuttle buses, using the shuttle service operating at Charleroi Airport in Belgium as a case study. The analysis focuses on evaluating key performance indicators such as incident solar irradiance on various surfaces of the vehicle body, thermal behaviour of the integrated PV modules during operation, and the amount of electrical energy generated across different segments of the route. By examining these aspects, the study aims to provide deeper insights into the viability and efficiency of VIPV technology in the context of sustainable airport access. Furthermore, by considering both ICE and electric buses, this study also evaluates the impact of VIPV energy generation on fuel and energy savings, with particular attention to potential cost reductions and emission decreases resulting from reduced fuel consumption in ICE buses.

6.7. Case Study

As a case study, we analysed a dataset related to the Charleroi Airport shuttle bus, which connects the airport to Brussels Gare du Midi station. As previously mentioned, the primary objective of this study is to evaluate the performance of VIPV systems under real-world dynamic conditions across different operational environments. The route is divided into three distinct segments based on the surrounding environment and traffic characteristics: the highway section, the semi-urban (or transition) area, and the dense urban area near the station. Therefore, the initial segment of the trip, specifically the portion between the terminal inside the airport and the start of the highway, was excluded from the analysis. This decision was made due to the short duration and irregular vehicle dynamics in that segment, which do not offer a representative or consistent condition for assessing solar energy production. Figure 6.18-a illustrates the shuttle bus route from the airport to the city, while Figure 6.18-b presents the corresponding azimuth angle variations along this pathway.

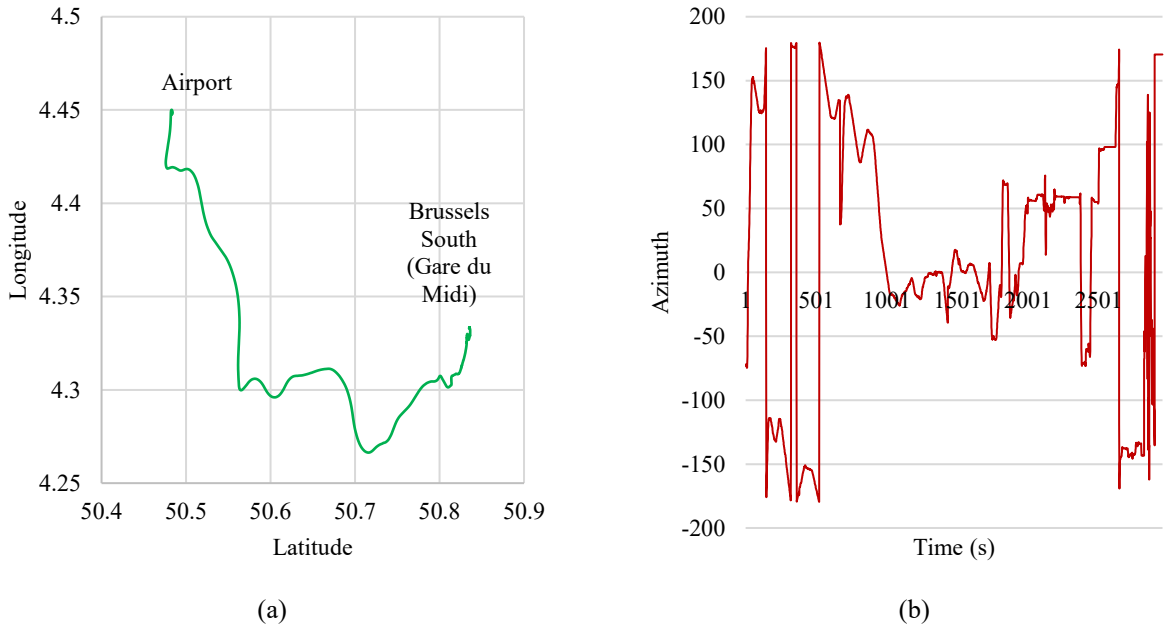

(a) (b)

Figure 6.18. (a) The pathway of the shuttle route from Charleroi Airport to Brussels South Station, and (b) the variations in azimuth angle during the trip, based on real-time data collected using MATLAB Mobile.

Figure 6.19 presents the speed profile of the shuttle bus across the three main segments of the route. As evident from the figure, each segment demonstrates distinct driving characteristics. The highway portion exhibits the highest and most stable speeds, while the semi-urban section shows moderate speed fluctuations. The urban area is characterized by the lowest average speed and frequent stops due to traffic lights, congestion, and intersections. These variations are important as they directly influence both the thermal and electrical behaviour of the VIPV system, particularly through their impact on airflow (and thus module cooling) and energy demands.

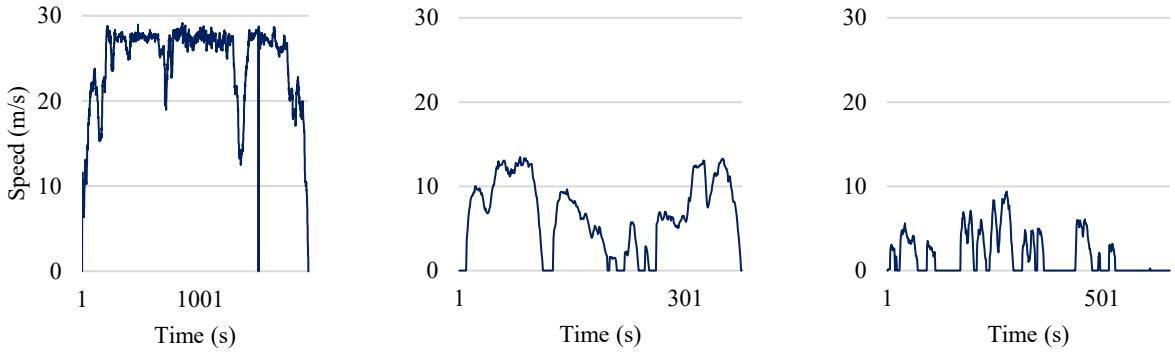

(a) (b) (c)

Figure 6.19. Speed profiles of the vehicle during the trip in three different zones: (a) highway, (b) semi-urban, and (c) urban areas.

In addition to vehicle speed, the amount of solar irradiance reaching the PV surfaces is significantly affected by environmental shading conditions, which vary across the route. Based on both a literature review and considering the conditions of the studied pathway, shading losses were incorporated into the model as fixed factors applied to the direct irradiance component (G_b) in each segment [52], [107], [114]. Specifically, shading was estimated at 20% for the highway segment (due to its open surroundings), 30% for the semi-urban area (featuring intermittent obstructions), and 40% for the dense urban zone (characterized by buildings, trees, and frequent overhead structures). It was assumed that the PV modules operate at their maximum power point (MPP). While partial shading can challenge MPP tracking, the assumed shading ratio implicitly accounts for these losses. Therefore, the analysis emphasizes peak output potential rather than complete electrical behaviour of the PV system, offering a simplified yet representative performance estimate [45], [114].

It should be noted that the same method as mentioned in Section 6.2 were used for this part. The PV module technology used in the simulations was crystalline silicon (c-Si). Detailed specifications and electrical parameters of this technology are provided in Table 6.6. Finally, Table 6.7 provides a breakdown of the total surface areas available on the vehicle for photovoltaic integration, along with the percentage of each surface that is effectively covered by PV modules.

Table 6.6. Specifications of the PV module [81].

PV Module	Efficiency (%)	k (%/°C)	U_0 ($W/m^2 \cdot °C$)	U_1 ($W/m^3 \cdot °C$)
c-Si	21.6	−0.47	30.02	6.28

Table 6.7. PV coverage and area for different surfaces of vehicle [114].

Surfaces	$A\ (m^2)$	α (%)
Top	33.20	60
Back	8.81	75
Right	44.1	40
Left	44.1	40

6.8. Results and Discussion

All results related to irradiance and PV module temperature variations presented in this study correspond to simulations conducted at noon local time. To assess the seasonal influence on the performance of the VIPV system, the analysis was performed for two representative dates throughout the year: 17 December and 30 July, corresponding to winter and summer conditions, respectively. The results of this analysis, illustrating the spatial and seasonal distribution of incident irradiance on each surface, are presented in Figure 6.20.

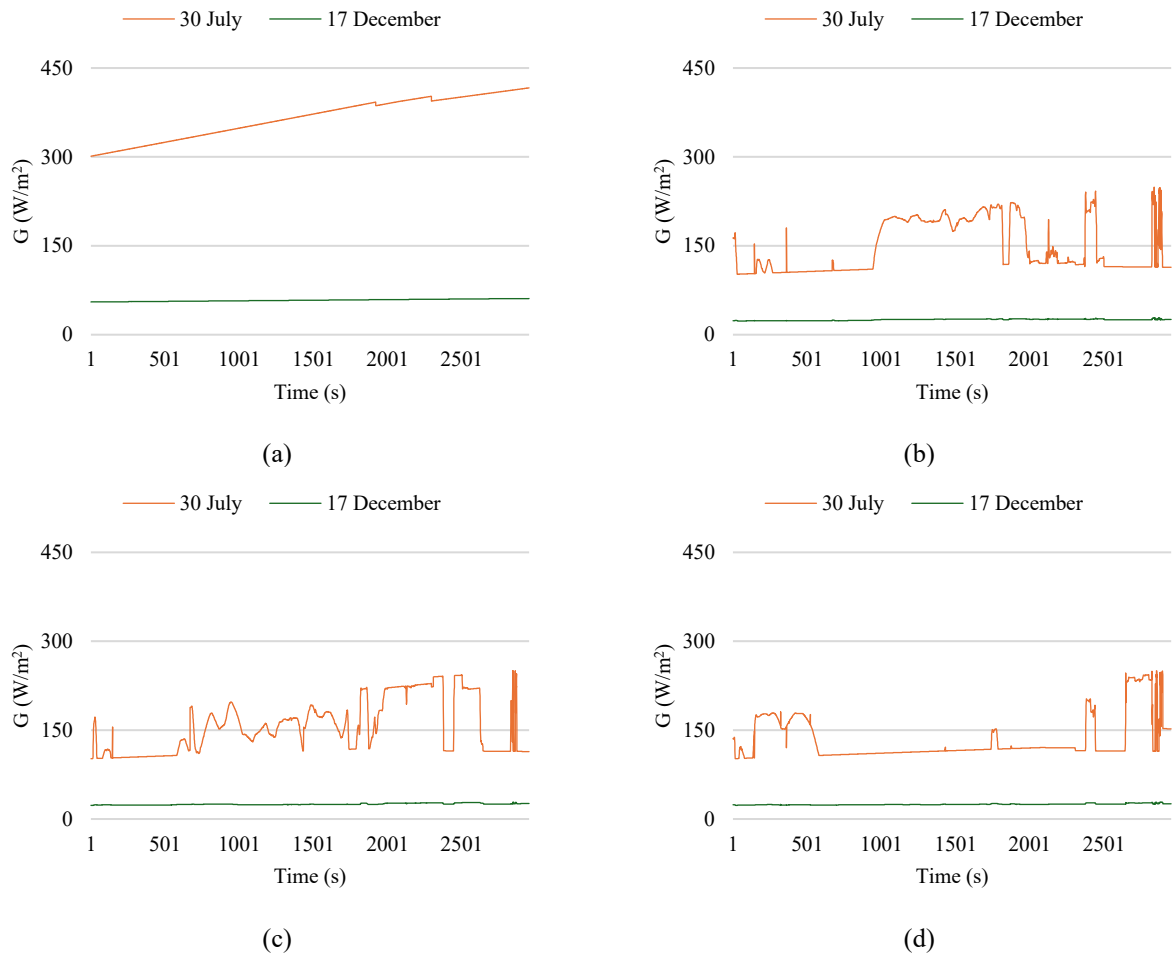

Figure 6.20. Variations in received irradiance on different surfaces of the vehicle at 12:00 for two representative days: (a) top, (b) back, (c) right, and (d) left surfaces.

Driving conditions and variations in vehicle orientation have a substantial influence on the irradiance received by PV modules integrated into different surfaces of the vehicle. This variation in irradiance directly affects the thermal behaviour of the modules, as higher irradiance increases heat input, while factors such as wind speed and vehicle motion contribute to convective cooling. The resulting module temperature profiles across different trip sections are presented in Figure 6.21. As expected, module temperatures were lowest in winter and highest in summer, reflecting seasonal irradiance and ambient conditions. Temperature fluctuations were more pronounced in the urban section due to frequent stops and reduced airflow, which limit convective cooling. Conversely, the highway segment showed more stable, lower temperatures due to sustained vehicle speed and better airflow.

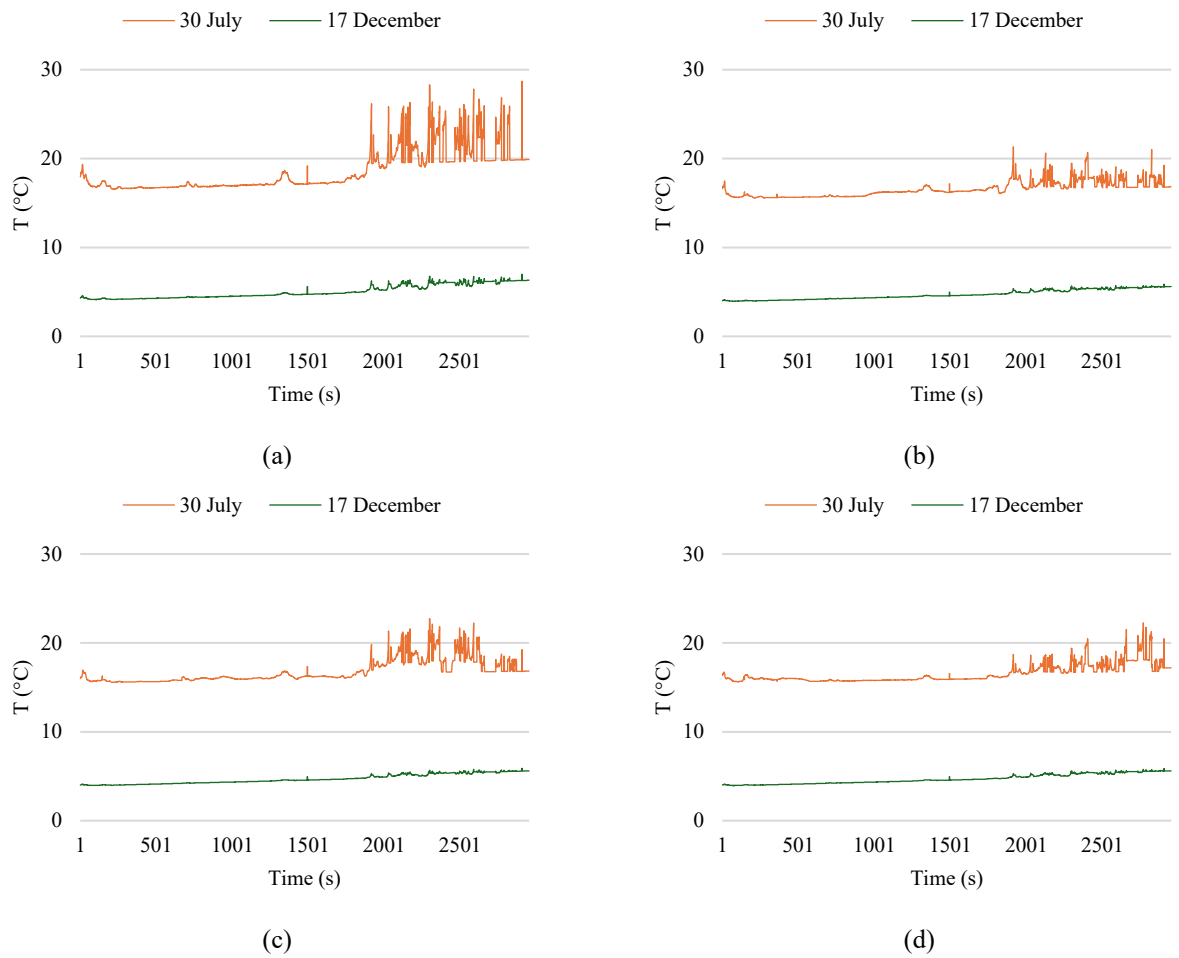

Figure 6.21. Temperature variations of PV modules integrated into different surfaces of the vehicle at 12:00 for two representative days: (a) top, (b) back, (c) right, and (d) left surfaces.

The shuttle route is operated frequently throughout the day. To simplify the analysis, it was assumed that while one bus travels from the airport to the city, another one travels in the reverse direction, allowing the trip from the airport to the city to be repeated once every hour. Although the actual number of trips may be higher depending on the fleet size and passenger demand, this, one-trip per hour, assumption was used as a baseline scenario. Using this framework, the variation in energy production from the VIPV system was analysed across different hours of the day, and for two representative months, July and December. The results of this analysis are illustrated in Figure 6.22.

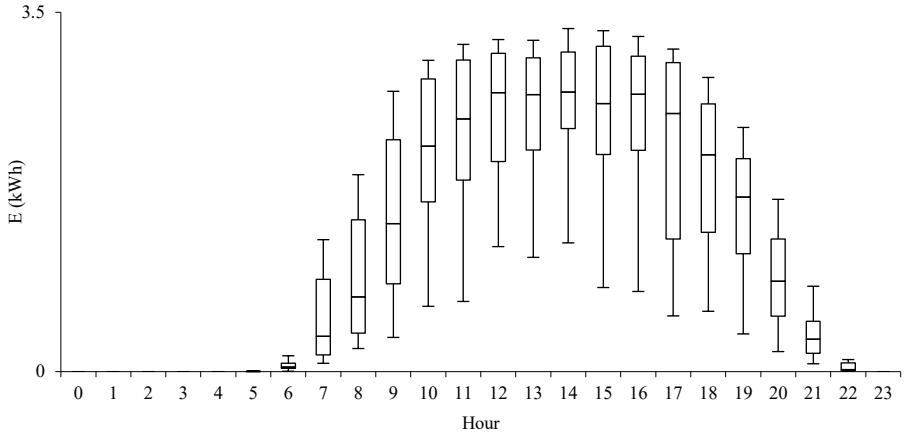

(a)

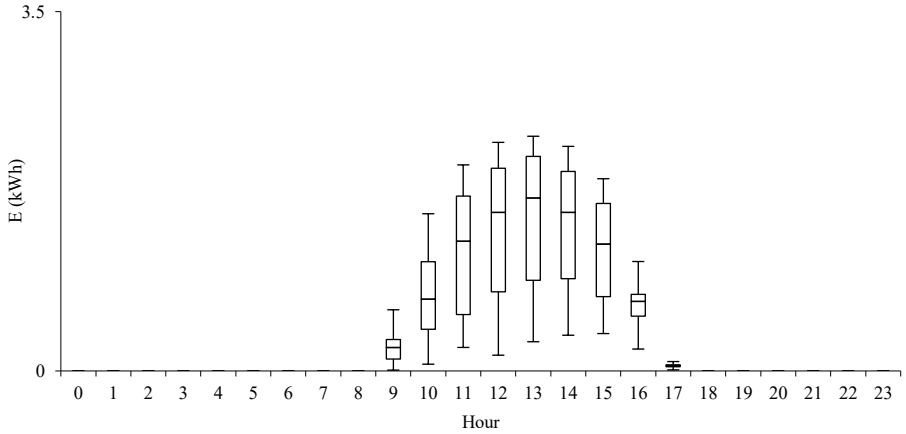

(b)

Figure 6.22. Variations in energy production during the trip from integrated PV modules in each hour on different surfaces of the vehicle in two different months: (a) July and (b) December.

As expected, energy production is higher during the summer due to increased solar irradiance and longer daylight hours. In July, the duration over which the VIPV system can generate power extends approximately from 5:00 to 22:00, while in December, it is limited to a shorter period, from around 9:00 to 17:00.

Under the same operational assumptions (the trip from the airport to the city to be repeated once every hour), the annual energy production of the VIPV system for each bus was also evaluated. The monthly energy yield from each surface of the bus is presented in Figure 6.23 The results reveal that the highest energy generation occurs during May, June, and July, which corresponds to periods of higher solar irradiance and longer daylight duration.

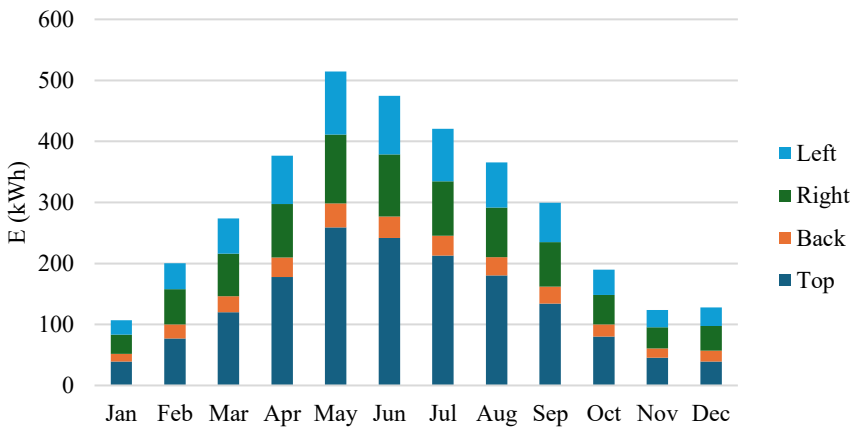

Figure 6.23. Monthly variations of total energy produced by integrated PV modules on different surfaces of a bus.

While the roof consistently provides the largest share of energy production, vertical surfaces such as the left and right sides make non-negligible contributions, especially in spring and summer when the sun is higher in the sky and the bus is exposed to varying orientations along the route. The back surface, although smaller in area, still adds incremental yield. This highlights the importance of considering all available surfaces in VIPV design, since their combined effect increases the overall production and reduces the variability linked to a single orientation.

Based on the calculated energy production and the defined operational scenario, the total energy generated by the VIPV system for each bus over a year is estimated to be approximately 3474 kWh. It is important to note that this value corresponds solely to the one-way trip from the airport to the city station (for a single bus), specifically from the highway entry point to the station.

If we consider the grid emission factor for Belgium, 0.110 kg CO_2/kWh [212], the avoided emissions from using solar energy instead of grid electricity would amount to approximately 382 kg CO_2/kWh. It is important to clarify that this figure reflects the gross avoided emissions, without accounting for emissions associated with the manufacturing and installation of the PV system itself.

In a separate scenario where the same VIPV configuration is applied to internal combustion engine (ICE) buses of similar size and surface area, the savings in fuel, emissions, and cost can also be estimated.

$$Emissions_{ICE} = E \cdot \frac{V_{Fuel} \cdot C_{Fuel}}{\eta_{Alt}} \tag{6.11}$$

For diesel fuel, the fuel-to-energy ratio (V_{Fuel}) was assumed to be 0.220 l/kWh, and the CO_2 emission factor (C_{Fuel}) was set at 2.6 kg CO_2/l [56]. Additionally, the average cost of diesel in Belgium was €1.68 per litre [201]. Considering the efficiency of the vehicle's alternator (η_{Alt}), assumed to be 67% [56], the total annual fuel savings resulting from the use of VIPV is approximately 1141 litres. This corresponds to an avoided emission of about 3 tons of CO_2 and a fuel cost saving of approximately €1916 per year.

These results highlight two key insights. First, the relative environmental and economic benefits of VIPV are significantly higher for ICE buses than for e-buses, given the higher carbon intensity and cost of diesel compared to grid electricity in Belgium. Second, the performance of VIPV systems in this context is shaped by the interplay of seasonal solar availability, bus orientation, and operational

patterns, underlining the value of simulation-based approaches that capture real driving data rather than relying on simplified assumptions.

6.9. Conclusions

This study modelled the real-time performance of VIPV on a shuttle bus route between Charleroi Airport and Brussels South Station, capturing how shading, vehicle orientation, and environmental conditions impact energy generation and thermal behaviour. The route's diverse segments, highway, semi-urban, and urban, exhibited significant differences in shading and speed, which in turn influenced irradiance levels and module temperatures across vehicle surfaces emphasizing the need to consider dynamic driving and environmental factors when evaluating VIPV systems. While limited to a single case study, the findings highlight the potential of VIPV in public transport and suggest the importance of further research across varying routes and conditions, including detailed economic and environmental analyses like LCOE and LCA.

7

Conclusions and Future Perspectives

Transportation plays a pivotal role in modern societies, yet it remains one of the most difficult sectors to decarbonise. While electrification has become the dominant pathway for reducing emissions, its large-scale implementation still depends on the availability of low-carbon electricity and widespread charging infrastructure. This dependency creates both technical and systemic challenges, particularly in contexts where the electricity grid is constrained or carbon-intensive. In this scenario, Vehicle-Integrated Photovoltaic (VIPV) technology offers a complementary route to clean mobility by generating renewable energy directly on-board vehicles. However, the real potential of VIPV has often been evaluated through simplified or isolated approaches, without a consistent framework under real operating conditions.

The main objective of this thesis was therefore to develop a comprehensive framework for modelling, analysing, and applying VIPV systems in realistic transport contexts. The research was structured to move progressively from general theoretical foundations to applied and data-driven case studies, ensuring that each phase contributed to the construction of an integrated and transferable methodology. The work began with a broad examination of the environmental context and technological background that motivate the study of VIPV. The first chapter established the significance of transport electrification within global and European decarbonisation strategies and introduced VIPV as an emerging option capable of supporting this transition. The subsequent analysis of fundamental parameters, including surface geometry, curvature, solar irradiance, module technology, and thermal behaviour, provided the physical basis needed to understand and simulate VIPV performance. Building on this foundation, the thesis developed a stepwise methodological structure designed to address the main limitations of existing approaches.

In the first stage, a generalised methodology was proposed to evaluate VIPV performance in conditions where real driving data are unavailable or unpredictable. This approach was particularly relevant for disaster and emergency scenarios, where VIPV-equipped vehicles can act as mobile power units during grid outages. The methodology focused on estimating achievable energy production based on solar resource availability, vehicle configuration, and simplified operational assumptions. Its flexibility allowed the assessment of different vehicle types and environmental conditions without requiring high-resolution inputs.

In the second stage, the work advanced toward a data-driven methodology capable of describing real-time VIPV behaviour under dynamic operation. Using real driving data collected through MATLAB Mobile, the model integrated vehicle speed, trajectory, and orientation with meteorological parameters to compute irradiance, module temperature, and energy yield every second. This methodology represented a substantial step forward, as it enabled the simulation of VIPV systems under realistic and time-resolved conditions. The resulting framework, implemented in MATLAB as VIPVLIB, combines optical, thermal, and electrical sub-models and can be adapted to different

vehicles and PV technologies. The next phase unified the two methodologies into a comprehensive and modular framework, applied to airport ground vehicles. This integration demonstrated that both simplified and data-driven approaches can coexist, providing complementary tools depending on data availability and modelling purpose.

Across all the applications, the framework proved capable of representing the strong interdependence between environmental, geometric, and operational variables that characterise VIPV systems. It was shown that irradiance distribution and thermal behaviour are highly context-dependent, influenced by surface orientation, shading, and driving patterns. The integration of thermal models based on Faiman's formulation, adapted for mobile conditions, improved the estimation of temperature and power output by accounting for convective cooling during motion and the inertia of the module. These features significantly enhanced the realism of performance predictions compared to traditional steady-state approaches.

The research also confirmed that the energy yield of VIPV systems is determined not only by the efficiency of the PV technology but by the combination of design, geometry, and operation. Roof-mounted modules generally remain the most productive, but curved and vertical panels can contribute substantially, especially in diffuse or low-sun conditions typical of winter and dense urban areas. This multidimensional interaction between motion, orientation, and irradiance highlights the necessity of an integrated model chain. Beyond the technical findings, the thesis demonstrated that the developed framework is transferable and scalable. It can be applied to both small and large vehicles, stationary or moving, individual units or fleets. The modularity of the approach allows new sub-models or datasets to be introduced without altering the overall structure, ensuring its applicability to future research and industrial design. This scalability also provides a bridge between research and policy, supporting the evaluation of VIPV as part of broader transport electrification strategies.

Another central contribution of this thesis lies in the way it connects methodological innovation with real-world application. Rather than presenting isolated models, the work proposed a coherent process for moving from conceptual analysis to operational validation. The stepwise logic, starting from a general approach, evolving into a data-driven method, and finally merging them into a complete framework, provides a structured pathway that future researchers can replicate and extend. This process not only enhances the technical credibility of VIPV simulations but also establishes a reference for comparing results across studies and contexts. The outcomes of the thesis also have strategic implications. By demonstrating that part of the energy demand of vehicles can be met directly through integrated photovoltaics, the research highlights VIPV as a complementary solution to reduce grid dependence and energy costs in electric mobility. For public transport systems and institutional fleets, VIPV can lower operational emissions and support the transition to sustainable urban transport. For critical services and disaster-response operations, it can provide autonomous, renewable power under emergency conditions. In all these contexts, the technology contributes not only to decarbonisation but also to energy resilience and flexibility, two emerging priorities in the sustainable mobility landscape.

To consolidate and compare the outcomes of the different VIPV applications investigated in this thesis, Table 7.1 summarises the main performance indicators obtained across all case studies. The table includes results derived from both generalised and data-driven modelling approaches and reports key technical, environmental, and economic metrics, such as energy yield, equivalent solar driving range, avoided CO_2 emissions, and indicative cost indicators where available. By presenting these results in a unified format, the table highlights how VIPV performance varies with vehicle type

and operational context, and provides a concise quantitative synthesis supporting the broader conclusions of this work.

Table 7.1. Summary of VIPV performance indicators across all case studies, including energy yield, equivalent solar driving range, avoided CO_2 emissions, and indicative economic metrics, derived using generalised and data-driven modelling approaches.

Application (Scenario)	Case Study	Max. Energy yield	Solar Range (km)	Saved Emissions (Ton CO_2)	Max. System Cost (€/Wp)
Disasters (Generalised Approach)	Ambulance	1.9 (MWh/Year)	3235	0.49	-
	Truck	9.5 (MWh/Year)	7633	2.48	-
	Container	67.1 (kWh/Day)	-	-	-
	Mobile operating room	155.8 (kWh/Day)	-	-	-
Campus (Data-Driven approach)	Minibus	4.3 (MWh/Year)	-	ICE: 3.5 / EV: 2	-
Airport (Generalised Approach)	Bus	6.6 (MWh/Year)	5500	2.5	1.2
	Minibus	2.1 (MWh/Year)	5000	0.8	1.1
	Luggage Truck	0.7 (MWh/Year)	6180	0.3	0.9
Public Transportation (Data-Driven approach)	Tram	10.6 (MWh/Year)	-	3.3	2.6
	Bus	10.9 (MWh/Year)	-	3.4	LCOE (€): 0.25
	Airport Shuttle Bus	3.5 (MWh/Year)	-	3	Saved Fuel (l): 1141

Energy yields are reported on either an annual or daily basis depending on the application and obtained results, particularly for emergency and mobile power scenarios. The equivalent solar range represents the distance that can be covered using energy generated by the VIPV system, based on vehicle-specific energy consumption assumptions. Avoided CO_2 emissions are calculated by comparison with conventional grid electricity or fuel-based operation, depending on the scenario. Economic indicators are reported in different forms (system cost per installed watt, levelized cost of electricity, or equivalent saved fuel) according to the scope and objectives of each case study.

While the developed framework and findings mark significant progress, the research also revealed areas for further investigation. The modelling could be refined through more detailed geometric and optical representations, including ray-tracing to capture complex shading and reflection effects. Integration with advanced thermal–fluid models or computational fluid dynamics (CFD) would improve the accuracy of temperature estimation under variable wind and motion conditions. Future studies should also explore the inclusion of battery behaviour, vehicle energy management, and fleet-level optimisation, enabling a more comprehensive assessment of system-level impacts. Moreover, the combination of VIPV with Vehicle-to-Grid (V2G) strategies could open new opportunities for flexible, decentralised energy systems in which vehicles actively support grid stability and renewable integration.

In conclusion, this thesis contributes both a conceptual and methodological advancement in the study of Vehicle-Integrated Photovoltaics. It establishes a clear process for analysing VIPV performance, bridging theoretical understanding with empirical application. The developed framework, flexible, data-oriented, and multidisciplinary, offers a solid foundation for future research, industrial design, and policy evaluation. Ultimately, the findings confirm that vehicles can evolve from passive consumers of energy into active producers within the renewable ecosystem. VIPV is not merely an experimental concept but a realistic component of future transport systems, capable of supporting the broader transition toward decentralised, low-carbon mobility.

Appendix A. Outlook on Advanced Shading Modelling and Experimental Integration

As discussed throughout the thesis, one of the potential extensions of the proposed data-driven approach is the development of more advanced and realistic shading models. These models can integrate detailed geometric and environmental information derived from digital elevation model (DEM), building heights, vegetation, and other surface features [54], [57], [106]. By integrating these datasets, the model can reproduce more realistic shading conditions, allowing for a refined estimation of irradiance losses for both the direct and diffuse components.

A.1. Shading Losses

As illustrated in Figure A.1, for an infinitely long canyon with width W and an effective building height H, the obstruction angle experienced by a point within the canyon varies with both its horizontal position (middle or edge of the street) and the azimuthal orientation of the incident solar rays, denoted by γ [113].

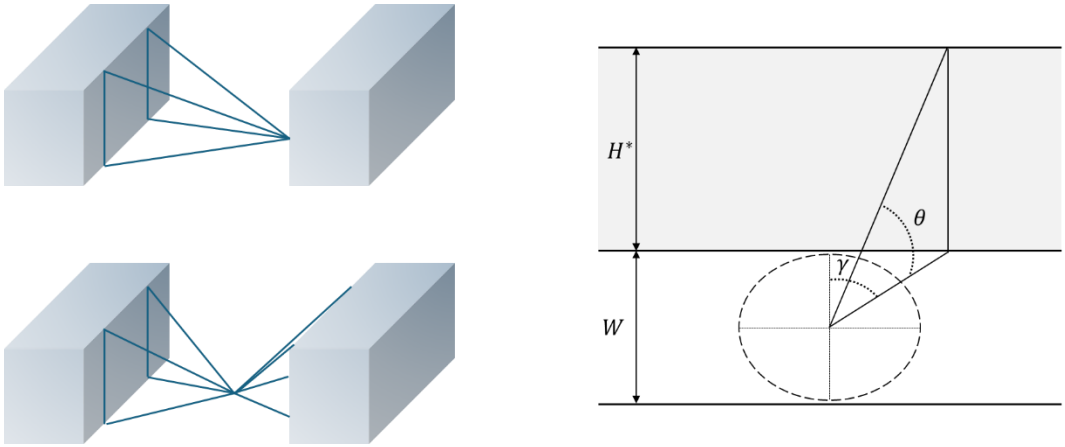

Figure A.1. Schematic diagram of obstruction angle for two positions along the street (left top: middle; left bottom: near edge) and angle definitions [113].

The obstruction angles for the middle of the street (θ_m) or the edge of the street (θ_e) can be calculated as follows [113]:

$$\theta_m = \tan^{-1}\frac{H}{W/2\ \sqrt{1+\tan^2\gamma}} \quad \text{(A.1)}$$

$$\theta_e = \tan^{-1}\frac{H}{W\ \sqrt{1+\tan^2\gamma}}\ when\ \gamma \in \left[-\frac{\pi}{2},\frac{\pi}{2}\right]\ and\ \frac{\pi}{2}\ elsewhere \quad \text{(A.2)}$$

When diffuse solar irradiation is considered isotropic, it depends solely on the Sky View Factor (SVF), the fraction of the visible sky. Consequently, it becomes independent of the sun's position and therefore of parameters such as latitude, seasonal declination, or the orientation of the surrounding urban geometry. The resulting diffuse irradiation loss can be estimated using the SVF (for a vehicle roof assumed flat and horizontal), defined as [213]:

$$Loss\ [\%] = 1 - SVF = 1 - \frac{1}{2\pi}\int_{-\pi}^{\pi}\cos^2\bar{\theta}\,d\gamma = 1 - \cos^2\bar{\theta} \quad \text{(A.3)}$$

For direct irradiation (Figure A.2), the beam component is considered blocked whenever the solar elevation angle (θ_2) is lower than the local obstruction angle (θ_1) [106].

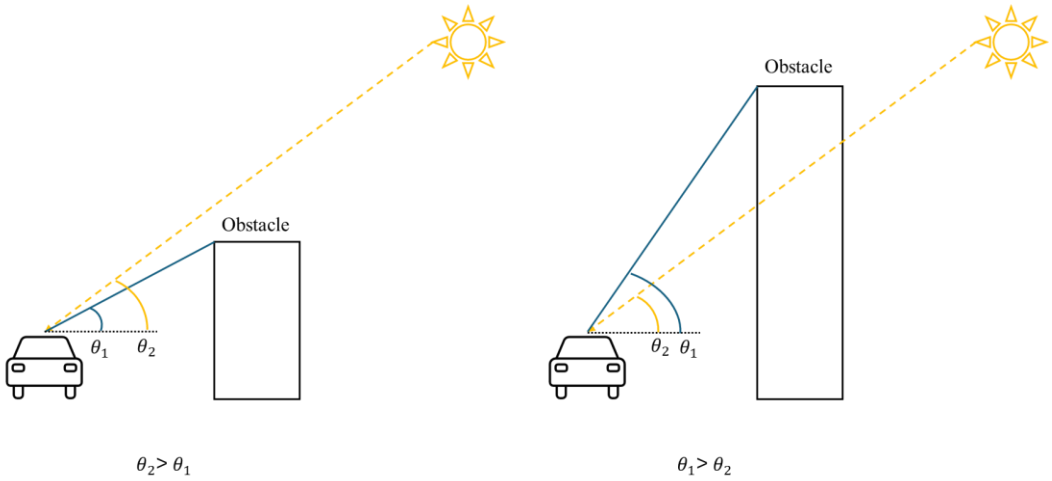

Figure A.2. Illustration of obstacle shadows caused by the relative difference between the solar elevation angle (θ_2) and the obstruction angle (θ_1): (a) Measuring point shaded ($\theta_1 > \theta_2$); (b) Measuring point unshaded ($\theta_1 < \theta_2$) [106].

A.1.1. Preliminary Shading Analysis for the UNIPA Campus Area

In this context, an initial demonstration was performed for a representative area of the University of Palermo campus (Viale delle Scienze). The geometric data, including building heights and coordinates, were obtained from available datasets provided by the University, and the ground elevation was extracted from DEM sources. The domain was discretized into 3×3 m grid cells, and for a single trip, the obstruction angles and sky view factors were computed following the methodology proposed by Kim et al. [106], which were adapted and implemented within the VIPVLIB framework. This allowed the model to determine the spatial distribution of shading losses along the travelled path. Vegetation and small-scale obstacles (e.g., trees, light poles) were not included in this preliminary analysis; however, their integration is feasible in the next step.

Figure A.3. Study area at the University of Palermo campus (Viale delle Scienze). (Source: Google Earth)

To illustrate the procedure, the PVGIS Typical Meteorological Year (TMY) dataset [112] was used as the irradiance input. The corresponding results (Figure A.4) are therefore presented only as a demonstration of the modelling workflow, rather than as actual measured data. To accurately represent real conditions, real-time geographical and irradiance datasets are required. In the next phase, the model has to be integrated with measured irradiance and meteorological data obtained from the fixed monitoring systems installed within the UNIPA campus.

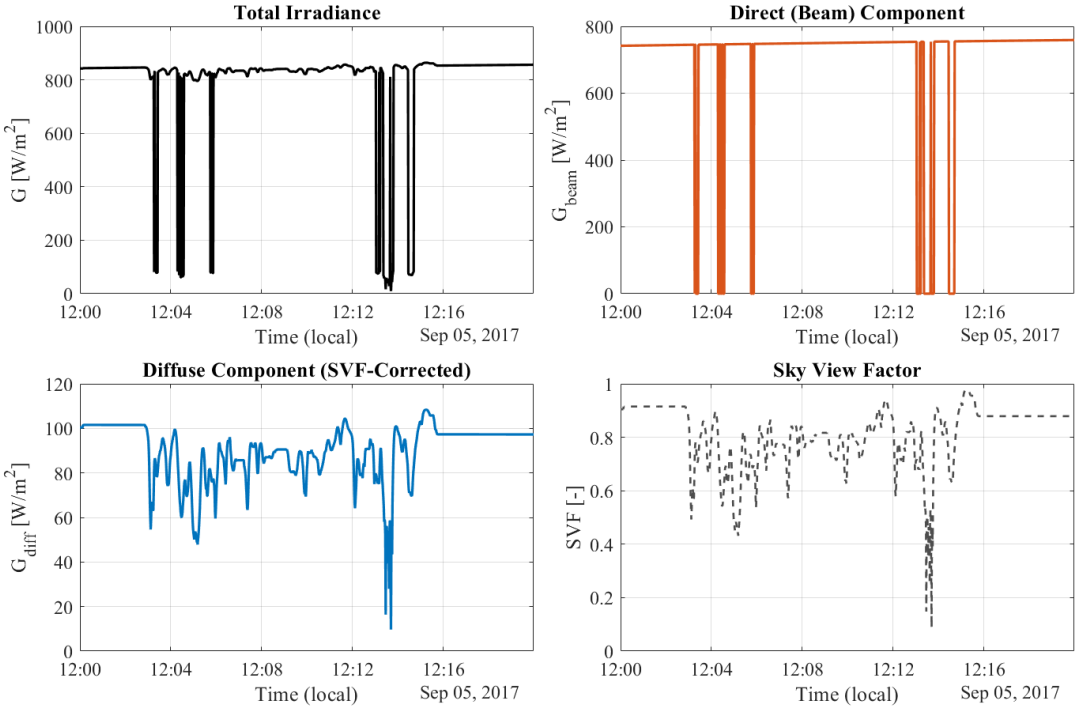

Figure A.4. Time series of total, beam, diffuse irradiance, and Sky View Factor during a representative simulated trip on 5 September at 12:00 local time.

A.2. Experimental Setup for Possible Next Validation

As a complementary effort, a prototype experimental setup was assembled to measure the actual irradiance received on a vehicle rooftop during motion.

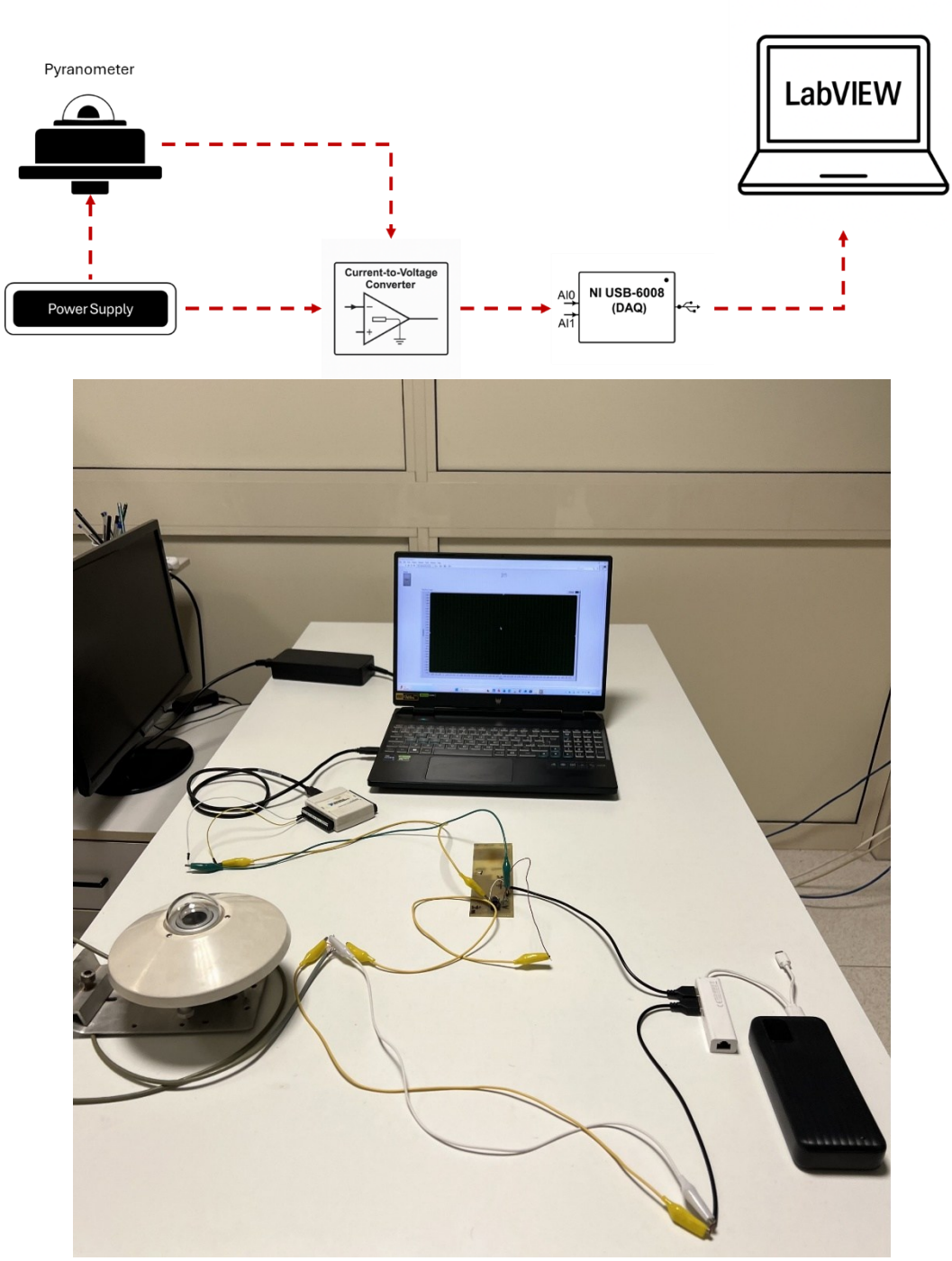

Figure A.5. Schematic diagram of the experimental setup and its corresponding laboratory photo.

The system (Figure A.5) consists of:

- a pyranometer mounted horizontally on the vehicle rooftop,
- a current-to-voltage converter interfaced with an NI USB-6008 data acquisition unit,
- and a laptop running LabVIEW for continuous monitoring and logging of the pyranometer output.

The devices powered by a DC supply, ensuring stable operation and consistent data acquisition during the trip. The setup was assembled and tested within the UNIPA campus, confirming full data acquisition capability; however, the complete measurement campaign could not be conducted due to time constraints. Nevertheless, these developments represent an essential preparatory step toward the future improvement of the proposed modelling framework under real operating conditions. The collected data and the established methodology will serve as a foundation for further refinement of the current approach and as an initial step toward more detailed experiments and studies aimed at assessing the effects of partial shading on the irradiance, temperature, and energy performance of VIPV systems.

Acknowledgement

This work was financed by the European Union—NextGenerationEU (National Sustainable Mobility Center CN00000023, Italian Ministry of University and Research Decree n. 1033—17/06/2022, Spoke 12).

Dr. Silvia Licciardi were supported by the following project: “Network 4 Energy Sustainable Transition—NEST”, code PE0000021, CUP B73C22001280006, Spoke 7, funded under the National Recovery and Resilience Plan (NRRP), Mission 4, by the European Union—NextGenerationEU.

This work was also funded by the Portuguese Fundação para a Ciência e a Tecnologia (FCT) I.P./MCTES through national funds (PIDDAC) – UIDB/50019/2020 (https://doi.org/10.54499/UIDB/50019/2020), UIDP/50019/2020 (https://doi.org/10.54499/UIDP/50019/2020), LA/P/0068/2020 (https://doi.org/10.54499/LA/P/0068/2020), and IDL research grant UI/BD/151496/2021.

List of Publications

Journal Papers

- **Hamid Samadi**, Guido Ala, Valerio Lo Brano, Pietro Romano, and Fabio Viola. "Investigation of effective factors on vehicles integrated photovoltaic (VIPV) performance: a review" World Electric Vehicle Journal 14, no. 6 (2023): 154. (https://doi.org/10.3390/wevj14060154)
- **Hamid Samadi**, Guido Ala, Antonino Imburgia, Silvia Licciardi, Pietro Romano, and Fabio Viola. "Evaluating the Role of Vehicle-Integrated Photovoltaic (VIPV) Systems in a Disaster Context" World Electric Vehicle Journal 16, no. 4 (2025): 190. (https://doi.org/10.3390/wevj16040190)
- **Hamid Samadi**, Guido Ala, Miguel Centeno Brito, Giulia Marcon, Pietro Romano, and Fabio Viola. "Vehicle-Integrated Photovoltaic (VIPV) for Sustainable Airports: A Flexible Framework for Performance Assessment" Sustainability 17, no. 20 (2025): 9246. (https://doi.org/10.3390/su17209246)
- **Hamid Samadi**, Guido Ala, Miguel Centeno Brito, Marzia Traverso, Silvia Licciardi, Pietro Romano, and Fabio Viola. "A Novel Model Chain for Analysing the Performance of Vehicle-Integrated Photovoltaic (VIPV) Systems" 16, no. 11 (2025): 619. (https://doi.org/10.3390/wevj16110619)
- Silvia Licciardi, Maurizio La Villetta, Guido Ala, Elisa Francomano, Pietro Catrini, Rossano Musca, Antonio Piacentino, Eleonora Riva Sanseverino, and **Hamid Samadi**. "LSTM-Based Classification of Building Energy Profiles Across Multiple Cities" (**Under Review - IEEE TRANSACTIONS ON INDUSTRY APPLICATIONS**)

Conferences

- **Hamid Samadi**, Guido Ala, Valerio Lo Brano, Pietro Romano, Fabio Viola, and Rosario Miceli. "Potential and Methods of Integrating Solar Cells into Vehicles" In 2023 International Conference on Clean Electrical Power (ICCEP), pp. 715-720. IEEE, 2023. (**Terrasini, Italy, 27-29 June 2023**) (https://doi.org/10.1109/ICCEP57914.2023.10247366)

- Guido Ala, Pietro Catrini, Mariano G. Ippolito, Maurizio La Villetta, Silvia Licciardi, Rossano Musca, Antonio Piacentino, Eleonora Riva Sanseverino, and **Hamid Samadi**. "Deep Learning for Smart Grid and Energy Context" In 2023 Asia Meeting on Environment and Electrical Engineering (EEE-AM), pp. 1-6. IEEE, 2023. (**Hanoi, Vietnam, 13-15 November 2023**) (https://doi.org/10.1109/EEE-AM58328.2023.10447021)

- Silvia Licciardi, Guido Ala, Elisa Francomano, Pietro Catrini, Maurizio La Villetta, Rossano Musca, Antonio Piacentino, Eleonora Riva Sanseverino, and **Hamid Samadi**. "Long Short Term Memory Neural Network and Energy Applications in the Smart Grid Framework" In 2024 IEEE 8th Forum on Research and Technologies for Society and Industry Innovation (RTSI), pp. 36-41. IEEE, 2024. (**Milano, Italy, 18-20 September 2024**) (https://doi.org/10.1109/RTSI61910.2024.10761755)

- **Hamid Samadi**, Guido Ala, Antonino Imburgia, Silvia Licciardi, Pietro Romano, and Fabio Viola. " The Potential of Integrating Solar Cells into Practical Vehicles During Disasters " (**Poster**) In 2024 Rete Italiana del Fotovoltaico per la ricerca, lo sviluppo e l'innovazione (Rete IFV). (**Bolzano, Italy, 11-12 June 2024**)

- **Hamid Samadi**, Guido Ala, Miguel Centeno Brito, Silvia Licciardi, Pietro Romano, and Fabio Viola. "A New Path to Airport Sustainability: Exploring the Technical and Economic Viability of VIPV Systems" **Presented**: 2025 IEEE 6th International Conference on Clean and Green Energy Engineering (CGEE). (**Zagreb, Croatia, 23-25 August 2025**)

- **Hamid Samadi**, Guido Ala, Miguel Centeno Brito, Marchelo Marchese, Silvia Licciardi, Pietro Romano, and Fabio Viola. "Solar Mobility for Urban Transit: Performance and Feasibility of VIPV in Bus Fleets" **Presented**: 2025 IEEE 66th International Scientific Conference on Power and Electrical Engineering of Riga Technical University (RTUCON). (**Riga, Latvia, 23-25 October 2025**)

- **Hamid Samadi**, Guido Ala, Miguel Centeno Brito, Silvia Licciardi, Pietro Romano, and Fabio Viola. "Driving Toward Sustainability: Evaluating Solar Assisted Shuttle Buses" **Presented**: 2025 IEEE 66th International Scientific Conference on Power and Electrical Engineering of Riga Technical University (RTUCON). (**Riga, Latvia, 23-25 October 2025**)

- **Hamid Samadi**, Guido Ala, Miguel Centeno Brito, Silvia Licciardi, Pietro Romano, and Fabio Viola. "Energy Production and Emission Reduction Potential of VIPV Systems for Urban Trams" **Presented**: 2025 IEEE 66th International Scientific Conference on Power and Electrical Engineering of Riga Technical University (RTUCON). (**Riga, Latvia, 23-25 October 2025**)

References

[1] "World Health Organization. Ambient (outdoor) air quality and health. Accessed: Oct. 17, 2025. [Online]. Available: https://www.who.int/news-room/fact-sheets/detail/ambient-(outdoor)-air-quality-and-health".

[2] Y. Bakkar, E. Bark, G. Prause, and S. Ul-Durar, "Green Deal and financing sustainable transport in Europe: A target costing analysis," *Transp Policy (Oxf)*, vol. 163, pp. 185–198, Mar. 2025, doi: 10.1016/j.tranpol.2025.01.014.

[3] "IEA. Global CO_2 emissions by sector, 2019-2022. Paris: IEA; 2023. Licence: CC BY 4.0. Accessed: Oct. 17, 2025. [Online]. Available: https://www.iea.org/data-and-statistics/charts/global-co2-emissions-by-sector-2019-2022".

[4] "IEA. Global CO_2 emissions from transport by sub-sector in the Net Zero Scenario, 2000-2030. Paris: IEA; 2023. Licence: CC BY 4.0. Accessed: Oct. 17, 2025. [Online]. Available: https://www.iea.org/data-and-statistics/charts/global-co2-emissions-from-transport-by-sub-sector-in-the-net-zero-scenario-2000-2030-2".

[5] "Eurostat. Greenhouse gas emissions by source sector, EU — change from 1990 to 2022 (million tonnes of CO_2 equivalent & % change). Accessed: Oct. 17, 2025. [Online]. Available: https://ec.europa.eu/eurostat/statistics-explained/index.php?title=File:Greenhouse_gas_emissions_by_source_sector,_EU,_change_from_1990_to_2022_(million_tonnes_of_CO2_equivalent_and_%25_change)_rev.png".

[6] "IEA. Energy consumption in transport by fuel in the Net Zero Scenario, 1975-2030. Paris: IEA; 2023. Licence: CC BY 4.0. Accessed: Oct. 17, 2025. [Online]. Available: https://www.iea.org/data-and-statistics/charts/energy-consumption-in-transport-by-fuel-in-the-net-zero-scenario-1975-2030".

[7] "European Environment Agency. Premature deaths in the EU-27 due to $PM_{2.5}$ levels above the 2021 WHO guidelines and distance to the zero pollution target, 2005-2020. Accessed: Oct. 17, 2025. [Online]. Available: https://www.eea.europa.eu/en/analysis/maps-and-charts/premature-deaths-in-the-eu-1".

[8] Y. Bakkar, E. Bark, G. Prause, and S. Ul-Durar, "Green Deal and financing sustainable transport in Europe: A target costing analysis," *Transp Policy (Oxf)*, vol. 163, pp. 185–198, Mar. 2025, doi: 10.1016/j.tranpol.2025.01.014.

[9] H. G. Herzog, R. F. Calili, and M. F. Ludovico de Almeida, "Assessing the decarbonisation potential of light-duty vehicle fleet electrification in Brazil," *Transp Res D Transp Environ*, vol. 146, p. 104895, Sep. 2025, doi: 10.1016/j.trd.2025.104895.

[10] "IEA. Global electric car sales, 2014-2024. Paris: IEA; 2025. Licence: CC BY 4.0. Accessed: Oct. 17, 2025. [Online]. Available: https://www.iea.org/data-and-statistics/charts/global-electric-car-sales-2014-2024".

[11] "IEA. Global stock of public charging points by region, 2018-2024. Paris: IEA; 2025. Licence: CC BY 4.0. Accessed: Oct. 17, 2025. [Online]. Available: https://www.iea.org/data-and-statistics/charts/global-stock-of-public-charging-points-by-region-2018-2024".

[12] "IEA. Global stock of public charging points by speed, 2018-2024. Paris: IEA; 2025. Licence: CC BY 4.0. Accessed: Oct. 17, 2025. [Online]. Available: https://www.iea.org/data-and-statistics/charts/global-stock-of-public-charging-points-by-speed-2018-2024".

[13] "IEA. Battery electric car price premium compared to internal combustion engine cars, 2018-2023. Paris: IEA; 2024. Licence: CC BY 4.0. Accessed: Oct. 17, 2025. [Online]. Available: https://www.iea.org/data-and-statistics/charts/battery-electric-car-price-premium-compared-to-internal-combustion-engine-cars-2018-2023".

[14] “IEA. Type and location of public charging in selected regions and countries and the share of population living within 1 kilometre of a charger, 2024. Paris: IEA; 2025. Licence: CC BY 4.0. Accessed: Oct. 17, 2025. [Online]. Available: https://www.iea.org/data-and-statistics/charts/type-and-location-of-public-charging-in-selected-regions-and-countries-and-the-share-of-population-living-within-1-kilometre-of-a-charger-2024”.

[15] R. R. Timilsina, J. Zhang, D. B. Rahut, K. Patradool, and T. Sonobe, “Global drive toward net-zero emissions and sustainability via electric vehicles: an integrative critical review,” *Energy Ecol Environ*, vol. 10, no. 2, pp. 125–144, Apr. 2025, doi: 10.1007/s40974-024-00351-7.

[16] M. M. Taamneh and H. Y. Makahleh, “The prospects of adopting electric vehicles in urban contexts: A systematic review of literature,” *Transp Res Interdiscip Perspect*, vol. 31, p. 101420, May 2025, doi: 10.1016/j.trip.2025.101420.

[17] A. K. Tripathi *et al.*, “Integration of Solar PV Panels in Electric Vehicle Charging Infrastructure: Benefits, Challenges, and Environmental Implications,” *Energy Sci Eng*, vol. 13, no. 4, pp. 2135–2152, Apr. 2025, doi: 10.1002/ese3.70014.

[18] S. Aggarwal and A. K. Singh, “Electric vehicles the future of transportation sector: a review,” *Energy Sources, Part A: Recovery, Utilization, and Environmental Effects*, vol. 47, no. 1, pp. 11126–11146, Jun. 2025, doi: 10.1080/15567036.2021.1976322.

[19] G. Ramkumar, S. Kannan, V. Mohanavel, S. Karthikeyan, and A. Titus, “The future of green mobility: A review exploring renewable energy systems integration in electric vehicles,” *Results in Engineering*, vol. 27, p. 105647, Sep. 2025, doi: 10.1016/j.rineng.2025.105647.

[20] T. Tayagaki, K. Yamagoe, M. Komori, and M. Yoshita, “Measurement of current–voltage characteristics of curved photovoltaic modules for vehicle integration,” *Solar Energy Materials and Solar Cells*, vol. 290, p. 113699, Sep. 2025, doi: 10.1016/j.solmat.2025.113699.

[21] O. J. Oluwalana and K. Grzesik, “Solar-Powered Electric Vehicles: Comprehensive Review of Technology Advancements, Challenges, and Future Prospects,” *Energies (Basel)*, vol. 18, no. 14, p. 3650, Jul. 2025, doi: 10.3390/en18143650.

[22] L. Fauzan, Y. H. Sim, M. J. Yun, H. Choi, D. Y. Lee, and S. I. Cha, “Power from shaded photovoltaic modules through bypass-diode-assisted small-area high-voltage structures,” *Renewable and Sustainable Energy Reviews*, vol. 208, p. 115047, Feb. 2025, doi: 10.1016/j.rser.2024.115047.

[23] K. Araki, S. Matsushita, Y. Ota, S. Iwasaki, Y. Hosokawa, and K. Nishioka, “Rating vehicle-integrated photovoltaics: power and energy loss by curved surface,” *Solar Energy Materials and Solar Cells*, vol. 292, p. 113814, Oct. 2025, doi: 10.1016/j.solmat.2025.113814.

[24] M. E. Başoğlu, “Performance assessment of solar-powered electric vehicles: Importance of maximum power point tracking, range enhancement and charging frequency analysis under various operating and irradiance conditions,” *J Power Sources*, vol. 652, p. 237570, Oct. 2025, doi: 10.1016/j.jpowsour.2025.237570.

[25] B. Luo, S. Gallas, C. Micallef, J. Govaerts, K. Gryllias, and J. Poortmans, “Experimental and finite element modal analysis of photovoltaic modules for the design of next-generation vehicle-integrated PV applications,” *Solar Energy Materials and Solar Cells*, vol. 290, p. 113683, Sep. 2025, doi: 10.1016/j.solmat.2025.113683.

[26] M. Ben Said-Romdhane and S. Skander-Mustapha, “A Review on Vehicle-Integrated Photovoltaic Panels,” 2021, pp. 349–370. doi: 10.1007/978-3-030-64565-6_12.

[27] L. Zhang, F. Luo, and T. H. Rashidi, “Routing of Photovoltaic Integrated Solid Waste Collection Vehicles,” in *2025 IEEE International Conference on Mechatronics (ICM)*, IEEE, Feb. 2025, pp. 1–6. doi: 10.1109/ICM62621.2025.10934828.

[28] K. Araki, Y. Ota, A. Maeda, M. Kumano, and K. Nishioka, “Solar Electric Vehicles as Energy Sources in Disaster Zones: Physical and Social Factors,” *Energies (Basel)*, vol. 16, no. 8, p. 3580, Apr. 2023, doi: 10.3390/en16083580.

[29] H. Samadi, G. Ala, A. Imburgia, S. Licciardi, P. Romano, and F. Viola, “Evaluating the Role of Vehicle-Integrated Photovoltaic (VIPV) Systems in a Disaster Context,” *World Electric Vehicle Journal*, vol. 16, no. 4, p. 190, Mar. 2025, doi: 10.3390/wevj16040190.

[30] J. Bin Jahangir and M. A. Alam, “Urban informatics meets PV physics: The need for spatio-temporal data for global validation of city-aware vehicle-integrated PV models,” in *2025 IEEE 53rd Photovoltaic Specialists Conference (PVSC)*, IEEE, Jun. 2025, pp. 1407–1409. doi: 10.1109/PVSC59419.2025.11133254.

[31] N. R. Pochont and R. Sekhar Y, “Recent trends in photovoltaic technologies for sustainable transportation in passenger vehicles – A review,” *Renewable and Sustainable Energy Reviews*, vol. 181, p. 113317, Jul. 2023, doi: 10.1016/j.rser.2023.113317.

[32] H. Yavasoglu, B. Shani, A. Hasnain, B. Parlak, and A. Khaligh, “Analysis and System Design Optimization of PV Panel and Auxiliary Battery Integration for VIPV Electric Vehicles,” *IEEE Transactions on Transportation Electrification*, pp. 1–1, 2025, doi: 10.1109/TTE.2025.3600891.

[33] A. Meneghetti, F. Dal Magro, and A. Romagnoli, “Renewable energy penetration in food delivery: Coupling photovoltaics with transport refrigerated units,” *Energy*, vol. 232, p. 120994, Oct. 2021, doi: 10.1016/j.energy.2021.120994.

[34] S. Rodríguez-Romero *et al.*, “Analysis of Advanced Non-Isolated Topologies for Vehicle-Integrated Photovoltaic (ViPV) Systems in Urban Electric Transport Buses,” in *2025 IEEE 53rd Photovoltaic Specialists Conference (PVSC)*, IEEE, Jun. 2025, pp. 0492–0498. doi: 10.1109/PVSC59419.2025.11132502.

[35] B. Commault, T. Duigou, V. Maneval, J. Gaume, F. Chabuel, and E. Voroshazi, “Overview and Perspectives for Vehicle-Integrated Photovoltaics,” *Applied Sciences*, vol. 11, no. 24, p. 11598, Dec. 2021, doi: 10.3390/app112411598.

[36] L. E. Alanis *et al.*, “Thermal effect of VIPV modules in refrigerated trucks,” *Solar Energy Materials and Solar Cells*, vol. 275, p. 113000, Sep. 2024, doi: 10.1016/j.solmat.2024.113000.

[37] H. Samadi, G. Ala, V. Lo Brano, P. Romano, F. Viola, and R. Miceli, “Potential and Methods of Integrating Solar Cells into Vehicles,” in *2023 International Conference on Clean Electrical Power (ICCEP)*, IEEE, Jun. 2023, pp. 715–720. doi: 10.1109/ICCEP57914.2023.10247366.

[38] F. Martín *et al.*, “Relative angular response characterization in VIPV,” *Solar Energy Materials and Solar Cells*, vol. 276, p. 113063, Oct. 2024, doi: 10.1016/j.solmat.2024.113063.

[39] Y. Ota, T. Masuda, K. Araki, and M. Yamaguchi, “Curve-Correction Factor for Characterization of the Output of a Three-Dimensional Curved Photovoltaic Module on a Car Roof,” *Coatings*, vol. 8, no. 12, p. 432, Nov. 2018, doi: 10.3390/coatings8120432.

[40] M. A. Schüler *et al.*, “Towards fiber-reinforced front-sheets for lightweight PV modules in VIPV,” *Solar Energy Materials and Solar Cells*, vol. 277, p. 113048, Oct. 2024, doi: 10.1016/j.solmat.2024.113048.

[41] A. J. Carr *et al.*, “Solar Moves: Part 1, Modelling the impact of VIPV,” *Solar Energy Materials and Solar Cells*, vol. 275, p. 113023, Sep. 2024, doi: 10.1016/j.solmat.2024.113023.

[42] B. Fligier *et al.*, “Development of low-cost, light weight c-Si photovoltaic modules with potential for applications in VIPV,” *Solar Energy Materials and Solar Cells*, vol. 292, p. 113801, Oct. 2025, doi: 10.1016/j.solmat.2025.113801.

[43] F. Castro-Gallardo, J. Rabanal-Arabach, S. Rodríguez-Romero, and E. Fuentealba, “Development and Testing of Lightweight Photovoltaic Modules for Vehicle-Integrated Applications Using Epoxy Resins and Fiberglass,” in *2025 IEEE 53rd Photovoltaic Specialists Conference (PVSC)*, IEEE, Jun. 2025, pp. 1139–1142. doi: 10.1109/PVSC59419.2025.11132612.

[44] M. Yamaguchi *et al.*, “Analysis for Expansion of Driving Distance and CO 2 Emission Reduction of Photovoltaic-Powered Vehicles,” *IEEE J Photovolt*, vol. 13, no. 3, pp. 343–348, May 2023, doi: 10.1109/JPHOTOV.2023.3242125.

[45] C. Kutter, L. E. Alanis, D. H. Neuhaus, and M. Heinrich, “YIELD POTENTIAL OF VEHICLE INTEGRATED PHOTOVOLTAICS ON COMMERCIAL TRUCKS AND VANS,” 2021. [Online]. Available: https://www.researchgate.net/publication/355126708

[46] T. Golubev and R. R. Lunt, “Evaluating the Electricity Production of Electric Vehicle-Integrated Photovoltaics via a Coupled Modeling Approach,” in *2021 IEEE 48th Photovoltaic Specialists Conference (PVSC)*, IEEE, Jun. 2021, pp. 0155–0159. doi: 10.1109/PVSC43889.2021.9518941.

[47] T. Golubev and R. R. Lunt, “Evaluating the Electricity Production of Electric Vehicle-Integrated Photovoltaics via a Coupled Modeling Approach,” in *2021 IEEE 48th Photovoltaic Specialists Conference (PVSC)*, IEEE, Jun. 2021, pp. 0155–0159. doi: 10.1109/PVSC43889.2021.9518941.

[48] H. Samadi, G. Ala, V. Lo Brano, P. Romano, and F. Viola, “Investigation of Effective Factors on Vehicles Integrated Photovoltaic (VIPV) Performance: A Review,” *World Electric Vehicle Journal*, vol. 14, no. 6, p. 154, Jun. 2023, doi: 10.3390/wevj14060154.

[49] R. Peibst *et al.*, “Demonstration of Feeding Vehicle-Integrated Photovoltaic-Converted Energy into the High-Voltage On-Board Network of Practical Light Commercial Vehicles for Range Extension,” *Solar RRL*, vol. 6, no. 5, May 2022, doi: 10.1002/solr.202100516.

[50] Y. Ota, T. Masuda, K. Araki, and M. Yamaguchi, “Curve-Correction Factor for Characterization of the Output of a Three-Dimensional Curved Photovoltaic Module on a Car Roof,” *Coatings*, vol. 8, no. 12, p. 432, Nov. 2018, doi: 10.3390/coatings8120432.

[51] G. Wetzel, L. Salomon, J. Krügener, D. Bredemeier, and R. Peibst, “High time resolution measurement of solar irradiance onto driving car body for vehicle integrated photovoltaics,” *Progress in Photovoltaics: Research and Applications*, vol. 30, no. 5, pp. 543–551, May 2022, doi: 10.1002/pip.3526.

[52] A. J. Carr *et al.*, “Validation of shading model in SolarMoves,” *Solar Energy Materials and Solar Cells*, vol. 292, p. 113783, Oct. 2025, doi: 10.1016/j.solmat.2025.113783.

[53] F. Karoui, B. Chambion, F. Claudon, and B. Commault, “Integrated Photovoltaics Potential for Passenger Cars: A Focus on the Sensitivity to Electrical Architecture Losses,” *Applied Sciences*, vol. 13, no. 14, p. 8373, Jul. 2023, doi: 10.3390/app13148373.

[54] M. Centeno Brito, T. Santos, F. Moura, D. Pera, and J. Rocha, “Urban solar potential for vehicle integrated photovoltaics,” *Transp Res D Transp Environ*, vol. 94, p. 102810, May 2021, doi: 10.1016/j.trd.2021.102810.

[55] K. Araki, Y. Ota, A. Nagaoka, and K. Nishioka, “3D Solar Irradiance Model for Non-Uniform Shading Environments Using Shading (Aperture) Matrix Enhanced by Local Coordinate System,” *Energies (Basel)*, vol. 16, no. 11, p. 4414, May 2023, doi: 10.3390/en16114414.

[56] C. Lodi, A. Seitsonen, E. Paffumi, M. De Gennaro, T. Huld, and S. Malfettani, “Reducing CO 2 emissions of conventional fuel cars by vehicle photovoltaic roofs,” *Transp Res D Transp Environ*, vol. 59, pp. 313–324, Mar. 2018, doi: 10.1016/j.trd.2018.01.020.

[57] M. Oh, S.-M. Kim, and H.-D. Park, “Estimation of photovoltaic potential of solar bus in an urban area: Case study in Gwanak, Seoul, Korea,” *Renew Energy*, vol. 160, pp. 1335–1348, Nov. 2020, doi: 10.1016/j.renene.2020.07.048.

[58] K. Araki, Y. Ota, and K. Nishioka, “Testing and rating of vehicle-integrated photovoltaics: Scientific background,” *Solar Energy Materials and Solar Cells*, vol. 280, p. 113241, Jan. 2025, doi: 10.1016/j.solmat.2024.113241.

[59] K. Araki, Y. Ota, and M. Yamaguchi, “Measurement and Modeling of 3D Solar Irradiance for Vehicle-Integrated Photovoltaic,” *Applied Sciences*, vol. 10, no. 3, p. 872, Jan. 2020, doi: 10.3390/app10030872.

[60] K. Araki, Y. Ota, K.-H. Lee, N. Yamada, and M. Yamaguchi, “Curve Correction of the Energy Yield by Flexible Photovoltaics for VIPV and BIPV Applications Using a Simple Correction Factor,” in *2019 IEEE 46th Photovoltaic Specialists Conference (PVSC)*, IEEE, Jun. 2019, pp. 1584–1591. doi: 10.1109/PVSC40753.2019.8980729.

[61] Y. Ota, T. Masuda, K. Araki, and M. Yamaguchi, “Curve-Correction Factor for Characterization of the Output of a Three-Dimensional Curved Photovoltaic Module on a Car Roof,” *Coatings*, vol. 8, no. 12, p. 432, Nov. 2018, doi: 10.3390/coatings8120432.

[62] Y. Ota, K. Araki, A. Nagaoka, and K. Nishioka, “Facilitating vehicle-integrated photovoltaics by considering the radius of curvature of the roof surface for solar cell coverage,” *Clean Eng Technol*, vol. 7, p. 100446, Apr. 2022, doi: 10.1016/j.clet.2022.100446.

[63] K. Araki, Y. Ota, and M. Yamaguchi, “Measurement and Modeling of 3D Solar Irradiance for Vehicle-Integrated Photovoltaic,” *Applied Sciences*, vol. 10, no. 3, p. 872, Jan. 2020, doi: 10.3390/app10030872.

[64] K. Araki, Y. Ota, K.-H. Lee, N. Yamada, and M. Yamaguchi, “Curve Correction of the Energy Yield by Flexible Photovoltaics for VIPV and BIPV Applications Using a Simple Correction Factor,” in *2019 IEEE 46th Photovoltaic Specialists Conference (PVSC)*, IEEE, Jun. 2019, pp. 1584–1591. doi: 10.1109/PVSC40753.2019.8980729.

[65] M. Yamaguchi *et al.*, “Analysis for the Potential of High-Efficiency and Low-Cost Vehicle-Integrated Photovoltaics,” *Solar RRL*, vol. 7, no. 8, Apr. 2023, doi: 10.1002/solr.202200556.

[66] M. Yamaguchi *et al.*, “Development of high-efficiency and low-cost solar cells for PV-powered vehicles application,” *Progress in Photovoltaics: Research and Applications*, vol. 29, no. 7, pp. 684–693, Jul. 2021, doi: 10.1002/pip.3343.

[67] Y. Ota, K. Araki, A. Nagaoka, and K. Nishioka, “Evaluating the Output of a Car-Mounted Photovoltaic Module Under Driving Conditions,” *IEEE J Photovolt*, vol. 11, no. 5, pp. 1299–1304, Sep. 2021, doi: 10.1109/JPHOTOV.2021.3087748.

[68] S. Kim, M. Holz, S. Park, Y. Yoon, E. Cho, and J. Yi, “Future Options for Lightweight Photovoltaic Modules in Electrical Passenger Cars,” *Sustainability*, vol. 13, no. 5, p. 2532, Feb. 2021, doi: 10.3390/su13052532.

[69] A. C. Martins, V. Chapuis, A. Virtuani, and C. Ballif, “Robust Glass-Free Lightweight Photovoltaic Modules With Improved Resistance to Mechanical Loads and Impact,” *IEEE J Photovolt*, vol. 9, no. 1, pp. 245–251, Jan. 2019, doi: 10.1109/JPHOTOV.2018.2876934.

[70] “Kutter, C., Basler, F., Alanis, L. E., Markert, J., Heinrich, M., & Neuhaus, D. H. (2020, September). Integrated lightweight, glass-free PV module technology for box bodies of commercial trucks. In Presented at the 37th European PV Solar Energy Conference and Exhibition (Vol. 7, p. 11).”.

[71] “Flixbus fleet tests 18% CIGS panels. 2020 ; Available from: https://www.pv-magazine.eom/2020/02/11/flixbus-fleet-tests-18-cigs-panels/.”.

[72] M. Yamaguchi *et al.*, “Overview of Si Tandem Solar Cells and Approaches to PV-Powered Vehicle Applications,” *MRS Adv*, vol. 5, no. 8–9, pp. 441–450, Feb. 2020, doi: 10.1557/adv.2020.66.

[73] N. Yamada, “Vehicle-Integrated 3D-PV Module with III-V and Si Solar Cells,” in *2020 47th IEEE Photovoltaic Specialists Conference (PVSC)*, IEEE, Jun. 2020, pp. 2324–2326. doi: 10.1109/PVSC45281.2020.9300929.

[74] D. Sato, K. Lee, K. Araki, T. Masuda, M. Yamaguchi, and N. Yamada, “Design of low-concentration static III-V/Si partial CPV module with 27.3% annual efficiency for car-roof application,” *Progress in Photovoltaics: Research and Applications*, vol. 27, no. 6, pp. 501–510, Jun. 2019, doi: 10.1002/pip.3124.

[75] K. Araki *et al.*, “How did the knowledge of CPV contribute to the standardization activity of VIPV?,” 2020, p. 060001. doi: 10.1063/5.0032997.

[76] M. Nukunudompanich, D. Sriprapai, and S. Sontikaew, “Aspects of optical and thermal performances in flexible perovskite solar cells made of nanomaterials with potential for development of vehicle-integrated photovoltaics,” *Mater Today Proc*, vol. 66, pp. 3163–3167, 2022, doi: 10.1016/j.matpr.2022.06.397.

[77] F. Di Giacomo, A. Fakharuddin, R. Jose, and T. M. Brown, “Progress, challenges and perspectives in flexible perovskite solar cells,” *Energy Environ Sci*, vol. 9, no. 10, pp. 3007–3035, 2016, doi: 10.1039/C6EE01137C.

[78] J. Macias, R. Herrero, R. Nunez, and I. Anton, “On the effect of cell interconnection in Vehicle Integrated Photovoltaics: modelling energy under different scenarios,” in *2021 IEEE 48th Photovoltaic Specialists Conference (PVSC)*, IEEE, Jun. 2021, pp. 1336–1339. doi: 10.1109/PVSC43889.2021.9518935.

[79] M. Abdelhamid, S. Pilla, R. Singh, I. Haque, and Z. Filipi, “A comprehensive optimized model for on-board solar photovoltaic system for plug-in electric vehicles: energy and economic impacts,” *Int J Energy Res*, vol. 40, no. 11, pp. 1489–1508, Sep. 2016, doi: 10.1002/er.3534.

[80] R. Peibst *et al.*, “Demonstration of Feeding Vehicle-Integrated Photovoltaic-Converted Energy into the High-Voltage On-Board Network of Practical Light Commercial Vehicles for Range Extension,” *Solar RRL*, vol. 6, no. 5, May 2022, doi: 10.1002/solr.202100516.

[81] N. M. Kumar, S. S. Chopra, M. Malvoni, R. M. Elavarasan, and N. Das, “Solar Cell Technology Selection for a PV Leaf Based on Energy and Sustainability Indicators—A Case of a Multilayered Solar Photovoltaic Tree,” *Energies (Basel)*, vol. 13, no. 23, p. 6439, Dec. 2020, doi: 10.3390/en13236439.

[82] M. Yamaguchi *et al.*, “Analysis of temperature coefficients and their effect on efficiency of solar cell modules for photovoltaics-powered vehicles,” *J Phys D Appl Phys*, vol. 54, no. 50, p. 504002, Dec. 2021, doi: 10.1088/1361-6463/ac1ef8.

[83] M. Yamaguchi *et al.*, “Analysis for Effects of Temperature Rise of PV Modules upon Driving Distance of Vehicle Integrated Photovoltaic Electric Vehicles,” *Energy Power Eng*, vol. 16, no. 04, pp. 131–150, 2024, doi: 10.4236/epe.2024.164007.

[84] Y. Hayakawa, D. Sato, and N. Yamada, “Measurement of the Convective Heat Transfer Coefficient and Temperature of Vehicle-Integrated Photovoltaic Modules,” *Energies (Basel)*, vol. 15, no. 13, p. 4818, Jun. 2022, doi: 10.3390/en15134818.

[85] F. A. Tiano, G. Rizzo, M. Marino, and A. Monetti, “Evaluation of the potential of solar photovoltaic panels installed on vehicle body including temperature effect on efficiency,” *eTransportation*, vol. 5, p. 100067, Aug. 2020, doi: 10.1016/j.etran.2020.100067.

[86] R. Bharti, J. Kuitche, and M. G. TamizhMani, “Nominal Operating Cell Temperature (NOCT): Effects of module size, loading and solar spectrum,” in *2009 34th IEEE Photovoltaic Specialists Conference (PVSC)*, IEEE, Jun. 2009, pp. 001657–001662. doi: 10.1109/PVSC.2009.5411408.

[87] D. Faiman, “Assessing the outdoor operating temperature of photovoltaic modules,” *Progress in Photovoltaics: Research and Applications*, vol. 16, no. 4, pp. 307–315, Jun. 2008, doi: 10.1002/pip.813.

[88] N. Patel, B. E. Pieters, K. Bittkau, E. Sovetkin, K. Ding, and A. Reinders, “Assessing the accuracy of two steady-state temperature models for onboard passenger vehicle photovoltaics applications,” *Progress in Photovoltaics: Research and Applications*, vol. 32, no. 11, pp. 790–798, Nov. 2024, doi: 10.1002/pip.3832.

[89] M. O. Román *et al.*, “Satellite-based assessment of electricity restoration efforts in Puerto Rico after Hurricane Maria,” *PLoS One*, vol. 14, no. 6, p. e0218883, Jun. 2019, doi: 10.1371/journal.pone.0218883.

[90] J. Popke and C. Harrison, “Energy, Resilience, and Responsibility in Post-Hurricane Maria Dominica: Ethical and Historical Perspectives on ‘Building Back Better,’” *Journal of Extreme Events*, vol. 05, no. 04, p. 1840003, Dec. 2018, doi: 10.1142/S2345737618400031.

[91] R. Der Sarkissian, A. Dabaj, Y. Diab, and M. Vuillet, “Evaluating the Implementation of the ‘Build-Back-Better’ Concept for Critical Infrastructure Systems: Lessons from Saint-Martin’s Island Following Hurricane Irma,” *Sustainability*, vol. 13, no. 6, p. 3133, Mar. 2021, doi: 10.3390/su13063133.

[92] S. Unal and S. E. Dagteke, “Enhancement of fuel cell based energy sustainability for cell on wheels mobile base stations used in disaster areas,” *Int J Hydrogen Energy*, vol. 75, pp. 567–577, Jul. 2024, doi: 10.1016/j.ijhydene.2024.03.320.

[93] M. Reveles Miranda, D. Pacheco Catalán, A. Fleitas Menéndez, and R. Barbosa, “Analysis of the economic feasibility of a PV system with hydrogen and supercapacitors-based hybrid energy storage for rural community shelter in Yucatán, México,” *Int J Hydrogen Energy*, vol. 108, pp. 171–184, Mar. 2025, doi: 10.1016/j.ijhydene.2024.05.214.

[94] A. K. Candan, A. R. Boynuegri, and N. Onat, “Home energy management system for enhancing grid resiliency in post-disaster recovery period using Electric Vehicle,” *Sustainable Energy, Grids and Networks*, vol. 34, p. 101015, Jun. 2023, doi: 10.1016/j.segan.2023.101015.

[95] M. Amin Vaziri Rad, A. Shahsavari, F. Rajaee, A. Kasaeian, F. Pourfayaz, and W.-M. Yan, “Techno-economic assessment of a hybrid system for energy supply in the affected areas by natural disasters: A case study,” *Energy Convers Manag*, vol. 221, p. 113170, Oct. 2020, doi: 10.1016/j.enconman.2020.113170.

[96] H. Saboori, “Enhancing resilience and sustainability of distribution networks by emergency operation of a truck-mounted mobile battery energy storage fleet,” *Sustainable Energy, Grids and Networks*, vol. 34, p. 101037, Jun. 2023, doi: 10.1016/j.segan.2023.101037.

[97] Q. Li, T. Li, and A. Zanelli, “Performance evaluation of flexible photovoltaic panels for energy supply in post-disaster emergency shelters,” *Journal of Building Engineering*, vol. 98, p. 111285, Dec. 2024, doi: 10.1016/j.jobe.2024.111285.

[98] H. Saboori and S. Jadid, “Optimal scheduling of mobile utility-scale battery energy storage systems in electric power distribution networks,” *J Energy Storage*, vol. 31, p. 101615, Oct. 2020, doi: 10.1016/j.est.2020.101615.

[99] G. He, J. Michalek, S. Kar, Q. Chen, D. Zhang, and J. F. Whitacre, “Utility-Scale Portable Energy Storage Systems,” *Joule*, vol. 5, no. 2, pp. 379–392, Feb. 2021, doi: 10.1016/j.joule.2020.12.005.

[100] A. Borodinecs, D. Zajecs, K. Lebedeva, and R. Bogdanovics, “Mobile Off-Grid Energy Generation Unit for Temporary Energy Supply,” *Applied Sciences*, vol. 12, no. 2, p. 673, Jan. 2022, doi: 10.3390/app12020673.

[101] M. Ben Said-Romdhane and S. Skander-Mustapha, “A Review on Vehicle-Integrated Photovoltaic Panels,” 2021, pp. 349–370. doi: 10.1007/978-3-030-64565-6_12.

[102] G. Almonacid, F. J. Muñoz, J. de la Casa, and J. D. Aguilar, “Integration of PV systems on health emergency vehicles. The FIVE project,” *Progress in Photovoltaics: Research and Applications*, vol. 12, no. 8, pp. 609–621, Dec. 2004, doi: 10.1002/pip.558.

[103] T. Hasan, S. Jamaludin, and W. W. Nik, “Analysis of intelligent solar ICU water ambulance to optimize energy,” *Annals of Medicine & Surgery*, vol. 80, Aug. 2022, doi: 10.1016/j.amsu.2022.104141.

[104] A. Roudbari, A. Nateghi, B. Yousefi-khanghah, H. Asgharpour-Alamdari, and H. Zare, “Resilience-oriented operation of smart grids by rescheduling of energy resources and electric vehicles management during extreme weather condition,” *Sustainable Energy, Grids and Networks*, vol. 28, p. 100547, Dec. 2021, doi: 10.1016/j.segan.2021.100547.

[105] K. Rahimi and B. Chowdhury, “A hybrid approach to improve the resiliency of the power distribution system,” in *2014 North American Power Symposium (NAPS)*, IEEE, Sep. 2014, pp. 1–6. doi: 10.1109/NAPS.2014.6965472.

[106] H. Kim, J. Ku, S.-M. Kim, and H.-D. Park, “A new GIS-based algorithm to estimate photovoltaic potential of solar train: Case study in Gyeongbu line, Korea,” *Renew Energy*, vol. 190, pp. 713–729, May 2022, doi: 10.1016/j.renene.2022.03.130.

[107] K. Araki, Y. Ota, A. Nagaoka, and K. Nishioka, “3D Solar Irradiance Model for Non-Uniform Shading Environments Using Shading (Aperture) Matrix Enhanced by Local Coordinate System,” *Energies (Basel)*, vol. 16, no. 11, p. 4414, May 2023, doi: 10.3390/en16114414.

[108] A. Tiwari and M. Darbari, *Emerging Trends in Computer Science and Its Application*. London: CRC Press, 2025. doi: 10.1201/9781003606635.

[109] Z. S. Almajali and S. A. Aldmour, “Single-Axis Solar Tracker System for Maintaining Southward Orientation of Solar Cells in Solar Cars,” in *2023 IEEE Jordan International Joint Conference on Electrical Engineering and Information Technology (JEEIT)*, IEEE, May 2023, pp. 211–216. doi: 10.1109/JEEIT58638.2023.10185858.

[110] “Efficiency and Decarbonization Indicators in Italy and in the Biggest European Countries. Edition 2023. 2023. Available online: https://www.isprambiente.gov.it/files2023/pubblicazioni/rapporti/r386-2023.pdf (accessed on 15 June 2024).”.

[111] “Remund, J.; Müller, S.C.; Schmutz, M.; Graf, P. Meteonorm Version 8. In Proceedings of the EU PVSEC 2020, Lisbon, Portugal, 7–11 September 2020.”.

[112] “European Commission; Joint Research Centre. Photovoltaic Geographical Information System (PVGIS). 2024. Available online: https://ec.europa.eu/jrc/en/pvgis (accessed on 7 February 2025).”.

[113] M. C. Brito, R. Amaro e Silva, D. Pera, I. Costa, and D. Boutov, “Effect of urban shadowing on the potential of solar-powered vehicles,” *Progress in Photovoltaics: Research and Applications*, vol. 32, no. 2, pp. 73–83, Feb. 2024, doi: 10.1002/pip.3737.

[114] K. Mallon, F. Assadian, and B. Fu, “Analysis of On-Board Photovoltaics for a Battery Electric Bus and Their Impact on Battery Lifespan,” *Energies (Basel)*, vol. 10, no. 7, p. 943, Jul. 2017, doi: 10.3390/en10070943.

[115] O. Kanz, A. Reinders, J. May, and K. Ding, “Environmental Impacts of Integrated Photovoltaic Modules in Light Utility Electric Vehicles,” *Energies (Basel)*, vol. 13, no. 19, p. 5120, Oct. 2020, doi: 10.3390/en13195120.

[116] “Araki, K.; Karr, A.J.; Chabuel, F.; Commault, B.; Derks, R.; Ding, K.; Duigou, T.; Ekins-Daukes, N.J.; Gaume, J.; Hirota, T.; et al. State-of-the-Art and Expected Benefits of PV-Powered Vehicles. 2021. Available online: https://iea-pvps.org/wp-content/uploads/2021/07/IEA_PVPS_T17_State-of-theart-and-expected-benefits-of-VIPV_report.pdf (accessed on 6 June 2024).”.

[117] Konrad Mertens, *Photovoltaics: Fundamentals, Technology, and Practice*, 2nd Edition. 2018.

[118] “Leloux, J.; Taylor, J.; Moretón, R.; Narvarte, L.; Trebosc, D.; Desportes, A.; Solar, S. Monitoring 30,000 PV systems in Europe: Performance, faults, and state of the art. In Proceedings of the 31st European Photovoltaic Solar Energy Conference and Exhibition, Hamburg, Germany, 14–18 September 2015; pp. 1574–1582.”.

[119] “Types of Containers, Dimensions and Characteristics of Containers. 2023. Available online: https://www.groupe-rdt.com/en/useful-information/types-of-containers/ (accessed on 20 November 2023).”.

[120] “Mobile Surgery Unit. Available online: https://www.expandable-trailers.com/applications/mobile-surgery-unit (accessed on 10 April 2024).”.

[121] “Semi. The Future of Trucking Is Electric. 2023. Available online: https://www.tesla.com/semi (accessed on 20 November 2023).”.

[122] “WAS 500 E-RTW. 2023. Available online: https://www.was-vehicles.com/de/innovation/was-500-e-rtw.html (accessed on 20 November 2023).”.

[123] “Global Solar Atlas. 2024. Available online: https://globalsolaratlas.info/map/ (accessed on 28 December 2024).”.

[124] C. Park, H. Park, H. Jeon, K. Choi, and J. Suh, “Evaluation and Validation of Photovoltaic Potential Based on Time and Pathway of Solar-Powered Electric Vehicle,” *Applied Sciences*, vol. 13, no. 2, p. 1025, Jan. 2023, doi: 10.3390/app13021025.

[125] “REGULATION (EC) No 561/2006 OF THE EUROPEAN PARLIAMENT AND OF THE COUNCIL on the Harmonisation of Certain Social Legislation Relating to Road Transport and Amending Council Regulations (EEC) No 3821/85 and (EC) No 2135/98 and Repealing Council Regulation (EEC) No 3820/85. 2023. Available online: https://eur-lex.europa.eu/resource.html?uri=cellar:5cf5ebde-d494-40eb-86a7-2131294ccbd9.0005.02/DOC_1&format=PDF (accessed on 10 November 2023).”.

[126] “Hirota, T.; Kamiya, Y.; Komoto, K. Feasibility Study of Onboard PV for Passenger Vehicle Application. Trans. Soc. Automot. Eng. Jpn. 2020, 51.”.

[127] “Le Series. 2023. Available online: https://www.sungoldsolar.com/flexible-solar-panel/le/ (accessed on 30 December 2023).”.

[128] “Duo Series Dual Axis Solar Tracking Systems. 2025. Available online: https://www.pvsolarfirst.com/Products_details/Duo_Series_Dual_Axis_Solar_Tracking_Systems.html (accessed on 15 February 2025)”.

[129] “Single Axis Tracker. 2025. Available online: https://lumaxenergy.com/assets/datasheets/single-axis-tracker/SAT.pdf (accessed on 15 February 2025)”.

[130] N. Kuttybay *et al.*, "Assessment of solar tracking systems: A comprehensive review," *Sustainable Energy Technologies and Assessments*, vol. 68, p. 103879, Aug. 2024, doi: 10.1016/j.seta.2024.103879.

[131] S. Jogunuri, R. Kumar, and D. Kumar, "Sizing an off-grid photovoltaic system (A case study)," in *2017 International Conference on Energy, Communication, Data Analytics and Soft Computing (ICECDS)*, IEEE, Aug. 2017, pp. 2618–2622. doi: 10.1109/ICECDS.2017.8389927.

[132] F. C. Mat, S. E. Binti Mokhtar, M. Badrol Hisyam, and S. Wadi Harun, "Smart Power Management System for Ambulance," *IOP Conf Ser Mater Sci Eng*, vol. 854, no. 1, p. 012070, May 2020, doi: 10.1088/1757-899X/854/1/012070.

[133] H. Drinhaus, C. Schumacher, J. Drinhaus, and W. A. Wetsch, "W(h)at(t) counts in electricity consumption in the intensive care unit," *Intensive Care Med*, vol. 49, no. 4, pp. 437–439, Apr. 2023, doi: 10.1007/s00134-023-07013-y.

[134] N. A. Dieleman and C. Jagtenberg, "Electric ambulances: will the need for charging affect response times?," 2024. doi: 10.2139/ssrn.4874479.

[135] "New Energy and Industrial Technology Development Organization. NEDO, PV-Powered Vehicle Strategy Committee. 2018. Available online: https://www.nedo.go.jp/content/100885778.pdf (accessed on 29 June 2024).".

[136] G. Ala *et al.*, "Different Scenarios of Electric Mobility: Current Situation and Possible Future Developments of Fuel Cell Vehicles in Italy," *Sustainability*, vol. 12, no. 2, p. 564, Jan. 2020, doi: 10.3390/su12020564.

[137] G. Ala *et al.*, "Electric Mobility in Portugal: Current Situation and Forecasts for Fuel Cell Vehicles," *Energies (Basel)*, vol. 14, no. 23, p. 7945, Nov. 2021, doi: 10.3390/en14237945.

[138] N. Patel, K. Bittkau, B. E. Pieters, E. Sovetkin, K. Ding, and A. Reinders, "Impact of Additional PV Weight on the Energy Consumption of Electric Vehicles With Onboard PV," *IEEE J Photovolt*, vol. 14, no. 2, pp. 319–329, Mar. 2024, doi: 10.1109/JPHOTOV.2024.3359446.

[139] F. Karoui, B. Chambion, F. Claudon, and B. Commault, "Integrated Photovoltaics Potential for Passenger Cars: A Focus on the Sensitivity to Electrical Architecture Losses," *Applied Sciences*, vol. 13, no. 14, p. 8373, Jul. 2023, doi: 10.3390/app13148373.

[140] F. Karoui, F. Claudon, B. Chambion, S. Catellani, and B. Commault, "Estimation of integrated photovoltaics potential for solar city bus in different climate conditions in Europe," *J Phys Conf Ser*, vol. 2454, no. 1, p. 012007, Mar. 2023, doi: 10.1088/1742-6596/2454/1/012007.

[141] M. Yamaguchi *et al.*, "Development of high-efficiency and low-cost solar cells for PV-powered vehicles application," *Progress in Photovoltaics: Research and Applications*, vol. 29, no. 7, pp. 684–693, Jul. 2021, doi: 10.1002/pip.3343.

[142] A. C. Martins, V. Chapuis, A. Virtuani, and C. Ballif, "Robust Glass-Free Lightweight Photovoltaic Modules With Improved Resistance to Mechanical Loads and Impact," *IEEE J Photovolt*, vol. 9, no. 1, pp. 245–251, Jan. 2019, doi: 10.1109/JPHOTOV.2018.2876934.

[143] G. Wetzel, L. Salomon, J. Krügener, D. Bredemeier, and R. Peibst, "High time resolution measurement of solar irradiance onto driving car body for vehicle integrated photovoltaics," *Progress in Photovoltaics: Research and Applications*, vol. 30, no. 5, pp. 543–551, May 2022, doi: 10.1002/pip.3526.

[144] K. Araki, Y. Ota, and K. Nishioka, "Testing and rating of vehicle-integrated photovoltaics: Scientific background," *Solar Energy Materials and Solar Cells*, vol. 280, p. 113241, Jan. 2025, doi: 10.1016/j.solmat.2024.113241.

[145] H. Samadi, M. J. Hosseini, A. A. Ranjbar, and Y. Pahamli, "Thermohydraulic performance of new minichannel heat sink with grooved barriers," *International Communications in Heat and Mass Transfer*, vol. 144, p. 106753, May 2023, doi: 10.1016/j.icheatmasstransfer.2023.106753.

[146] M. Sadinezhad Fard, M. Rahimi, Y. Pahamli, H. Samadi, and R. Bahrampoury, "Cooling performance of sliver solar cells in low concentration PV system with ribbed-groove mini-channel heat sink," *International Journal of Thermal Sciences*, vol. 200, p. 108955, Jun. 2024, doi: 10.1016/j.ijthermalsci.2024.108955.

[147] Y. Hayakawa, D. Sato, and N. Yamada, “Measurement of the Convective Heat Transfer Coefficient and Temperature of Vehicle-Integrated Photovoltaic Modules,” *Energies (Basel)*, vol. 15, no. 13, p. 4818, Jun. 2022, doi: 10.3390/en15134818.

[148] M. Yamaguchi *et al.*, “Analysis of temperature coefficients and their effect on efficiency of solar cell modules for photovoltaics-powered vehicles,” *J Phys D Appl Phys*, vol. 54, no. 50, p. 504002, Dec. 2021, doi: 10.1088/1361-6463/ac1ef8.

[149] R. Perez, P. Ineichen, R. Seals, J. Michalsky, and R. Stewart, “Modeling daylight availability and irradiance components from direct and global irradiance,” *Solar Energy*, vol. 44, no. 5, pp. 271–289, 1990, doi: 10.1016/0038-092X(90)90055-H.

[150] D. L. King, J. A. Kratochvil, and W. E. Boyson, “Measuring solar spectral and angle-of-incidence effects on photovoltaic modules and solar irradiance sensors,” in *Conference Record of the Twenty Sixth IEEE Photovoltaic Specialists Conference - 1997*, IEEE, pp. 1113–1116. doi: 10.1109/PVSC.1997.654283.

[151] J. A. Duffie and W. A. Beckman, *Solar Engineering of Thermal Processes*. Wiley, 2013. doi: 10.1002/9781118671603.

[152] J. Rakovec and K. Zakšek, “On the proper analytical expression for the sky-view factor and the diffuse irradiation of a slope for an isotropic sky,” *Renew Energy*, vol. 37, no. 1, pp. 440–444, Jan. 2012, doi: 10.1016/j.renene.2011.06.042.

[153] Y. Ota, K. Araki, A. Nagaoka, and K. Nishioka, “Facilitating vehicle-integrated photovoltaics by considering the radius of curvature of the roof surface for solar cell coverage,” *Clean Eng Technol*, vol. 7, p. 100446, Apr. 2022, doi: 10.1016/j.clet.2022.100446.

[154] K. S. Anderson, C. W. Hansen, W. F. Holmgren, A. R. Jensen, M. A. Mikofski, and A. Driesse, “pvlib python: 2023 project update,” *J Open Source Softw*, vol. 8, no. 92, p. 5994, Dec. 2023, doi: 10.21105/joss.05994.

[155] C. Thiel *et al.*, “Impact of climatic conditions on prospects for integrated photovoltaics in electric vehicles,” *Renewable and Sustainable Energy Reviews*, vol. 158, p. 112109, Apr. 2022, doi: 10.1016/j.rser.2022.112109.

[156] N. Manoj Kumar, A. Ghosh, and S. S. Chopra, “Power Resilience Enhancement of a Residential Electricity User Using Photovoltaics and a Battery Energy Storage System under Uncertainty Conditions,” *Energies (Basel)*, vol. 13, no. 16, p. 4193, Aug. 2020, doi: 10.3390/en13164193.

[157] N. Campagna, V. Castiglia, F. Gennaro, A. A. Messina, and R. Miceli, “Fuel Cell-Based Inductive Power Transfer System for Supercapacitor Constant Current Charging,” *Energies (Basel)*, vol. 17, no. 14, p. 3575, Jul. 2024, doi: 10.3390/en17143575.

[158] B. manufacturer Karsan, “ELECTRIC MINIBUS with Zero Emissions, Karsan e-JEST.” Accessed: Sep. 16, 2024. [Online]. Available: https://www.karsan.com/en/e-jest-highlights#e-jest-specs

[159] I. with the support of P. P. G. Fraunhofer Institute for Solar Energy Systems, “Photovoltaics Report,” 2024. Accessed: Nov. 18, 2024. [Online]. Available: https://www.ise.fraunhofer.de/content/dam/ise/de/documents/publications/studies/Photovoltaics-Report.pdf

[160] EUROPEAN COMMISSION, “Technical Guidelines for the preparation of applications for the approval of innovative technologies pursuant to Regulation (EC) No 443/2009 and Regulation (EU) No 510/2011,” 2015.

[161] C. Lodi, S. Gil-Sayas, D. Currò, S. Serra, and Y. Drossinos, “Full-battery effect during on-board solar charging of conventional vehicles,” *Transp Res D Transp Environ*, vol. 96, p. 102862, Jul. 2021, doi: 10.1016/j.trd.2021.102862.

[162] Istituto Superiore per la Protezione e la Ricerca Ambientale, “Efficiency and decarbonization indicators in Italy and in the biggest European Countries. Edition 2023,” 2023.

[163] R. Miceli and F. Viola, “Designing a Sustainable University Recharge Area for Electric Vehicles: Technical and Economic Analysis,” *Energies (Basel)*, vol. 10, no. 10, p. 1604, Oct. 2017, doi: 10.3390/en10101604.

[164] M. Peyvandi, A. Hajinezhad, and S. F. Moosavian, “Investigating the intensity of GHG emissions from electricity production in Iran using renewable sources,” *Results in Engineering*, vol. 17, p. 100819, Mar. 2023, doi: 10.1016/j.rineng.2022.100819.

[165] “Global Electricity Review 2023 / Country and Region Deep Dives,” https://ember-energy.org/latest-insights/global-electricity-review-2023/country-and-region-deep-dives/#iran.

[166] X. Zhang and K. Xu, “Statistical data-based prediction of carbon dioxide emission factors of China’s power generation at carbon peak in 2030,” *Case Studies in Thermal Engineering*, vol. 51, p. 103633, Nov. 2023, doi: 10.1016/j.csite.2023.103633.

[167] “A2A will reduce greenhouse gas emissions by 46% by 2030,” https://www.gruppoa2a.it/en/media/press-releases/a2a-will-reduce-greenhouse-gas-emissions-46-2030?utm_source=chatgpt.com.

[168] “ENEL BOOSTS ITS 2030 GREENHOUSE GAS EMISSION REDUCTION TARGET TO 80% FROM 70%, SBTi-CERTIFIED,” https://corporate.enel.it/content/dam/enel-common/press/en/2020-October/Enel%20SBTI%20upgraded.pdf?utm_source=chatgpt.com.

[169] O. Kanz, A. Reinders, J. May, and K. Ding, “Environmental Impacts of Integrated Photovoltaic Modules in Light Utility Electric Vehicles,” *Energies (Basel)*, vol. 13, no. 19, p. 5120, Oct. 2020, doi: 10.3390/en13195120.

[170] New Energy and Industrial Technology Development Organization, “PV-Powered Vehicle Strategy Committee Interim Report,” 2018.

[171] O. Kanz, K. Bittkau, K. Ding, J. May, and A. Reinders, “Environmental Impacts of Integrated Photovoltaic Modules in Light Utility Vehicles,” in *Photovoltaic Solar Energy*, Wiley, 2024, pp. 567–577. doi: 10.1002/9781119578826.ch35.

[172] M. Traverso, F. Asdrubali, A. Francia, and M. Finkbeiner, “Towards life cycle sustainability assessment: an implementation to photovoltaic modules,” *Int J Life Cycle Assess*, vol. 17, no. 8, pp. 1068–1079, Sep. 2012, doi: 10.1007/s11367-012-0433-8.

[173] P. Hoth, L. Heide, A. Grahle, and D. Göhlich, “Vehicle-Integrated Photovoltaics—A Case Study for Berlin,” *World Electric Vehicle Journal*, vol. 15, no. 3, p. 113, Mar. 2024, doi: 10.3390/wevj15030113.

[174] M. Clemente, L. Van Sundert, M. Salazar, and T. Hofman, “A Framework to Estimate Life Cycle Emissions for Vehicle-Integrated Photovoltaic Systems,” in *2024 IEEE Vehicle Power and Propulsion Conference (VPPC)*, IEEE, Oct. 2024, pp. 1–6. doi: 10.1109/VPPC63154.2024.10755198.

[175] F. Karoui, B. Chambion, F. Claudon, and B. Commault, “Integrated Photovoltaics Potential for Passenger Cars: A Focus on the Sensitivity to Electrical Architecture Losses,” *Applied Sciences*, vol. 13, no. 14, p. 8373, Jul. 2023, doi: 10.3390/app13148373.

[176] IEA Photovoltaic Power Systems Programme (PVPS), “Environmental Life Cycle Assessment of Electricity from PV Systems,” 2023.

[177] L. Tous *et al.*, “Overview of key results achieved in H2020 HighLite project helping to raise the EU PV industries’ competitiveness,” *Progress in Photovoltaics: Research and Applications*, vol. 31, no. 12, pp. 1409–1427, Dec. 2023, doi: 10.1002/pip.3667.

[178] N. Scarlat, M. Prussi, and M. Padella, “Quantification of the carbon intensity of electricity produced and used in Europe,” *Appl Energy*, vol. 305, p. 117901, Jan. 2022, doi: 10.1016/j.apenergy.2021.117901.

[179] M. Parhamfar, “Towards green airports: Factors influencing greenhouse gas emissions and sustainability through renewable energy,” *Next Research*, vol. 1, no. 2, p. 100060, Dec. 2024, doi: 10.1016/j.nexres.2024.100060.

[180] S. Sreenath, K. Sudhakar, and A. F. Yusop, “Airport-based photovoltaic applications,” *Progress in Photovoltaics: Research and Applications*, vol. 28, no. 8, pp. 833–853, Aug. 2020, doi: 10.1002/pip.3265.

[181] A. Ajayi, P. C.-K. Luk, L. Lao, and M. F. Khan, “Energy Forecasting Model for Ground Movement Operation in Green Airport,” *Energies (Basel)*, vol. 16, no. 13, p. 5008, Jun. 2023, doi: 10.3390/en16135008.

[182] M. Alruwaili and L. Cipcigan, “Airport electrified ground support equipment for providing ancillary services to the grid,” *Electric Power Systems Research*, vol. 211, p. 108242, Oct. 2022, doi: 10.1016/j.epsr.2022.108242.

[183] Y. Xiang, H. Cai, J. Liu, and X. Zhang, “Techno-economic design of energy systems for airport electrification: A hydrogen-solar-storage integrated microgrid solution,” *Appl Energy*, vol. 283, p. 116374, Feb. 2021, doi: 10.1016/j.apenergy.2020.116374.

[184] B. K. Yadav, R. Yadav, M. Jahangiri, S. S. Priya, T. R. Bajracharya, and K. Sudhakar, “Decarbonizing airport using solar and wind farm: A case of Biratnagar, Nepal,” *e-Prime - Advances in Electrical Engineering, Electronics and Energy*, vol. 8, p. 100583, Jun. 2024, doi: 10.1016/j.prime.2024.100583.

[185] P. Ollas *et al.*, “Evaluating the role of solar photovoltaic and battery storage in supporting electric aviation and vehicle infrastructure at Visby Airport,” *Appl Energy*, vol. 352, p. 121946, Dec. 2023, doi: 10.1016/j.apenergy.2023.121946.

[186] https://github.com/hamidsmd/VIPVLIB, “VIPVLIB.”

[187] E. Vartiainen, G. Masson, C. Breyer, D. Moser, and E. Román Medina, “Impact of weighted average cost of capital, capital expenditure, and other parameters on future utility-scale PV levelised cost of electricity,” *Progress in Photovoltaics: Research and Applications*, vol. 28, no. 6, pp. 439–453, Jun. 2020, doi: 10.1002/pip.3189.

[188] “Electricity Maps, Accessed: Jul. 9, 2025. [Online]. Available: https://www.electricitymaps.com”.

[189] “US dollar (USD). Accessed: Jul. 13, 2025. [Online]. Available: https://www.ecb.europa.eu/stats/policy_and_exchange_rates/euro_reference_exchange_rates/html/eurofxref-graph-usd.en.html ”.

[190] “Electricity prices. Accessed: Jul. 13, 2025. [Online]. Available: https://www.globalpetrolprices.com/electricity_prices/”.

[191] “Electricity prices for non-household consumers (2024-S2), Accessed: Jun. 6, 2025. [Online]. Available: https://ec.europa.eu/eurostat/databrowser/view/nrg_pc_205__custom_17400202/default/table?lang=en ”.

[192] https://www.alke.com/airport-luggage-vehicles, “Alke’ Airport luggage vehicles.”

[193] F. Pellitteri, A. U. Rahman, A. O. Di Tommaso, M. Ricco, G. Di Capua, and R. Miceli, “Power Management Strategies for Tramway Networks Supported by Energy Storage Systems and Renewable Sources,” in *2025 IEEE 19th International Conference on Compatibility, Power Electronics and Power Engineering (CPE-POWERENG)*, IEEE, May 2025, pp. 1–6. doi: 10.1109/CPE-POWERENG63314.2025.11027300.

[194] A. Cano, P. Arévalo, D. Benavides, and F. Jurado, “Sustainable tramway, techno-economic analysis and environmental effects in an urban public transport. A comparative study,” *Sustainable Energy, Grids and Networks*, vol. 26, p. 100462, Jun. 2021, doi: 10.1016/j.segan.2021.100462.

[195] Y. Yan, Q. Li, W. Chen, B. Su, J. Liu, and L. Ma, “Optimal Energy Management and Control in Multimode Equivalent Energy Consumption of Fuel Cell/Supercapacitor of Hybrid Electric Tram,” *IEEE Transactions on Industrial Electronics*, vol. 66, no. 8, pp. 6065–6076, Aug. 2019, doi: 10.1109/TIE.2018.2871792.

[196] Q. Li, T. Wang, C. Dai, W. Chen, and L. Ma, “Power Management Strategy Based on Adaptive Droop Control for a Fuel Cell-Battery-Supercapacitor Hybrid Tramway,” *IEEE Trans Veh Technol*, vol. 67, no. 7, pp. 5658–5670, Jul. 2018, doi: 10.1109/TVT.2017.2715178.

[197] Y. Han, Q. Li, T. Wang, W. Chen, and L. Ma, “Multisource Coordination Energy Management Strategy Based on SOC Consensus for a PEMFC–Battery–Supercapacitor Hybrid Tramway,” *IEEE Trans Veh Technol*, vol. 67, no. 1, pp. 296–305, Jan. 2018, doi: 10.1109/TVT.2017.2747135.

[198] P. Arévalo, A. Cano, and F. Jurado, “Comparative study of two new energy control systems based on PEMFC for a hybrid tramway in Ecuador,” *Int J Hydrogen Energy*, vol. 45, no. 46, pp. 25357–25377, Sep. 2020, doi: 10.1016/j.ijhydene.2020.06.212.

[199] “VIPVLIB. Available: https://github.com/hamidsmd/VIPVLIB”.

[200] https://www.amat.pa.it/tram/, “Tram.”

[201] “Diesel prices. Accessed: Aug. 15, 2025. [Online]. Available: https://www.globalpetrolprices.com/Belgium/diesel_prices/”.

[202] “Electricity prices for household consumers - bi-annual data (from 2007 onwards). Accessed: Jul. 14, 2025. [Online]. Available: https://ec.europa.eu/eurostat/databrowser/view/nrg_pc_204/default/table?lang=en”.

[203] “Charging stations for electric cars in Palermo. Accessed: Aug. 15, 2025. [Online]. Available: https://chargemap.com/cities/palermo-IT”.

[204] ICAO, “The World of Air Transport in 2021 ,” https://www.icao.int/sustainability/WorldofAirTransport/Pages/the-world-of-air-transport-in-2021.aspx.

[205] S. Mahesh and S. C. Calvert, “Decarbonizing airport access: A review of landside transport sustainability,” *Transp Res D Transp Environ*, vol. 140, p. 104625, Mar. 2025, doi: 10.1016/j.trd.2025.104625.

[206] L. Rupcic, E. Pierrat, K. Saavedra-Rubio, N. Thonemann, C. Ogugua, and A. Laurent, “Environmental impacts in the civil aviation sector: Current state and guidance,” *Transp Res D Transp Environ*, vol. 119, p. 103717, Jun. 2023, doi: 10.1016/j.trd.2023.103717.

[207] N. Zuniga-Garcia and R. B. Machemehl, “Impact of Transportation Network Companies on Ground Access to Airports: A Case Study in Austin, Texas,” *Transportation Research Record: Journal of the Transportation Research Board*, vol. 2675, no. 12, pp. 13–27, Dec. 2021, doi: 10.1177/03611981211031205.

[208] M. Wei, C. Yang, and T. Liu, “An Integrated Multi-Objective Optimization for Dynamic Airport Shuttle Bus Location, Route Design and Departure Frequency Setting Problem,” *Int J Environ Res Public Health*, vol. 19, no. 21, p. 14469, Nov. 2022, doi: 10.3390/ijerph192114469.

[209] S. Helber, J. Broihan, Y. Jang, P. Hecker, and T. Feuerle, “Location Planning for Dynamic Wireless Charging Systems for Electric Airport Passenger Buses,” *Energies (Basel)*, vol. 11, no. 2, p. 258, Jan. 2018, doi: 10.3390/en11020258.

[210] L. Tous *et al.*, “Overview of key results achieved in H2020 HighLite project helping to raise the EU PV industries’ competitiveness,” *Progress in Photovoltaics: Research and Applications*, vol. 31, no. 12, pp. 1409–1427, Dec. 2023, doi: 10.1002/pip.3667.

[211] Z. Liu *et al.*, “Data-driven simulation-based planning for electric airport shuttle systems: A real-world case study,” *Appl Energy*, vol. 332, p. 120483, Feb. 2023, doi: 10.1016/j.apenergy.2022.120483.

[212] “Emissions in Belgium. Accessed: Aug. 15, 2025. [Online]. Available: https://www.nowtricity.com/country/belgium/”.

[213] N. Helbig, H. Löwe, and M. Lehning, “Radiosity Approach for the Shortwave Surface Radiation Balance in Complex Terrain,” *J Atmos Sci*, vol. 66, no. 9, pp. 2900–2912, Sep. 2009, doi: 10.1175/2009JAS2940.1.